REFLUX CONDENSATION PHENOMENA

IN

SINGLE VERTICAL TUBES

by

RENE GIRARD

A Thesis

Submitted to the School of Graduate Studies

in Partial Fulfilment of the Requirements

for the Degree

Ph.D. in Nuclear Engineering

McMaster University

SEPTEMBER 1985

Reflux Condensation Phenomena in Single Vertical Tubes

DOCTOR OF PHILOSOPHY (1985)
(Nuclear Engineering)

McMASTER UNIVERSITY
Hamilton, Ontario

TITLE: Reflux Condensation Phenomena in Single Vertical Tubes

AUTHOR: René Girard, B.Sc.A. (Ecole Polytechnique de Montréal)

M. Ing. (nucléaire) (Ecole Polytechnique de Montréal)

SUPERVISOR: Dr. J.-S. Chang

Number of pages: xxxix, 395

ABSTRACT

Reflux condensation in vertical inverted U-tube steam generators forms an important heat removal mechanism for nuclear reactors in certain accidents. Reflux condensation phenomena in single vertical tubes were studied for two well defined boundary conditions to develop an improved understanding of the mechanisms governing heat removal and liquid holdup. A correspondence between an imposed boundary condition and its resulting flow regime has been made where total reflux condensation occurs for an imposed drop across the tube and fill and dump cycling occurs for an imposed steam flow rate at the tube inlet.

Total reflux condensation is characterized by a flow pattern made by a single-phase region oscillating over a two-phase region. This flow regime can be maintained indefinetely while the average single-phase and two-phase region lengths remain constant. It is also characterized by the complete condensation of the injected steam with all the condensate flowing back to the tube inlet.

Fill and dump cycling is characterized by a cyclical operation where, during one cycle, the length of the

single-phase region increases at the expense of the two-phase region until a point where the system becomes unstable and the single-phase region is ejected from the top of the tube. All the injected steam is condensed and contrary to total reflux condensation, not all the condensate flows back to the tube inlet. Instead, part of the condensate is carried over the condensation length to form the single-phase region. This flow regime could be qualified as dynamic as opposed to quasi-static for total reflux condensation.

Experimental measurements were made in three single vertical tubes with a cooling jacket. These data show fill and dump cycling to be more efficient than total reflux condensation in condensing steam and to allow the condensate not to be trapped in the tube as in total reflux condensation. In addition, the experimental data suggest that total reflux condensation could be well the limiting flow regime for fill and dump cycling as the cycle period becomes very long and consequently it could define conservative lower bounds for the values of total heat removal.

An analysis of counter-current film-wise condensation was conducted to model total reflux condensation. central to this model is an extended Nusselt's model of film-wise condensation, a linearized stability analysis of the condensate film flow and the use of three concepts: critical layer, maximum mechanical energy transfer and film instability. The agreement between the experimental data and the prediction of total heat removal (via condensation rates) and liquid holdup is satisfactory. Both the present model and the experimental data show that flooding occurs at the tube inlet and plays a key role in defining the heat removal and the distribution of condensate in the tube. In particular, it is shown that for a given inlet cooling water temperature, the flooding flow rates, in terms of the Kutateladze variable, are nearly independent of the tube diameter and the system pressure. In general, for a given tube size and system pressure, the inlet cooling water temperature has a notable influence on the value of the flooding flow rates, except for the smaller tube size, and it does not affect the amount of condensate holdup in the tube.

The results of the present work could be used in small-break LOCA analyses were the present model could estimate the heat removal capabilities of steam generators and the amount of coolant (condensate holdup) trapped in the steam-generator tubes that would be available for core cooling.

A mes parents et à mes deux soeurs qui ont su

maintenir en moi la flamme du désir de vaincre.

ACKNOWLEGMENTS

The author is thankful to Dr. J.-S. Chang for his supervision, patience and continuing encouragement. The generosity, friendship, support, encouragement, and fruitful discussions with Dr. J.S. Kirkaldy are gratefully acknowledged. The help and support of the two other members of the Ph.D. commitee Dr. J. Vlachopoulos and Dr. C.M. Crowe are also gratefully acknowledged. Studying under their guidance made the time spent at McMaster University a challenging and rewarding experience.

The invaluable help of Mr. Emmanuel C. Morala in the process of setting up the two apparatuses, in preparing and testing the NOVA III computer, in designing, building up and testing the needed electronics is gratefully acknowledged. He was a key person in the experimental program of this thesis. Mr. Geno Innocente, Mr. Willie Schrader and Mr. Yosh Kitamura of the Intrumentation Machine Shop showed a high degree of competence and a sense of professionalism in machining the various parts of the two apparatusses and in giving many useful advices. Their help is gratefully acknowledged. The same goes to Mr. Leo Matikanen of the Glass

Shop, Mr. Jim Meyer of the Engineering Machine Shop and to Mr. Bill McMicking of the Student Machine Shop. The help from Kenrick Chin for the many repairs of the NOVA III is gratefully appreciated.

The high sense of professionalism and the high degree of competence of Ms. Marianne Van der Wel and Ms. Maria Romanowski of the Computer Center in the great help provided are highly appreciated.

The many fruitful discussions with Dr. Pak T. Wan and Dr. Shripad T. Revankar played an important role in the modelling of total reflux condensation. The great help form Dr. Shripad T. Revankar in performing the fill and dump cycling and the upward co-current annnular flow experiments are gratefully acknowledged.

The very fruitful interactions with my friends in NRB: Esam Hussein, Peter Yuen, Francis Tran, Deitrich Abraham, Joel Miller, Leo Lightstone, Ed Beaver, Richard Tervo, Diane Lowe, and Dave Bot made my stay at McMaster a very pleasant experience.

The financial assistance from the Ministère de l'Education du Québec through 3 years Québec-Ontario Exchange Scholarship, from the Ontario Ministry of Colleges and Universities through an Ontario Graduate Scholarship, from McMaster University through a University Graduate

Scholarship and from Rockwell International through a Graduate Scholarship is gratefully acknowledged. The financial assistance from Ontario Hydro is also gratefully acknowledged. The help provided by the Institut de Génie Energétique of Ecole Polytechnique de Montreal by making many of their facilities available to complete this thesis is gratefully acknowledged.

The efficiency, the care, the patience and tireless effort of Miss Hélène Létourneau in keeping up with my many changes during the typing of this thesis are gratefully appreciated.

TABLE OF CONTENTS

LIST OF ILLUSTRATIONS

Reflux Condenser Section

Figures G.45 to G.50: Local Measurements in 1.27 cm O.D. Tube with TCwl = 45°C 356

LIST OF TABLES

CHAPTER 1

INTRODUCTION

A schematic of the CANDU PHWR(*) nuclear steam supply system is shown in Figure 1.1 where under normal operating conditions the fuel is well cooled by the reactor coolant circulated by the primary pumps. This mode of fuel cooling may be disrupted or may deteriorate under various accident scenarios where loss of forced circulation occurs.

These accident scenarios define conditions where steam generators can act as an important heat sink. An illustration of this important possibility can be seen by considering a situation where heat (perhaps at decay levels) is generated in the reactor core and only a portion of it can be transported out through a small leak or break in the primary heat transport system. In this case, there may be some additional heat losses through the system piping components, but the steam generators become the major heat sink.

Coolant loss can result from valve breakdown,

(*) CANDU PHWR: CANada Deuterium Uranium Pressurized Heavy-Water Reactor.

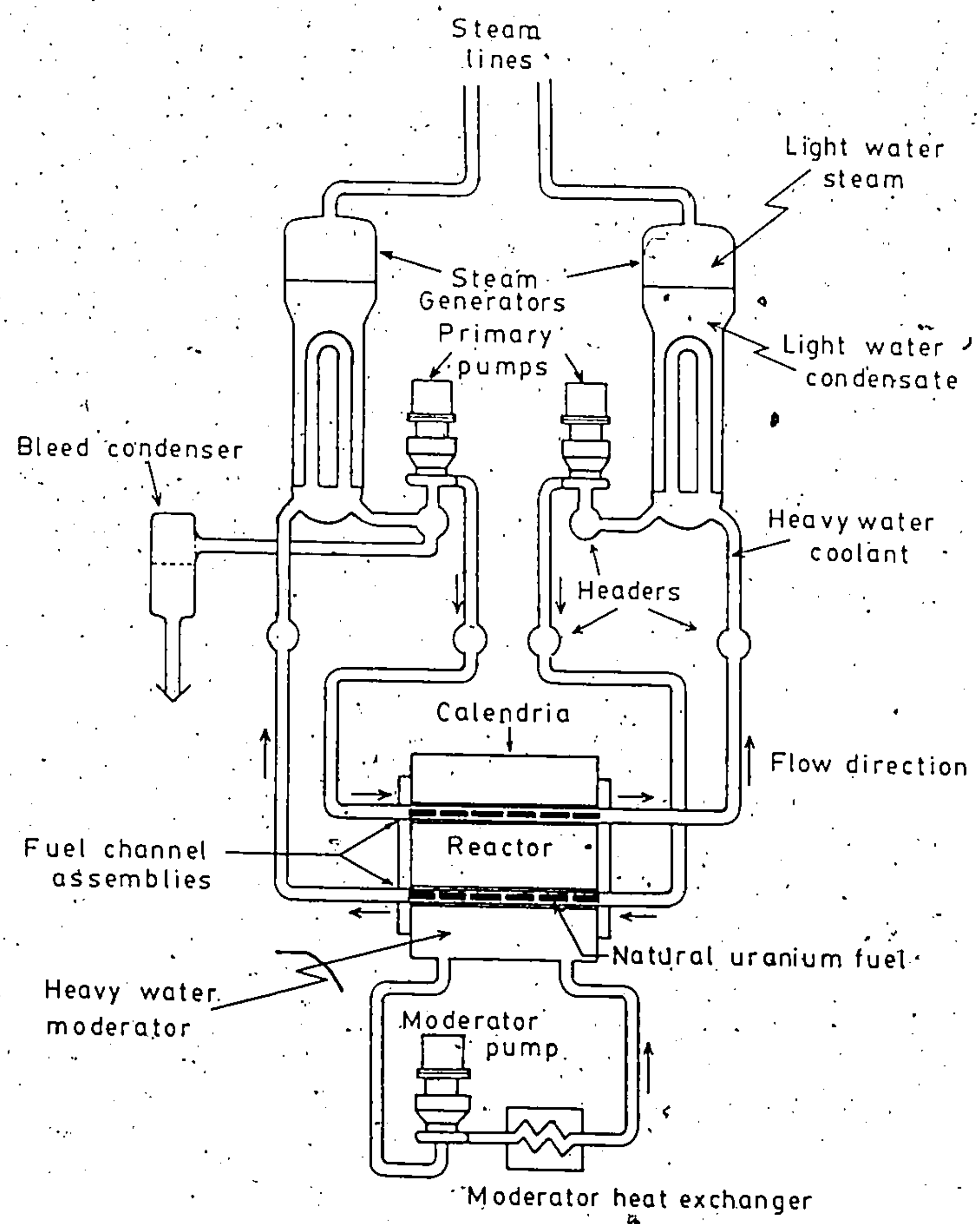

FIGURE 1.1 CANDU Nuclear Steam Supply System

break in instrumentation lines, or the malfunction of the refuelling machine, or less probable, from the break of a feeder and/or a header. Table 1.1 gives the distribution of the piping diameters found in a typical CANDU heat transport system [1]. It can be seen that small breaks (diameter <100 mm) are the most probable.

Depending on the particulars of the accident scenario [2,84], such as the primary pumps rundown time, the location and size of the break, and the details of the emergency core cooling system, different heat removal mechanisms may occur in the steam-generator tubes. These include reflux condensation, single and two-phase thermosyphoning.

From a reactor safety point of view, the single-phase and two-phase thermosyphoning modes of core cooling are reasonably well understood [2]; however, the present understanding of reflux condensation phenomena does not permit an adequate estimate of the heat removal capabilities of the steam generators when reflux condensation is the postulated heat rejection mechanism. In general, the heat rejected to the secondary side is greater with two-phase thermosyphoning than with reflux condensation. It is therefore of primary importance to study reflux condensation to estimate the maximum amount of heat that can be rejected to the secondary side of the steam generators when they are

TABLE 1.1: DISTRIBUTION OF PIPING DIAMETERS IN A TYPICAL CANDU HEAT TRANSPORT SYSTEM (Reproduced from |1|)

TYPE OF PIPING WITH TYPICAL DIAMETER	LENGTH (m)	PERCENTAGE OF TOTAL
Steam generator tubes (14 mm)	405 000	91.35
Instrumentation lines (approx. 10 mm)	18 300	4.12
Feeders (50 mm to 90 mm)	14 000	3.15
Pressure tubes (100 mm)	5 500	1.24
Other small diameter pipes (< 150 mm)	400	0.09
Large diameter pipes (> 150 mm)	200	0.05

available as heat sink with reflux condensation as the postulated heat rejection mechanism. This could result in establishing estimates for the lower bounds of their heat removal capabilities.

1.1 REFLUX CONDENSATION PHENOMENA

Reflux condensation phenomena in a vertical tube are characterized by an upward vapor flow that condenses on the relatively colder tube wall. The condensate flows back by gravity towards the tube entrance counter-current to the vapor flow. The counter-current nature of the flow regime makes it prone to condensate flow limitation due to film instability known as the flooding phenomenon.

The phenomena encountered in a relatively short reflux condenser with increasing inlet vapor flow are basically as follows [3]. At low vapor flow a smooth falling liquid film is observed. An increase in vapor flow causes the appearance of small disturbance waves on the interface of the film, these are particularly marked at the tube entrance. A further increase in vapor flow causes the waves at the tube entrance to increase such that an intermittent churn-annular flow is established; however, the reflux rate increases only slightly. Eventually, a vapor velocity is reached which is sufficient to eject liquid from the top of the tube, this is accompanied by an important rise in pressure drop across the tube, as shown in Figure 1.2, and is usually taken to be the flooding point. If the vapour flow is increased further an upward co-current annular flow is eventually established.

In a typical CANDU 600 MWe steam generator, the minimum straight length found in the U-tubes is about 8 meters. For the accident conditions described above, where reflux condensation is the expected heat removal mechanism, the straight lengths in each U-tube can be considered as a long reflux condenser. For this case it is not clear yet if the phenomena encountered will be the same as the one that have been observed in a relatively short reflux condenser. The role of flooding could be similar for both cases; however, due to the length, it could have different consequences on the condensate flow distribution and then on the phenomena occurring in the system. Also, due to the geometry of the steam generators we could have tube-to-tube instabilities and oscillations which will obviously affect the type of phenomena present in the system.

Flooding in reflux condensation can be associated to flooding in an adiabatic system with mass transfer at the liquid-gas interface. The film stability will depend on the resulting restoring force acting on the wavy interface made of the simultaneous action of surface tension, gravity, and condensation mass transfer. This force is opposed against

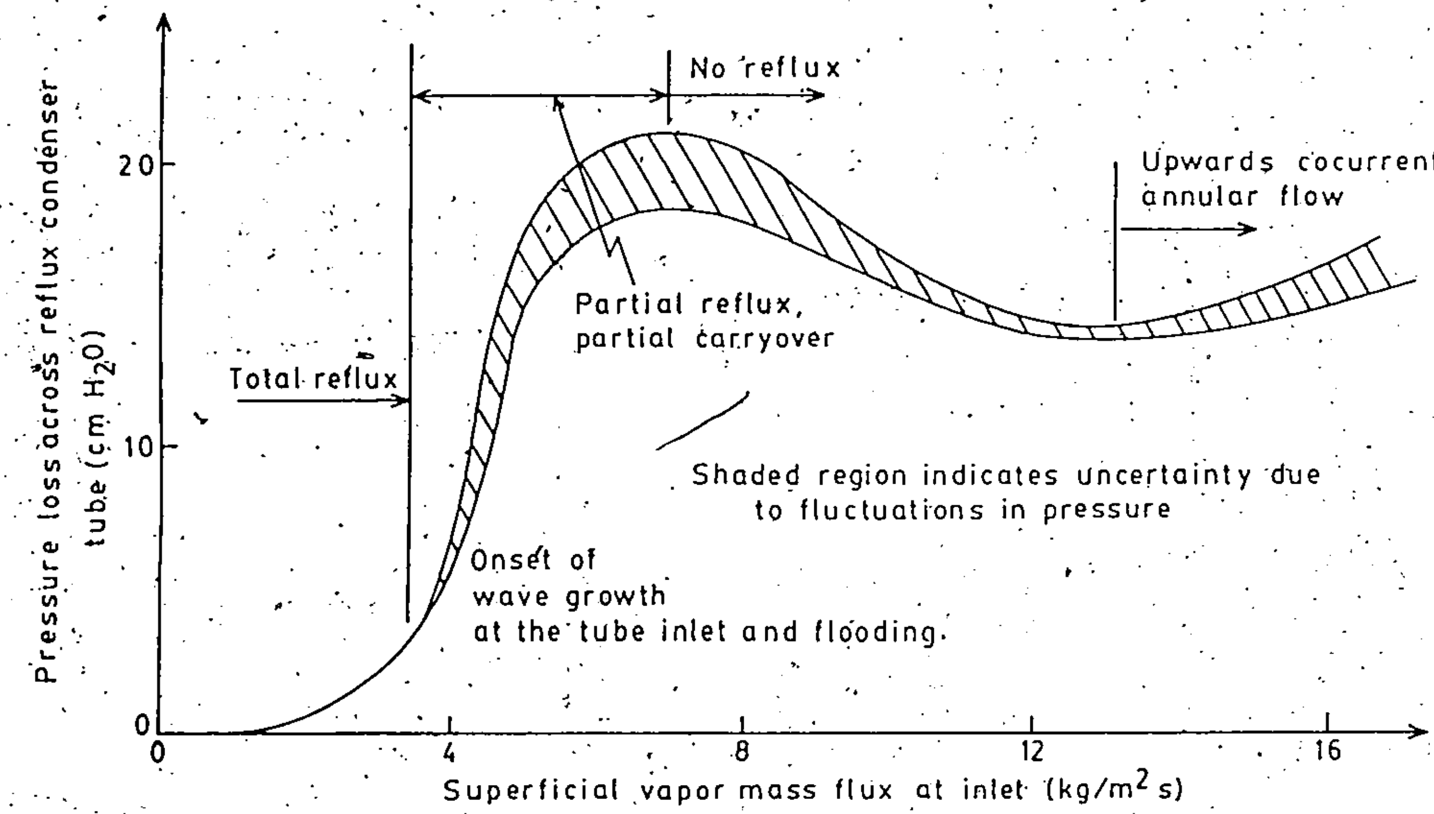

FIGURE 1.2 Pressure Drop Characteristic Curve for a Relatively Short Reflux Condenser (After Deakin [3])

the force from the normal and tangential stresses due to the gas flowing over the wavy interface. The net force acting on the interface will be dissipative in nature and could do work on the interface leading to a net transfer of mechanical energy from either the gas to liquid phase or the inverse. The wavy interface implies the existence of a critical layer at a position from the interface where the celerity of the waves equals the velocity of the phase in which the critical layer is present. In general, for counter-current annular flow with waves moving downwards with the film, the critical layer can occur in both phases or neither phase as opposed to co-current annular flow, where normally the maximum velocity in the liquid film occurs at the interface, and consequently the critical layer can only be in the gas phase. This implies that a critical layer cannot exist in the liquid film if one already exists in the gas phase. The position of this critical layer determines the sense of the net transfer of mechanical energy. In counter-current flow, the position of the critical layer could be such that a net transfer of mechanical energy from the gas to the liquid phase and film stability is ensured if this net transfer of mechanical energy is absorbed by viscous dissipation. In the case where the transferred mechanical energy is not completely absorbed, film instability occurs and leads to the growth of disturbance waves and consequently flooding takes place.

The mathematical modelling of reflux condensation can be done by extending the classical Nusselt's theory of film-wise condensation to the case where three of the basic assumptions are relaxed: the drag on the steam-water interface and consequently the momentum transfer through the film are no longer negligible, plus the heat transfer is not by conduction alone but also by convection. A model of reflux condensation is not complete without taking into account the flooding phenomenon. In the mathematical modeling of the flooding phenomenon, the two concepts of critical layer and film instability can be used to determine the value of the critical wave length corresponding to the maximum amount of mechanical energy that can be transfer to the liquid film. This critical wavelength is related to a critical positive amplification factor which in turn corresponds to a minimum interfacial friction velocity necessary to have flooding in the tube. This minimum value of the interfacial friction velocity will give by definition the value of the steam mass flow rate at the flooding point. These three concepts: critical layer, film instability and maximum energy transfer along with an extended Nusselt's of film-wise condensation form the basis of the present experimental and analytical study.

1.2 LITERATURE SURVEY

Only few papers exist on the general topic of reflux condensation, especially in the case of long reflux condensers. On the other hand, many papers are available on the general topic of flooding; however, the majority consider adiabatic systems exclusively, only few of them are on the flooding phenomenon with condensation mass transfer.

1.2.1 Reflux Condensation

The predominant modes of coolant circulation mentioned above have been observed to occur in experimental test rigs [2,4,5,8,9,86,87]. These experiments were done to show the influence of such parameters as power, reduced water inventories on the primary and secondary sides, and noncondensible gas on the ability of the system to remove heat at decay level.

Steady-state and transient experiments were conducted with the PKL [4] and the Semiscale Mod-4 [5] test facilities. Steady-state reflux condensation, single-phase and two-phase thermosyphoning modes of operation were established by draining discrete amount of coolant from the primary circuit and allowing sufficient time for steady-state conditions to be achieved between drains. The overall loop natural circulation mass flow rate was found to vary considerably, depending on system mass inventory. The variation in loop mass flow rate with inventory reflects a transition from single-phase to two-phase thermosyphoning to reflux condensation. The later mode of heat removal was found to occur for primary mass inventories of 70 to 80%, i.e. when the steam generator tubes and hot leg are nearly voided of coolant and the steam generated in the core is condensed in the steam generator tubes. During transient experiments, all the major operating modes were observed including reflux condensation, single-phase and two-phase thermosyphoning. A description of the above mentioned physical phenomena can be found in [6], where the influence of various PWR (American) design parameters in the consequences of small-break LOCAs is discussed and classes of small-break LOCAs are defined based on break area. In general, most of the description given in that reference could be transposed to CANDU reactor; however, some design particularities such as the inverted U-bend at the primary circulation pumps (see Figure 1.1) may affect the overall behavior of the system [7].

In all the accident cases mentioned above the steam generator can be assimilated to an inverted U-tube steam condenser. A study [8] on the flow regimes in an array with steam condensation reveals four possible modes of condensation. The array was made of four inverted glass U-tubes connected to plenums as in an actual steam generator. At high inlet steam mass flow rate co-current annular flow occurs in all the tubes with condensate and steam flowing into the exit plenum. As the steam flow rate is reduced, one or more tubes begin to be blocked maintaining a steady state water column above the two phase region where the condensate flowing back to the tube entrance (reflux rate) was supposed to be determined by a flooding criterion and the others are still with co-current annular flow. A subsequent reduction in the steam flow rate initiates a fill and dump cycle with wide oscillations in pressure, it is not mentioned whether some or no condensate was flowing back to the tube inlet. For still lower flow rates, reflux condensation occurs with all the condensate returning to the tube inlet. The same experiment was performed for a single inverted U-tube, no tube blockage was observed; instead, a direct transition from co-current annular flow to fill and dump mode of operation occurred as the inlet steam flow rate is reduced. Reflux condensation eventually prevailed as the steam flow is further reduced.

Another study [88] in an array with the same number (4) of inverted glass U-tube as in the set-up used by Calia and Griffith [8], show only three possible flow regimes: reflux condensation without water column, reflux consensation with water column and co-current annular flow.

The flow regime where fill and dump cycle occurs, was not observed. This difference between the two studies could be attributed to the way steam is injected in the inlet plenum, resulting in a different boundary condition in each system and also to the possible interactions between the tubes that could have a significant influence on the flow regimes boundaries.

Studies [9,87] in a single inverted U-tube confirmed these later observations and they indicated that for a fixed inlet steam mass flow rate the three regimes (reflux condensation, fill and dump mode and co-current flow) could be made to occur by changing the cooling water flow rate instead of the inlet steam flow rate.

For the case of imposed constant pressure drops across a single inverted U-tube steady-state reflux condensation has been observed with water column blocking the tube [86]. It should be noted here that no clear correspondance between an imposed boundary condition on the system and its resulting flow regime has been mentioned yet in the open literature.

Moreover, an important characteristic of the phenomena observed is the existence of a range of inlet steam flow rate and cooling conditions where a steady or intermittent accumulation of condensate is present in the system in the form of water columns above the two phase regions. In an actual highly voided reactor system this accumulated condensate could represent a significant amount of inventory unavailable for core cooling. This could be the phenomena occurring when the two-phase thermosyphoning mode of reactor core cooling breaks down.

For single tube systems, most of the work done on reflux condensation were, until recently, experimental in nature, the emphasis was on the determination of the flooding point and of the system pressure drop characteristic curve as a function of the inlet steam mass flow rate. In most studies relatively short vertical reflux condenser were used [10-12,16], i.e. with set-ups having a tube length-diameter ration (ℓ/D) less than 100, where in a CANDU steam generator it is about 800. In general, the characteristic curve, shown in Figure 1.2, was observed, Deihl and Koppany [11] suggest the existence of a critical diameter above which the flooding velocity remains constant where on the contrary English et al. [10] suggest continuous influence of the tube diameter. Deakin et al. [12] use only one tube size their study. The entrance condition was shown by English et al. to have an influence on the flooding velocity. No tube blockage or fill and dump cycles, similar to the one mentioned before [8,9,86], has been mentioned in these previous studies.

Deakin [3] did a comparison of the various flooding correlations, the results are presented in Figure 1-3a,b where the Andale correlation is taken from the paper of English et al. [10]. The ratio L/G can be define as the amount of condensate flowing back to the tube inlet divided by the inlet steam mass flow rate. The two figures illustrate a significant discrepancy between the various correlations, the largest one is found in Figure 1.3a where, in the case of total condensation (L/G = 1) Deihl and Koppany predict a flooding velocity 1.7 times the one predicted by English et al. The Wallis correlation [13, p.339-341] for adiabatic system:

$$j_g^{*1/2} + m\, j_\ell^{*1/2} = C \tag{1.1}$$

where,

$j_k^{*1/2}$: $j_k \rho_k [gD(\rho_\ell - \rho_g)]$

and j_k : superficial volumetric flux (m^3/m^2-s)

ρ_k : density of phase "k" (kg/m^3)

g : gravitational constant (9.81 m/s)

D : tube inside diameter (m)

ρ_ℓ : liquid phase density (kg/m^3)

ρ_g : gas phase density (kg/m^3)

m,C : constants

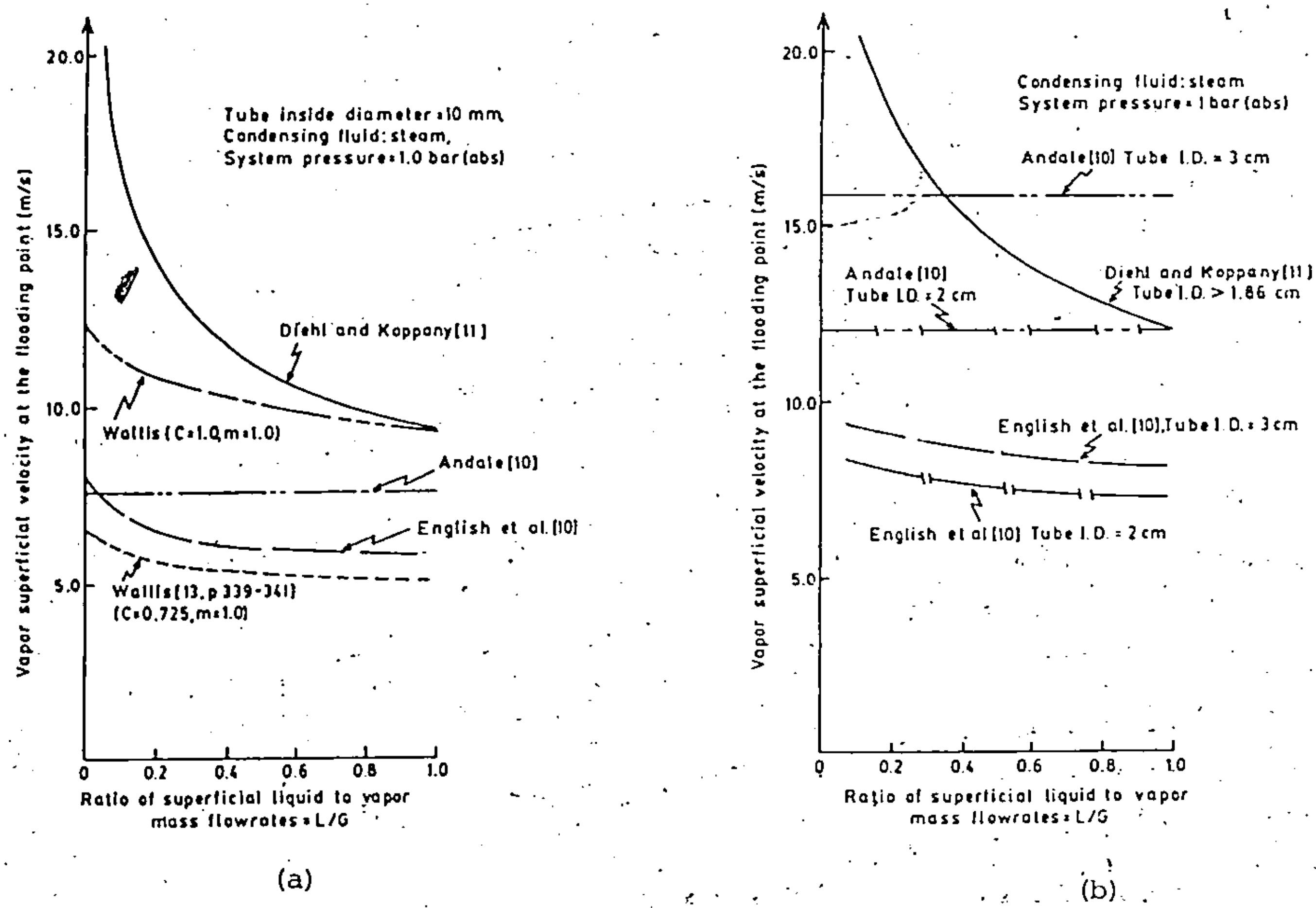

FIGURE 1.3 Comparison of the Various Flooding Correlations (After Deakin [3])

is also shown for two different values of "C", which depend on the entrance conditions. An examination of Figure 1.3a and 1.3b shows qualitatively that all the correlations agree on the fact that the smallest flooding velocity occurs in the case of total reflux condensation (L/G = 1). This implies in an inverted U-tube condenser that if the ratio L/G is less than one at the inlet of one leg, more steam could be condensed overall, assuming the fraction of the steam flow not condensed by reflux condensation in the inlet leg, will be condensed in the outlet leg. Then, total reflux condensation with steady-state water column represents, in the context of reactor safety, the worst case that can occur, because it could defines lower bounds for the heat from the core that can be rejected to the steam generators secondary side.

Tien et al. [16] studied reflux condensation in a vertical closed-type thermosyphon with the condenser lenght-diameter ratio (ℓ/D) equal to 14.6, they studied the effect of interfacial shear stresses on reflux condensation heat transfer and their experimental results show a deviation of ±15% from the classical Nusselt solution [18] and they concluded that it was difficult to attribute the scattering of the data to the effect of interfacial shear stresses. For their system, having a tube length-diameter ratio ℓ/D around 150, Calia and Griffith [8] did not addressed the problem of finding a quantitative criterion for counter-current flow limitation and the heat transfer in reflux condensation with or without tube blockage; however, they suggest the use of Wallis correlation (see equation (1.1)).

Another relevant paper to the present study is that of Russell [14] where the system length-diameter ratio (ℓ/D) is about 250 and the air cooled mild steel reflux condenser was inclined 57^{o} from the horizontal. The pressure drop characteristic curve for that system is presented in Figure 1.4, where it is compared with the result of Deakin and al. [12]. It can be seen that the value of the length-diameter ratio (ℓ/D) of the condenser used has not only a strong influence on the shape of the characteristic curve but also on the overall behaviour of the system, where a cycling operation takes place above a critical inlet steam flow rate.

The nature of this cycling operation is very similar to the fill and dump mode of operation for a single inverted U-tube [8,9]. Before reaching the range of flow rates where cycling operation occurs, Russell did observe tube blockage with a steady-state water column above a two-phase region where the selected pressure drop across the tube could be held indefinitely; however, Calia and Griffith did not observed the same phenomena in their single tube experiments, in fact they suggest that for an imposed

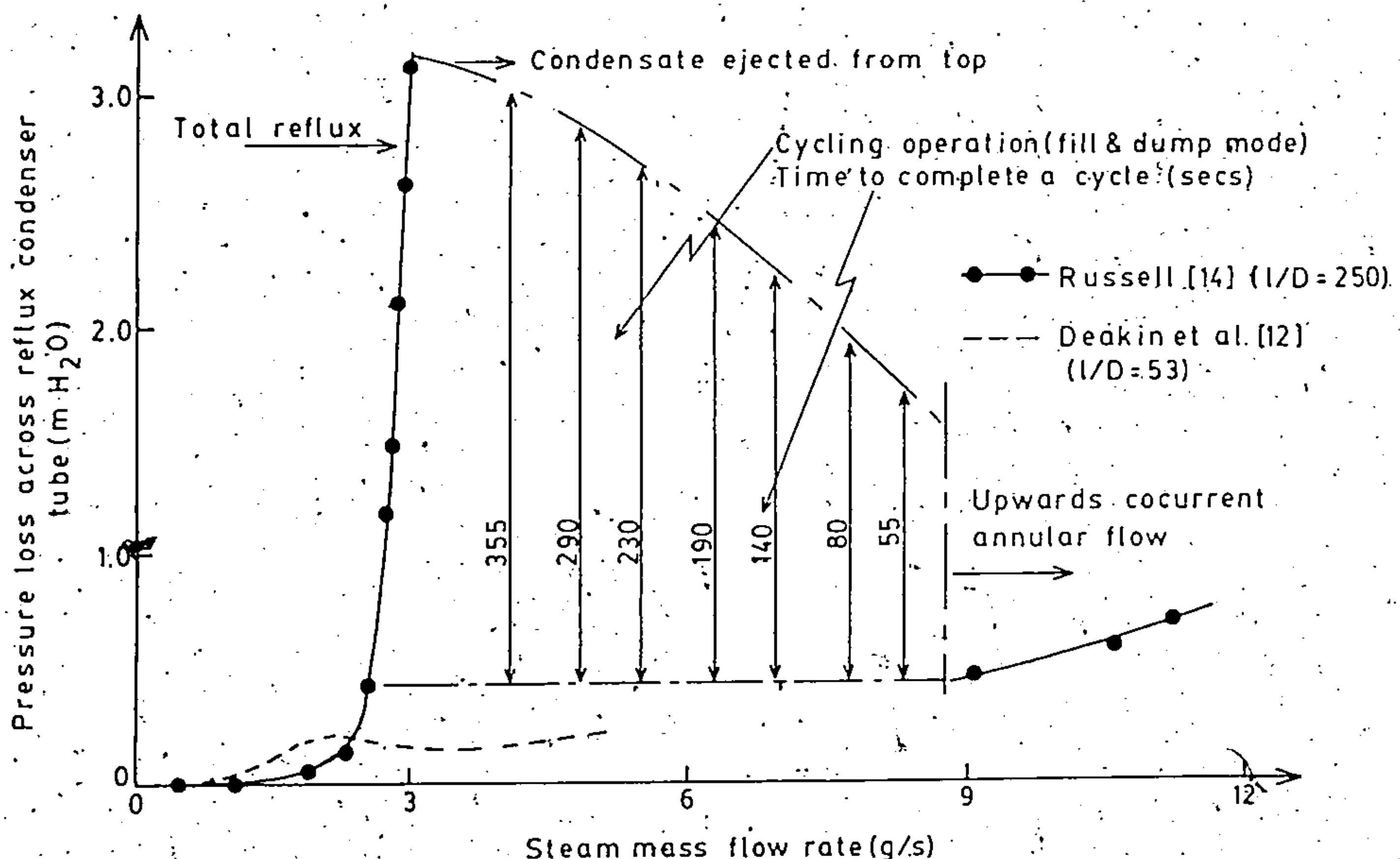

FIGURE 1.4 Comparison Between Experimental Data from Relatively Long ($\ell/D = 250$) and Short ($\ell/D = 53$) Reflux Condensers (After Russell [14])

pressure drop across the tube, reflux condensation with or without a steady-state water column occurs and for an imposed steam mass flow rate the fill and dump modes cycling operation occurs. The difference in the observation made could be due to the orientation of the tube, the boundary conditions used, and the possible presence of non-condensible gas in Russell's experiments.

It can be seen that the open literature presents few experimental studies on reflux condensation and fewer analytical studies are available [15-17] and all three are relatively recent. In all these analytical studies, the annular flow regime was assumed and Nusselt-type analysis were conducted to investigate the influence of interfacial shear and momentum transfer through the film on counter-current film-wise condensation.

Seban and Hodgson [15] presented an analysis where the influence of interfacial shear stresses is included by the means of modified pipe friction coefficient. Their solution includes the case of completely downward (counter-current), partially upward or completely upward (co-current) film flow but requires an a priori knowledge of the film thickness at the tube inlet. In addition, no qualification of the various flow conditions studied with respect to a flooding criterion is presented. The results obtained from their numerical simulation are compared only to the case of laminar film condensation on a vertical plate with upward vapor flow in which vapor flow depletion is assumed to be negligible. No comparison to experimental data is included in their study.

Tien et al. [16] presented an analysis where the influence of interfacial shear stresses is done by the means of a friction coefficient, constant along the condensation length, and given as an input parameter. Their numerical simulation showed a significant influence of the interfacial drag as the heat transfer coefficient is reduced in comparison with the classical Nusselt theory. The influence is enhanced as the tube diameter is reduced and/or as the system experiences an increase in either the condensation length, the heat flux or the operating pressure. Also, they recommended the use of a Wallis-Kutateladze type of flooding correlation [19-20] and they suggested values for the constants "m" and "C".

Sun et al. [17] presented an analysis where the influence of interfacial shear stresses is done similarly as in the work of Seban and Hodgson; however, they used a different correlation for the interfacial friction factor. Their numerical simulation consisted in the calculation of condensation length as a function of the inlet steam flow rate. The computation stops when the steam flow rate reaches the flooding value, the Kutateladze flooding criterion [22] was used in their study and it corresponds to a point where no downflow of liquid occurs [23].

Finally, it should be noted that the available open literature on reflux condensation does not present a systematic study on the influence of the condenser tube diameter and ends geometry, steam flow rate, cooling water temperature, amount of non-condensible gas in the system and system pressure on the phenomena occurring in a vertical single-tube steam condenser. All these for the following two tube ends boundary conditions: an imposed constant pressure drop across the tube ends and an imposed steam flow rate at the tube inlet. Very little experimental data are available at this time on the influence of these parameters on the rate of condensation, condensation length, single-phase length and axial pressure, temperature, void fraction and local heat removal profiles. These experimental data are needed for the validation and development of models in small-break LOCAs [17] safety analyses.

1.2.2 Flooding

Many papers have been published on the general topic of flooding because of the importance of the flooding phenomenon in the emergency cooling of nuclear reactors and recently in long-term core cooling under non-forced circulation conditions. In most of this work, flooding correlations were developed from data taken in air-water systems and some investigation varied the physical properties of the phases, the entrance conditions, or the dimensions of the system and related these changes to the onset of flooding. A limited amount of studies have been presented on the theoretical analysis of flooding with and without phase change at the liquid-gas interface. The brief discussion of this earlier work presented below, will focus mainly on the papers which are important from the stand point of the present study and more can be found in two excellent reviews [25,29] on counter-current two-phase flow and flooding published recently.

In vertical adiabatic systems, several investigators [19,21,23,26-29] have observed that as the flow approaches the flooding condition, the liquid film becomes highly agitated and forms a standing wave at a certain axial position along the tube and the standing wave plus the accumulated liquid above it, begin to churn and pulsate up toward the liquid injection point, where the propagating speed of the churning motion depends on the flow rates. In particular, some investigators [19,21,23,26,30] observed that for low liquid flow rate flooding occurs at the bottom inlet of the tube and for high liquid flow rate flooding occurs near the point of liquid injection. On the other hand, many investigators suggested that flooding takes place as a result of the formation of an unstable wave that rapidly grows until it bridges the tube; however, measurements [23,26] have shown that bridging does not really occur.

The end geometries, the dimensions of the system and the physical properties (viscosity and surface tension) were found to have a notable influence on the onset of flooding. The tube diameter has been shown to have a strong influence on the flooding point [11,26,28] and the influence of the end geometries were shown to decrease with increasing tube diameters [19,21,30], where for large tubes the maximum possible gas flux reaches an asymptotic value [30]. An increase in surface tension was observed to have a stabilizing effect [19,21], i.e. the gas velocity necessary for flooding at a given liquid flow rate decreases substantially as the liquid surface tension decreases. The contrary was observed for viscosity as it has destabilizing effect as it increases [13,p.339-341, 19,20,31]; however, an opposite result has been reported [26].

As many other complex flow situations, the exact mathematical treatment for vertical counter-current two-phase flow is quite formidable. Extensive idealizations are required to simplify the governing equations in order to obtain any solution, either numerically or analytically. Bankoff and Lee [26] give a classification where several different view points have been expressed for the analytical models. Three classes have been defined:

(i) models in which flooding results form an interface instability due to the different velocities of the two superimposed phases [19,20,28,32,38,41];

(ii) models based upon a combination of interfacial instability and flow maximization (envelope theory) [19,20], or flow maximization alone [30,33];

(iii) models based upon a postulated interfacial shape [34-37].

The comparison of various models with each other and with experimental data [23,25] reveals that the most successful model to predict flooding velocities is given by Cetinbudaklar and Jameson [32] and is based on the interfacial instability of a viscous liquid film; however, the model starts to overpredict the flooding velocity for high liquid flow rates (Re > 1000). This discrepancy could be due to the change in flooding point position as mentioned before. This model includes the effects of surface tension and viscosity explicitly and it predicts well the effect of an increase in viscosity on the flooding velocity [32]. It can also account for the effect of the entrance conditions by varying the entrance interfacial friction factor; however, the effects of the tube diameter are included implicitly.

In that viscous flow model, flooding is postulated to occur when the mechanical energy transfer from the gas phase to the liquid phase is such that travelling waves start to grow and are no longer propagated downward. This postulate has been used successfully in a recent flooding and flow reversal study [38] in which the travelling waves are associated to kinematic waves [39] and previously in a bubble colum study [14, p.139-135]. This postulate is in fact the observation made by several investigations [19,21,24,26-29] put in mathematical form. The other models, although simpler, are reported [25] to be less successful in predicting the data. They do not take into account the entrance condition which appears to be important at high gas flow rates. The models appear to follow the trend shown by the experimental data for an increase in surface tension; however, for an increase in viscosity some models show opposite results [19,20,40].

Condensation mass transfer may play an important role in the mechanism of flooding in reflux condensation. Almost all the work done on flooding in steam-water systems involves direct contact condensation as opposed to indirect contact condensation as in reflux condensation. Theoretical analyses [33,41] on systems involving direct contact condensation showed that condensation mass transfer has a significant stabilizing effect; however, the differences between experimental results from condensing and adiabatic flows are not significant if flooding takes place at the tube inlet and the exit liquid reaches nearly the saturation temperature [25]. There is no theoretical analysis in the open literature on the interface stability in indirect contact condensation (film-wise condensation) where the condensate film interacts with an upward flow of vapor. However, many studies exist that are not directly applicable to flooding in reflux condensation [42-55] but they are related closely to the present theme. They do help to clarify to a certain extend the flooding phenomenon with condensation mass transfer.

1.3 OBJECTIVE AND SCOPE OF THE PRESENT STUDY

The objective of the present study is to develop an improved understanding of the mechanisms governing heat removal and liquid hold-up in reflux condensation in vertical tubes.

In Chapter 1, the justification and the potential application of the present work are outline, along with a brief discussion on the physical definition of reflux condensation and flooding. A literature survey of the available work on reflux condensation shows the present status of the research in that field, thereby pointing out the future research needs. Also included is a brief critical review of the work done on flooding in condensing and adiabatic systems, to indicate that most, if not all, of the existing studies are not directly applicable to reflux condensation in long tubes and suggesting new developments needed.

Chapter 2 briefly describes the physical arrangement of the two experimental apparatuses built and the characteristics of the sensors used for the experimental tests. The experimental procedures and data acquisition and processing software used in the present study are outlined. The chapter ends by the matrix of the experiments given in tabular form along with the dimensions of the tubes used.

Chapter 3 begins by a description of the global behavior of the system for the two boundary conditions studied. These conditions are: either an imposed constant pressure drop across the tube or an imposed inlet steam flow rate. The flow [illegible] and patterns observed for these conditions, are also presented. The chapter ends by the presentation of a phenomenological model to simulate the system behavior when the first test condition is applied.

Chapter 4 presents the experimental results based on the different flow regimes and tube diameters. Three different tube diameters are used in the experiments to see the effect of tube size but only one entrance condition is considered: square edge. The comparison between the experimental data corresponding to the first boundary condition and the model is also presented.

Chapter 5 contains the conclusions and recommendations of the present study.

CHAPTER 2

EXPERIMENTAL APPARATUSES AND PROCEDURES

2.1 REFLUX CONDENSER

2.1.1 Description of the apparatus

In Chapter 1, we have demonstrated that reflux condensation is one of the phenomena that may occur in vertical inverted U-tube steam generators during a small-break LOCA. This phenomenon must be analysed to see if the heat removal capability of steam generator will be sufficient to preserved the integrity of the core in the case of such accident. To this end, reflux condensation was studied in isolation from possible interactions with other system components. A single vertical tube was used to simplify the system as much as possible. It was understood that such a geometry would eliminate the possibility of tube-to-tube instabilities and oscillations. The boundary conditions at each end of the condenser tube were controlled to impose essentially either a constant pressure drop across the tube or a constant steam injection at the tube inlet.

The experimental apparatus is shown schematically in Figure 2.1 It consists of a series of eight consecutive double pipe heat exchangers made of pyrex glass with a total length of 4.81 m. The first to sixth sections are 0.305 m long and the last two sections are 0.606 m and 2.17 m long, respectively. The sections are linked together by Teflon spacers between cooling sections. Teflon spacers allow measurements of pressures, temperatures at the center and near the wall inside the inner tube and the injection of water in each cooling jacket, as shown in Figure 2.2. The inner tube is connected at the bottom to a steam inlet plenum and at the top to an outlet plenum, by a small section of copper tubing. Both plenums are thermally insulated with glass wool.

The steam flow circuit is shown in Figure 2.1, the steam flow rate is adjusted at the control station, then it goes through an orifice meter and a horizontal pipe with a 90^{o} elbow (turned downward) at the end before being discharged into the plenum. Upstream of the orifice meter the thermodynamic state of the steam is evaluated by pressure and temperature measurements.

The flow rates in the cooling-water jackets are individually controlled and measured by valves and orifice meters. The upper plenum is mounted with the combination of a pop and standard relief valve used when the system is

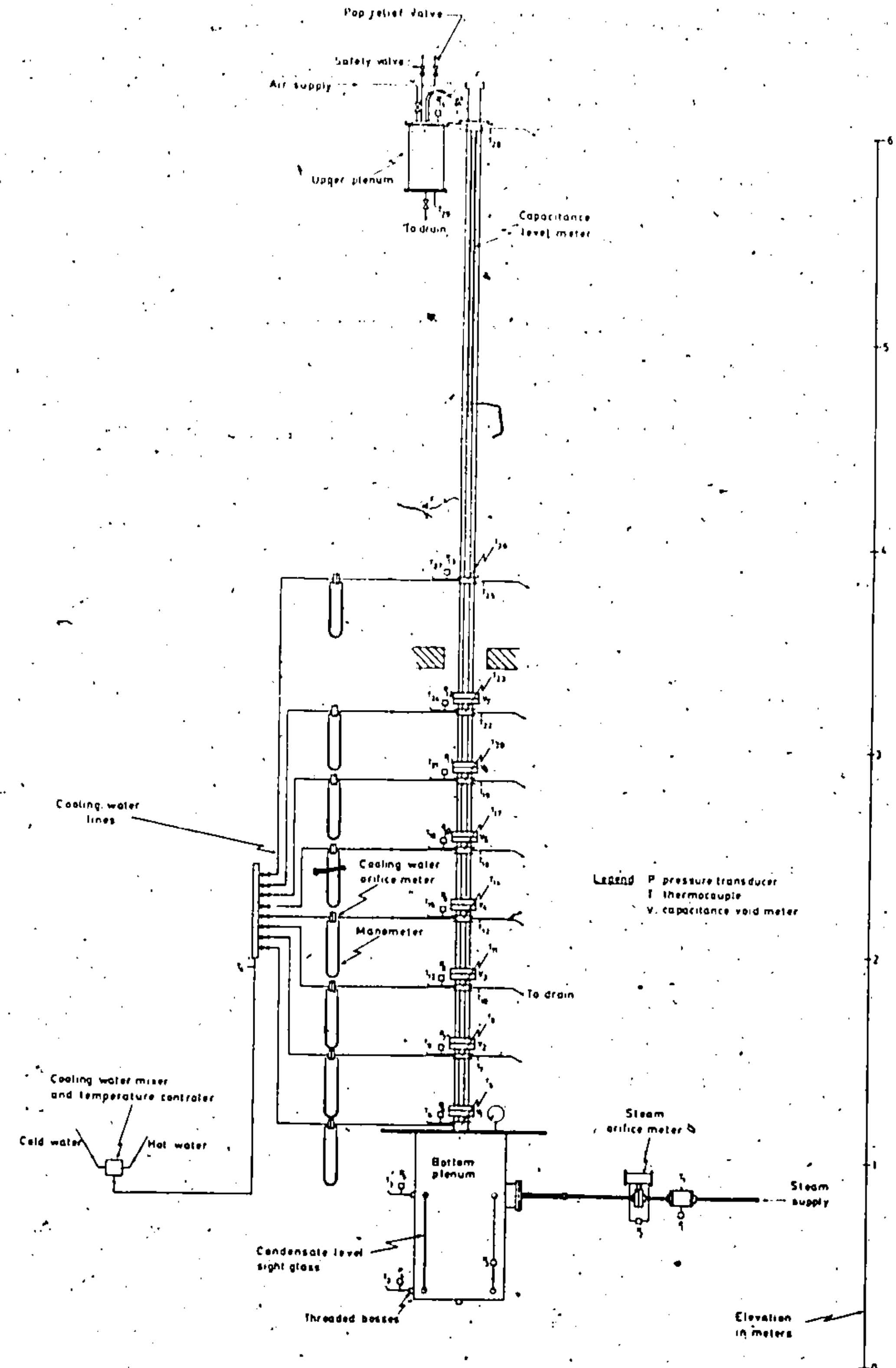

FIGURE 2.1 Schematic of the Reflux Condenser

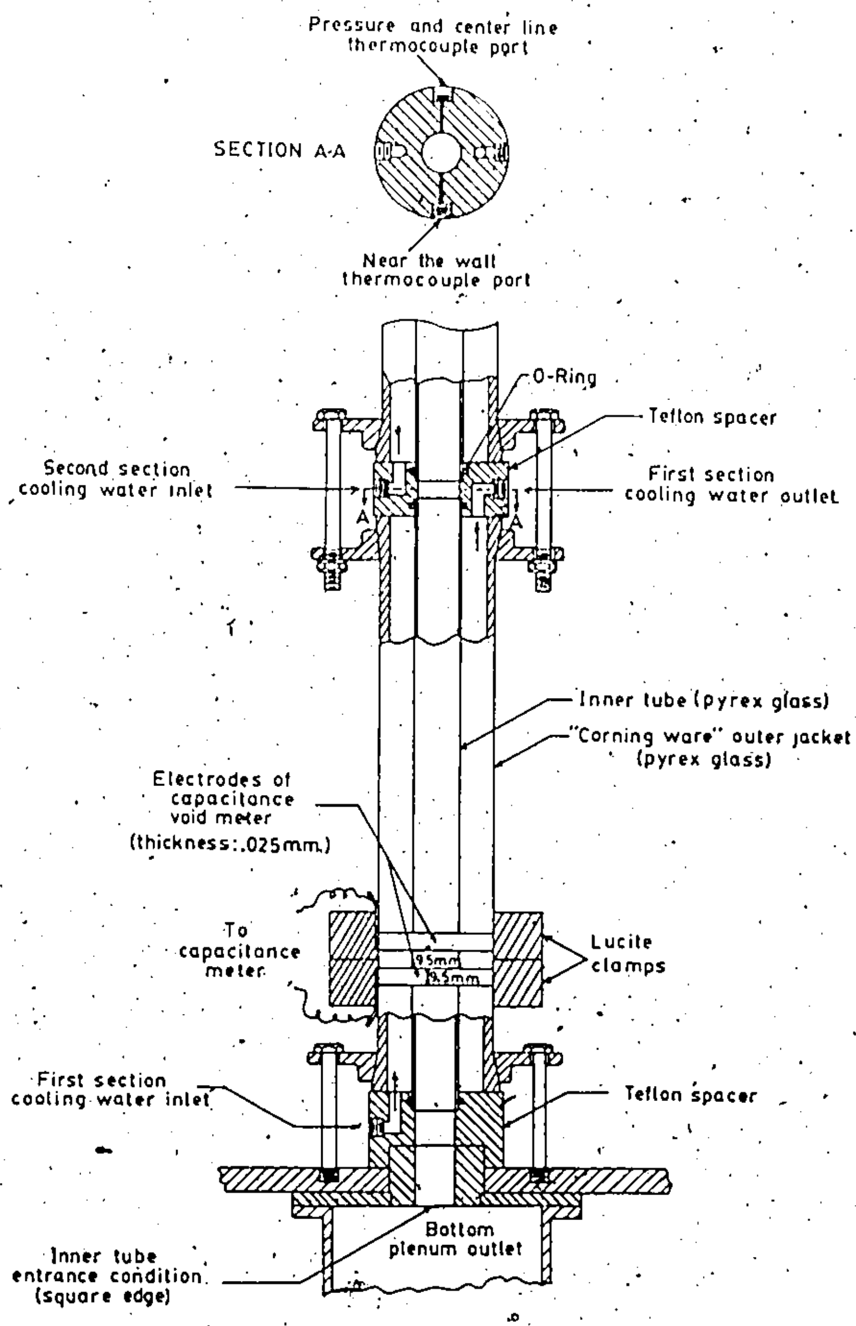

FIGURE 2.2 Typical Arrangement for a Reflux Condenser Section

pressurized. Photographs of the apparatus are shown in Figure 2.3.

2.1.2 Methods of Measurements

2.1.2.1 Steam Flow Rate Instrumentations

For all the reflux condensation experiments, an orifice meter is used to measure the amount of steam injected in the system. The mechanical design details, the method of calibration and the error analysis are exposed in Appendix A. The main result of the error analysis is that the maximum error on the steam flow rate measurement is ±5%.

A differential pressure transducer (P3 in Figure 2.1) is installed to meter the rate of accumulation of the condensate in the bottom plenum. This provides a mean of comparison for the steam orifice meter readings.

For all the fill and dump experiments and the upward co-current annular flow experiments the outflow at the top is condensed and collected in a graduated cylinder for a certain time, giving the steam flow rate injected. The error on these measurements is less than ±5%.

meters for the empty inner tube are recorded.

In the second part, steam from the McMaster Power Plant is introduced in the system to established reflux condensation. This mode of operation is maintained until the water in the bottom plenum is completely replaced by condensate at about the same temperature of the steam. This process takes about two to three hours and it ensures that all the other components are properly warmed up. After this stage is achieved, the steam flow is stopped and reflux condensation is suppressed. Then, the initialization to zero of each pressure transducer (except P3) is checked and reflux condensation is established again.

In the third part, the amount of non-condensible gas flowing with the steam is measured. The steam flow rate is also recorded by the NOVA III computer from the steam orifice-meter and, for comparison purpose, from the condensate level meter. This measurement is done to provided a basis to convert the non-condensible gas flow rate from absolute units to percentage per weight.

Finally, it should be mentioned that the start-up phase takes between four to five hours before it is completed.

2.3.1.2 The Experimental Phase

Three types of experiments are possible with the present apparatus, they are: total reflux condensation, fill and dump mode and natural circulation (upward annular flow). Each type of experiment has its particular boundary conditions set by the valves at the control station. This control station is made of two valves with pneumatic actuators, one for high flow the other for low flow and it can be thought as an interface between the high pressure steam line from the power plant and the experimental set-up. The low flow valve was used in all the experiments. The control station was such that it was possible to impose either a constant pressure drop across the tube or a constant mass flow rate at the tube inlet. In the constant pressure drop mode, the opening of the valve is controlled to maintain a manually set pressure drop across the valve giving in practice a situation where the flow is regulated to maintain a constant pressure downstream of the valve, i.e. in the bottom plenum of the set-up. In the constant mass flow rate mode, the same valve is opened until the desired operating point is reached. This mode of operation is achieved because of the critical flow established across the valve.

Each type of experiments commands its own set of experimental procedure which depends mainly on the capability of the NOVA III computer. After some preliminary experiments the following sets of experimental procedures were adopted.

2.3.1.2.1 Total Reflux Condensation

Total reflux condensation is established by setting the control station in the constant pressure drop mode of operation. In general, the flow regime observed is a quasi-steady state where a water column is oscillating on the top of two-phase region and with constant pressures in the bottom and top plenums. It is assumed that the process under study is ergodic. This implies, in practice, that the order of data acquisition from the different kinds of sensors, is unimportant.

The data acquisition was done with the following sequence:

(i) at about every three minutes, the signals from the sensors of the condensate level meter and the steam orifice meter are read. Then, the time average, the standard deviation and the minimum and maximum values of each signal are computed and recorded.

Sensors(*) : T1, T2 and P1, P2, P3

Subprograms(**) : CONDLEVEL, STEAMFLOW

(ii) the levels of the Meriam Blue Fluid in each leg of the manometers of the cooling water orifice meters are read and along with the time averages, standards deviations, minimum and maximum values of the signals from each thermocouple on the secondary side (temperature at cooling jacket outlet) and the common inlet cooling water temperature (Thermocouple T4);

Sensors: T4, T7, T10, T13, T16, T19, T22, T25, T28

Subprograms: MANOMETER, SECONDSIDE

(iii) the signals of each capacitance void meter are read

(*) This refers to sensors used (see Fig 2.1).

(**)This refers to the subprograms called in the data acquisition program "RFLXAC" (see section 2.3.2) and recorded one after the other until the whole two-phase region is covered;

Sensors: V1, V2, V3,..., V7

Subprogram: VOIDFRAC

(iv) the signals from the sensors on the primary side are read and recorded in the form of a matrix where each line contains the full signal of the associated sensor. The matrix was filled column by column at a speed of about 100 ms per column;

Sensors: P1, P2 and P4 to P14 / T1, T2, T3, T5, T6, T8, T9, T11, T12, T14, T15, T17, T18, T20, T21, T23, T24, T26, T27, T29

Subprogram: PRIMESIDE

(v) the signal from the capacitance liquid level meter in the top cooling section is read and recorded, if the length of the water column is long enough;

Sensor: Capacitance level meter

Subprogram: WATCOLEVEL

(vi) the steam pressure indicated by the Bourdon gauge connected on the bottom plenum is read and recorded along with the lengths of the single phase (water column) and two-phase region obtained by visual observation;

Subprogram: PRESHEIGHT

(vii) step (ii) is repeated again.

The experimental conditions determine the number of steps to be covered, the above procedure is description of what is done in general. It also indicated the data taken to obtain a picture as complete as possible of the phenomena occurring for one experimental condition (one rate of condensation). An average time of 45 to 60 minutes is needed to do one experiment.

2.3.1.2.2 Fill and Dump Mode

Fill and dump mode of operation is established by setting the control station in the constant mass flow rate mode of operation. The phenomena observed are cyclic in nature: two flow regimes take place in a continuous succession. The first flow regime is partial reflux/carry over and the second is upward co-current annular flow. The transition occurs when the single phase region, build up by the partial carry over, has filled up the tube and is being discharged in the upper plenum. This condensate and the subsequent steam/water mixture are separated in the upper plenum and flow out to be cooled down and condensed in two heat exchangers attached, for the circumstance, to two outlet parts on the upper plenum. The total amount of condensate collected per cycle is calculated as being the average rate of condensation. The data acquisition was done with the following sequence:

(i) at about every three minutes, the signal from the pressure transducer (P3) the condensate level meter is read. Then, the time average, the standard deviation and minimum and maximum values of the signal are computed and recorded;

Sensor: P3

Subprogram: CONDLEVEL

(ii) step (ii) described in section 2.3.1.2.1 is integrally done;

(iii) we monitor the part of the cycle where partial reflux/carry over occurs;

Sensors: P5 to P14 and T6,T9,T12,T14, T18,T21,T24, T27

Subprogram: PRIME2

(iv) we monitor the part of the cycle where the transition from partial reflux/carry over to upward co-current annular flow occurs;

Sensors: P5 to P14 and T6,T9,T12,T14,T18, T24,T27

Subprogram: PRIME3

(v) the condensate is collected at the end of each cycle.

Usually more than one cycle is monitored and the time required to cover all the steps in the above procedure, for <u>one</u> experimental condition, is often longer than one hour.

2.3.1.2.3 Upward Co-current Annular Flow

Upward co-current annular flow is estabished by setting the control station in either the constant pressure drop mode or the constant mass flow rate mode of operation. In general, the flow regime observed is a steady state upward co-current annular flow. The experimental procedure is exactly the same as for the total reflux condensation experiments (see Section 2.3.1.2.1) except for the steam mass flow rate measured in the same way as in the fill and dump mode case.

2.3.1.2.4 Remarks

At the beginning of the experimental program two points of the calibration curve of each thermocouple were checked to see if at $0^{o}C$ and at $100^{o}C$ the responses were the same as the one given by the calibration curve. The results indicated a good agreement between the measured value and the calibration curve value within the limits of accuracy certified by the manufacturer ($\pm 0.5^{o}C$).

Before any set of experiments, the pressure tranducer were calibrated. This had to be done often and it has generated a large amount of calibration curves that is too bulky to be included here; however, the linearity, within the limits specified by the manufacturer (±1/2%, F.S.), was always obtained. This is based on the fact that the standard deviation of the calibration points to a first order fit was always very small and the linear-correlation coefficient [69, p.121] was always very close to one, indicating a nearly complete correlation.

2.3.2 Data Acquisition System and Processing Software

A total of 60 sensors and devices are connected to the reflux condenser: 29 thermocouples, 14 pressure transducers, 7 capacitance void meters, 1 capacitance level meter, 1 steam and 8 cooling water orifice meters. This makes the use of a data acquisition system necessary. The schematic diagram of the data acquisition and processing scheme is shown in Figure 2.8.

The data acquisition system consists of a NOVA III computer with a device called Real Time Peripheral (RTP). This device is a low level analog input system with a multiplexed analog to digital converter that scans at a maximum rate 8 kHz and serves as an interface between the NOVA III computer and the channels of analog information. The control of the data acquisition process is done by the BASIC language program "RFLXAC" (ReFLuX ACquisition) by which the NOVA III computer address the RTP, selects a particular channel and adjusts the internal amplifier for the correct gain and digital scaling. The digitalized analog values are then echoed back to the computer and eventually stored on the hard disk under a certain format. Then, the data is reformatted and written on magnetic tapes by using the BASIC language program "REFMT" (REForMaT). The magnetic tapes are brought to the McMaster Computing Center where their contents are read by a CDC Cyber 815 computer with a special FORTRAN V language program called "NOVACDC" and written on disk files. Then, this data is process by another FORTRAN V language program called ARFLXC (Analysis of ReFLuX Condensation). Finally, it should be mentioned that the

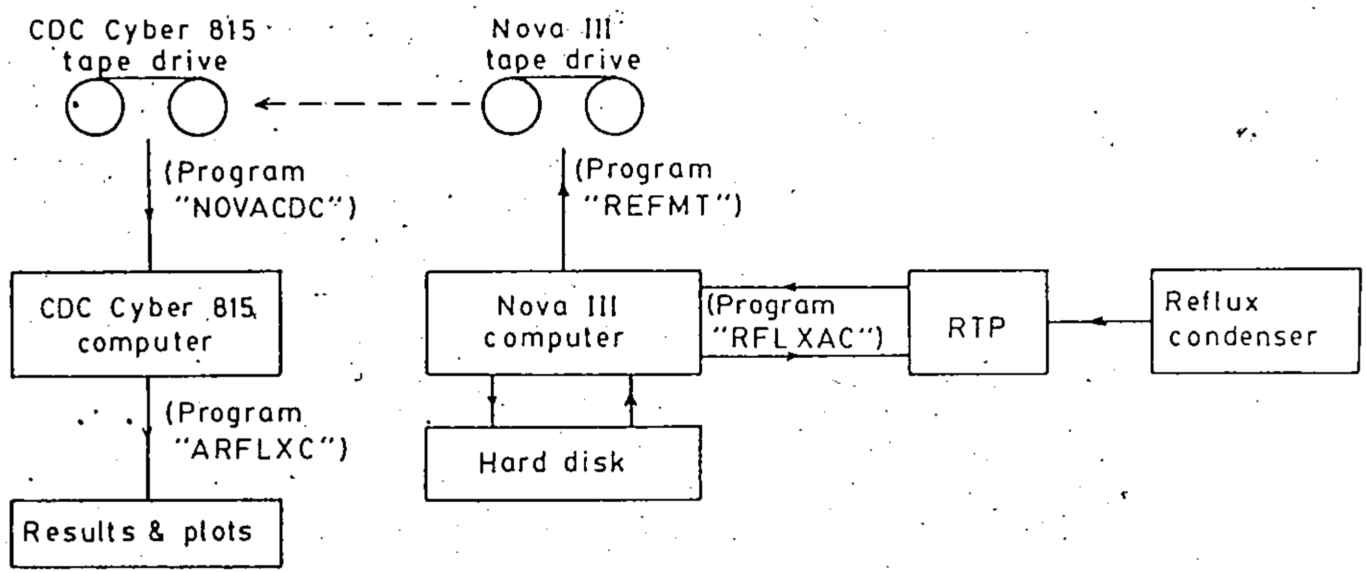

FIGURE 2.8 Schematic of the Data Acquisition System and the Data Processing System

minimum reading time per channel achieved with the present system is 4 msec, this was found to give a sufficient data acquisition speed.

The program "RFLXAC" is the data acquisition software used in the three kind of experiments performed. Due to its size (about 1800 lines) and to the small part of the core memory available, the program was written in an overlay structure to make an efficient utilisation of the computer resources. A simplified flow chart of the program is shown in Figure 2.9 where the purpose of each subprogram has been given in section 2.3.1.

The programs "REFMT" and "NOVACDC" are the software that does the fast transfer of data from the NOVA III (16 bits/word) to the Cyber 815 (60 bits/word) via magnetic tapes. This software allows many experiments to be performed in one day, the data being stored on magnetic tape, and it gives access to all the capabilities and the features of a modern mainframe computer such as the Cyber 815.

The program "ARFLXC" is the data processing program mainly used to put the data in engineering units, to do a preliminary analysis on converted data and to plot the results of the preliminary analysis. Due to its large size

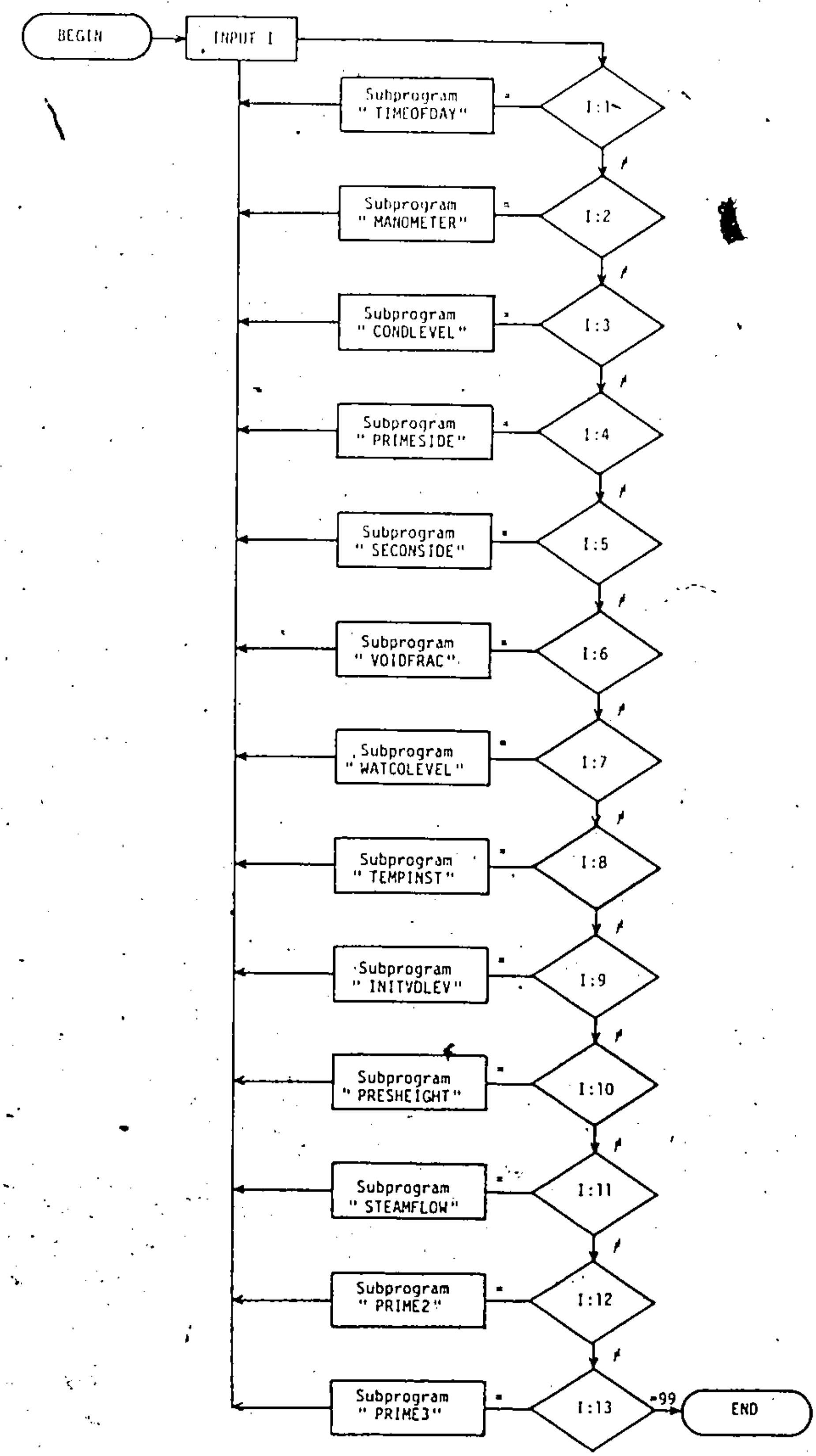

FIGURE 2.9 Flow Chart of Program "RFLXAC"

(about 5000 lines), a CDC utility called UPDATE [71] was used for maintaining and updating the program. UPDATE is a software utility that puts the source of a program into a special format that enable the user to easily tailor the program to meet his own needs. A simplified flow chart of the program is shown in Figure 2.10.

The listings of the program above mentioned, are obviously too long to be included here, even in an appendix, but they can be found in [72].

2.4 MATRIX OF EXPERIMENTS

In this section, the matrix of the experiments covered in the experimental program is given in Table 2.1, it gives the range of parameters studied and the conditions of the experiments. In the experiments, three tube sizes were used: 2.54 cm (1") O.D., 1.91 cm (3/4") O.D. and 1.27 cm (1/2") O.D. The dimensions of the tubes and the cooling jacket are given in Table 2.2.

For the same type of experiments, it was not possible to have the same range or value of cooling water temperature. For example, we can see in the reflux condensation experiments, that the coldest temperature available

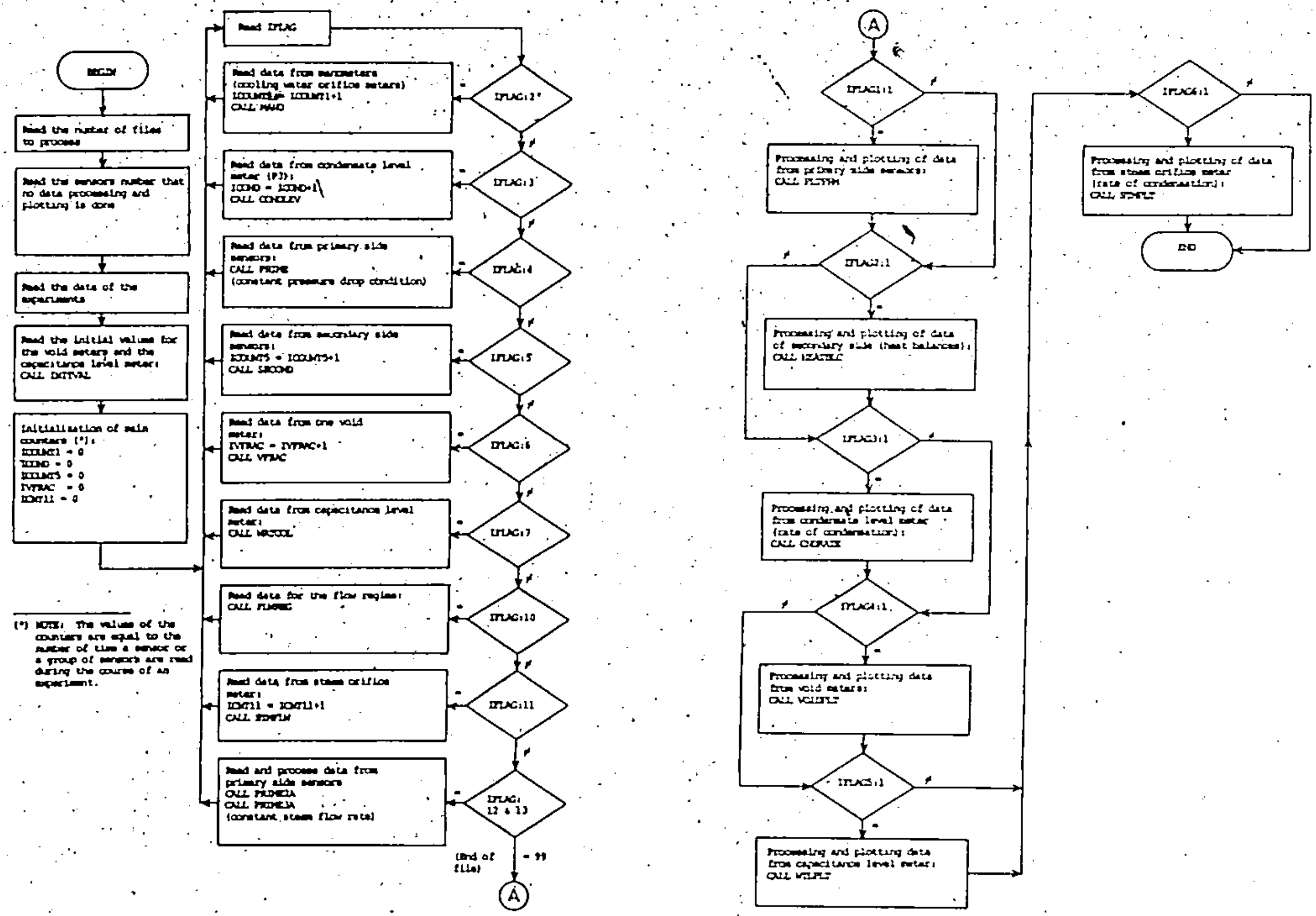

FIGURE 2.10 Flow Chart of Program 'ARFLXAC'

TABLE 2.1 Matrix of Experiments

	EXPERIMENTS WITH UPPER PLENUM PRESSURIZED	EXPERIMENTS WITH UPPER PLENUM OPEN TO ATMOSPHERE	MAXIMUM SYSTEM PRESSURE REACHED WITH UPPER PLENUM PRESSURIZED (kPag)			NOMINAL INLET COOLING WATER TEMPERATURE (°C)		
TUBE SIZE (cm) / TYPE OF EXPERIMENT	For all tube size	For all tube size	1.27	1.91	2.54	1.27	1.91	2.54
1. Total reflux condensation	YES	YES	56	56	62(**)	18,45	14,45	10,20,30,45
2. Fill and dump mode	NO	YES	N/A(*)	N/A	N/A	18	14	12
3. Upward co-current annular flow	NO	YES	N/A	N/A	N/A	18	14	18

(*): N/A = not applicable

(**): the pressurization was done for nominal inlet cooling water temperature of 10 and 45°C only.

TABLE 2.2: DIMENSIONS OF TUBES AND COOLING JACKET

TUBE NO.	OUTSIDE DIAMETER (cm)	INSIDE DIAMETER (cm)	THICKNESS (cm)	ℓ/D RATIO
1	2.54	2.06	0.24	233
2	1.91	1.59	0.16	303
3	1.27	0.95	0.16	506
COOLING JACKET	5.95	5.08	0.435	

at that time is 10^{o}C for the 2.54 cm tube, 14^{o}C for the 1.91 cm tube and 18^{o}C for the 1.27 cm tube. This is due to the time of year the experiments take place: in winter 10^{o}C cooling water is easily available but not in summer. The other temperature shown in Table 2.1 for the other types of experiments are the coldest temperature available on the day of the experiments.

CHAPTER 3

AN ANALYSIS OF COUNTER-CURRENT FILM-WISE CONDENSATION IN VERTICAL TUBES

3.1 GENERAL VISUAL OBSERVATIONS

The length-diameter ratio (ℓ/D), for all the tube sizes considered in this study, is greater than 230 (see Table 2.2) so that the present experimental set-up can be classified as a long reflux condenser.

3.1.1 Observations for an Imposed Pressure Drop Across the Tube

In all the experiments, an increase in the imposed constant pressure drop across the tube implies an increase in the tube inlet steam flow rate. In these cases, the steam control valve does the necessary slight adjustments on the steam flow to maintain that constant pressure drop. The steam control valve is then said to be set in the constant pressure mode of operation.

Figure 3.1 illustrates in a schematic way the phenomena observed for an increasing imposed pressure drop corresponding to an increasing steam mass flow rate.

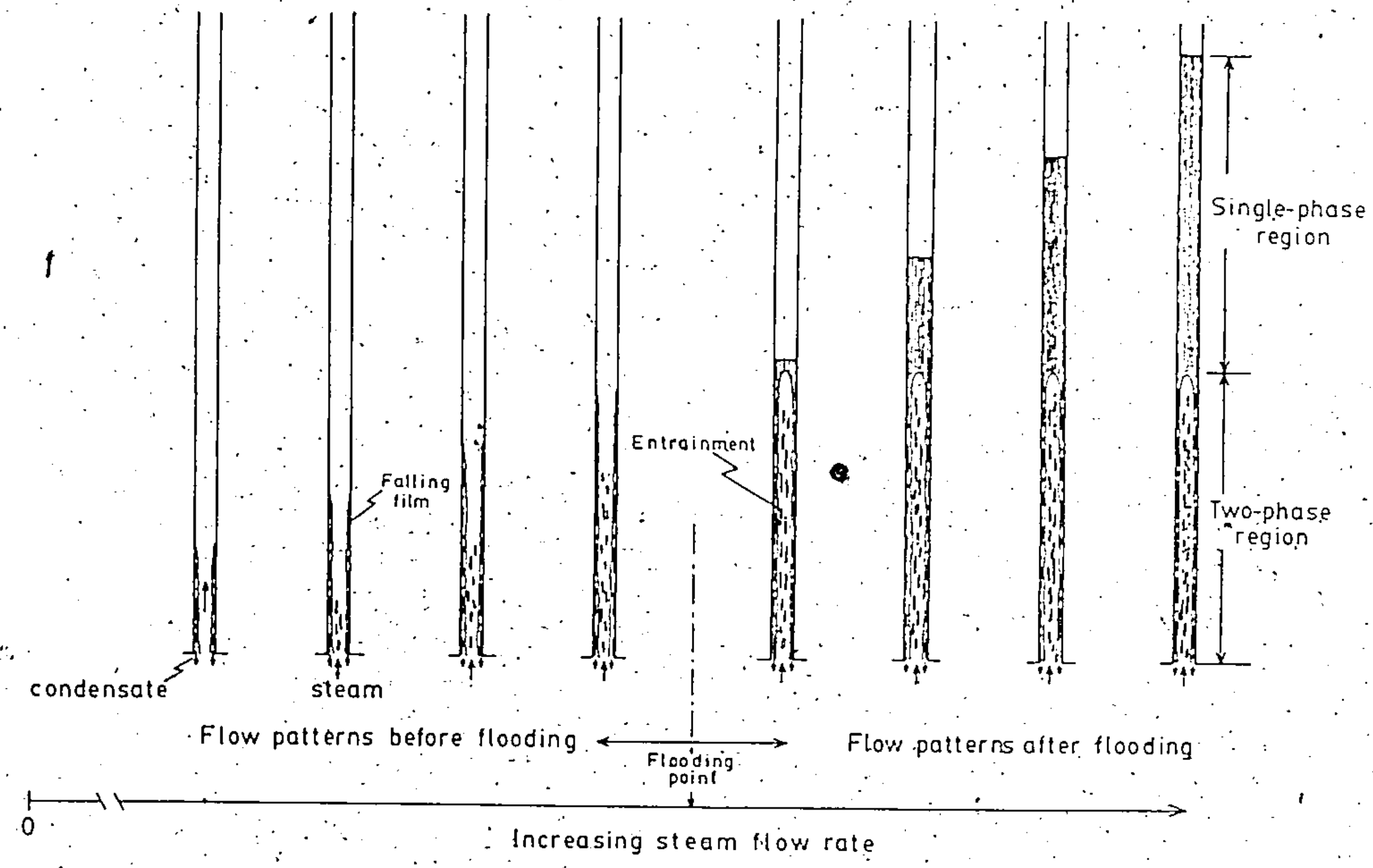

FIGURE 3.1 Flow Patterns Observed for an Imposed Pressure Drop Across the Tube

Each situation shown represents the same inner tube of the present reflux condenser with the two-phase flow pattern corresponding to a different imposed constant pressure drop. To go from one flow pattern to another, the steam control valve was adjusted until the desired flow pattern was seen.

Before flooding occurs, the phenomena observed were similar to what occur in a short reflux condenser (see Section 1.1). Flooding in a short reflux condenser causes the condensate to be ejected from the top; however, the phenomena observed in the present system were different: when the flooding point is reached the condensate, instead of being ejected from the tube, is ejected from the average condensation (two-phase) region to accumulate in the form of a water column (single phase region). In the case where a new constant pressure drop is imposed across the tube for a situation with a water column oscillating over the two-phase region, the system undergoes a small transient, in which the flooding point is reached, resulting in a new quasi-static situation with a water column of increased length oscillating over a two-phase region of unchanged length. Each of the flow regimes shown in the last four tubes in Figure 3.1 are examples of quasi-static situations observed that could be held indefinitely where the average lengths of the single-phase and the two-phase regions remain constant. For these later situations, the condensate level meter indicated that a significant amount of condensate was collected in the bottom plenum. It will be shown experimentaly in Chapter 4, that in all the situations shown in Figure 3.1, all the injected steam is condensed and its condensate flowed back counter-current to the upward steam flow. In the present study, this flow regime is called total reflux condensation and could be qualified as quasi-static.

The flow pattern observed in the two-phase region was intermittent churn-annular counter-current flow with entrainment in the form of droplet aggregates, in the vapor core, pulsating upward towards the end of the two-phase region. These droplet aggregates were observed to originate from the formation of a standing wave near the tube inlet and the accumulation of condensate above it. The action of the vapor flow was then to tear off part of accumulated condensate (including the condensate in the wave) forming the droplet aggregates. In vertical two-phase flow, the slug flow pattern can be described [89,p.389] as a succession of cap-shaped bubbles moving upward with the region between the bubbles being mostly filled by liquid. So, the liquid plays the role of the matrix in that flow pattern. In the present study, the flow pattern observed, in the vapor core alone, could be called "an inverted-slug flow" where the matrix of the flow pattern is the vapor phase and the role of the cap-shaped bubbles is played by the droplet aggregates.

As already mentioned, an increase in the imposed pressure drop across the tube results in an increase in the water column length. Tnen one can infer from the flow pattern observations presented above that the net transport of condensate to the single-phase could be done by the droplets aggregates pulsating upward towards the end of the two-phase region.

3.1.2 Observations for an Imposed Steam Flow Rate

In these experiments the steam control valve is set to deliver a prescribed constant steam flow rate. Because the upstream absolute pressure was much higher (630 kPa) than the maximum operating pressure, critical flow was established at the valve. The steam control valve is then said to be set in the constant flow rate mode of operation.

In all the experiments with an imposed constant steam flow rate at the tube inlet, all the phenomena before flooding occurs, were the same as the one observed for the first boundary condition as illustrated in a schematic way in Figure 3.2. Each of the first four tubes represents a flow pattern for one imposed steam flow rate below the one at the flooding point.

For steam flow rates corresponding to the flooding point and beyond it, condensate is ejected from the average

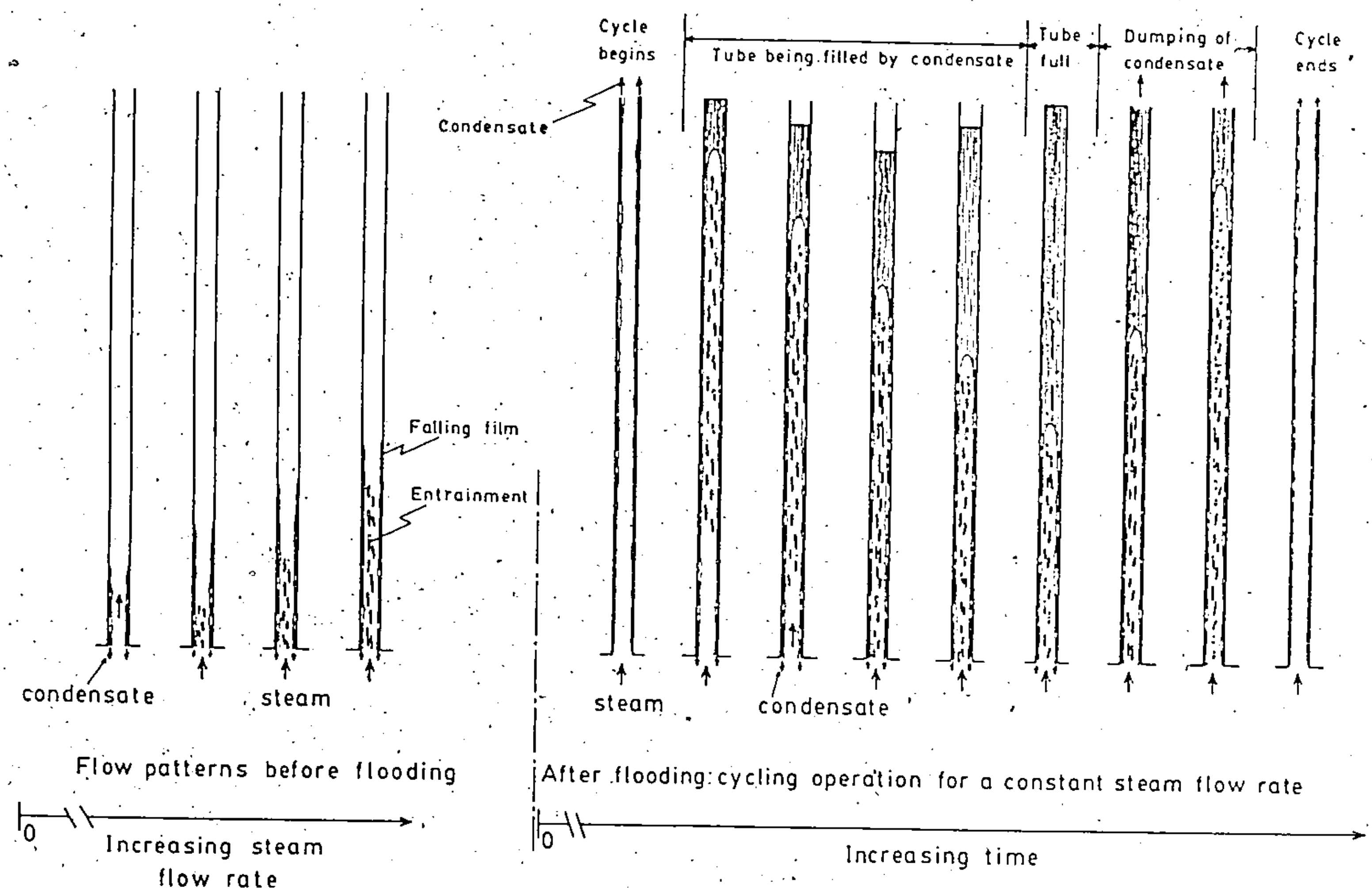

FIGURE 3.2 Flow Patterns Observed for an Imposed Steam Flow Rate at the Tube Inlet

condensation region to accumulate in the form of a water column; however, the similarities between the phenomena observed for the two boundary conditions stop here. As we increase the steam flow rate and cross the flooding point, the reflux condenser exhibits a cyclical operation. What occurs in that mode is illustrated in a schematic way in the last nine tubes of Figure 3.2 for one cycle and one fixed steam flow rate. The cycle begins with an upward co-current annular flow present in the tube and as time goes on condensate starts to fill the tube in the form of a water column, with the consequence of a decrease in the two-phase region length. This phenomenon goes on up to a point where the tube cannot accumulate more condensate. At that point the system becomes unstable and the whole water column is dumped from the top of the tube and the flow becomes an upward co-current annular flow for a period of time always less than the time necessary for the filling part of the cycle. This ends one cycle and a new cycle starts again. This mode of operation is similar to the first one as it can be maintained <u>indefinitely</u>; however, the lengths of the single-phase and two-phase regions are not remaining constant. Although most of the condensate is ejected from the top of the tube, the condensate level meter indicated that some condensate is collected in the bottom plenum during this cycling mode of operation. In the present study, this flow regime is called fill and dump cycle and could be qualified as dynamic as opposed to the quasi-static flow regime corresponding to the first boundary condition.

The flow patterns observed were upward co-current annular flow just after the water column has been ejected and churn-annular counter-current flow with entrainment during the time the carried-over condensate fills the tube. The entrainment took the form of droplet aggregates pulsating upward towards the end of the two-phase region. As it is shown in Chapter 4, the periods of the fill and dump cycles are in the order of minutes. Tnis allowed enough time to observe the churn-annular flow pattern when present and it was found that the phenomena were the same as in the two-phase region of the total reflux condensation flow regime.

3.1.3 Remarks on the Visual Observations Made

Each boundary condition gives rise to a well defined flow regime: total reflux condensation for an imposed pressure drop and fill and dump cycle for an imposed steam flow rate at the tube inlet. Although these flow regimes were observed by other investigators [8,9,86,87], it appears that the correspondence, being made here, between an imposed boundary condition on the system and its resulting flow regime has not been mentioned earlier in the open literature. The two flow regimes observed are different in nature: one is quasi-static and the other is dynamic;

however, they do have one flow pattern in common: churn-annular counter-current flow with entrainment.

The flooding criterion used is the same for the two boundary conditions. It can be pictured as being the point where the steam flow rate is such that a water column starts to build up resulting in a change in the bottom plenum pressure. An equivalent definition of the flooding criterion can be stated as being the point where the steam flow rate is such that a standing wave, with respect to the condensate film interfacial velocity, appears near the tube inlet and a net transport of condensate occurs by the mean of droplet aggregates pulsating upward. The two criteria are equivalent because it is the net transport of condensate upward that gives rise to the presence of a water column which in turn is the cause of an increase in the bottom plenum pressure. In the present study the first definition was used as the flooding criterion in all the experimental work, because it is reproducible and easily traceable. The present flooding criterion has similarities with the one used by Chung et al. [19,21] in a adiabatic system. The other formulation is simply the one used by Cetinbudaklar and Jameson [32] and it is used, as presented later in the linearized stability analysis analysis of the condensate film flow.

3.2 MATHEMATICAL MODELLING OF TOTAL REFLUX CONDENSATION

In this section we present the mathematical model simulating the series of quasi-static situations occurring when different constant pressure drops are imposed across the tube (see Section 3.1.1). The mathematical modelling of the phenomena occurring for imposed constant inlet steam flow rates (see Section 3.1.2) is not addressed in the present study. However, the model for the quasi-static situations could be used as the starting point of a more elaborated model simulating fill and dump cycle.

The present mathematical model of total reflux condensation is made of two parts:

(i) an extension of the classical Nusselt's theory to the case where three of the basic assumptions [85, p. 314-315] are relaxed: the interfacial drag on the steam-water interface and consequently the momentum transfer through the film are no longer negligible and the heat transfer is done by conduction and convection;

(ii) a linearized stability analysis of the condensate film flow perturbed by the upward condensing steam flow.

The extended Nusselt's theory is used to provide the characteristics of the base flow: condensation length, single-phase length (if any), axial distributions of the condensate Reynolds number and film thickness. These are used in the solution of the eigenvalue problem resulting from the linearized stability analysis to predict the value of the inlet steam flow rate that satisfies the flooding criterion given in Section 3.1.3.

3.2.1 An Extended Nusselt's Theory

The exact mathematical modelling of reflux condensation is quite formidable because of the counter-current nature of the flow and the complex pattern of the waves travelling on the steam-water interface. Extensive idealizations are required to simplify the governing equations if any solution, either analytical or numerical, is to be obtained. In Figure 3.3, we show the idealization of the configuration of the flow pattern used in the present base flow model. The assumption made are:

(i) the flow pattern is steady-state counter-current annular flow with no entrainment of condensate from the film in the vapor core and with a smooth interface;

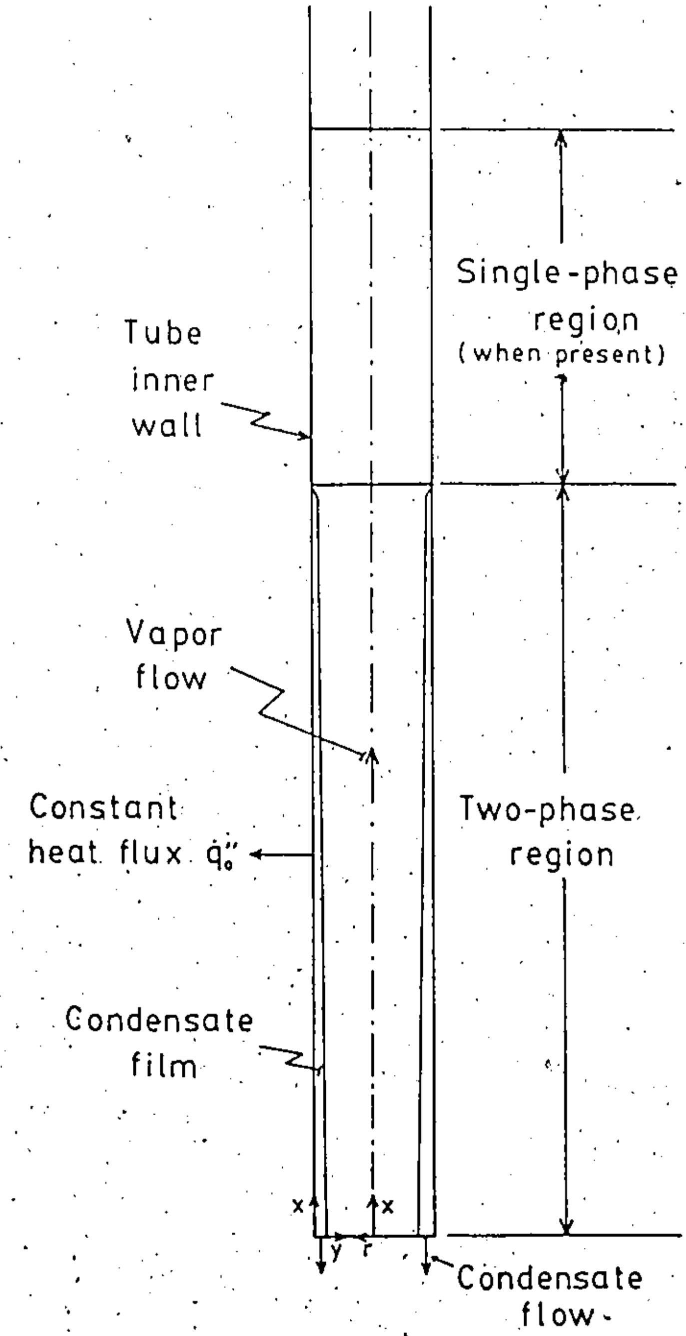

FIGURE 3.3 Flow Pattern Idealization of Total Reflux Condensation

(ii) the flow of condensate in the film is laminar;

(iii) the film thickness of the condensate is negligibly small when compared to the tube inner radius;

(iv) the axial velocity profile in the vapor core is nearly uniform and much greater than the interfacial condensate film velocity;

(v) the pressure is the same in each phase and it is only a function of the axial position "x";

(vi) the heat flux at the inner wall of the tube is constant;

(vii) the thermal-hydraulic properties of both phases are constant and evaluated at saturation. The saturation pressure is taken to be the bottom plenum pressure;

(viii) the condensation shear stresses at the steam-water interface have small influence on the characteristics of the base flow.

In deriving the classical Nusselt's film-wise condensation theory the main step is to obtain a differential equation for the axial variation of the film thickness. The assumptions made in Nusselt's classical theory lead to a linear differential equation resulting in a closed form solution of the base flow: axial variations of the film thickness, heat transfer coefficient and condensate flow. In the present derivation of an extended Nusselt's theory the main step is again to obtain a differential equation for the axial variation of the film thickness. The methodology used is similar to the one in the classical Nusselt's theory [85, p. 314-317] and its is as follows:

(i) obtain the radial and axial velocity profiles in the condensate film in terms of the film thickness by solving the liquid phase momentum equation with the aid of the vapor phase momentum equation and the continuity equation of each phases;

(ii) obtain the condensate film temperature profile again in terms of the film thickness by using the velocity profiles in solving the energy equation;

(iii) then, obtain the differential equation for the film thickness by substituting the temperature profile in the equation resulting from the combinaison of the heat and mass interfacial jump conditions.

The geometry of the system being cylindrical, the local instantaneous conservation equations can be written as follows (90, p. 83-85 and p. 315-316).

Mass conservation:

$$\frac{\partial}{\partial x}(\rho_\ell\ r\ u_\ell) + \frac{\partial}{\partial r}(\rho_\ell\ r\ v_\ell) = 0 \tag{3.1}$$

$$\frac{\partial}{\partial x}(\rho_g\ r\ u_g) + \frac{\partial}{\partial r}(\rho_g\ r\ v_g) = 0 \tag{3.2}$$

Momentum conservation:

$$\frac{\partial}{\partial x}(\rho_\ell u_\ell^2 r) + \frac{\partial}{\partial r}(\rho_\ell u_\ell v_\ell r) = - r\frac{\partial p}{\partial x} + \mu_\ell \frac{\partial}{\partial r}\left(r\frac{\partial u_\ell}{\partial r}\right) - g\ (\rho_\ell - \rho_g)\ r \tag{3.3}$$

$$\frac{\partial}{\partial x}(\rho_g u_g^2 r) + \frac{\partial}{\partial r}(\rho_g u_g v_g r) = - r\frac{\partial p}{\partial x} + \mu_g \frac{\partial}{\partial r}\left(r\frac{\partial u_\ell}{\partial r}\right) - g\ \rho_g\ r \tag{3.4}$$

Energy conservation:

$$\frac{\partial}{\partial x}(r\ \rho_\ell\ c_{p\ell}\ u_\ell\ T_\ell) + \frac{\partial}{\partial r}(r\ \rho_\ell\ c_{p\ell}\ v_\ell\ T_\ell) = k_\ell \frac{\partial}{\partial r}\left(r\ \frac{\partial T_\ell}{\partial r}\right) \tag{3.5}$$

where

x: axial distance from tube entrance (m)

r: radial distance from tube centre line (m)

u_ℓ, u_g: respectively the axial velocities of the condensate and the steam (m/s)

v_ℓ, v_g: respectively the radial velocities of the condensate and the steam (m/s)

T_ℓ: condensate film temperature (^oC)

p: absolute pressure (N/m_2)

$c_{p\ell}$: specific heat capacity of the condensate ($J/kg\ ^oC$)

k_ℓ: thermal conductivity of the condensate ($W/m-^oC$)

μ_ℓ, μ_g: respectively the dynamic viscosity of the condensate and the steam (kg/m-s)

Before deriving the velocity profile in the condensate film, we first state, based on the first assumption, that mass conservation is satisfied at each cross-section of the two-phase region. Then, we can write:

$$-\int_{R-\delta}^{R} \rho_{\ell}\, u_{\ell}\, r\, dr = R\Gamma = \int_{0}^{R-\delta} \rho_{g}\, u_{g}\, r\, dr \qquad (3.6)$$

where

R: the tube inner diameter (m)

Γ: condensate mass flow rate per unit width (kg/m - s)

δ: film thickness (m)

The method used to derive the equation of motion of the condensate film is similar to the one employed in the derivation of the integral equations of boundary layer on flat plate [45, pp 144-146].

The integration of condensate and vapor momentum equations respectively from $r = R - \delta(x)$ to $r = R$ and from $r = 0$ to $r = R - \delta(x)$, combined with the integration of their respective mass conservation equations and the use of Leibnitz formula [91, p. 360] results in the following expression for the pressure gradient:

$$\frac{R^2}{2}\frac{\partial p}{\partial x} = \mu_\ell R \left.\frac{\partial u_\ell}{\partial r}\right|_R - \left(\frac{2R\delta - \delta^2}{2}\right)(\rho_\ell - \rho_g)\, g$$

$$-\mu_\ell (R - \delta)\left(\frac{\partial u_\ell}{\partial r}\right)_\delta + (u_\ell^\delta - u_g^\delta)\, R\, \frac{d\Gamma}{dx} + \mu_g (R - \delta)\left(\frac{\partial u_g}{\partial r}\right)_\delta \quad (3.7)$$

$$- \frac{d}{dx}\int_{R-\delta}^{R} \rho_\ell\, u_\ell^2\, r\, dr - \frac{d}{dx}\int_{0}^{R-\delta} \rho_g\, u_g^2\, r\, dr$$

By the no-slip conditions at the steam-water interface, we have that:

(i) $u_\ell^\delta = u_g^\delta$

(ii) $\mu_g (R - \delta)\left(\frac{\partial u_g}{\partial r}\right)_\delta = \mu_\ell (R - \delta)\left(\frac{\partial u_\ell}{\partial r}\right)_\delta$

where "δ" indicates an evaluation at the steam-water interface. The simplification of equation (3.7) by the use of the no-slip conditions results in an expression for the pressure gradient that can be introduced in equation (3.7). Then, the condensate momentum conservation equation can be written as:

$$\rho_\ell u_\ell \frac{\partial u_\ell}{\partial x} + \rho_\ell v_\ell \frac{\partial v_\ell}{\partial r} = \mu_\ell \frac{1}{r} \frac{\partial}{\partial r} \left(r \frac{\partial u_\ell}{\partial r} \right) - g (\rho_\ell - \rho_v)$$

$$- \frac{2\mu_\ell}{R} \left(\frac{\partial u_\ell}{\partial r} \right)_R - \left(\frac{2R\delta - R^2}{R^2} \right) g (\rho_\ell - \rho_g) \tag{3.8}$$

$$+ \frac{2}{R^2} \frac{d}{dx} \int_0^{R-\delta} \rho_g u_g^2 r \, dr + \frac{2}{R^2} \int_{R-\delta}^{R} \rho_\ell u_\ell^2 r \, dr$$

In the present study, the condensation process occurs in the presence of a body force (gravity) and forced convection of the steam and the condensate as a Prandlt number greater or equal to one. For a flow of that type, one can neglect the inertia terms in the condensate momentum equation [92] i.e. in equation (3.8) the left hand side and the last term on the right hand side can be dropped. Using equation (3.6) with the fourth assumption, one can write the following approximation:

$$\frac{2}{R^2} \frac{d}{dx} \int_0^{R-\delta} \rho_g u_g^2 r \, dr = \frac{4}{\rho_g R^2} \frac{d}{dx} \Gamma^2 \tag{3.9}$$

Introducing the change in coordinate $y = R - r$, where "y" is the transverse coordinate as shown in Figure 3.3 and simplifying equation (3.8), one can write the equation of motion for the condensate film as follows:

$$\mu_\ell \frac{\partial^2 u_\ell}{\partial y^2} - g(\rho_\ell - \rho_g) + \frac{4}{\rho_g R^2} \frac{d}{dx} \Gamma^2 = 0 \qquad (3.10)$$

with the following boundary conditions:

B.C.1 $\quad y = 0 \quad ; \quad u_\ell = 0$

B.C.2 $\quad y = \delta \quad ; \quad \mu_\ell \frac{\partial u_\ell}{\partial y} = \frac{f_i}{2} \rho_g (u_g - u_{\ell i}) |u_g - u_{\ell i}|$

where

f_i: interfacial friction factor

$u_{\ell i}$: interfacial condensate velocity (m/s)

and with the second boundary condition formulated taking into account the eight assumption. Considering the fourth assumption, the second boundary condition can be written in the following form:

B.C.2 $\quad y = \delta \quad ; \quad u_\ell \frac{\partial u_\ell}{\partial y} = \frac{f_i}{2} \rho_g u_g^2$

The integration of equation (3.10) with the application of the boundary condition gives:

$$u_\ell = g\,\frac{(\rho_\ell - \rho_g)}{u_\ell}\left(\frac{y^2}{2} - y\,\delta\right) - \frac{4}{\mu_\ell\,\rho_g\,R^2}\,\frac{d\Gamma^2}{dx}\left(\frac{y^2}{2} - y\,\delta\right) + \frac{f_i}{2u_g}\,\frac{1}{\rho_g}\,\frac{4\Gamma^2}{R^2}\,y \qquad (3.11)$$

We define the following characteristic length and velocity plus non-dimensional numbers and distances:

δ_o = film thickness at the tube entrance (m)

$u_o = g\,\dfrac{(\rho_\ell - \rho_g)}{2\mu_\ell}\,\delta_o^2$, the interfacial condensate film velocity in the case of no drag from vapor flow (m/s)

$Re_o = \rho_\ell\,\dfrac{u_o}{u_\ell}\,\delta_o$, Reynolds number based on u_o and δ_o

$S = \dfrac{4\rho_\ell}{\rho_g}\,\dfrac{1}{\bar{R}^2}$

$Re_\delta = \dfrac{\Gamma}{\mu_\ell}$, Reynolds number based on the mass flow rate per unit width

with $\bar{x} = x/\delta_o$, $\bar{y} = y/\delta_o$ and $\bar{R} = R/\delta_o$

In non-dimensional form equation (3.11) becomes:

$$\bar{u}_\ell = (\bar{y}^2 - 2\bar{\delta}\bar{y}) - \frac{S}{2}\,\frac{1}{Re_o}\,\frac{d^2 Re_\delta^2}{d\bar{x}^2}(\bar{y}^2 - 2\bar{\delta}\bar{y}) + \frac{f_i}{2}\,\frac{S}{Re_o}\,Re_\delta^2\,\bar{y} \tag{3.12}$$

where $\bar{u}_\ell = u_\ell/u_o$ and from the mass conservation equation, the transverse velocity profile is

$$\bar{v}_\ell = G\,\frac{d\bar{\delta}}{d\bar{x}}\,\bar{y}^2 + \frac{S}{2}\,\frac{1}{Re_o}\,\frac{d^2\,Re_\delta^2}{d\bar{x}^2}\left(\frac{\bar{y}^3}{3} - \bar{\delta}\,\bar{y}^2\right) + \frac{S}{2Re_o}\,\frac{df_i}{d\bar{x}}\,Re_\delta^2\,\frac{\bar{y}^2}{2} + \frac{f_i}{2}\,\frac{S}{Re_o}\,\frac{d\,Re_\delta^2}{d\bar{x}}\,\frac{\bar{y}^2}{2} \tag{3.13}$$

where

$$\bar{v}_\ell = v_\ell/u_o\,,$$

$$G = 1 - \frac{S}{2}\,\frac{1}{Re_o}\,\frac{dRe_\delta^2}{d\bar{x}}$$

The expressions for the axial and transverse velocity profiles are known, we solve the energy conservation equation for the condensate film temperature profile in terms of the film thickness. Using the mass conservation equation and introducing the change of coordinate $y = R - r$, equation (3.5) can be written as:

$$u_\ell \frac{\partial T_\ell}{\partial x} + v_\ell \frac{\partial T_\ell}{\partial y} = \frac{\mu_\ell}{\rho_\ell \, Pr} \frac{\partial^2 T_\ell}{\partial y^2} \tag{3.14}$$

The following non-dimensional variables are defined to put equation (3.14) in non-dimensional form:

$$\Delta T_q = \frac{\dot{q}''_o \, \delta_o}{k_\ell} \; ; \quad \bar{T}_\ell = \frac{T_\ell - T_{sat}}{\Delta T_q}$$

$$Ku = \frac{c_{p\ell} \, \Delta T_q}{h_{fg}} \; ; \quad Pr = \frac{\mu_\ell}{c_{p\ell} k_\ell} \; ; \quad Pe = Pr \, Re_o$$

where

q''_o: constant heat flux at tube inner wall (W/m^2)

Pr: Prandlt number

Pe: Peclet number

Ku: Kutateladze number [52]

T_{sat}: saturation temperature (°C)

h_{fg}: latent heat (J/kg)

Then, equation (3.14) becomes:

$$\bar{u}_\ell \frac{\partial \bar{T}_\ell}{\partial \bar{x}} + \bar{v}_\ell \frac{\partial \bar{T}_\ell}{\partial \bar{y}} = \frac{1}{Pe} \frac{\partial^2 \bar{T}_\ell}{\partial \bar{y}^2} \tag{3.15}$$

with the following boundary conditions:

$$\text{B.C.1} \quad \text{at } \bar{y} = 0 \qquad \frac{\partial \bar{T}_\ell}{\partial \bar{y}} = 1$$

$$\text{B.C.2} \quad \text{at } \bar{y} = \bar{\delta} \qquad \bar{T}_\ell = 0$$

Rohsenow [93] modified Nusselt theory by relaxing one of the basic assumptions [85, p. 314-315]: the heat transfer is done by conduction and convection. His analysis results in an integro-differential equation for the film thickness that is solved by successive approximations of the temperature profile. He obtained the following expression for the non-dimensional temperature profile:

$$T_R = \eta + Ku' \left[-\frac{1}{8}\eta^4 + \frac{1}{40}\eta^5 \right] \tag{3.16}$$

where

$$Ku' = \frac{C_{p\ell}\,(T_s - T_w)}{h_{fg}\,(1 + \frac{3}{8}Ku)} \text{, modified Kutateladze number}$$

$\eta = \bar{y}/\bar{\delta}$, non-dimensional transverse coordinate

$$T_R = \frac{T_\ell - T_w}{T_s - T_w} \text{, non-dimensional temperature in Rohsenow analysis}$$

and assumed that $\frac{Ku'}{10} << 1$

Although Rohsenow analysis differs from the present study by the number of basic assumptions relaxed and the boundary condition at the wall (he used a constant temperature wall condition) one could assume in the present derivation a temperature profile having a form similar to equation (3.16):

$$\bar{T}_\ell = \eta + \bar{T}_p(\eta) \qquad (3.17)$$

where $\bar{T}_p = \bar{T}_p(\eta)$ is a higher order polynomial. Introducing equations (3.12), (3.13) and (3.17) in equation (3.15) and keeping first order terms only, we obtain:

$$\frac{d^2 \bar{T}_p}{d\eta^2} = \left\{ - G\eta^3 + 3G\eta^2 - \frac{f_i}{2Re_o} S \frac{Re_\delta^2}{\bar{\delta}} \eta^2 + \frac{dG}{d\bar{\delta}} \bar{\delta} \left(\frac{\eta^3}{3} - \eta^2 \right) + \frac{f_i}{2} \frac{S}{Re_o} \frac{dRe_o^2}{d\bar{\delta}} \frac{\eta^2}{2} \right\} Pe\ \bar{\delta}^3 \frac{d\bar{\delta}^3}{d\bar{x}} \qquad (3.18)$$

with the following boundary conditions

B.C.1 at $\eta = 0$ $\quad \dfrac{\partial \bar{T}_p}{\partial \eta} = \bar{\delta} - 1$

B.C.2 at $\eta = 1$ $\quad \bar{T}_p = 1$

Integration of equation (3.18) with the application of its boundary conditions and simplification by an order of magnitude analysis of the resulting expression give:

$$\bar{T}_\ell = \bar{\delta}\ (\eta-1) + \left\{ -\frac{G}{20}\ (\eta^5-1) + \frac{G}{4}\ (\eta^4-1) \right. \tag{3.19}$$
$$\left. + \frac{f_i}{24}\ S\ \frac{Re_\delta}{Re_o}\ \frac{dRe_\delta}{d\bar{\delta}}\ (\eta^4-1) - \frac{f_i}{24}\ \frac{S}{\bar{\delta}}\ \frac{Re_\delta^2}{Re_o}\ (\eta^4-1) \right\} Pe\ \bar{\delta}^3\ \frac{d\bar{\delta}}{d\bar{x}}$$

With the condensate film velocity and temperature profiles known, we can now derive the mass and energy jump conditions to obtain the desired differential equation for the film thickness. The mass energy jump conditions can be written as [47]:

mass:

$$\rho_\ell \left\{ v_\ell - \left[\frac{\partial \zeta}{\partial t} + u_\ell\ \frac{\partial \zeta}{\partial x} \right] (1 - \gamma) \right\} = \rho_g\ v_g \tag{3.20}$$

energy:

$$\rho_g\ v_g\ h_{fg} = -\ k_\ell\ \frac{\partial T_\ell}{\partial y} \tag{3.21}$$

where

$\gamma = \rho_g/\rho_\ell$

$\zeta(x,t)$ = thickness of the wavy film (m) (see Figure 3.4)

The right hand side of equation (3.20) is the condensation mass transfer and conservation of mass at each cross-section of the two-phase region results in:

$$\frac{d\Gamma}{dx} = \rho_g \; v_g \tag{3.22}$$

Introducing equation (3.22) in equation (3.21) we obtain in non-dimensional form:

$$\frac{dRe_\delta}{d\bar{x}} = -\frac{Ku}{Pr}\frac{\partial \bar{T}_\ell}{\partial \bar{y}} \quad \text{at} \quad \bar{y} = \bar{\delta} \tag{3.23}$$

By definition we have:

$$Re_\delta = \frac{\Gamma}{\mu_\ell} = -\int_0^\delta \rho_\ell \frac{u_\ell}{\mu_\ell}\, dy \tag{3.24}$$

Introducing equation (3.12) in equation (3.24) we obtain:

$$\mathrm{Re}_\delta = \frac{4}{3}\,\frac{\mathrm{Re}_o\,\bar{\delta}^3}{[1 + (1 + 2F)^{1/2}]} \qquad (3.25)$$

where

$$F = \frac{P_1\,\bar{\delta}^5}{3} \text{ and } P_1 = f_1\,S\,\mathrm{Re}_o$$

Replacing the derivatives in equation (3.23) by their expressions obtained from equations (3.19) and (3.25), the following differential equation for the dimensionless film thickness is obtained:

$$\mathrm{Re}_o\,\frac{\mathrm{Pr}}{3\,\mathrm{Ku}}\,\frac{d\bar{\delta}^3}{d\bar{x}} = -\left[\frac{4}{1 + B_1} - \frac{20}{3}\,\frac{F}{B_1(1 + B_1)^2} + \mathrm{Ku}\left\{\frac{3}{4} + \frac{8}{3}\,\frac{F}{(1 + B_1)^2}\left[\frac{11}{3} - \frac{40}{9}\,\frac{F}{B_1(1 + B_1)}\right]\right\}\right]^{-1} \qquad (3.26)$$

where

$$B_1 = (1 + 2F)^{1/2}$$

From equation (3.7) and the no-slip conditions the pressure gradient can be written as:

$$\frac{\partial \bar{p}}{\partial \bar{x}} = -\left[\frac{4}{\gamma}\,\frac{1}{Re_o^2}\,\frac{1}{\bar{R}^2}\,\frac{dRe_\delta^2}{d\bar{x}} + \frac{f_i\,S}{\bar{R}\;Re_o^2}\,Re_\delta^2\right] \tag{3.27}$$

where

$$\bar{p} = p/\rho_\ell u_o^2$$

and the value of the derivative of Re_δ with respect to $\bar{x}$ is obtained from equation (3.25) and the result is as follow:

$$\frac{dRe_\delta}{d\bar{x}} = 2Re_o\,\bar{\delta}^2\,\frac{d\bar{\delta}}{d\bar{x}}\,\frac{1}{(1 + B_1)}\left[2 - \frac{10}{3}\,\frac{F}{B_1}\right] \tag{3.28}$$

The interfacial friction factor "f_i" is calculated from the Bharathan-Wallis correlation [30] and takes the following form:

$$f_i = .005 + A(\delta^*)^B \tag{3.29}$$

where

$$\log_{10} A = -0.56 + \frac{9.07}{D^*}$$

$$B = 1.63 + \frac{4.74}{D^*}\;;\quad \delta^* = \frac{\delta}{a}$$

$D^* = \dfrac{D}{a}$ $(2.6 \le D^* \le 56)$

D = tube inner diameter (m)

$a = [\sigma / g(\rho_\ell - \rho_g)]^{1/2}$ (m)
(Laplace coefficient [98, p. 173])

σ = surface tension (N/m)

This correlation was chosen because it was obtained from vertical air-water counter-current flow data and, suprisingly, it is the only one available in the open literature at this time [25,98] that is recommended to close the present set of equations. Other investigators used modified Fanning factors to take into account the increased roughness of the steam-water interface due to the presence of travelling waves [15] and the condensation shear stress [17], but these were not validated against vertical counter-current annular flow data.

In summary, equations (3.6), (3.19), (3.26), (3.27), (3.28) are the governing equations of the present model of film-wise condensation. Similar results were reported recently [16] for a short reflux condenser (ℓ/D = 14.6) with a different inner wall boundary condition than in the present study: the inner wall was assumed to be at constant temperature. Another difference is the choice of the characteristic length and condensate velocity used in putting the equations in non-dimensional form, which is common to both the extended Nusselt theory and, as it will be shown below, to the stability analysis. The choice of constant inner wall heat flux as boundary condition is based on the experimental evidence that the cooling side heat transfer resistance is much larger than the one on the condensing side. Experimental data from steam condensation on a horizontal cylinder with a high cooling side heat transfer resistance are shown to be in better agreement with a theory based on a constant wall heat flux boundary condition [94], giving support to the choice of boundary condition just made.

It is interesting to study the behavior of equation (3.26) as the interfacial friction goes to zero or in mathematical term as F goes to zero. We have:

$$\lim_{F\to 0} \frac{d\bar{\delta}^3}{d\bar{x}} = - \frac{3\ Ku}{Re_o\ Pr} \left[2 + \frac{3\ Ku}{4}\right]^{-1} \qquad (3.30)$$

Assuming here that Ku << 1 and using the binomial theorem we can have that:

$$\frac{d\bar{\delta}^3}{d\bar{x}} = - \frac{3\ Ku}{Re_o\ Pr} \qquad (3.31)$$

with the following boundary conditions

$$\text{B.C.1.} \quad \text{at} \quad \bar{x} = \bar{L} \quad \bar{\delta} = 0$$
$$\text{B.C.2.} \quad \text{at} \quad \bar{x} = \bar{x} \quad \bar{\delta} = \bar{\delta}$$

where

$\bar{L} = L/\delta_o$
L: condensation length (m)

Integration of equation (3.31) with the application of the boundary condition and the definitions of Ku, Re_o and Pr, results in the following equation for the dimensional film thickness as reported by other investigators [16,94]:

$$\delta(x) = \left[\frac{3\dot{q}_o'' \mu_\ell \,(L - x)}{\rho_\ell \,(\rho_\ell - \rho_g)\, g \, h_{fg}}\right]^{1/3} \tag{3.32}$$

By definition we have that $\bar{\zeta}^{(0)} = \bar{\delta} = 1$ at the tube inlet. At that position and with the condition of no interfacial shear, equation (3.25) becomes:

$$Re_\delta = \frac{2}{3} Re_o \tag{3.33}$$

which is a relation that can be obtained from falling film theory [90, p. 39-40]. The agreement of equations (3.32) and

(3.33) with results found in the open literature may be used to check the validity of the present mathematical modelling of total reflux condensation. This completes the presentation of the present extended Nusselt's theory.

3.2.2 A Linearized Stability Analysis of Film-Wise Condensation

In this section a linearized stability analysis of film-wise condensation is exposed and its purpose is to compute the steam flow rate that leads to flooding for a prescribed base flow. It differs from previous studies by the nature of the perturbations considered, their consequences and the inclusion of tube diameter, surface tension and viscosity effects. In the present system the condensate film is perturbed by counter-current condensing steam flow. Then, the perturbations considered are those related to the hydrodynamics of the two-phase flow and the condensation mass transfer. Moreover, it is hypothesized that they cause the formation of standing waves which in turn lead to flooding. A linearized stability analysis can also give the interesting result of being able to identify the relative strength of each component of the net force acting on the interface. That knowledge could give justifications of the assumptions that would be made in the derivation of simpler models.

In Figure 3.4 the idealized flow situation near the tube entrance is shown The assumptions made in the present stability study are:

(i) flooding occurs at the tube inlet;

(ii) the velocity profile in the steam core is no longer assumed to be flat; instead, the universal velocity profile [95, p. 54] is assumed to be valid;

(iii) the local approximation method [97] is valid for the present case of film-wise condensation;

(iv) the amplitude of the wave is assumed to be infinitesimal and their wavelength is considered to be long with respect to the base flow film thickness.

In the study of the stability of boundary layer flows, the problem can be reduced to an eigenvalue problem formulated in terms of the governing equations for the disturbance amplitude functions and the boundary condition

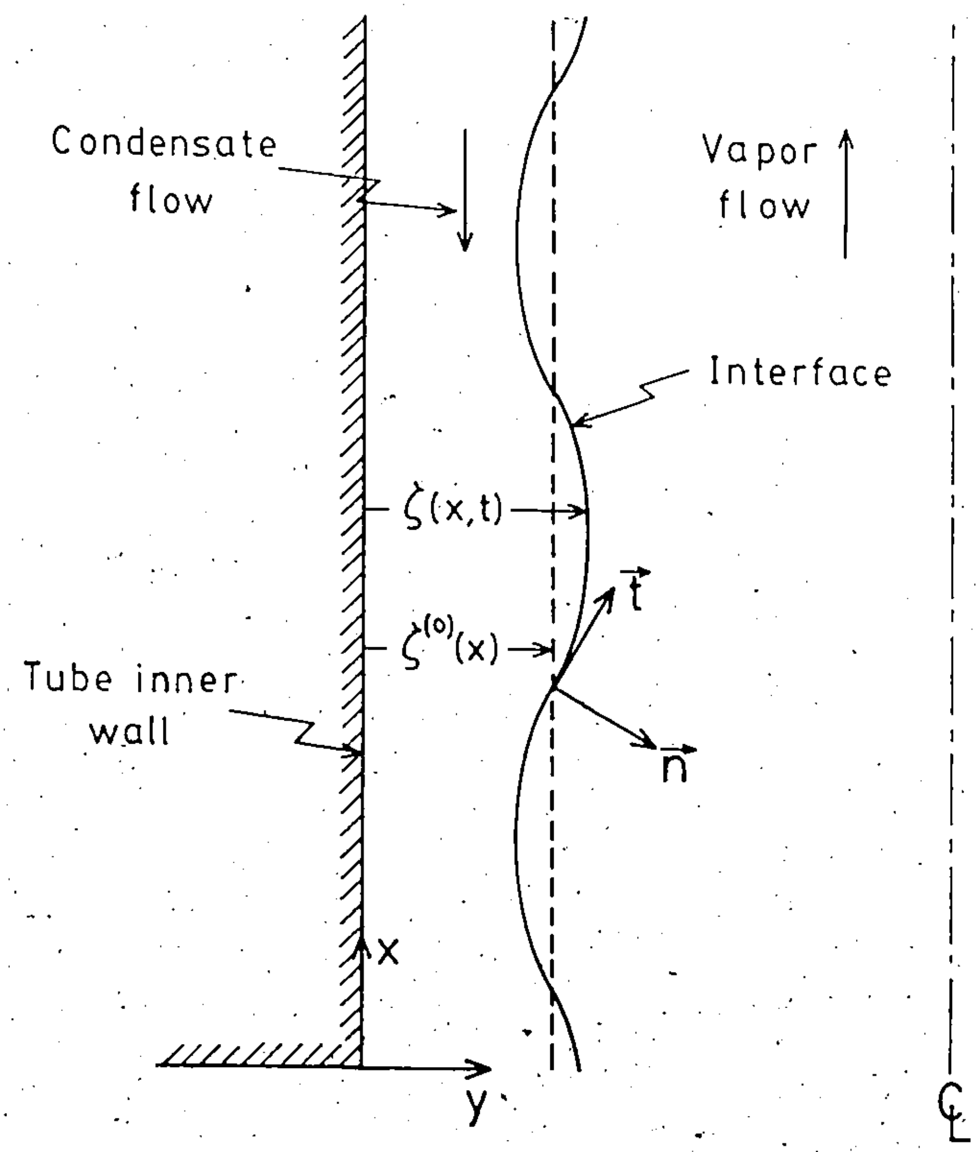

FIGURE 3.4 Flow Situation Idealization Near the Tube Inlet

at the wall and at a large distance from it [45, p. 442]. Thus, the field over which the disturbances exist is unbounded in one direction. In the present case, the flow field of interest (the condensate film) is bounded by the tube wall and a wavy interface. The presence of the wavy interface results in a different formulation of the eigenvalue problem when compared to the case of a boundary layer over a flat plate. The difference lies in the use of interfacial disturbance jump conditions to represent the conditions of the disturbance amplitude velocity and temperature functions (eigenfuntions) at the wavy interface.

The formulation of the present stability problem consists in the Orr-Sommerfeld and the perturbed energy equations with the necessary boundary and interfacial disturbance jump conditions. The detailed derivations of the two governing equations for the disturbance amplitude functions and the boundary conditions have been previously reported [45, pp. 438-442, 50, 52, 97] and will be omitted. The equations are given in the full statement of the eigenvalue problem below. On the other hand, the appropriate expressions of the interfacial disturbance jump conditions for the present problem have not been exposed in the opened literature yet and the derivation of these conditions is the object of the following section.

3.2.2.1 The Interfacial Disturbance Jump Conditions

In the derivation of the base flow model, the various assumptions made lead to a formulation of the governing equations in rectangular coordinates. To be consistent, the same system of coordinates and methodology of reduction to non-dimensional form will be used to formulate the interfacial disturbance jump conditions and the eigenvalue problem.

The lowest limit of stability being obtained by considering two-dimenisional disturbances [45, p. 442] we let the interface to be perturbed by a infinitesimal disturbance of the form:

$$\zeta^{(1)} = \zeta_o^{(1)} \exp(ik(x - ct)) \tag{3.34}$$

where

$c = c_r + ic_i$, the complex wave velocity (m/s)

$i = (-1)^{1/2}$

$k = 2\pi/\lambda$, the wave number (m^{-1})

λ : the wave length (m)

t : time (s)

$\zeta^{(1)}$: film thickness infinitesimal disturbance (m)

$\zeta_o^{(1)}$: maximum amplitude of the film thickness infinitesimal disturbance (m)

Only the real part of equation (3.34) has physical significance. The disturbance will grow exponentially with time when $c_i > 0$ leading to a film instability and for $c_i < 0$ the interface will be stable. In the derivation of the Orr-Sommerfeld, a stream function is introduced and it takes the following form:

$$\psi(x_o,y,t) = \phi(x_o,y)\exp(ik(x - ct)) \tag{3.35}$$

making use of the local approximating method (see third assumption) and noting that "x_o" is the position along the tube where the stability analysis is applied, in the present case $x_o = 0$. To ease the presentation, the "x_o" will be omitted in the rest of the derivation. From the definition of the stream function [45, p. 441] we can express the disturbance velocities as:

$$u_\ell^{(1)} = \frac{\partial\psi}{\partial y} = \frac{d\phi}{dy}\exp(ik(x - ct)) \tag{3.36}$$

$$v_\ell^{(1)} = -\frac{\partial\psi}{\partial x} = -(ik)\,\phi(y)\exp(ik(x - ct)) \tag{3.37}$$

which satisfy the perturbed steady-state form of the continuity equation. For the pressure and the temperature the disturbance functions are written as:

$$p_k^{(1)} = P_k(y)\exp(ik(x - ct));\ k = \ell,g \tag{3.38}$$

$$T_{\ell}^{(1)} = S(y)\exp(ik(x - ct)) \qquad (3.39)$$

where

$p_k^{(1)}$: disturbance pressure in phase k (N/m^2)

$P_k(y)$: disturbance pressure amplitude in phase k (N/m^2)

$T_{\ell}^{(1)}$: disturbance temperature in condensate film (^oC)

$S(y)$: disturbance temperature amplitude in condensate film (^oC)

With these definitions, the derivation of the interfacial disturbance jump conditions is as follow:

<u>energy:</u>

By introducing equation (3.20) in equation (3.21), the energy jump condition can be written in non-dimensional form, as:

$$\bar{v}_{\ell} - \left[\frac{\partial\bar{\zeta}}{\partial\bar{t}} + \bar{u}_{\ell}\,\frac{\partial\bar{\zeta}}{\partial\bar{x}}\right] = -\,\frac{Ku}{Pe}\,\frac{\partial\bar{T}_{\ell}}{\partial\bar{y}} \qquad (3.40)$$

For laminar flows, the theory of stability decomposes the motion into a base flow and into a disturbance superimposed on it [45, p.439]. The same methodology is used here. Let

$$\bar{u}_\ell = \bar{u}_\ell^{(0)} + \bar{u}_\ell^{(1)} \; ; \; \bar{v}_\ell = \bar{v}_\ell^{(0)} + \bar{v}_\ell^{(1)}$$

$$\bar{\zeta} = \bar{\zeta}^{(0)} + \bar{\zeta}^{(1)} \; ; \; \bar{T}_\ell = \bar{T}_\ell^{(0)} + \bar{T}_\ell^{(1)} \tag{3.41}$$

$$\bar{\zeta} = \zeta/\delta_o \; ; \; \bar{\zeta}^{(0)} = \bar{\delta}$$

where the superscripts "(0)" and "(1)" indicate respectively a base flow variable and a perturbed flow variable and the extended Nusselt's theory developed in Section 3.2.1 will be used to supply the values of the base flow variables. It should be noted here that in Section 3.2.1 all the variables are base flow variables and the superscript "(0)" has not been used to designate them for a clearer presentation of the analysis.

Introducing the definitions of variables (3.41) and the non-dimensional form of equation (3.34), (3.36), (3.37), and (3.39) in equation (3.40) and transforming onto the base flow the resulting expression, the following interfacial energy disturbance jump condition is obtained:

$$i\bar{k}\,\bar{\phi}(\bar{y}) + i\bar{k}\,(\bar{u}_\ell^{(0} - \bar{c}^{(0)})\,\bar{\zeta}_o^{(1)} = + \frac{Ku}{Pe}\frac{d\bar{S}}{d\bar{y}} \quad \text{at} \quad \bar{y} = \bar{\zeta}^{(0)} = \bar{\delta} \tag{3.42}$$

where

$\bar{k} = 2\pi\delta_o/\lambda$; $\bar{\phi}(\bar{y}) = \phi(y)/u_o\delta_o$

$\bar{c}^{(0)} = c_r/u_o + i\, c_i/u_o$; $\bar{S}(\bar{y}) = S(y)/\Delta T_q$

momentum (normal projection):

The normal projection of the momemtum jump condition can be written in non-dimensional form as [46, p.104, 47]:

$$\bar{\tau}_{yy,g} = -\bar{p}_\ell + \frac{2\partial\bar{v}_\ell}{Re_o\partial\bar{y}} + \frac{(1-\gamma)}{\gamma}\left[\bar{v}_\ell - \frac{\partial\bar{\zeta}}{\partial\bar{t}} + \bar{u}_\ell\frac{\partial\bar{\zeta}}{\partial\bar{x}}\right]^2 - We\frac{\partial^2\bar{\zeta}}{\partial\bar{x}^2} \quad \text{at} \quad \bar{y} = \bar{\zeta} \tag{3.43}$$

and introducing equation (3.40) in the last equation we have:

$$\bar{\tau}_{yy,g} = -\bar{p}_\ell + \frac{2}{Re_o}\frac{\partial\bar{v}_\ell}{\partial\bar{y}} + \frac{(1-\gamma)}{\gamma}\frac{Ku^2}{Pe^2}\left(\frac{\partial\bar{T}_\ell}{\partial\bar{y}}\right)^2 - We\frac{\partial^2\bar{\zeta}}{\partial\bar{x}^2} \quad \text{at} \quad \bar{y} = \bar{\zeta} \tag{3.44}$$

where

$$\bar{\tau}_{yy,g} = -p_g + \frac{2M_r}{Re_o}\frac{\partial \bar{v}_g}{\partial \bar{y}}$$, the non-dimensional steam interfacial normal stress [97, p. 58]

$$We = \frac{\sigma}{\rho_\ell\, u_o^2\, \delta_o}$$; the Weber number

σ = surface tension (N/m)

$M_r = \mu_g/\mu_\ell$

The variables in the expression for the non-dimensional steam interfacial normal stress can be defined in the same way as in equation (3.41). Introducing such definitions lead to the following equation for the disturbances:

$$\bar{\tau}^{(1)}_{yy,g} = \frac{P_s\ \bar{\zeta}^{(1)}}{Re_o} + \frac{2M_r}{Re_o}\frac{\partial \bar{v}^{(1)}_g}{\partial \bar{y}} \qquad (3.45)$$

where P_s is a non-dimensional disturbance normal stress that will be defined later in the present study by a constitutive equation. The combination of the no-slip condition at the interface [47] and the continuity equation and the introduction of perturbed values (like in eq. 3.41) of the variables in the resulting expression yield:

$$\frac{\partial \bar{v}_g^{(1)}}{\partial \bar{y}} = - \frac{\partial^2 \bar{\zeta}^{(1)}}{\partial \bar{x}^2} (\bar{v}_g^{(0)} - \bar{v}_\ell^{(0)}) - \frac{\partial \bar{v}_\ell^{(1)}}{\partial \bar{x}} \tag{3.46}$$

at $\bar{y} = \bar{\zeta}$

By an order of magnitude analysis and the use of the base flow energy jump condition (Eq. 3.21) one can show that;

$$\frac{\partial \bar{v}_g^{(1)}}{\partial \bar{y}} = \frac{\partial^2 \bar{\zeta}^{(1)}}{\partial \bar{x}^2} \frac{1}{\gamma} \frac{Ku}{Pe} \frac{\partial \bar{T}_\ell^{(0)}}{\partial \bar{y}} \quad \text{at} \quad \bar{y} = \bar{\zeta} \tag{3.47}$$

Introducing equation (3.47) in equation (3.45) yields:

$$\tau_{yy,g}^{(1)} = \frac{P_s \bar{\zeta}^{(1)}}{Re_o} + \frac{2M_r}{Re_o} \frac{\partial^2 \bar{\zeta}^{(1)}}{\partial \bar{x}^2} \frac{1}{\gamma} \frac{Ku}{Pe} \frac{\partial \bar{T}_\ell^{(0)}}{\partial \bar{y}} \tag{3.48}$$

at $\bar{y} = \bar{\zeta}$

The jump condition expressed by equation (3.44) is non-linear by the presence of the square of the derivative of condensate film temperature with respect to the transverse coordinate. With the replacement of the variables by their perturbed values, linearization and transformation onto the base flow (i.e. at $\bar{y}=\bar{\delta}=\bar{\zeta}^{(0)}$) it can be shown that:

$$\left(\frac{\partial \bar{T}_\ell}{\partial \bar{y}}\right)^2 = \left(\frac{\partial \bar{T}_\ell^{(0)}}{\partial \bar{y}}\right)^2 + 2\,\frac{\partial \bar{T}_\ell^{(0)}}{\partial \bar{y}}\,\frac{\partial \bar{T}_\ell^{(1)}}{\partial \bar{y}} + 2\,\bar{\zeta}^{(1)}\,\frac{\partial \bar{T}_\ell^{(0)}}{\partial \bar{y}}\,\frac{\partial^2 \bar{T}_\ell^{(0)}}{\partial \bar{y}^2}, \quad \text{at} \quad \bar{y} = \bar{\zeta} = \bar{\delta} \tag{3.49}$$

and from equation (3.19) it can be assumed that:

$$2\bar{\zeta}^{(1)}\,\frac{\partial \bar{T}_\ell^{(0)}}{\partial \bar{y}}\,\frac{\partial^2 \bar{T}_\ell^{(0)}}{\partial \bar{y}^2} << 2\,\frac{\partial \bar{T}_\ell^{(0)}}{\partial \bar{y}}\,\frac{\partial \bar{T}_\ell^{(1)}}{\partial \bar{y}} \tag{3.50}$$

By introducing the perturbed values of the variables in equation (3.44), combining the result with equations (3.48) and (3.49) and inequality (3.50) and transforming the expression onto the base flow, the disturbance pressure in the condensate film can be written as:

$$\bar{p}_\ell^{(1)} = -\,We\,\frac{\partial^2 \bar{\zeta}^{(1)}}{\partial \bar{x}^2} - \frac{P_s \bar{\zeta}^{(1)}}{Re_o} + \frac{2}{Re_o}\,\frac{\partial \bar{v}_\ell^{(1)}}{\partial \bar{y}} - \frac{2M_r}{\gamma Re_o}\,\frac{Ku}{Pe}\,\frac{\partial \bar{T}_\ell^{(0)}}{\partial \bar{y}}\,\frac{\partial^2 \bar{\zeta}^{(1)}}{\partial \bar{x}^2} + 2\,\frac{(1-\gamma)}{\gamma}\,\frac{Ku^2}{Pe^2}\,\frac{\partial \bar{T}_\ell^{(0)}}{\partial \bar{y}}\,\frac{\partial \bar{T}_\ell^{(1)}}{\partial \bar{y}} \tag{3.51}$$

The introduction of equation (3.34) in equation (3.51) and the multiplication of the result by "$i\bar{k}$" gives:

$$i\bar{k}\,\bar{P}_{\ell}(\bar{y}) = \left[i\bar{k}^{3}\,We - \frac{i\bar{k}P_{s}}{Re_{o}} + i\bar{k}^{3}\,\frac{2M_{r}}{Re_{o}\gamma}\,\frac{Ku}{Pe}\,\frac{\partial \bar{T}_{\ell}^{(0)}}{\partial \bar{y}}\right]\bar{\zeta}_{o}^{(1)} + 2\,(1 - M_{r})\,\frac{\bar{k}^{2}}{Re_{o}}\,\frac{d\bar{\phi}}{d\bar{y}} + 2\,\frac{(1-\gamma)}{\bar{\gamma}}\,\frac{Ku^{2}}{Pe^{2}}\,\frac{\partial \bar{T}_{\ell}^{(0)}}{\partial \bar{y}}\,\frac{d\bar{S}}{d\bar{y}} \tag{3.52}$$

The x-axis momentum equation in rectangular coordinates is valid locally and in particular at the interface. By going through the same methodology as exposed above, the perturbed flow x-axis momentum equation can be written as:

$$i\bar{k}\,\bar{P}(\bar{y}) = \frac{\Gamma}{Re_{o}}\left[\frac{d^{3}\bar{\phi}}{d\bar{y}^{3}} - k^{2}\,\frac{d\bar{\phi}}{d\bar{y}}\right] + (i\bar{k})\left[\frac{\partial \bar{u}_{\ell}^{(0)}}{\partial \bar{y}}\,\bar{\phi}(\bar{y}) - (\bar{u}_{\ell}^{(0)} - \bar{c}^{(0)})\,\frac{d\bar{\phi}}{d\bar{y}}\right] \tag{3.53}$$

Elimination of the pressure term between equations (3.52) and (3.53) and taking into consideration that $M_r \ll 1$ give the following expression for the normal projection of the disturbance momentum jump condition:

$$\frac{d^3\bar{\varphi}}{d\bar{y}^3} - 3\bar{k}^2 \frac{d\bar{\phi}}{d\bar{y}} + i\bar{k}\ Re_o \left[\frac{\partial \bar{u}_\ell^{(0)}}{\partial \bar{y}} \bar{\phi}(\bar{y}) - (\bar{u}_\ell^{(0)} - \bar{c}^{(0)}) \frac{d\bar{\phi}}{d\bar{y}}\right]$$
$$- i\bar{k}\left[\bar{k}^2\ We\ Re_o - P_s + 2\bar{k}^2 \frac{M_r}{\gamma}\frac{Ku}{Pe}\frac{\partial \bar{T}_\ell^{(0)}}{\partial \bar{y}}\right]\bar{\zeta}_o^{(1)} \tag{3.54}$$

$$- 2(i\bar{k})\frac{(1-\gamma)}{\gamma}\frac{Ku^2}{Re_o Pr^2}\frac{\partial \bar{T}_\ell^{(0)}}{\partial \bar{y}}\frac{d\bar{S}}{d\bar{y}} = 0 \quad \text{at } \bar{y} = \bar{\zeta}^{(0)} = \bar{\delta}$$

momentum (tangential projection):

The tangential projection of the momentum jump condition can be written in non-dimensional form as [46, p.104, 47]:

$$\bar{\tau}_{xy,g} = \frac{1}{Re_o}\left(\frac{\partial \bar{u}_\ell}{\partial \bar{y}} + \frac{\partial \bar{v}_\ell}{\partial \bar{x}}\right) \tag{3.55}$$

The application of the same methodology used in the development of the normal projection results in the following expression for the tangential projection of the disturbance momentum jump condition:

$$T_s\ \bar{\zeta}_o^{(1)} = \frac{d^2\bar{\phi}}{d\bar{y}^2} + \bar{k}^2\ \bar{\phi}(\bar{y}) + \frac{\partial^2 \bar{u}_\ell^{(0)}}{\partial \bar{y}^2}\bar{\zeta}_o^{(1)} \tag{3.56}$$
$$\text{at } \bar{y} = \bar{\zeta}^{(0)} = \bar{\delta}$$

where T_s is a non-dimensional disturbance tangential stress that will be defined later in the present study by a constitutive equation.

The validity of equations (3.42), (3.54) and (3.56) can be checked by doing limit analysis and a comparison with the results of other investigators. With the reduction of the equations to the case of an adiabatic flow, equation (3.42) takes the form of the standard interfacial kinematic condition as given by Lamb [49, p.373] and equations (3.54) and (3.56) become equivalent to the interfacial disturbance jump conditions obtained by Cetinbudaklar and Jameson [32] for the case of an adiabatic counter-current two-phase flow. For non-adiabatic conditions as in film-wise condensation of stagnant steam ($P_s = 0$, $T_s = 0$ in eqs (3.54) and (3.56)) on a cooled vertical plate, all three equations reduce to expressions derived by Unsal and Thomas [44] with the differences that in their equations they have normalized the non-dimensional film thickness by setting $\bar{\zeta}^{(0)} = \bar{\delta} = 1$, in their normal projection fo the momentum jump condition they have neglected the following term:

$$\begin{pmatrix}\text{Term neglected by}\\ \text{Unsal and Thomas}\end{pmatrix} = 2\bar{k}^2 \frac{M_r}{Y} \frac{Ku}{Pe} \frac{\partial \bar{T}_\ell^{(0)}}{\partial \bar{y}} \qquad (3.57)$$

with no apparent justification and finally because of the steam is stagnant they have taken

$$\frac{\partial \bar{u}_\ell}{\partial \bar{y}} = 0 \quad \text{at} \quad \bar{y} = \bar{\delta}$$

where in our case it is different from zero.

The constitutive equations for the non-dimensional gas perturbation normal and tangential stresses remain to be exposed and the critical layer concept can be utilised to derive the necessary expression. It was Miles [54] who used first the concept of critical layer in the study of generation of surface waves by shear flow; he considered both phases to be inviscid. Later then, the concept was used again by Brooke-Benjamin [53] who considered the gas phase to be viscous in the derivation of P_s and T_s. Besides this difference between the two analyses, one similarity exists as they both considered the gas phase flow regime as being quasi-laminar with a mean velocity profile with the assumption that gas viscosity and turbulence have no other effects than to maintain the velocity profile. In general, the transfer of mechanical energy from the gas to the liquid phase occurs when the critical layer is near the interface and in counter-current two-phase flow the critical layer can exist in both phases or neither phase [95, pp.102-110].

The flooding criterion exposed in Section 3.1.3 implies that, at the flooding point, the steam flow rate leads to the formation of a wave at the tube inlet that first, does not propagate with respect to the condensate film surface and second, condensate is rapidly teared off by the steam flow to form a droplet aggregate that pulsates upward. Then, from the no-slip condition at the steam-water interface and the definition of the critical layer position, we have, at flooding, a critical layer at the interface and none in the phases. As mentioned by Cetinbudaklar and Jameson [32], Brooke-Benjamin [53] showed for this case that work can be done by the variable perturbing stresses acting on the waves.

The detailed derivations of P_s and T_s have been already presented [53,54] and they will be omitted here. The mathematical nature of their expressions is complex and quoting them from Cetinbudaklar and Jameson [32], who took into account the minor corrections from Craik [99], we have that the real and imaginary parts of P_s and T_s are:

$$P_{sr} = [1.0 + 0.644\ \Omega\ (3)^{1/2}]\ H_2 \tag{3.58a}$$

$$P_{si} = -\ 0.644\ \Omega\ H_2 \tag{3.58b}$$

$$T_{sr} = 0.686\ H_1^{2/3}\ H_2[1.0 + 1.288\ \Omega\ (3)^{1/2}] \tag{3.58c}$$

$$T_{si} = 0.686\ H_1^{2/3}\ H_2\ [(3)^{1/2} + 1.288\ \Omega] \tag{3.58d}$$

with

$$H_1 = k\ \nu_g / u_*$$

$$H_2 = \frac{2k^2\ u_*^2\ (\rho_g/\ \rho_\ell) g\ I}{1 + 1.288\ \Omega\ [(3)^{1/2} + 1.288\ \Omega]}$$

$$\Omega = H_1^{4/3}\ k\ I$$

$$I = \int_\delta^R u_g^{+2}\ \exp\ [\ k\ (y - \delta)\ ]\ dy$$

$$\bar{S}(\bar{y} = \bar{\delta}) = - \frac{\partial \bar{T}_\ell^{(0)}}{\partial \bar{y}}\ \bar{\zeta}_o^{(1)} \tag{3.59}$$

where

ν_g: kinematic viscosity of the steam (m^2/s)

u_*: $[f_{ie} u_{g,c\ell}^2/2]^{1/2}$ friction velocity (m/s) [32,100,p.170]

f_{ie}: effective interfacial friction factor at the tube inlet

$u_{g,c\ell}$: steam velocity at the center line of the tube (m/s)

u_g^+: non-dimensional local steam velocity

and the "universal velocity profile" [95,p.54] is assumed to represent adequately the non-dimensional steam velocity profile at the tube entrance.

3.2.2.2 The Eigenvalue Problem

The eigenvalue problem from the present stability analysis has to be formulated in terms of two governing equations for the disturbance amplitude functions and homogeneous boundary and jump conditions. Therefore, the two momentum jump conditions (eqs 3.54 and 3.56) and one of the boundary condition for the temperature disturbance amplitude function which is given as [44,52]:

$$\bar{S}(\bar{y} = \bar{\delta}) = - \frac{\partial \bar{T}_{\ell}^{(0)}}{\partial \bar{y}} \bar{\zeta}_o^{(1)} \qquad (3.59)$$

must be homogenized to be used in the statement of the eigenvalue problem. From equation (3.42) one can write:

$$\bar{\zeta}_o^{(1)} = \frac{1}{i\bar{k}(\bar{u}_{\ell}^{(0)} - \bar{c}^{(0)})} \frac{Ku}{Pe} \frac{d\bar{S}}{d\bar{y}} - \frac{\bar{\phi}(\bar{y})}{(\bar{u}_{\ell}^{(0)} - \bar{c}^{(0)})} \qquad (3.60)$$

The introduction of equation (3.60) in equations (3.54), (3.56) and (3.59) leads to the following statement of the eigenvalue problem:

(i) the Orr-Sommerfeld equation:

$$\frac{d^4\bar{\phi}}{d\bar{y}^4} - 2\bar{k}^2 \frac{d^2\bar{\phi}}{d\bar{y}^2} + \bar{k}^4 \bar{\phi}(\bar{y}) = i\bar{k}\, Re_o \left[(\bar{u}_\ell^{(0)} - \bar{c}^{(0)}) \frac{d^2\bar{\phi}}{d\bar{y}^2} - \bar{k}^2 \phi(\bar{y}) - \frac{\partial^2 \bar{u}_\ell^{(0)}}{\partial \bar{y}^2} \bar{\phi}(\bar{y}) \right] \tag{3.61}$$

(ii) the perturbed energy equation:

$$\frac{d^2\bar{S}}{d\bar{y}^2} - \bar{k}^2 \bar{S}(\bar{y}) = i\bar{k}\ Pe \left[(\bar{u}_\ell^{(0)} - \bar{c}^{(0)}) \bar{S}(\bar{y}) - \frac{\partial \bar{T}_\ell^{(0)}}{\partial \bar{y}} \bar{\phi}(\bar{y}) \right] \tag{3.62}$$

(iii) the boundary conditions:

B.C.1 at $\bar{y} = 0$ $\quad \bar{\phi}(0) = 0$ (3.63a)

B.C.2 at $\bar{y} = 0$ $\quad \dfrac{d\bar{\phi}(0)}{d\bar{y}} = 0$ (3.63b)

B.C.3 at $\bar{y} = 0$ $\quad \dfrac{d\bar{S}(0)}{d\bar{y}} = 0$ (3.63c)

B.C.4. at $\bar{y} = \bar{\delta}$

$$(\bar{u}_\ell^{(0)} - \bar{c}^{(0)}) \bar{S}(\bar{y}) - \frac{i}{\bar{k}} \frac{\partial \bar{T}_\ell^{(0)}}{\partial \bar{y}} \frac{Ku}{Pe} \frac{d\bar{S}}{d\bar{y}} - \frac{\partial \bar{T}_\ell^{(0)}}{d\bar{y}} \bar{\phi}(\bar{y}) = 0 \tag{3.63d}$$

(iv) momentum jump condition (normal projection):

$$
\begin{aligned}
& i(\bar{u}_\ell^{(0)} - \bar{c}^{(0)}) \left[\frac{d^3\bar{\phi}}{d\bar{y}^3} - 3\bar{k}^2 \frac{d\bar{\phi}}{d\bar{y}}\right] \\
& - \bar{k}(\bar{u}_\ell^{(0)} - \bar{c}^{(0)}) \, Re_o \left[\frac{\partial \bar{u}_\ell^{(0)}}{\partial \bar{y}} \bar{\phi}(\bar{y}) - (\bar{u}_\ell^{(0)} - \bar{c}^{(0)}) \frac{d\bar{\phi}}{d\bar{y}}\right] \qquad (3.64) \\
& - \left[\bar{k}^2 \, WeRe_o - P_s + 2\bar{k}^2 \frac{Mr}{\gamma} \frac{Ku}{Pe} \frac{\partial \bar{T}_\ell^{(0)}}{\partial \bar{y}}\right] \left(\bar{k}\bar{\phi}(\bar{y}) + i \frac{Ku}{Pe} \frac{d\bar{S}}{d\bar{y}}\right) \\
& + \bar{k}(\bar{u}_\ell^{(0)} - \bar{c}^{(0)})^2 \, 2 \, \frac{(1-\gamma)}{\gamma Re_o} \frac{Ku^2}{Pr^2} \frac{\partial \bar{T}_\ell^{(0)}}{\partial \bar{y}} \frac{d\bar{S}}{d\bar{y}} = 0
\end{aligned}
$$

(v) momentum jump condition (tangential projection):

$$
\begin{aligned}
& \left(T_s - \frac{\partial^2 \bar{u}_\ell^{(0)}}{d\bar{y}^2}\right) \bar{\phi}(\bar{y}) + \left[\frac{d^2\bar{\phi}}{d\bar{y}^2} + \bar{k}^2 \bar{\phi}(\bar{y})\right] (\bar{u}_\ell^{(0)} - \bar{c}^{(0)}) \qquad (3.65) \\
& + \frac{i}{\bar{k}} \frac{Ku}{Pe} \left(T_s - \frac{\partial^2 \bar{u}_\ell^{(0)}}{d\bar{y}^2}\right) \frac{d\bar{S}}{d\bar{y}} = 0
\end{aligned}
$$

The interplay between the perturbing and the restoring forces can be easily seen by an examination of equation (3.64). The term with the Weber number is related to surface tension and has a stabilizing effect (see Section 1.2.2). As demonstrated by Unsal and Thomas [44] condensaton mass transfer has a dual role in regards of film stability. The term with the Peclet number has a stabilizing effect because it has the same sign as the term with the Weber number and each contains the non-dimensional wave number at the same power. On the other hand, the term with the ratio Ku^2/Pr^2 has as a destabilizing effect on the basis that its sign is different from the term with the Weber number. The term with P_s contains, as exposed above (see equations 3.58a and b), wave number at the same power as in the term with the Weber number; however, its sign is different implying a destabilizing effect.

For a given base flow, the above eigenvalue problem contains five (5) parameters: Re_o, $\bar{k}$, u_*, $\bar{c}_r$, and $\bar{c}_i$. Of these the Reynolds number is specified by the given base flow and the non-dimensional wave number is to be considered given. From the transposition of the flooding criterion in mathematical terms (see Section 3.2.1.1), it is clear that at the flooding point, the wave celerity is equal to the interfacial condensate film velocity at the tube inlet, in dimensional form we have:

$$\bar{c}_r = \bar{u}_{\ell i} \quad \text{at} \quad \bar{x} = 0 \tag{3.66}$$

In total reflux condensation, $\bar{u}_{\ell i}$ depends on the inlet steam flow rate which in turn in related to the friction velocity u_*. Then, at the flooding point there is a relation between the friction velocity and the wave celerity, i.e. knowing one will give the other. The above eigenvalue problem will furnish two eigenfunctions $\bar{\phi}(\bar{y})$ and $\bar{S}(\bar{y})$ and one complex eigenvalue $\bar{c}=\bar{c}_r+i\bar{c}_i$ for each pair of values $\bar{k}, Re_o$. However, taking the same approach as Cetindubaklar and Jameson [32] it is the friction velocity and the amplification factor "$\overline{kc_i}$" that are computed first and by the relationships mentioned above, the complex eigenvalue $\bar{c}$ is obtained.

3.2.2.3 Solution to the Eigenvalue Problem

Besides direct numerical integration methods, there are three methods that can be used to solve the present eigenvalue problem: perturbation methods [44,50,52], method of Anshus and Goren [101] and the method of quadrature by differentiation [102]. The perturbation method is good only for small values of wave number and the other two for any value of wavenumber. In the present study, the method of Anshus and Goren is used for solving the eigenvalue problem because:

(i) The range of values of the wavenumber, for the present physical situation is not known and may be well outside a range of what is considered to be a "small wavenumber". Then, the perturbation method is seen as being too restrictive to be applied in the present study.

(ii) The method of Anshus and Goren consists by replacing the velocity and the temperature gradient in equations (3.61) and (3.62), normally functions of distance form the wall, by their values at the steam-water interface while the second derivative of the velocity profile is kept at its true value. ~~This~~ permits a simple solution to the present system of equations (eqs (3.61) and (3.62)) and the eigenvalues can be determined by a relatively simple numerical technique.

(iii) The method of quadrature by differentiation solves the eigenvalue problem without making any assumption on the velocity and temperature gradient profiles and the results are shown not to differ by much from the results obtained by the method of Anshus and Goren [52].

It involves lengthy calculations and its purpose is mainly to serve as a tool for benchmark calculations.

From the solution of the equations of the base flow model, the interfacial condensate film velocity and temperature gradient at the tube entrance are known. Substituting these values in equations (3.61) and (3.62) lead to a system of ordinary differential equations with constant coefficients.

Following Spindler [52] the solution of the system at $\bar{x} = 0$ can be written as:

$$\bar{\phi}(\bar{y}) = C_1 \sin\beta_1\bar{y} + C_2 \cos\beta_1\bar{y} + C_3 \sin\beta_2\bar{y} + C_4 \cos\beta_2\bar{y} \tag{3.67}$$

$$\bar{S}(\bar{y}) = C_5 \sin\beta_1\bar{y} + C_6 \cos\beta_1\bar{y} + C_7 \sin\beta_2\bar{y} + C_8 \cos\beta_2\bar{y} + C_9 \sin\beta_3\bar{y} + C_{10} \cos\beta_3\bar{y} \tag{3.68}$$

The introduction of equations (3.67) and (3.68) in the system of differential equation and the application of the two first boundary conditions result in the following solution:

$$\bar{\phi}(\bar{y}) = C_1 \left[\sin\beta_1\bar{y} - \frac{\beta_1}{\beta_2}\sin\beta_2\bar{y}\right] - C_2\,(\cos\beta_1\bar{y} - \cos\beta_2\bar{y}) \tag{3.69}$$

$$\begin{aligned}\bar{S}(\bar{y}) = {} & C_1 \left[\frac{L_1}{N_1}\sin\beta_1\bar{y} - \left(\frac{L_1}{N_2}\ \frac{\beta_1}{\beta_2}\right)\sin\beta_2\bar{y}\right] \\ & + C_2\left[\frac{L_1}{N_1}\cos\beta_1\bar{y} - \frac{L_1}{N_2}\cos\beta_2\bar{y}\right] \\ & + C_9\sin\beta_3\bar{y} - C_{10}\cos\beta_3\bar{y}\end{aligned} \tag{3.70}$$

where the expressions for $\beta_1, \beta_2, \beta_3$, L_1, N_1, and N_2 are given in Appendix F. The introduction of equations (3.69) and (3.70) in equations (3.63c), (3.63d), (3.64), and (3.65) results in a homogeneous system of linear equations for the constants C_1, C_2, C_9, C_{10} and noting that at the interface at the tube inlet ($\bar{x}=0$), $\bar{y}=\bar{\zeta}^{(0)}=\bar{\delta}=1$. A non-trivial solution for these constants exists if the determinant of the coefficients is equal to zero. The determinant is shown in Figure 3.5 where the definitions of the variables, not already defined, are given in Appendix F. After straightfoward algebraic manipulations the determinant reduces to the following algebraic equation:

$$
\begin{vmatrix}
L_1\beta_1\left(\frac{1}{N_1}-\frac{1}{N_2}\right) & 0 & \beta_3 & 0 \\[2ex]
\begin{array}{l}\beta_1\hat{c}\Big(i(b_{10}-3\bar{k}^2 b_{11}) \\ +\ \bar{k}\,Re_o\hat{c}\,b_{11}+a_6L_1b_{13}\Big) \\ -\left(a_4+\bar{k}\hat{c}\,Re_o\dfrac{\partial\bar{u}_\ell^{(0)}}{\partial\bar{y}}\right)b_{12} \\ +\ a_5L_1\beta_1b_{11}\end{array} &
\begin{array}{l}\beta_1\hat{c}\Big(i(b_{20}-3\bar{k}^2 b_{21}) \\ +\ \bar{k}Re_o\hat{c}b_{21}+a_6L_1b_{22}\Big) \\ -\left(a_4+\bar{k}\hat{c}\,Re_o\dfrac{\partial\bar{u}_\ell^{(0)}}{\partial\bar{y}}\right)b_{11} \\ +\ a_5L_1\beta_1b_{22}\end{array} &
-(a_5+\hat{c}a_6)\,\beta_3\cos\beta_3 & -(a_5+\hat{c}a_6)\,\beta_3\sin\beta_3 \\[2ex]
\begin{array}{l}\left(T_s-\dfrac{\partial^2\bar{u}_\ell^{(0)}}{\partial\bar{y}^2}\right)(b_{12}+a_1L_1\beta_1b_{13}) \\ +\ [\beta_1\hat{c}_{10}+\bar{k}^2 b_{12}]\,\hat{c}\end{array} &
\begin{array}{l}\left(T_s-\dfrac{\partial^2\bar{u}_\ell^{(0)}}{\partial\bar{y}^2}\right)(b_{11}+a_7L_1\beta_1b_{22}) \\ +\ [\beta_1c_{20}+\bar{k}^2b_{11}]\,\hat{c}\end{array} &
a_7\left(T_s-\dfrac{\partial^2\bar{u}_\ell^{(0)}}{\partial\bar{y}^2}\right)\beta_3\cos\beta_3 &
-a_7\left(T_s-\dfrac{\partial^2\bar{u}_\ell^{(0)}}{\partial\bar{y}^2}\right)\beta_3\sin\beta_3 \\[2ex]
\hat{c}L_1d_{10}-a_1L_1\beta_1b_{13}-a_2b_{12} & \hat{c}L_1b_{13}-a_1L_1\beta_1b_{22}-a_2b_{11} & \hat{c}\sin\beta_3-a_1\beta_3\cos\beta_3 & \hat{c}\cos\beta_3+a_1\beta_3\sin\beta_3
\end{vmatrix} = 0
$$

FIGURE 3.5 Determinant of the System of Homogeneous Linear Equations

$$F_t(u_*,\bar{c}_1) = \beta_1\beta_2(G_1D_1+G_2D_2) - \beta_1\beta_2(G_1D_2+G_2D_1)\cos\beta_1\cos\beta_2$$

$$-[G_1D_2\beta_2^2+G_2D_1\beta_1^2]\sin\beta_1\sin\beta_2 - \beta_1E(\beta_2^2-\beta_1^2)\sin\beta_2\cos\beta_1$$

$$+\beta_2E(\beta_2^2-\beta_1^2)\sin\beta_1\cos\beta_2 \tag{3.71}$$

$$+ Ku\frac{\partial\bar{T}_\ell^{(0)}}{\partial\bar{y}}\left[-F_{ht}^{(1)} + \frac{i\,F_{ht}^{(2)}}{\bar{k}\,Pe} - 2i\bar{k}^2\frac{Ku}{Pr}\frac{\partial\bar{T}_\ell^{(0)}}{\partial\bar{y}}(F_{ht}^{(3)}+F_{ht}^{(4)}) - E\,F_{ht}^{(5)} + F_{ht}^{(6)} - F_{ht}^{(7)} + F_{ht}^{(8)}\right] = 0$$

where the definitions of the variables are given in Appendix F. By its complex mathematical nature, equation (3.71) reduces to a set of two non-linear algebraic equations as follow:

$$F_t^{(r)}(u_*,\bar{c}_1) = 0 \tag{3.72a}$$

$$F_t^{(i)}(u_*,\bar{c}_1) = 0 \tag{3.72b}$$

where $F_t^{(r)}$ and $F_t^{(i)}$ are respectively the real and imaginary part of F_t. In the present study, the method of Powell [103] has been used to solve the set of equations (3.72).

The nature of the elements of equation (3.71) can be identified easily. All the terms in the square bracket multiplied by the Kutateladze number and the temperature gradient form an element related to heat transfer and all the remaining terms form an element related to the hydrodynamics of the two-phase flow. If the Kutateladze number and the temperature gradient at the interface are small, the flooding steam flow will depend mainly on the hydrodynamic conditions of the given base flow because the effects of condensation mass transfer on the condensate film stability will be negligible.

3.2.2.4 Remarks

The flooding criterion used in the present study is expressed by equation (3.67) and it is the same as in the study of Cetinbudaklar and Jameson [32]. Other investigators [13, p.134-135,104,105] suggest that flooding occurs when the kinematic waves [13,p.123,39] stop to propagate with respect to a fixed frame of reference. In the present system, the large waves formed at the tube entrance, when the flooding point is reached, contain mass that can be carried upward; consequently, they can be considered as kinematic waves and it is postulated that flooding occurs when these waves stop to propagate with respect to the condensate film velocity at the interface.

One could conclude to a notable discrepancy between the two flooding criteria, in fact, it is not the case. In the development of the present mathematical model, the condensate film thickness is assumed to be small with respect to the tube radius and simply from falling film flow theory [90, pp.37-41] the condensate film interfacial velocity will be small with respect to the steam velocity. In fact, in the region of the tube entrance with the influence of the interfacial shear the condensate film interfacial velocity will nearly be equal to zero with respect to a fixed frame of reference. Then, from equation (3.66), the celerity of the wave at the flooding point will be nearly zero with respect to a fixed frame of reference. Therefore, it can be concluded that the difference between the two criteria is small and they are, to a certain extent, equivalent.

3.2.3 Simulation of Total Reflux Condensation

In the development of the model the following steps have been covered:

(i) form visual observations two equivalent forms of the flooding criterion used is the present study have been defined

(ii) an extended Nusselt's theory has been derived

(iii) a linearized stability analysis of the condensate film has been carried out

(iv) the flooding criterion has been used to evaluate the wave celerity at the flooding point (see Equation (3.66))

(v) the use of the critical layer concept reported in the literature on wave generation has been given in the form of constitutive equation for the perturbing stresses P_s and T_s.

For a given base flow condition, the only free parameter in Equation (3.71) is the wavenumber and for each value of the wavenumber corresponds one pair of roots of Equation (3.71). The question is now to determine the critical wavenumber (wave length) that will correspond to a pair of roots that will be related to unstable flow conditions. The two concepts of maximum mechanical energy transfer and film instability can now be utilized to set up a simple criterion for the determination of that critical wavenumber. Figure 3.6 shows a variation of the non-dimensional amplification factor "$\overline{kc_i}$" as a function of the friction velocity u_* for a steam-water system at atmospheric pressure in a 2.54 cm O.D. tube and with f_{ie}=0.0185. Each curve corresponds to the solution of Equation (3.71) for

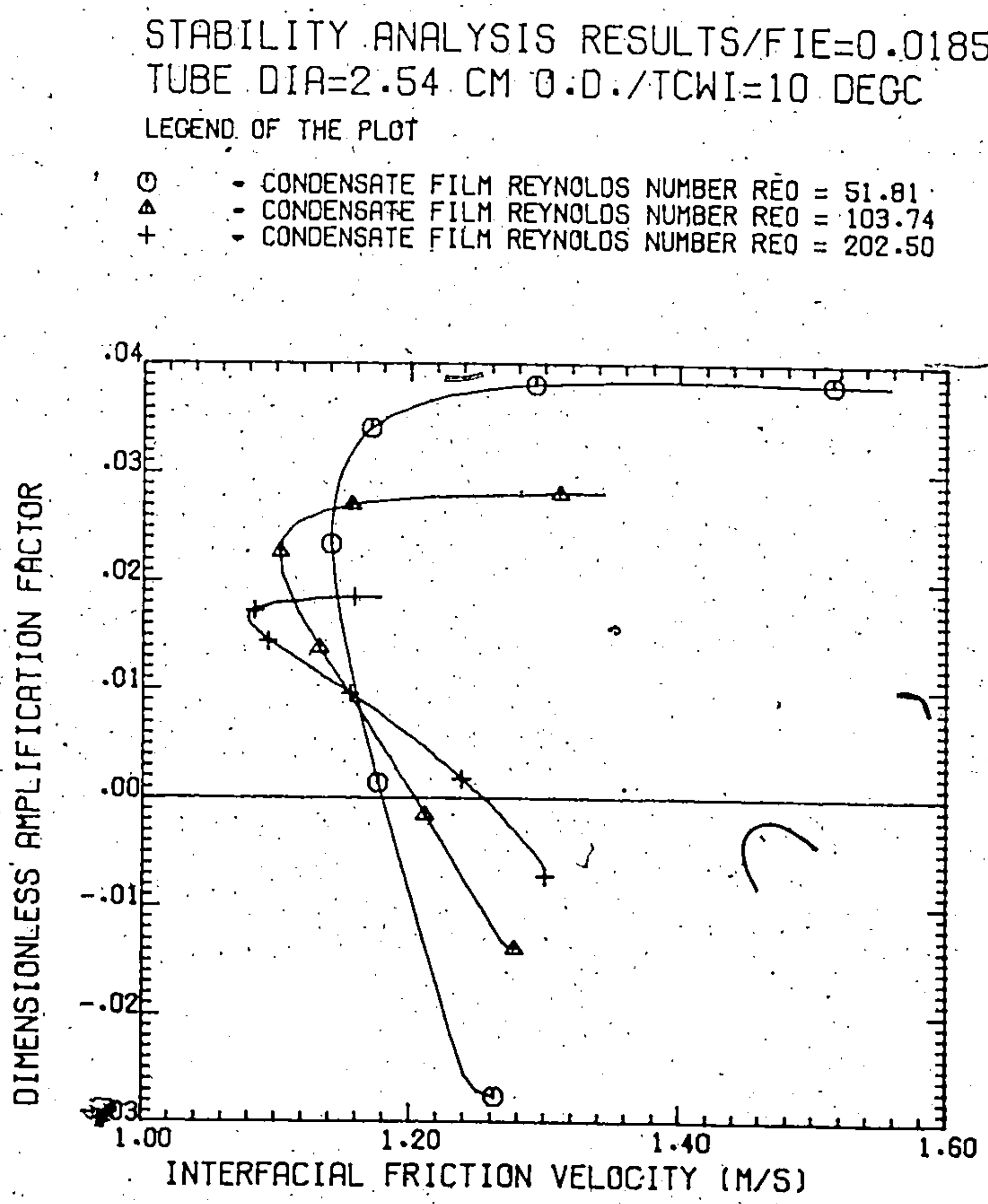

FIGURE 3.6 Variations of the Dimensionless Amplification Factor as a Function of the Interfacial Friction Velocity for Three Values of Re_o

a range of wavenumber with a given base flow condition indicated by the value of the Reynolds number. It can be seen that in the unstable region, where $\overline{kc_1}>0$, each curve goes through minimum value of u_*. It is the pair of roots corresponding to that minimum u_* that is a greatest interest since it defines that value of u_* below which all individual oscillations decay, whereas above that value at least some are amplified. In other words, it corresponds to flow conditions when the transfer of mechanical energy is at its maximum and it is all absorbed by viscous dissipation in the condensate film insuring its stability. This smallest friction velocity is the limit of stability with respect to the type of flow under considerations. Then, the steam flow rate at the flooding point is computed as follow. First, the steam velocity at the centerline is computed from the definition of the friction velocity. Second, it is multiplied by the ratio of the average velocity to the centerline velocity computed with the "universal velocity profile" [95, p.54] to obtain the average velocity. Third, the average velocity is multiplied by the steam density and the actual cross-sectional area of the steam flow. Figure 3.7 shows the effects of system pressure on the variations of the non-dimensional amplification factor as a function of the friction velocity. It can be seen that the minimum friction velocity decreases as the system pressure increases. This behavior indicates that the flooding velocity

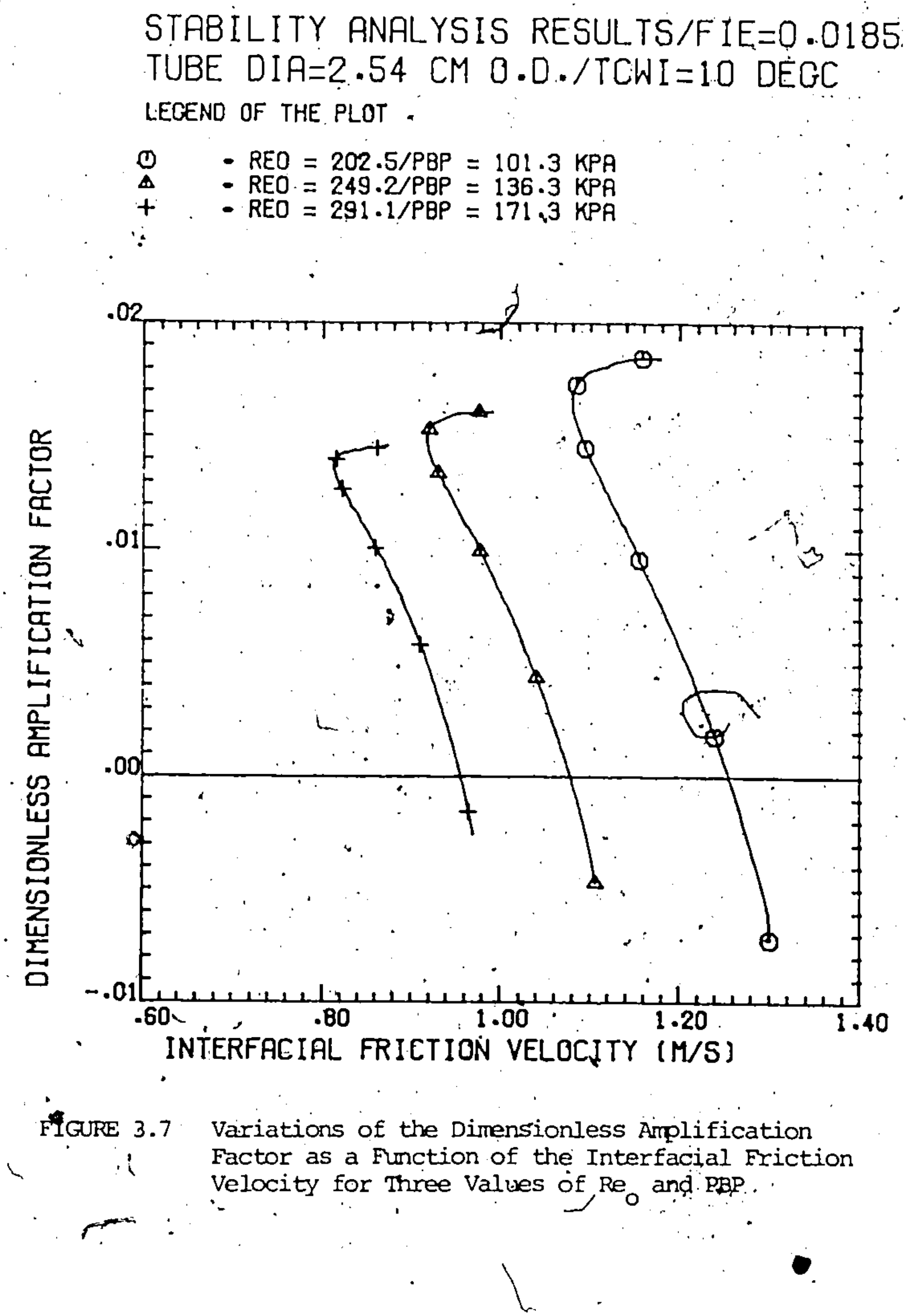

FIGURE 3.7 Variations of the Dimensionless Amplification Factor as a Function of the Interfacial Friction Velocity for Three Values of Re_o and PBP.

decreases as the system pressure increases; however, this variation is compensated by the fact that saturated steam density increases as pressure increases.

The characteristics of a base flow are obtained by solving the governing equations of the present model arising from the extended Nusselt's theory by applying global mass and energy balances. These balances mean that all the injected steam is condensed and all the condensate flows back to the tube entrance (no net flow at the entrance); they also mean that all the heat input i.e. (injected steam flow rate) x (latent heat) is transferred to the secondary side. Numerical experiments indicate that natural convection was the main heat removal mechanism on the secondary side. Correlations for vertical flat plates [100, pp.313-330] were assumed to be valid in regard of the results obtained for vertical cylinders [107].

The simulation of the sequence of quasi-static situations shown in Figure 3.1 is based on the flooding criterion presented in Section 3.1.3 (see Equation (3.66)), an extended Nusselt's theory, a linearized stability analysis with the application of three concepts; critical layer, maximum mechanical energy transfer and film instability and on the postulate that after flooding is reached, the reflux condenser still operates, on a time average basis, at the flooding point for each new boundary

<u>conditions defined by the new imposed pressure drop across the tube</u>. It should be noted here that such combination for the modelling of total reflux condensation has not been presented yet in the opened literature. In addition, the same characteristic length "δ_o" and velocity "u_o" have been used in the present extended Nusselt's theory and linearized stability analysis to obtain a <u>unified</u> model of total reflux condensation. The simulation is done by the computer progam REFLUX and a simplified flowchart of it is shown in Figure 3.8. The listing of the program, being too long to be included here, even in an appendix, can be found in [72]. The results of the simulation for most of the experimental conditions given in Table 2.1 is presented along with the experimental data in Chapter 4 where a comparison is made.

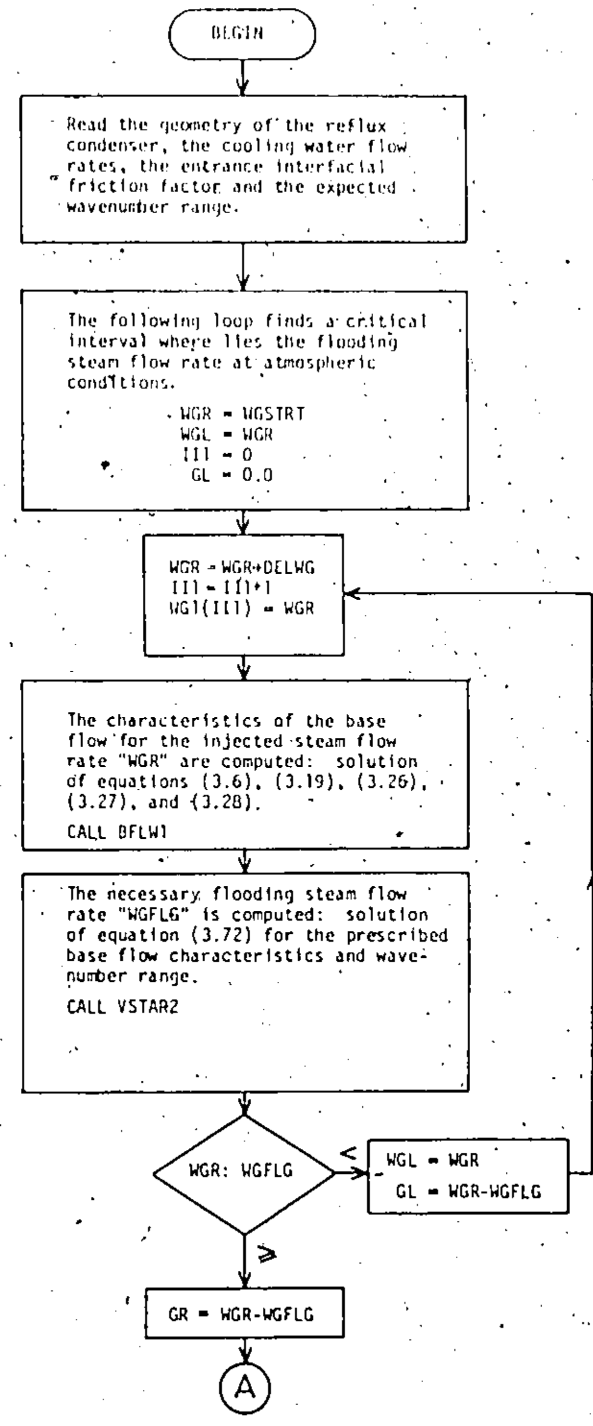

FIGURE 3.8 Flow Chart of Program "REFLUX"

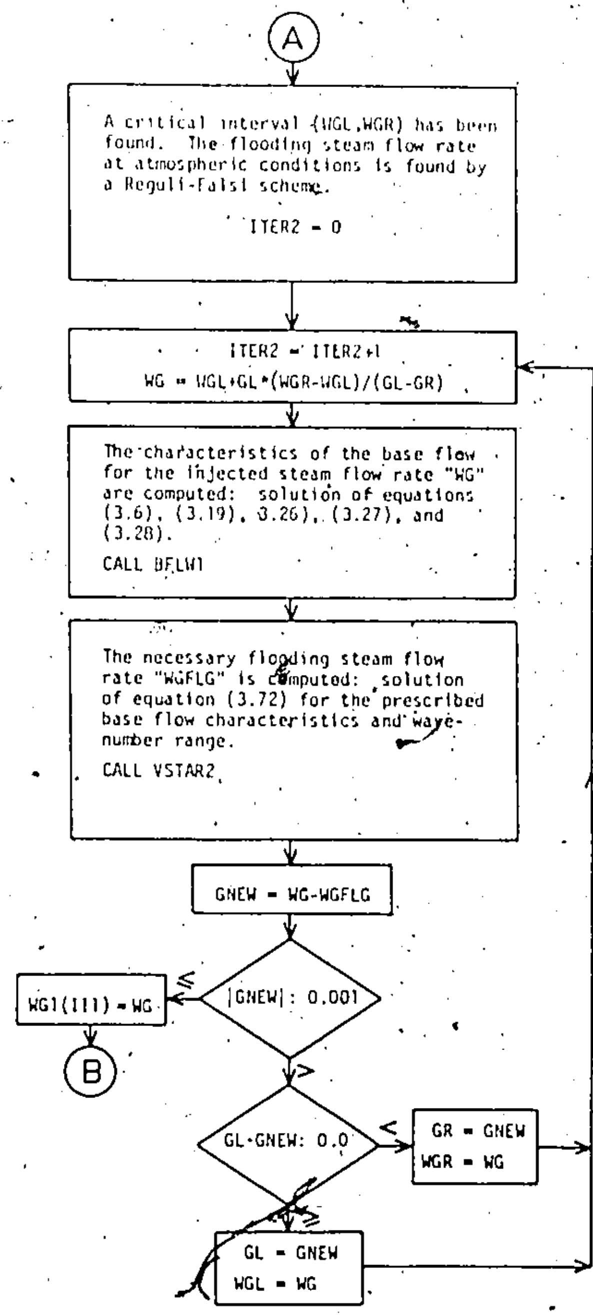

FIGURE 3.8 (continued)

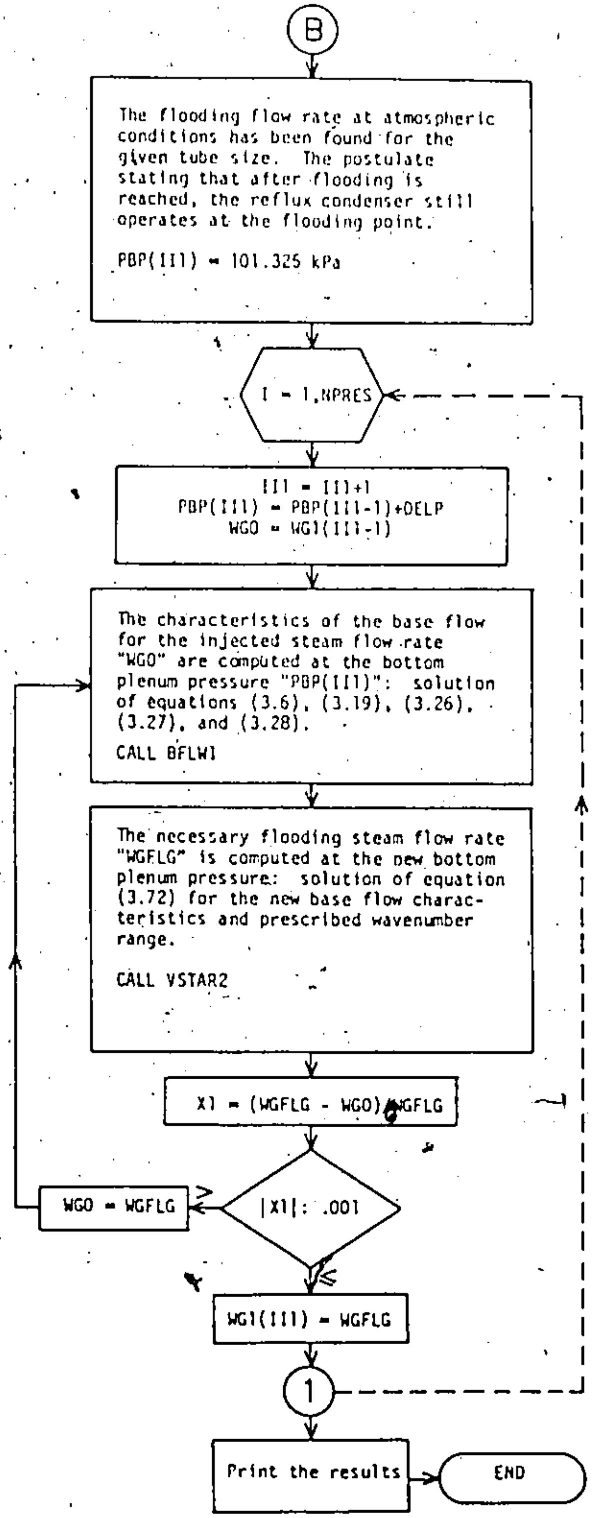

FIGRUE 3.8 (continued)

CHAPTER 4

EXPERIMENTAL RESULTS AND DISCUSSION

4.1 Results for Imposed Pressure Drops Across the Tube

In any heat transfer equipment where condensation takes place, the presence of non-condensible gases can adversely affect the condensation process [65]. In all total reflux condensation experiments, non-condensible gases were seen to evacuate the two-phase region through the single-phase region (if present) and to accumulate in the upper plenum. This observation led to the design of the non-condensible gases flow meter presented in Section 2.1.2.7.

The concentration of non-condensible gases in the steam from McMaster Power Plant was measured during the start-up phase of several experiments and the results for the 2.54 cm O.D. tube are presented in Appendix E. On the average, 0.009% per weight of non-condensible gases was flowing with the steam and the maximum amount measured was 0.0163% per weight. Sparrow et al. [65] (see also Collier [85, p.315]) showed that concentrations of non-condensible gases less than 0.5% per weight have little effect on the process of forced convection condensation. Then, for the level of concentration of non-condensible gases measured and the observation that they evacuated the two-phase region, the little effects of the non-condensible gases on the present condensation process is expected. The measurements of non-condensible gases concentration for total reflux condensation in the two other tube sizes, showed much smaller concentrations than for the 2.54 cm O.D. tube where in some cases the period of measurement was extended over many hours. To be conservative, it was concluded that the results for the 2.54 cm O.D. tube are valid for the other two tube sizes.

In most of the data presented here, the bottom plenum pressure has been taken as the main variable instead of the total pressure drop across the tube (between the two plenums). This choice allows the data to be shown for the cases where the upper plenum is opened to atmosphere and when it is pressurized by air, where the water column acts as a plug. The bottom plenum pressure can be thought as the total pressure drop for a reflux condenser of infinite length with an upper plenum open to atmosphere. In other words, the pressurization simulates, to a certain extent, an additional water column over the one already existing. Moreover, it allows us to bring out easily the meaning of the trend of the data.

Since the tube diameter is an important variable of the test matrix and could have an influence on the onset of flooding, the Kutateladze variable, K_i (see Equation (4.1)) [19-21], appears to be more suitable to present the condensate and steam flow rates in non-dimensional form. We have:

$$K_i = \frac{\rho_i^{1/2} \; j_i}{[g \; \sigma(\rho_\ell - \rho_g)]^{1/4}} \qquad i = \ell, g \qquad (4.1)$$

where all the variables have already been defined previously. From equation (4.1) it can be seen that K_i does not mask out any of the geometric dependences, whereas, the Wallis variable j_i^* (see equation (1.1)) masks out the diameter influence (if any). Therefore, K_i has been adopted in the present study to represent the flow rates in non-dimensional form.

The comparison between the readings from the steam orifice meter and the condensate level meter are shown in Appendix G (Figures G.1 to G.3) for each tube with the inlet cooling water temperature as the main parameter. The overall agreement between the two measurements is shown to be fairly good, where the correction (see Equation A.18, Appendix A) on the condensate level meter readings have been applied. The readings from the steam orifice meter are based on the thermal-hydraulic properties evaluated at the measured upstream pressure (P1 in Figure 2.1). The steam is assumed to be at saturation. These comparisons show that, for imposed pressure drops across the tube, total reflux condensation is really taking place in the reflux condenser. In addition, the average lengths of the single-phase and two-phase regions have been observed to remain constant for an imposed pressure drop across the tube. Then, to satisfy the principle of conservation of mass, the condition of no net flow must exists at both ends of the two phase region.

The observation of entrainment in the vapor core in the form of droplet aggregates pulsating upward towards the end of the two-phase region is mentioned in section 3.2.1. The total liquid holdup in the two-phase region can be assumed to be separated in two parts: one part in the form of condensate film and the other in the form of entrainment (droplet aggregates). The entrainment in the vapor core could be considered as an additional upward mass flow to the vapor flow. Then, based on the principle of conservation of mass we could suppose that:

(i) complete deposition of the entrainment on the condensate film should occur, which results in an additional downward mass flow with respect to the condensate flow actually exiting at the tube entrance;

(ii) on the average the deposition rate should be equal to the entrainment rate; in other words, to continuously have entrainment in the vapor core, part of the condensate film equal to the total deposition is entrained to be deposited again.

From the counter-current nature of total reflux condensation it can be suggested that part of the liquid holdup in the two-phase region could be <u>recirculated</u>.

The bulk of the experimental data is separated in four interrelated aspects: flooding, heat removal, liquid holdup and local measurements. Each of these aspects is the object of the following sections and in an additional section the oscillations of the single-phase region are briefly discussed.

4.1.1 <u>Flooding</u>

One of the main feature of total reflux condensation is the impossibility to vary independently the phases flow rates and temperatures as in the cases of air-water or air-steam/water flooding experiments. The rates of condensation obtained for the three tubes have been plotted in the $K_g^{1/2}-K_\ell^{1/2}$ plane in Figures 4.1a,b and c with the inlet cooling water temperature and the entrance interfacial friction factor (respectively TCWI and FIE in the figures) as the main parameters. It can be seen that in total reflux condensation, the steam and condensate flow rates on the flooding curves are, in terms of the Kutateladze variables, respectively in the high and low range when compared to the ranges of values these variables can have in adiabatic systems [19-21, 96] ($K_\ell^{1/2}$ and $K_g^{1/2}$ range between 0.0 and 2.5). It was mentioned in Chapter 1 that several investigators [19,21,23,26,30] observed in air-water flooding experiments that for low liquid flow rates, such as in the present case, flooding occurs at the tube inlet. In addition a sharp edge entrance condition will promote flooding at that location. Hence, the assumptions made in the stability analysis on the location of flooding (at the tube inlet) are partly justified by the above facts and the present experimental results.

The inlet cooling water temperature is shown to have a significant effect on the flooding point except in the case of the smallest tube (see Figure 4.1c). For the two other tube sizes (2.54 cm O.D. and 1.91 cm O.D.), the smaller the temperature gradient between the primary and

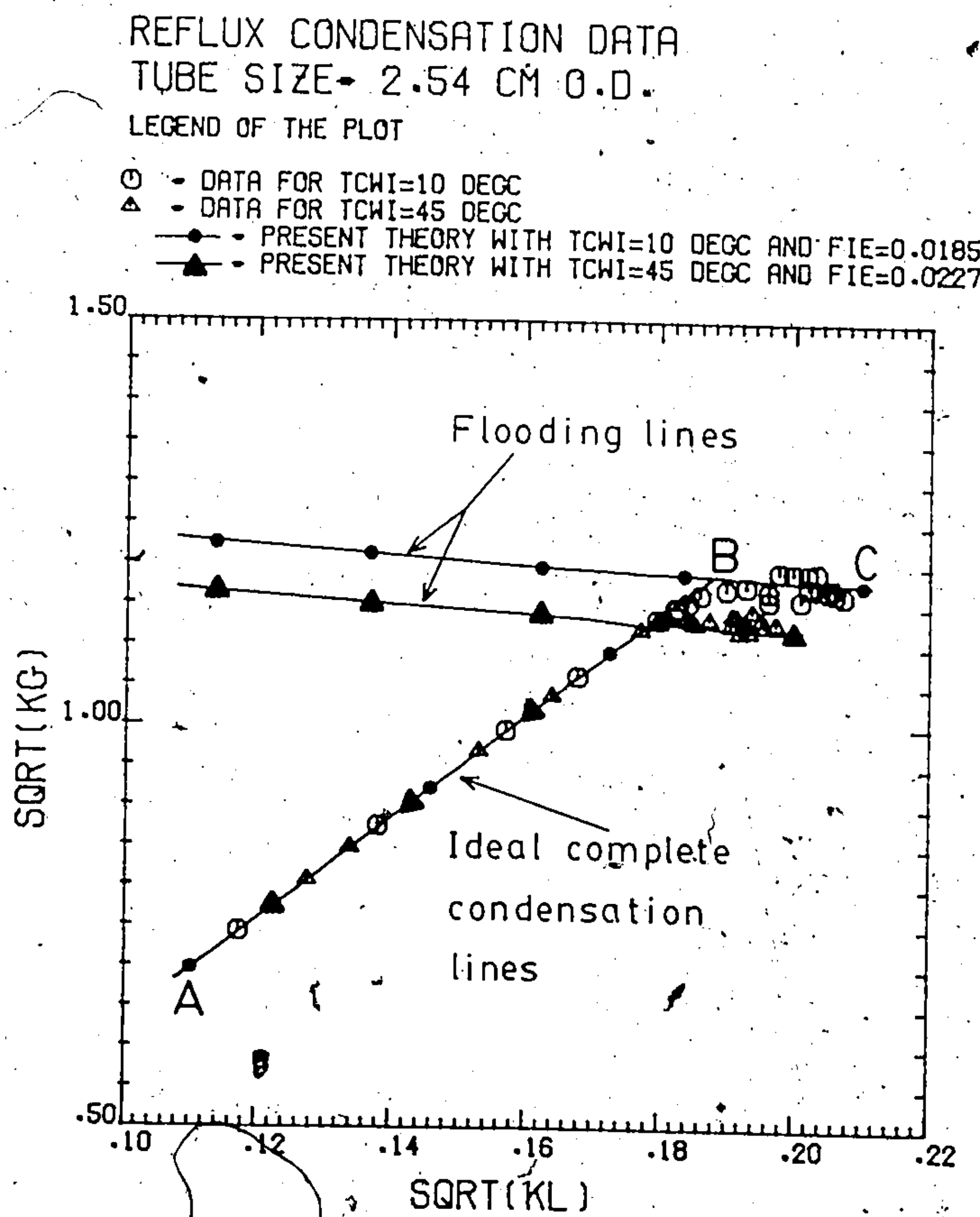

FIGURE 4.1a Reflux Condensation Data in the $K_g^{1/2}$-$K_\ell^{1/2}$ Plane for 2.54 cm O.D. Tube

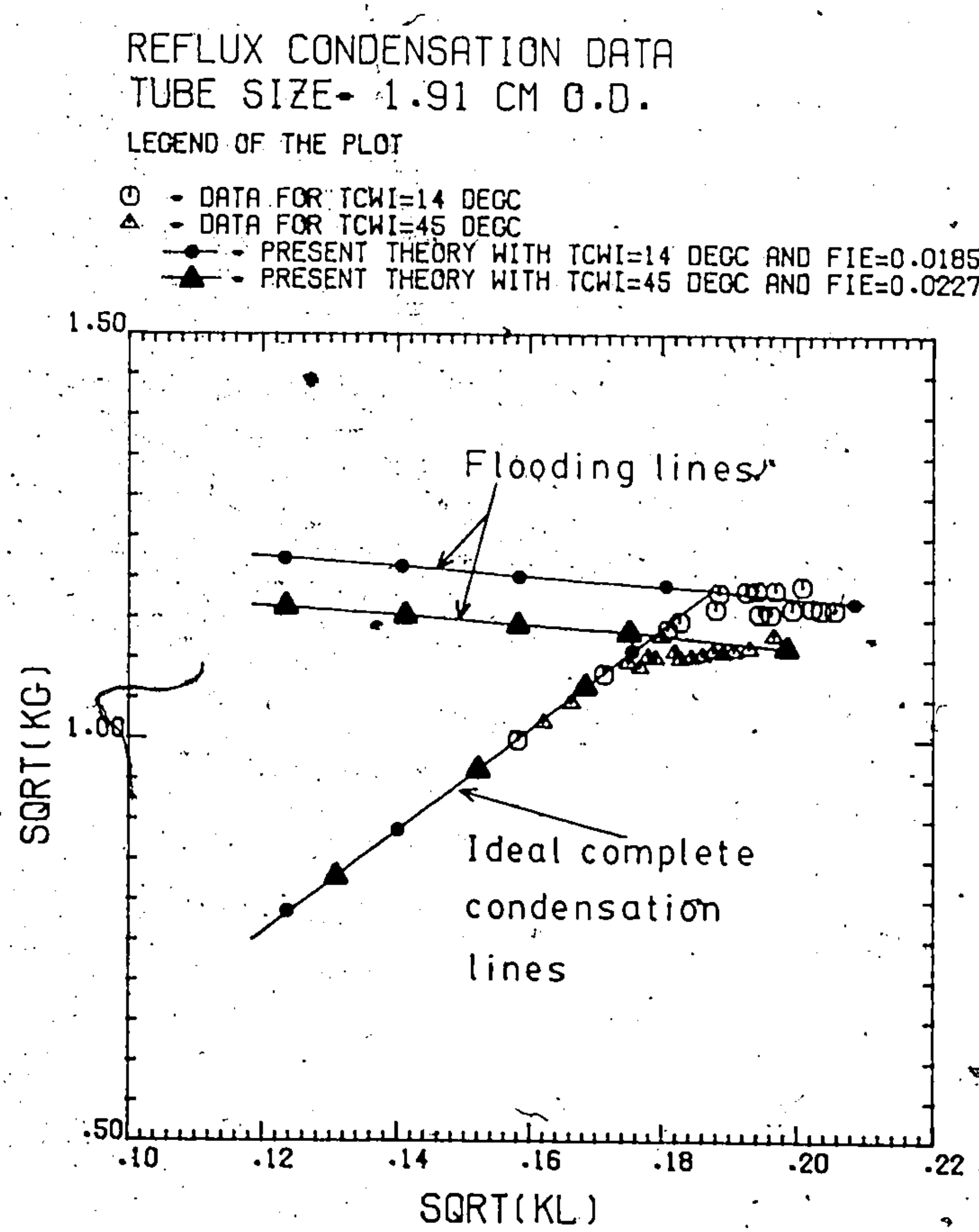

FIGURE 4.1b Reflux Condensation Data in the $K_g^{1/2}$-$K_\ell^{1/2}$ Plane for 1.91 cm O.D. Tube

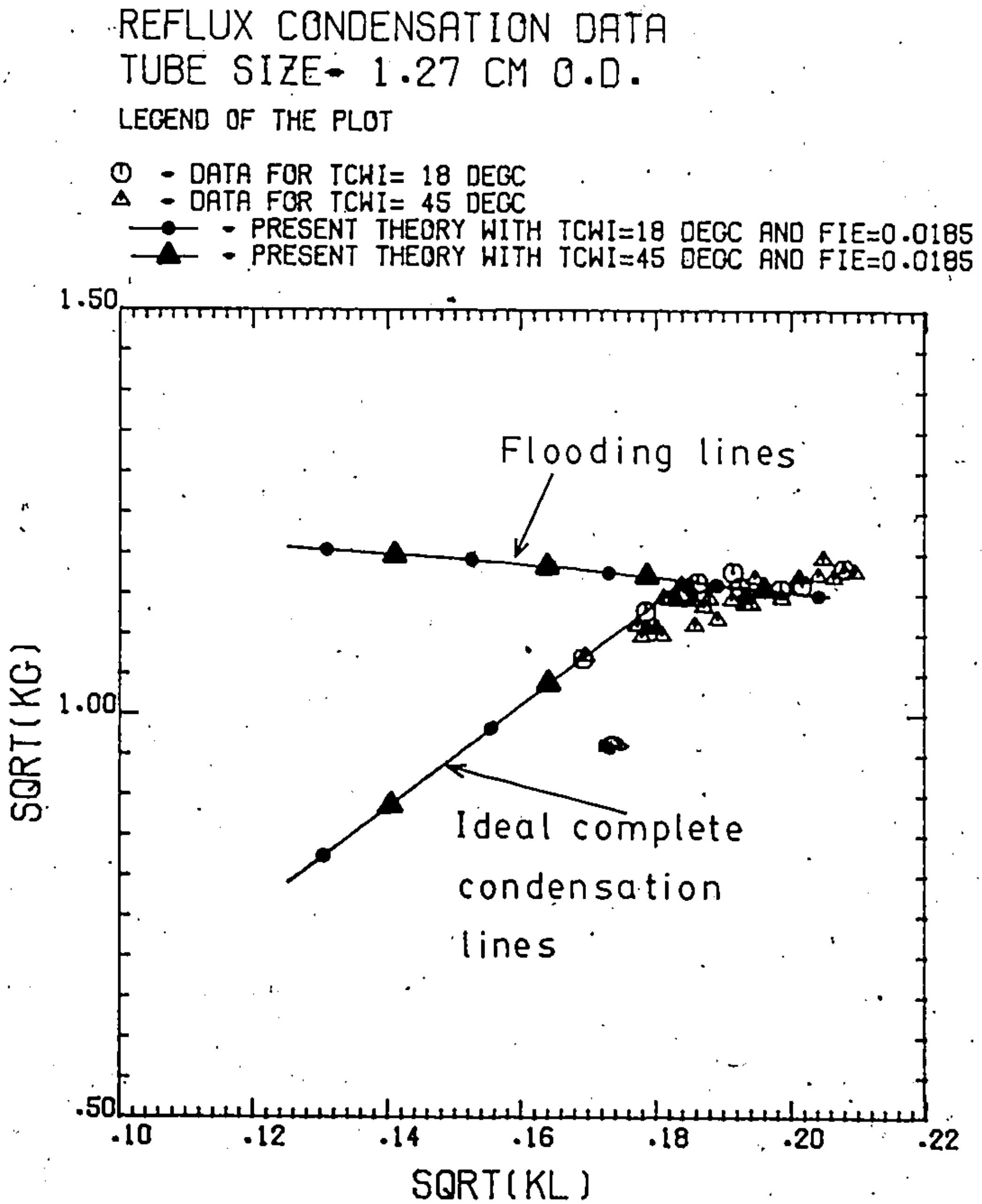

FIGURE 4.1c Reflux Condensation Data in the $K_g^{1/2}$-$K_\ell^{1/2}$ Plane for 1.27 cm O.D. Tube

the secondary sides is, the more the condensate film appears to be unstable, leading to a lower flooding point.

The experimental data shown in Figures 4.2a and b does not show a definite influence of the tube size on the flooding curve in terms of the Kutateladze variables. This behavior is similar to what has been found recently for air-water systems [19-21, 108].

Figures 4.3a,b and c show that as the steam flow is increased to reach the flooding point (near point B in Figure 4.3a) a water column starts to build up, during a short transient, to equilibrate the imposed pressure drop resulting in an increased pressure in the bottom plenum. After the flooding point has been reached, the trend in the experimental data shows no notable change in the condensation rates in terms of Kutateladze variable "K_g" as the pressure in the bottom plenum increases. This suggests that flooding at the tube inlet is the controlling process that causes the reflux condenser capability of condensing steam to "saturate" and it defines the maximum amount of steam flow that can be condensed in total reflux condensation mode.

In the model of total reflux condensation given in Chapter 3, the entrance interfacial friction factor f_{ie} is a free parameter that closes the set of equations.

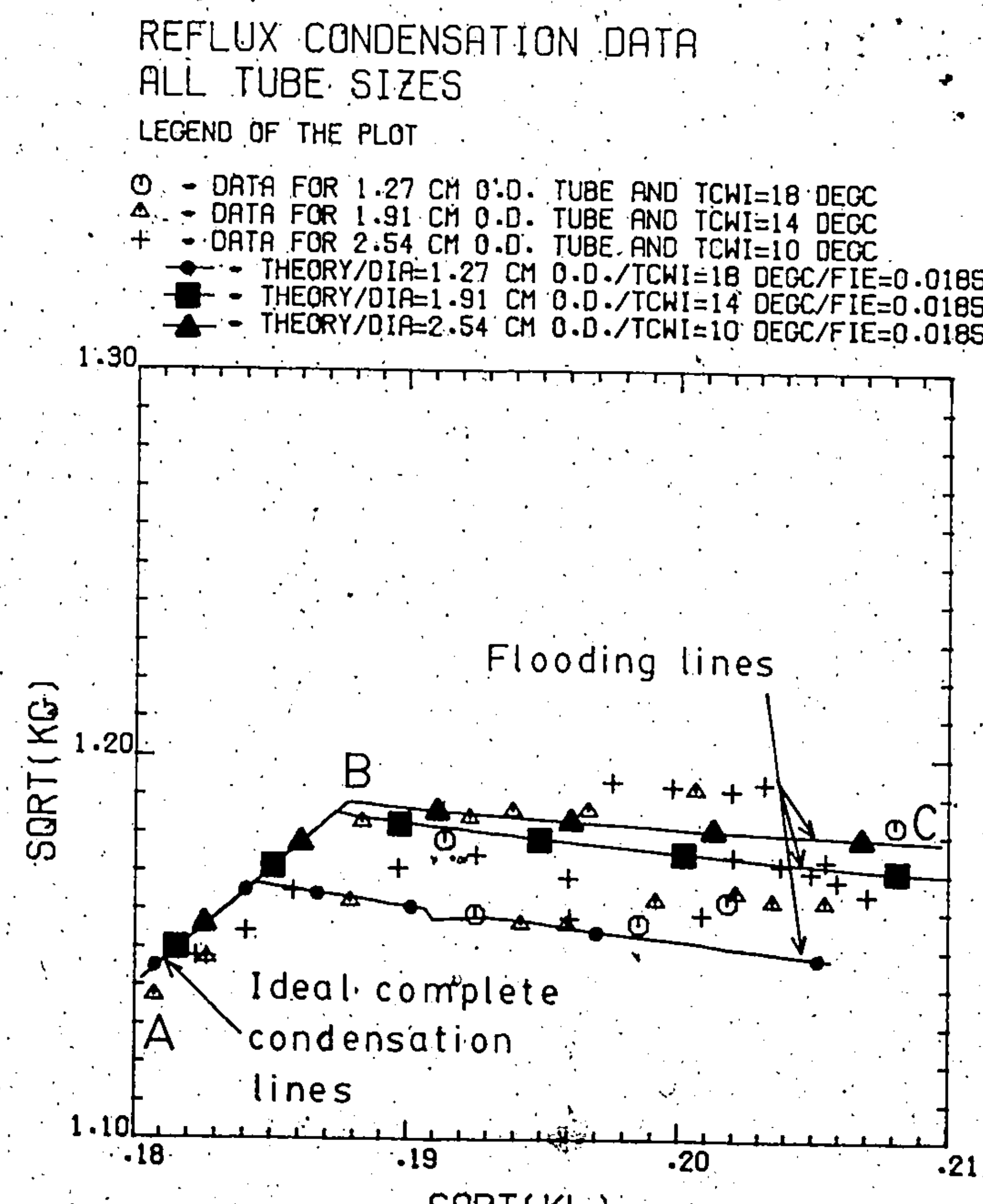

FIGURE 4.2a Reflux Condensation Data in the $K_g^{1/2}-K_\ell^{1/2}$ Plane for All Tube Size for the Coldest Cooling Water Temperature

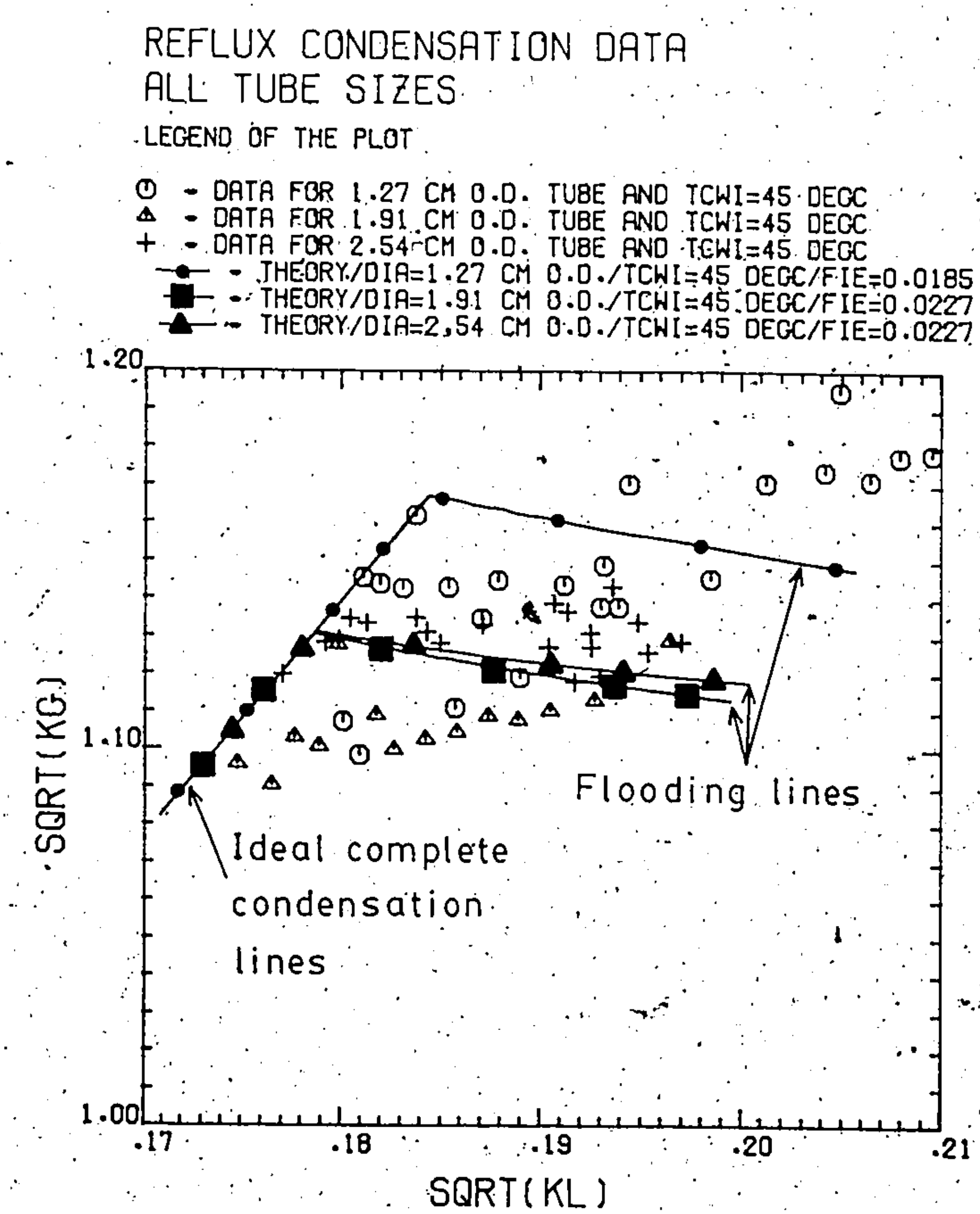

FIGURE 4.2b Reflux Condensation Data in the $K_g^{1/2}-K_\ell^{1/2}$ Plane for All Tube Size for the Hottest Cooling Water Temperature

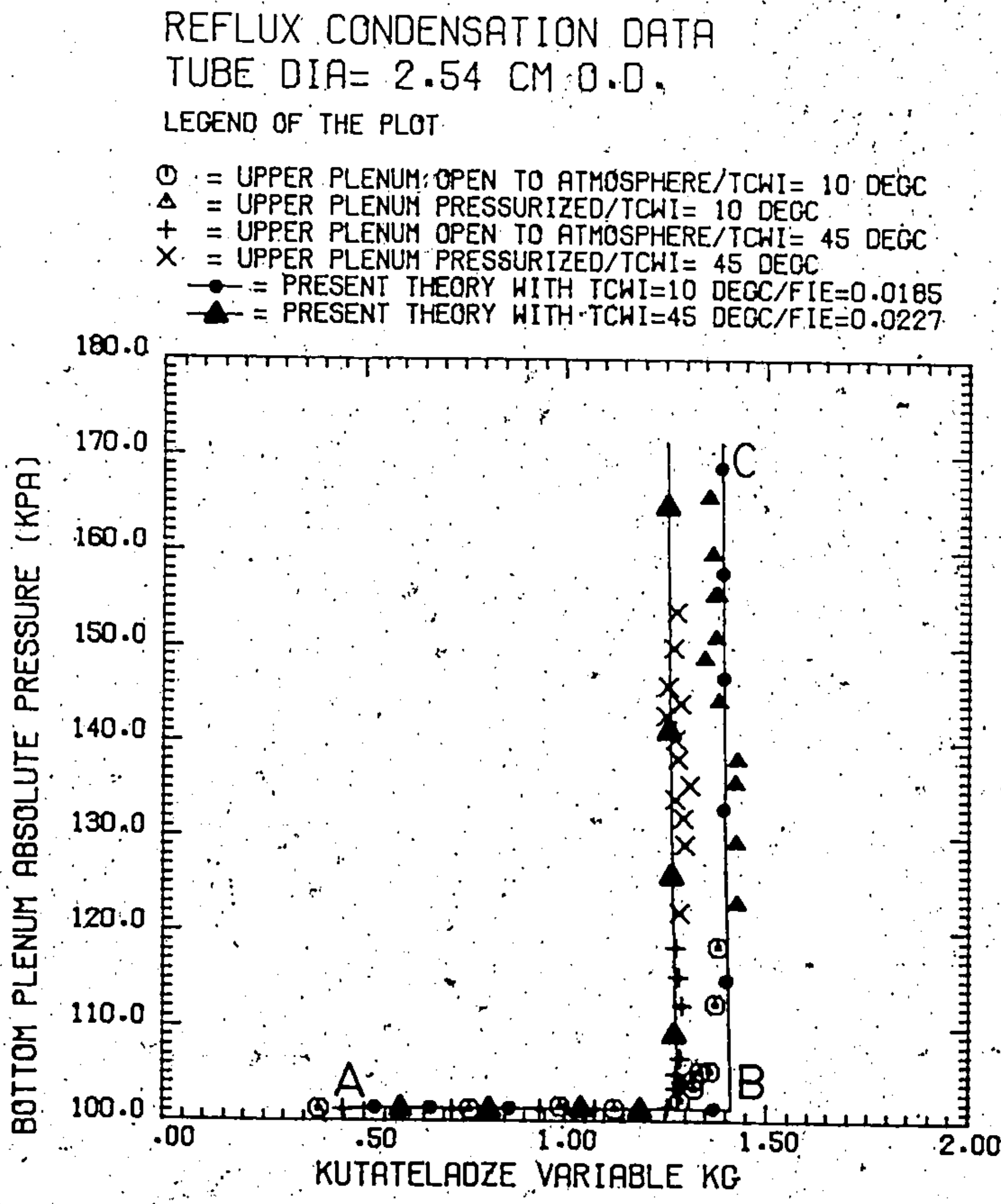

FIGURE 4.3a Variations of the Bottom Plenum Pressure as a Function of Steam Flow Rate for 2.54 cm O.D. Tube

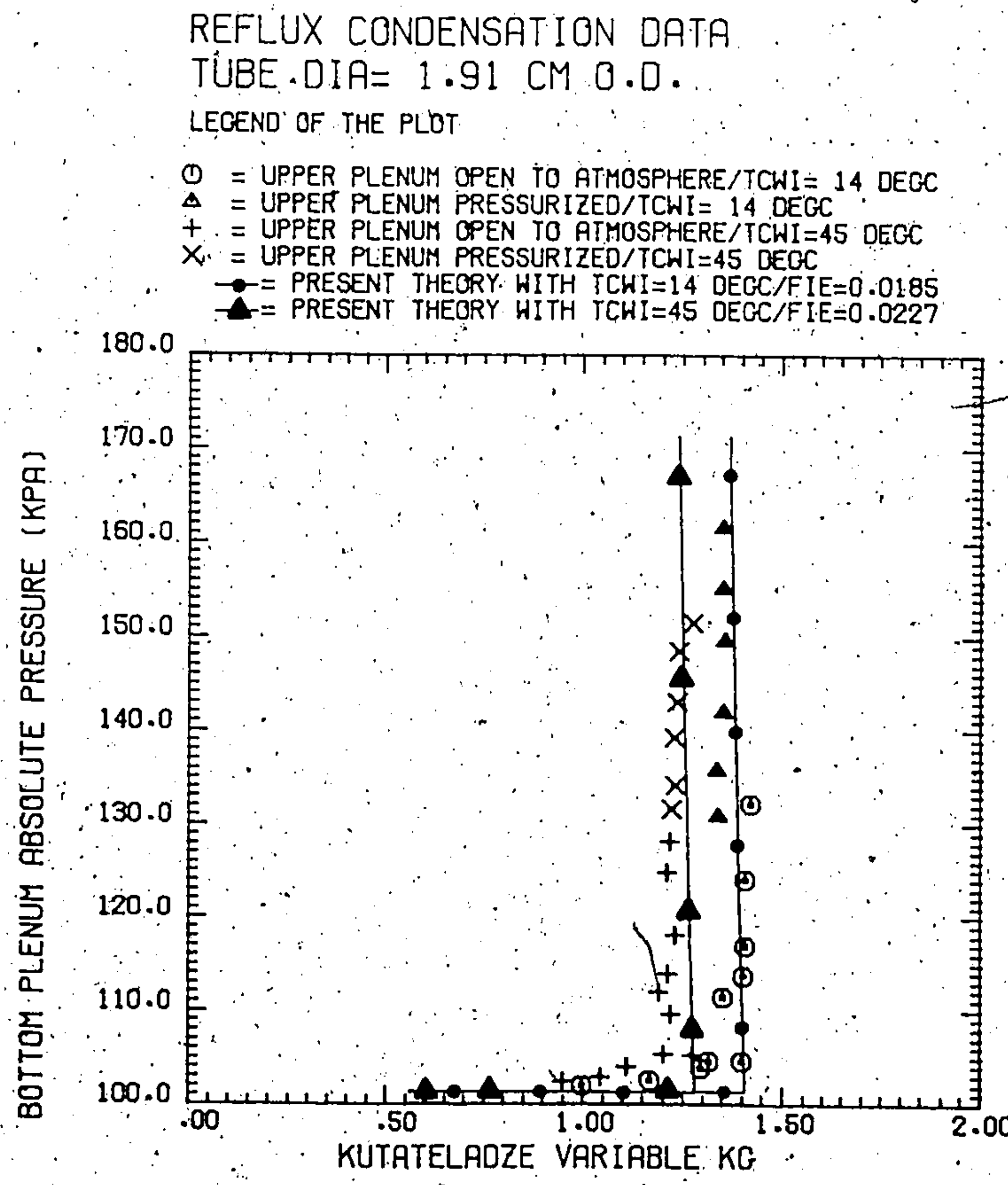

FIGURE 4.3b Variations of the Bottom Plenum Pressure as a Function of Steam Flow Rate for 1.91 cm O.D. Tube

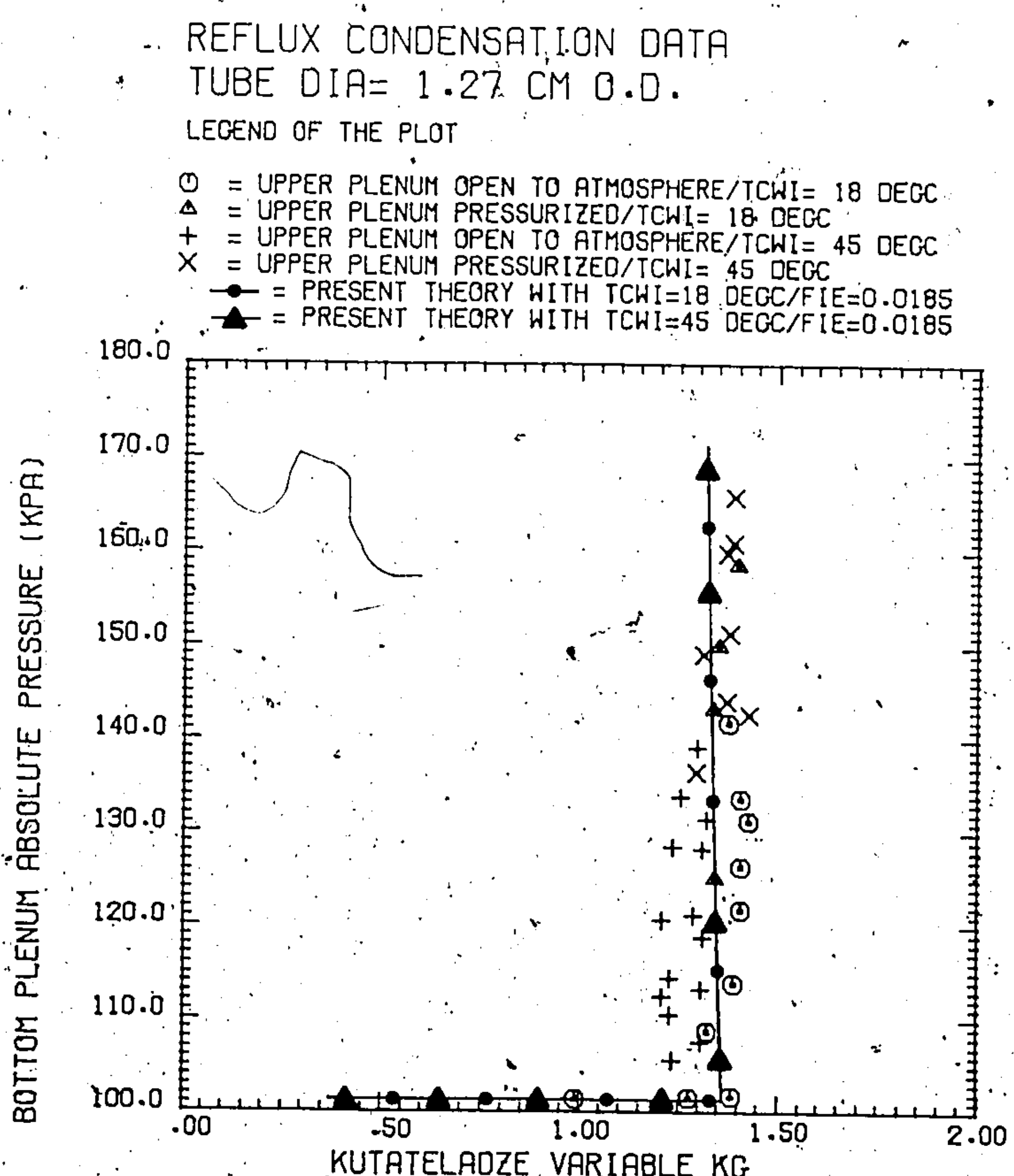

FIGURE 4.3c Variations of the Bottom Plenum Pressure as a Function of Steam Flow Rate for 1.27 cm O.D. Tube

In general, the entrance condition influences the value of that parameter that is usually greater than what the correlations (see for example Equation (3.29)) give for a position far from the entrance. Due to the complexity of the two- phase flow mechanics at the tube entrance, it is not possible yet to evaluate it by theoretical means and it must be evaluated empirically. As shown in Figures 4.1a,b and c and Figures 4.3a,b and c, the present model fits the experimental data for the three tube sizes fairly well with f_{ie} equal to 0.0185 for total reflux condensation with the lowest inlet cooling water temperature. In the case of total reflux condensation with the hottest cooling water temperature, the present fairly well with the same value of the parameter f_{ie} equal to 0.0227 but for the smallest tube the original value of f_{ie} (=0.0185) had to be used. It can also be seen that in all the cases the present model fits the corresponding experimental data within the error of steam flow measurements (±5% see Section 2.1.2.1) and it brings additional support for the assumptions made in the derivation of the present model.

For a given inlet cooling water temperature, the trends in the experimental data are not really affected by the variation of the tube diameter; however, the present model exhibits a little influence of the tube diameter on the flooding curve as illustrated in Figure 4.2a. The present model is seen to follow a behavior where as the tube diameter reduces, the ordinate of the flooding curve decreases and it is similar to the behavior of the Bharathan-Wallis model [30]. The results for the case of the hottest inlet cooling water temperature show the same behavior but only for the two larger tubes as depicted in Figure 4.2b and the behavior of the model for the 1.27 cm O.D. tube can be explained by the choice of the value for the parameter f_{ie}. A close examination of Figures 4.2a and b illustrates the facts that variations in both experimental and theoretical flow rates on the flooding curve as a function of the tube diameter, are within the experimental error in the steam flow measurements. Then, it is concluded that the influence of the tube diameter on the definition of the experimental flooding curve in total reflux condensation in terms of Kutateladze variables is negligible.

Two reasons can be given to the fact that in general for a prescribed inlet cooling water temperature the value of the parameter f_{ie} for all three tube sizes can be the same. Since, the influence of the tube diameter on the definition of the flooding curve is negligible and in Section 3.2.3 the prediction of the flooding flow rate was clearly shown to depend on the parameter f_{ie} (see the definition of the friction velocity u_*). Then, it can be concluded that f_{ie} should be a very weak function of the tube diameter. From a close examination of Figure 2.2 the entrance conditon can be associated to a sudden contraction and the equation for the friction loss factor e_v is given by [90, p.217]:

$$e_v = K(1 - \beta) \qquad (4.2)$$

where K is a constant and β is the ratio of the smaller cross- sectional area over the larger cross-sectional area. In the present system the largest tube inner diameter is 2.06 cm and the diameter of the bottom plenum outlet is 10.23 cm making $\beta << 1$. Therefore, "e_v" can be considered as being constant for all tube sizes with inner diameter less than 2.06 cm. Since the friction factor at the entrance being related to the friction loss factor [90, p.216] it can be concluded that it should not vary much with the tube diameter.

Although the values of f_{ie} used in the simulation are greater than what the Bharathan-Wallis correlation (see Equation 3.29) gives, they are still in the same order of magnitude. A reason for this can be inferred from a recent study on flooding in an air-water system [108]. It was found that for low water flow rate and no upward air flow, the water leaves the tube in the form of a liquid jet. When a counter-current flow of air occurs, the water jet is lifted and it wets the whole periphery of the entrance. If the same phenomenon is assumed to occur in reflux condensation it can be seen that the steam does not come into contact with the entrance wall most of the time but more with the slightly subcooled condensate film. Because of the possible direct contact condensation of the uprising steam on the condensate, the effects of the entrance geometry on the steam flow could be damped. This results in a situation where the uprising steam interacts with the condensate film, like in pure counter-current annular steam-water flow; however, the film surface fluctuations originate in part from the influence of the geometry of the entrance.

The variations of f_{ie} with the inlet cooling water temperature can be explained from the discussion on the interplay between the perturbing and the restoring forces presented in Section 3.2.2.2 based on equation (3.64). As the temperature difference between the primary and the secondary side decreases the restoring force from the pressure created by the condensation mass transfer also decreases leading to higher condensate film fluctuations as illustrated in Figures 4.4 and 4.5. For the smallest tube no definite difference in the fluctuations was measured as shows in Figure 4.6 and the level of the condensate film fluctuation is assumed to be the same, giving some support to the use of the same value for the parameter f_{ie} for the two cooling water temperatures. The program REFLUX was

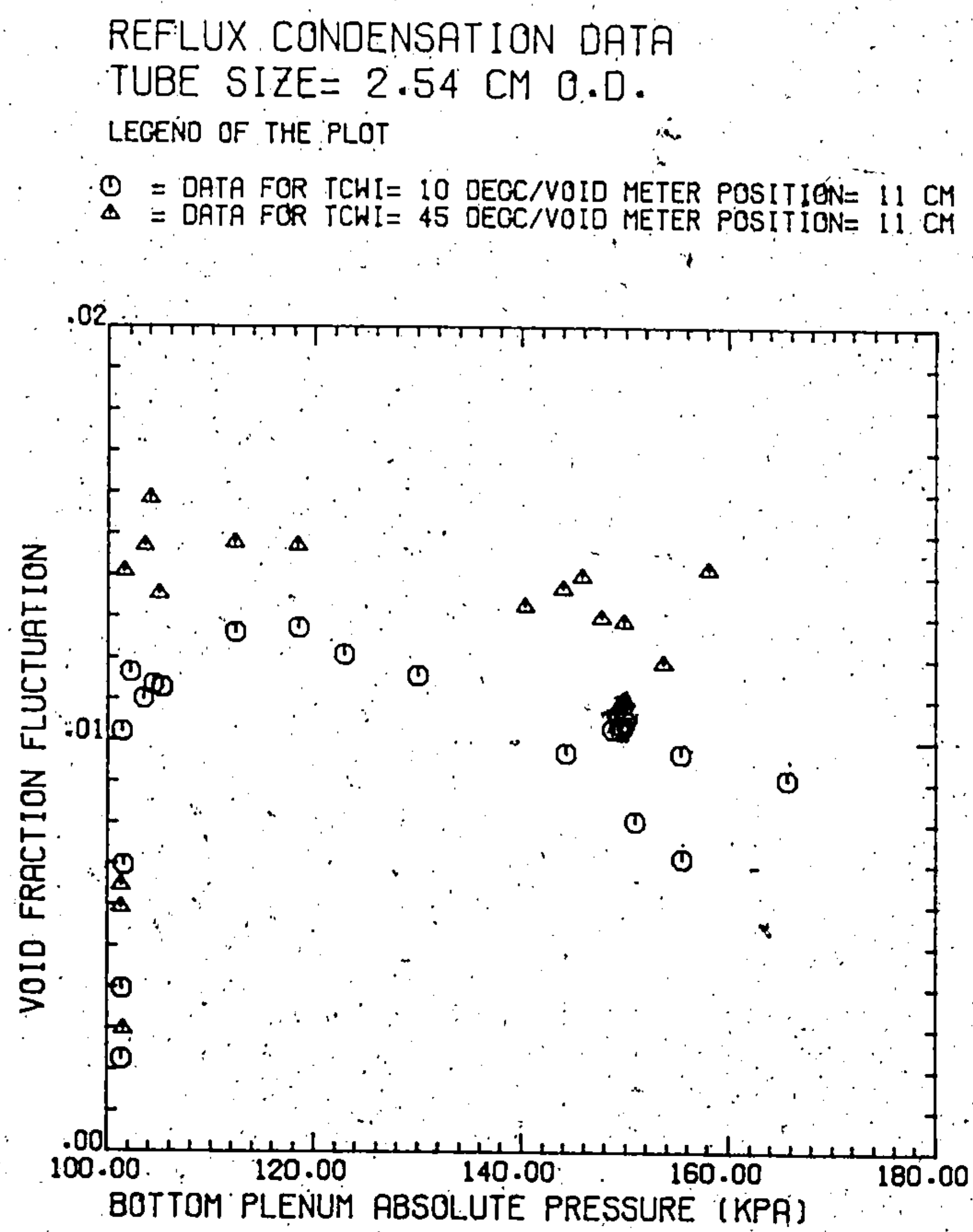

FIGURE 4.4 Variations of the Void Fraction Fluctuation as a Function of the Bottom Plenum Absolute Pressure for the 2.54 cm O.D. Tube

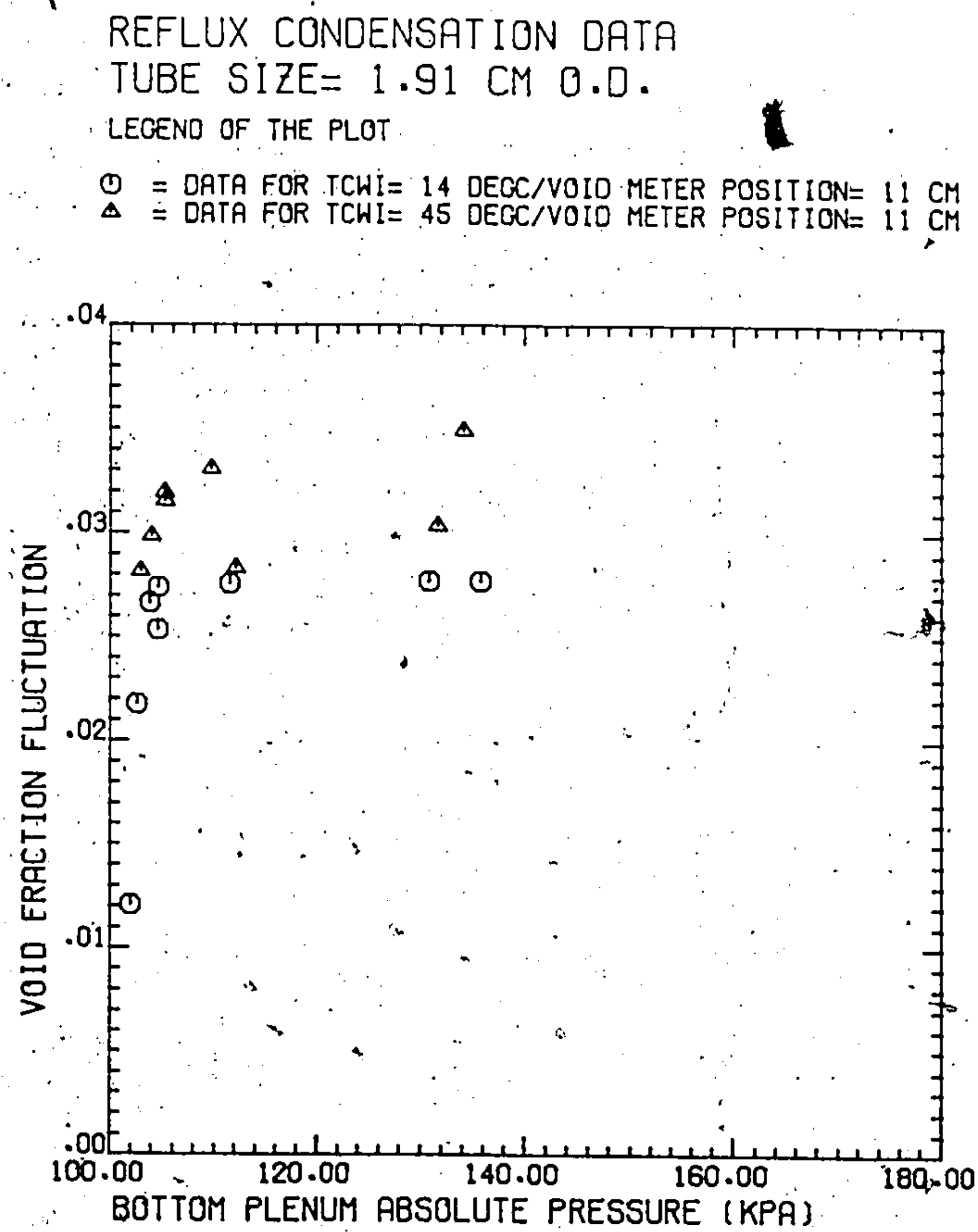

FIGURE 4.5 Variations of the Void Fraction Fluctuation as a Function of the Bottom Plenum Absolute Pressure for the 1.91 cm O.D. Tube

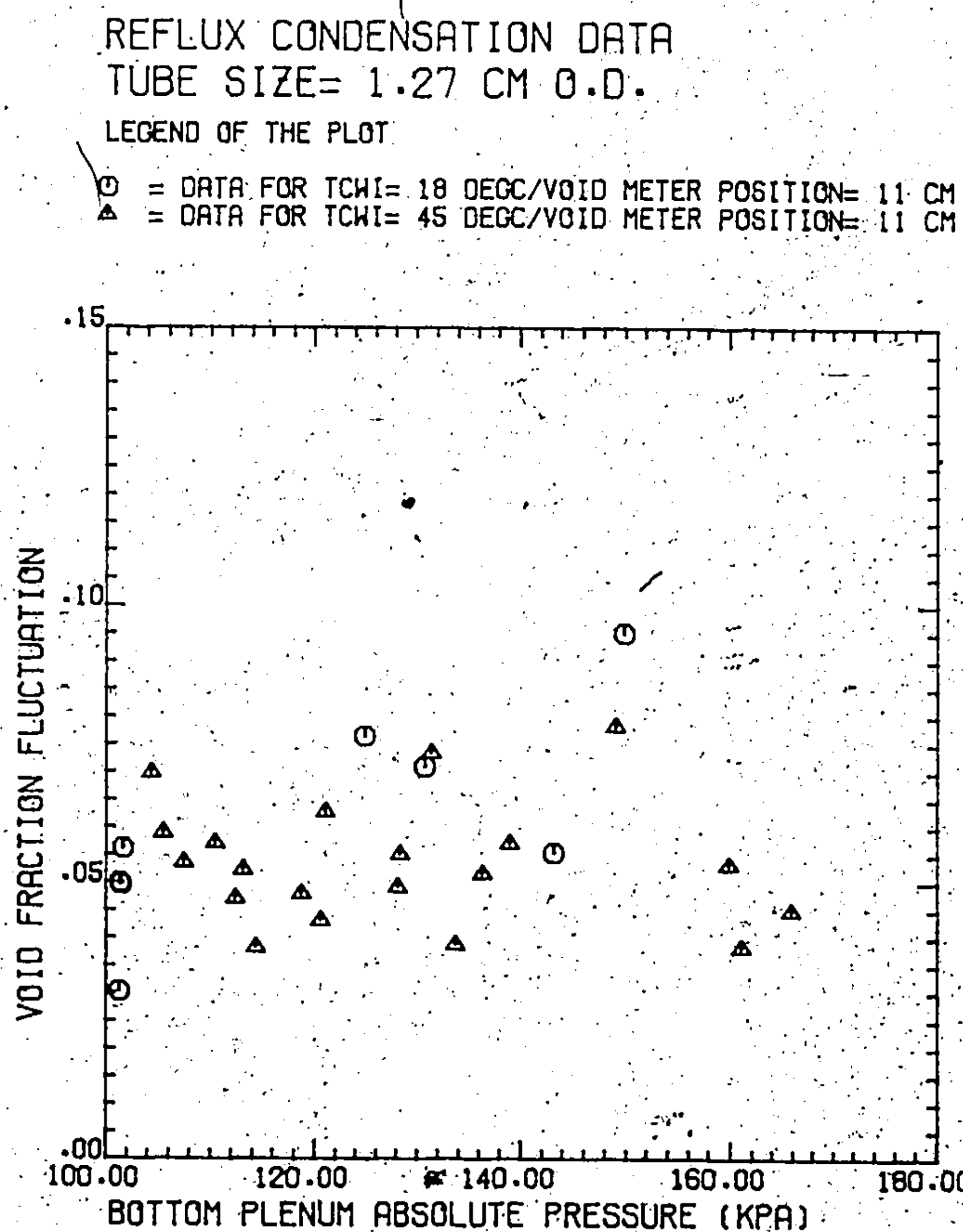

FIGURE 4.6 Variations of Void Fraction Fluctuation as a Function of Bottom Plenum Absolute Pressure for 1.27 cm O.D. Tube

run for the lowest and hottest inlet cooling water temperature with the same value of f_{ie} (=0.0185) and very little difference was found between the two cases in the computed condensation rates at flooding. It could mean that in equation 3.71 the element related to heat transfer is much smaller than the element related to the hydrodynamics of the the two-phase flow. Thus in total reflux condensation, flooding appears to depend more on the hydrodynamics than on the condensation heat and mass transfer. A recent study [33] on the stability of steam-subcooled water counter-current flow in an inclined channel results in similar findings. Also it could mean that the assumption of interfacial waves with infinitesimal amplitudes, made in the stability analysis, may be in some error. The possible presence of finite amplitude waves was introduced artificially in the model through the variation of parameter f_{ie} that must increase when the wave heights increase [95, p.87]. This increase in the value of f_{ie} is to take into account the increased roughness of the condensate film surface and the increased possibility of condensate film entrainment which was found to have a destabilizing effect on the film surface [19-21] and were not included in the present model.

For total reflux condensation in a 2.54 cm O.D. tube with inlet cooling water at 10°C the theoretical results define the path "ABC" in Figures 4.1a and 4.3a. The path follows the so-called "ideal complete condensation line" [25] (point A to point B) before reaching the flooding line (at point B) and following it (point B to point C). This global behavior has similarities with the ones presented previously by other investigators [17,106]. In other words, an output from a run of program REFLUX will show, for a given inlet cooling water temperature, the computed condensation rates defining path "ABC" on Figure 4.1a, 4.2a and 4.3a. This path can be considered as the response of the reflux condenser in terms of condensation rates to a variation in imposed pressure drops across the tube. The fairly good agreement between the present model and the experiments demonstrates the <u>truthfulness of the postulate stating that after flooding is reached, the reflux condenser still operates, on a time average basis, at the flooding point for each new imposed pressure drop across the tube and the capability of the model to predict the global behavior of the system in terms of condensation rates</u>.

Previous investigators [16,17,107] used Wallis-Kutateladze type correlations to predict flooding at the tube inlet. These correlations contain <u>two</u> constants (for example "m" and "C" in Equation (1.1)) that depends on the two-phase flow conditions and the entrance-exit geometries. These constants are found empirically to make the correlations fit the experimental data [19-21,26-31] and an interfacial heat transfer coefficient has to be supplied if heat transfer occurs between the phases [33,41]. The present model removes part of the empiricism by reducing the number of constant to <u>one</u> and for a given inlet cooling water temperature, the constant is a very weak function of the tube diameter; however, the entrance geometry could have a strong influence on the value of the constant as it is the case for adiabatic systems [19-21,27,29-30,32].

4.1.2 Heat Removal

In the preceding section, flooding at the tube was shown to be the controlling process that causes the reflux condenser capability of condensing steam to "saturate". It is for that reason that Figures 4.7a,b and c and 4.8a,b and c exhibit the variations shown for the heat removal and the two-phase region length as a function of the bottom plenum pressure.

Figures 4.7a,b and c show a sharp increase in the heat removal as a function of the bottom plenum pressure before the flooding point is reached and after, the increase is small but significant. Although this increase is not indicated by the variation of condensation rates in terms of Kutateladze variable K_g, it actually indicates that more steam is condensed as the bottom plenum pressure

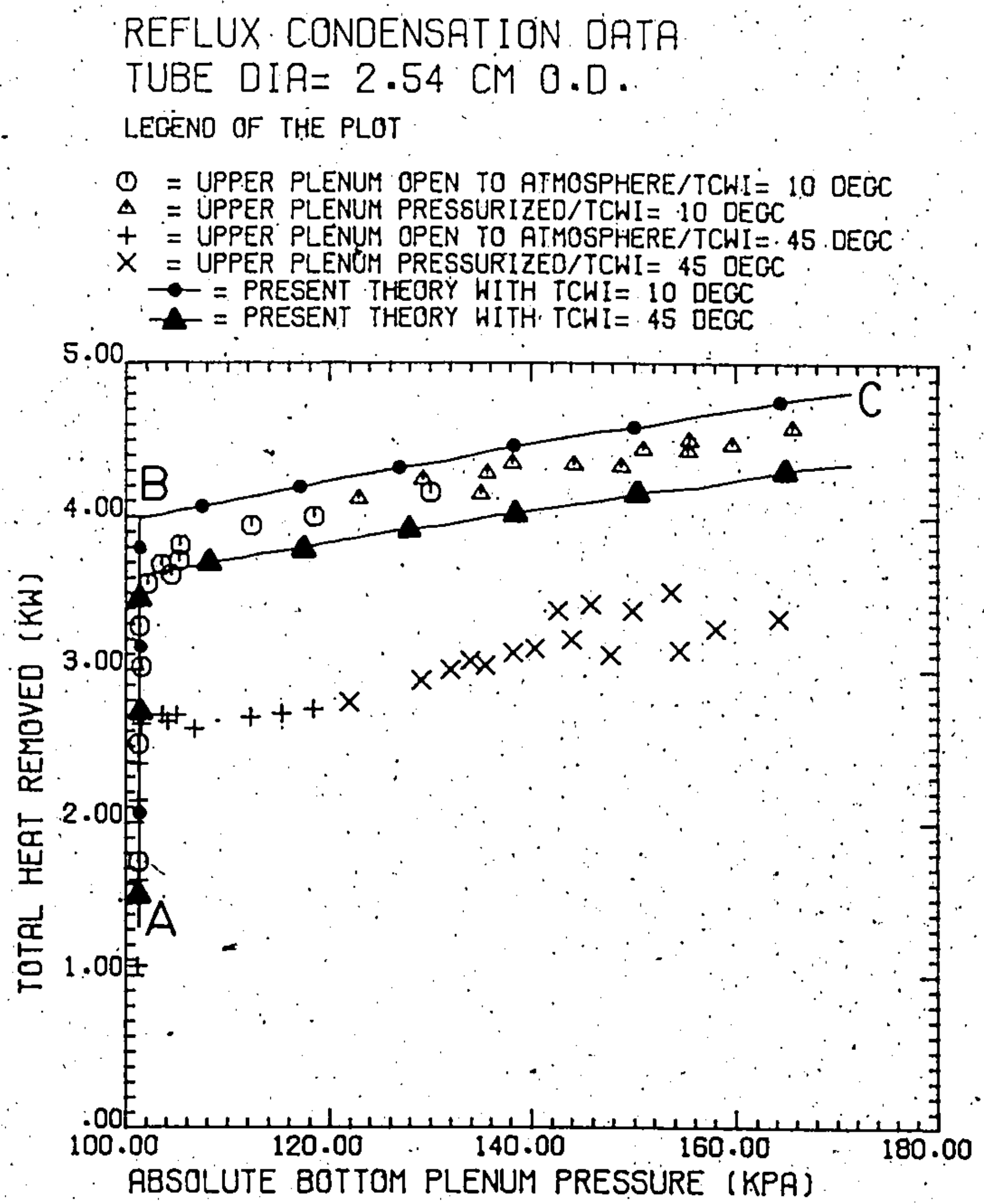

FIGURE 4.7a Variations of Total Heat Removed as a Function of Bottom Plenum Absolute Pressure for 2.54 cm O.D. Tube

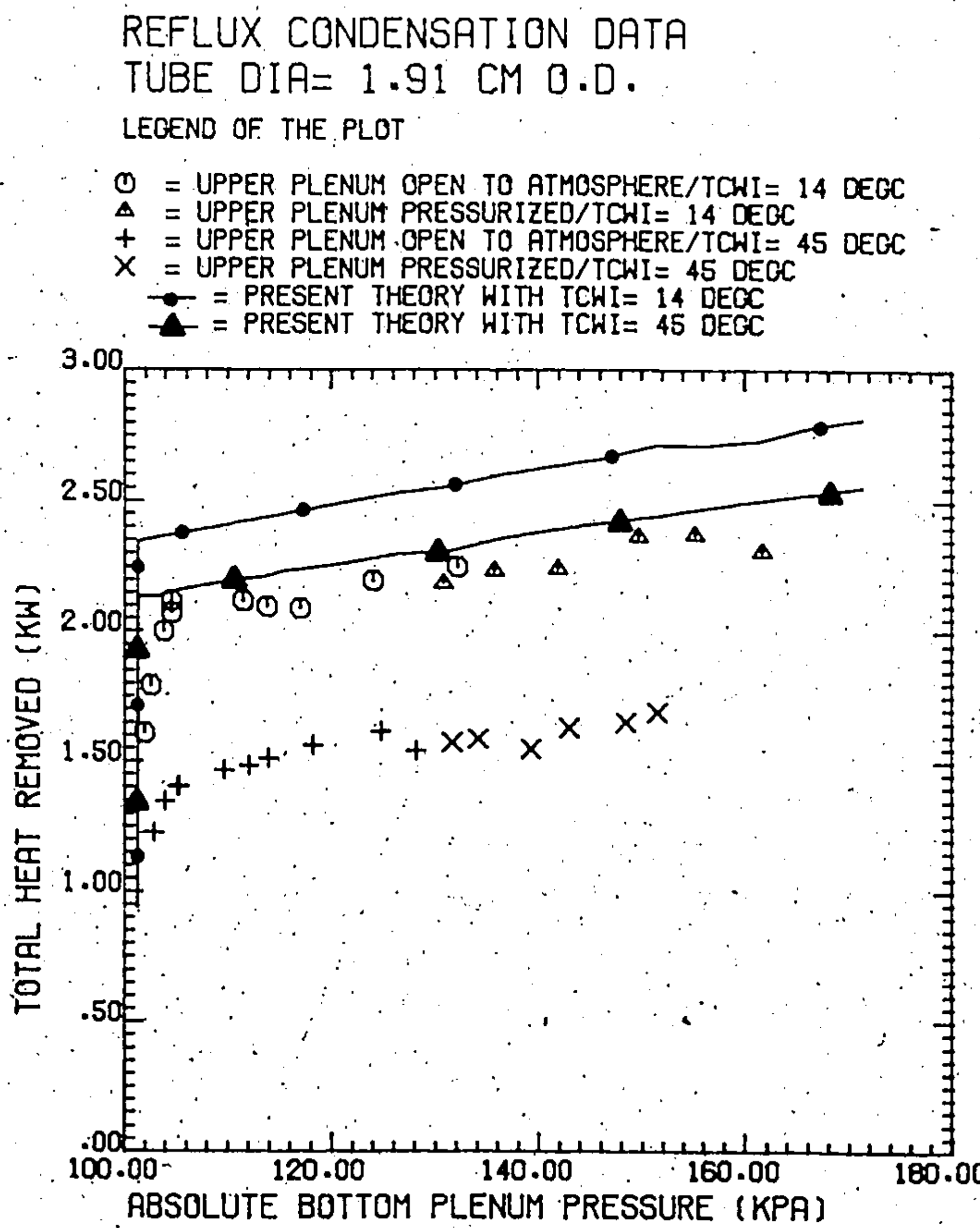

FIGURE 4.7b Variations of Total Heat Removed as a Function of Bottom Plenum Absolute Pressure for 1.91 cm O.D. Tube

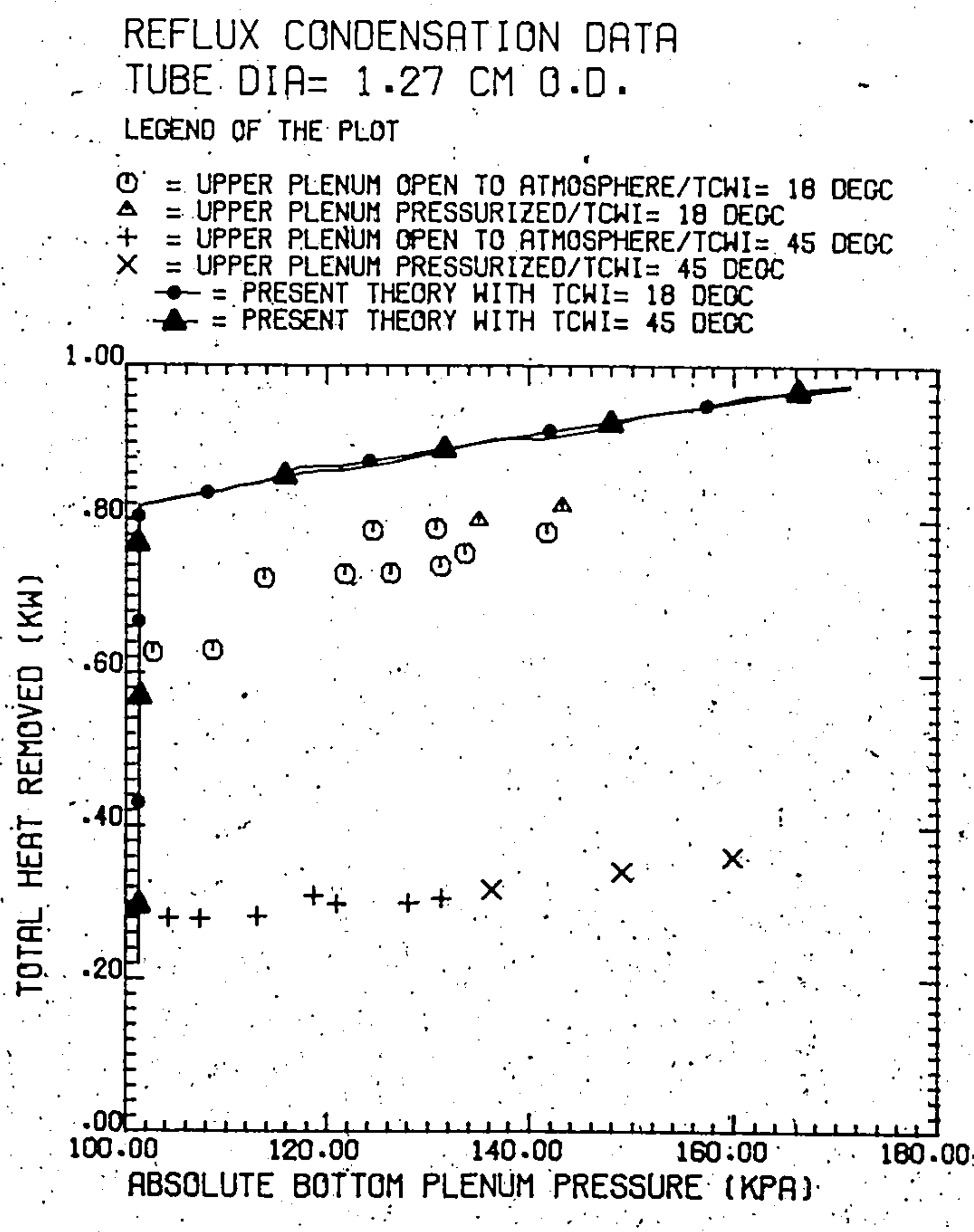

FIGURE 4.7c Variations of Total Heat Removed as a Function of Bottom Plenum Absolute Pressure for 1.27 cm O.D. Tube

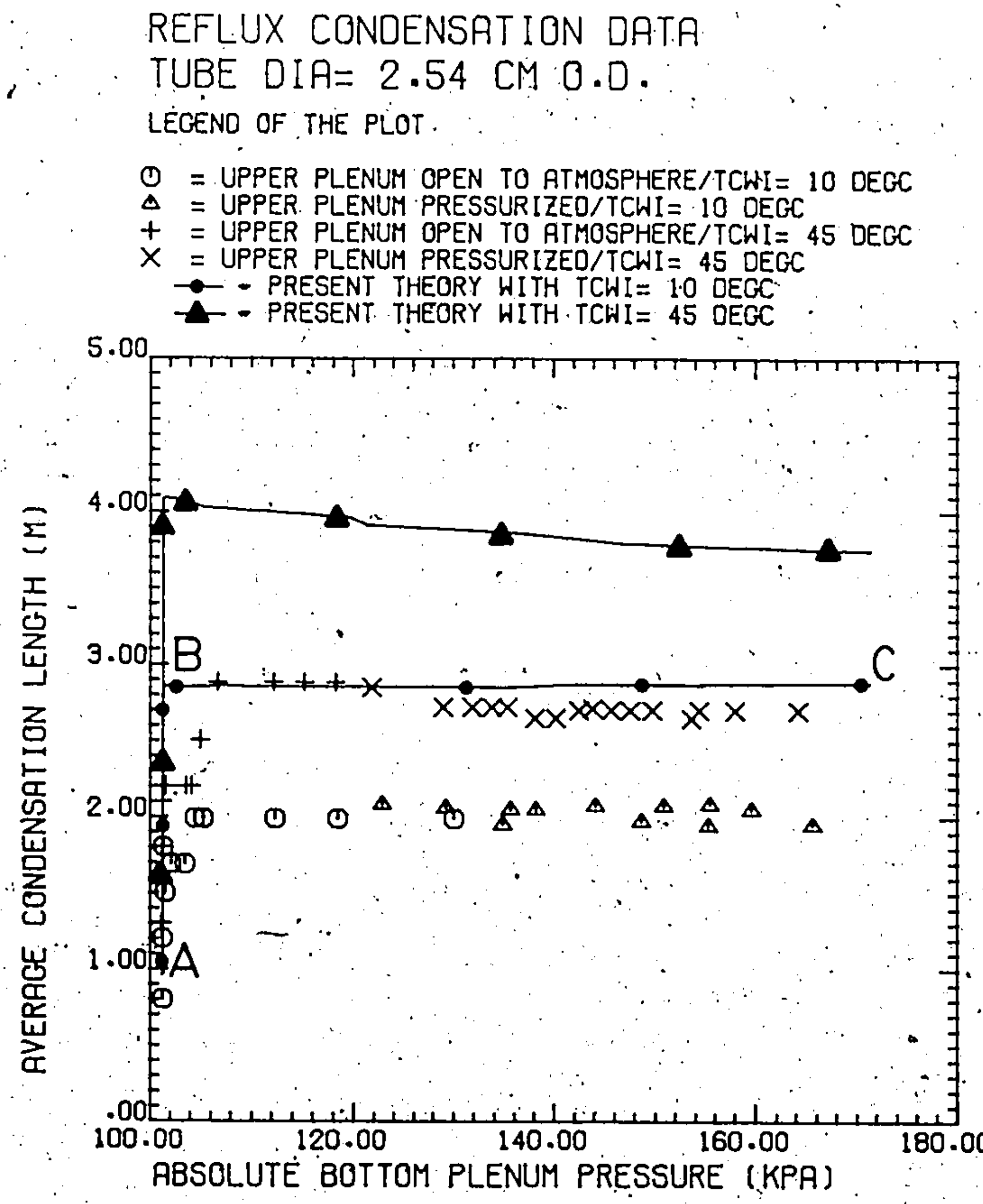

FIGURE 4.8a Variations of Average Condensation Length as a Function of Bottom Plenum Absolute Pressure for 2.54 cm O.D. Tube

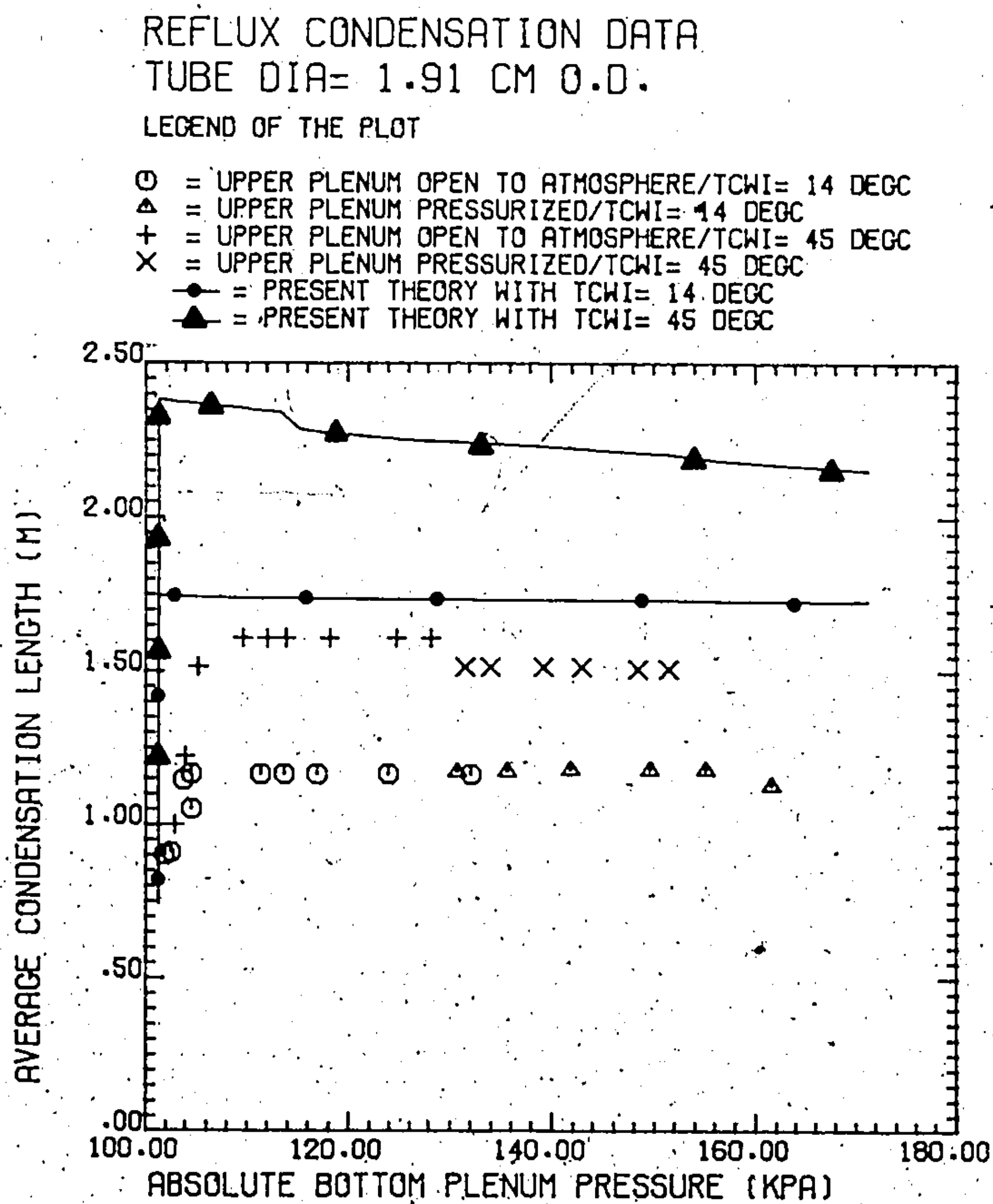

FIGURE 4.8b Variations of Average Condensation Length as a Function of Bottom Plenum Absolute Pressure for 1.91 cm O.D. Tube

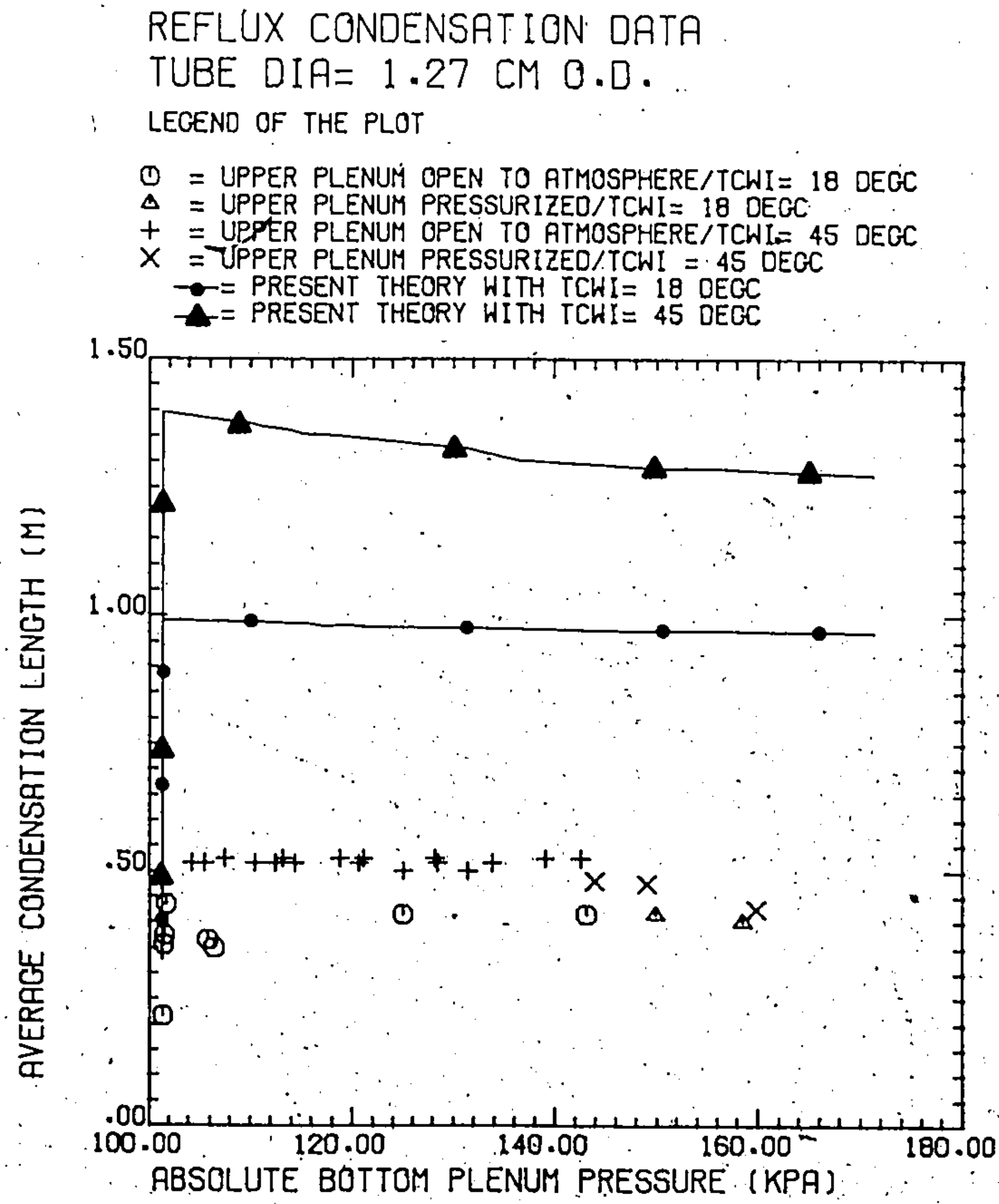

FIGURE 4.8c Variations of Average Condensation Length as a Function of Bottom Plenum Absolute Pressure for 1.27 cm O.D. Tube

increases. This small increase is due to a change in the flooding flow rate by the increase in the system pressure that defines new values for the thermal-hydraulic properties and to the increase in the rate of heat transfer by the increase in the steam saturation temperature.

Again the path "ABC" traced from the results of the simulation by the program REFLUX is indicated in Figure 4.7a and it can be seen that the general trend of the experimental data is followed. The discrepancy between the present model and the experimental data may be due to the heat losses from the secondary side to the surroundings that were not taken into account in the present model. This fact is clearly shown by the observation that the discrepancy between the present model and the experimental data is smaller for the case of the lowest inlet cooling water temperature than for the case of the hottest inlet cooling water temperature.

Figures 4.7a,b and c show a strong dependence of the amount of heat removal on the tube diameter where as the tube diameter increases the heat removal increases. Accordingly, the two-phase region lengths also show a strong dependence on the tube diameter as illustrated in Figures 4.8a,b and c where again as the tube diameter increases the two-phase region lengths (average condensation lengths) increase.

Again, the path "ABC" traced from the results of progam REFLUX is indicated in Figure 4.8a and it can be seen that the general trend in the experimental data is followed. Even, the little overshoot in the variation of the condensation length for the case of the hottest inlet cooling water temperature is, to a certain extent, predicted by the present model. The discrepancies between the predicted and measured values of the two-phase region lengths could be attributed to the following reasons. In the case of filmwise condensation of stagnant steam on a vertical cold plate, finite amplitude waves were found to enhance significantly the condensation heat transfer [112,113]. Similarly the possible presence of finite amplitude waves in the present system could have the same effect. Latent heat can be transferred from the steam to the entrained droplets which in turn are deposited and give up part of their heat by mixing with the slightly subcooled condensate film to be entrained again, in other words, the process of recirculation of part of the liquid holdup could enhance the heat transfer rate to the secondary side. Significant heat transport may occur between the two-phase and the single-phase regions. On the other hand, these phenomena will have to be included in the present model if a global stability analysis [86] of total reflux condensation in an inverted U-tube is to be performed since the distance between the top of the two-phase region and the U-bend, most probably filled with condensate, is an important factor in establishing the stability domain of the system.

The effect of the inlet cooling water temperature on the average length of the two-phase region is qualitatively well represented by the model as for an increase in the inlet cooling water temperature, we can see an increase in the average condensation length.

4.1.3 Liquid Holdup

In Section 1.1 a question was raised on the effects of flooding and the tube length on the condensate distribution in the tube. The obvious answer is the appearance of a single-phase region oscillating over a two-phase region (see Figure 3.1). Average lengths of single-phase and two-phase regions were measured and the results are given in Figures 4.9a,b and c for runs with the upper plenum open to atmosphere. For runs with the upper plenum pressurized, the results are given in Table 4.1a to 4.1f, where only the average single-phase lengths have been presented since the average two-phase lengths have already been presented in the previous section.

The trend in the effect of the inlet cooling water temperature on the average two-phase region lengths

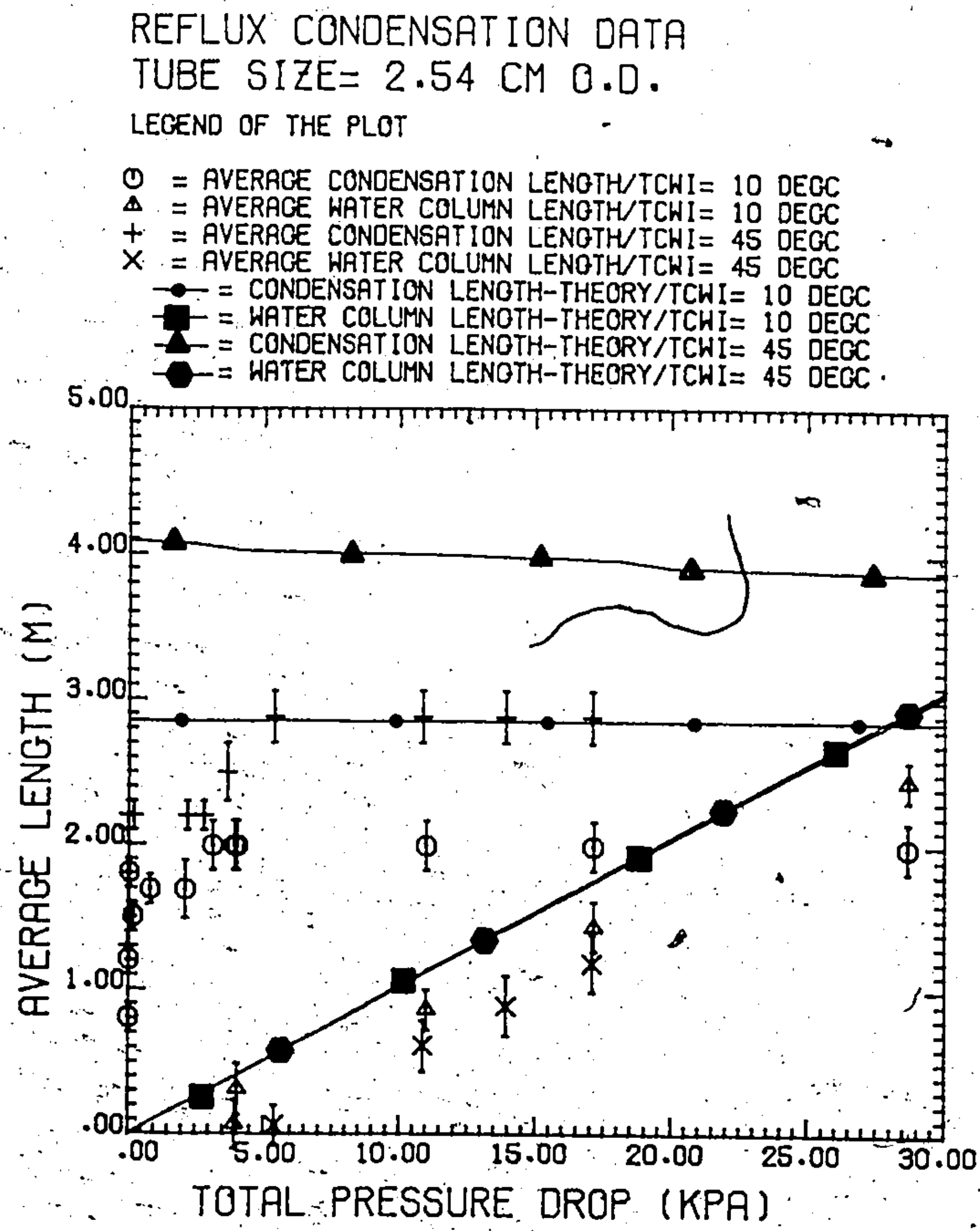

FIGURE 4.9a Variations of Average Condensation Length and Water-Column Length as a Function of Total Pressure Drop Across the Tube for 2.54 cm O.D. Tube

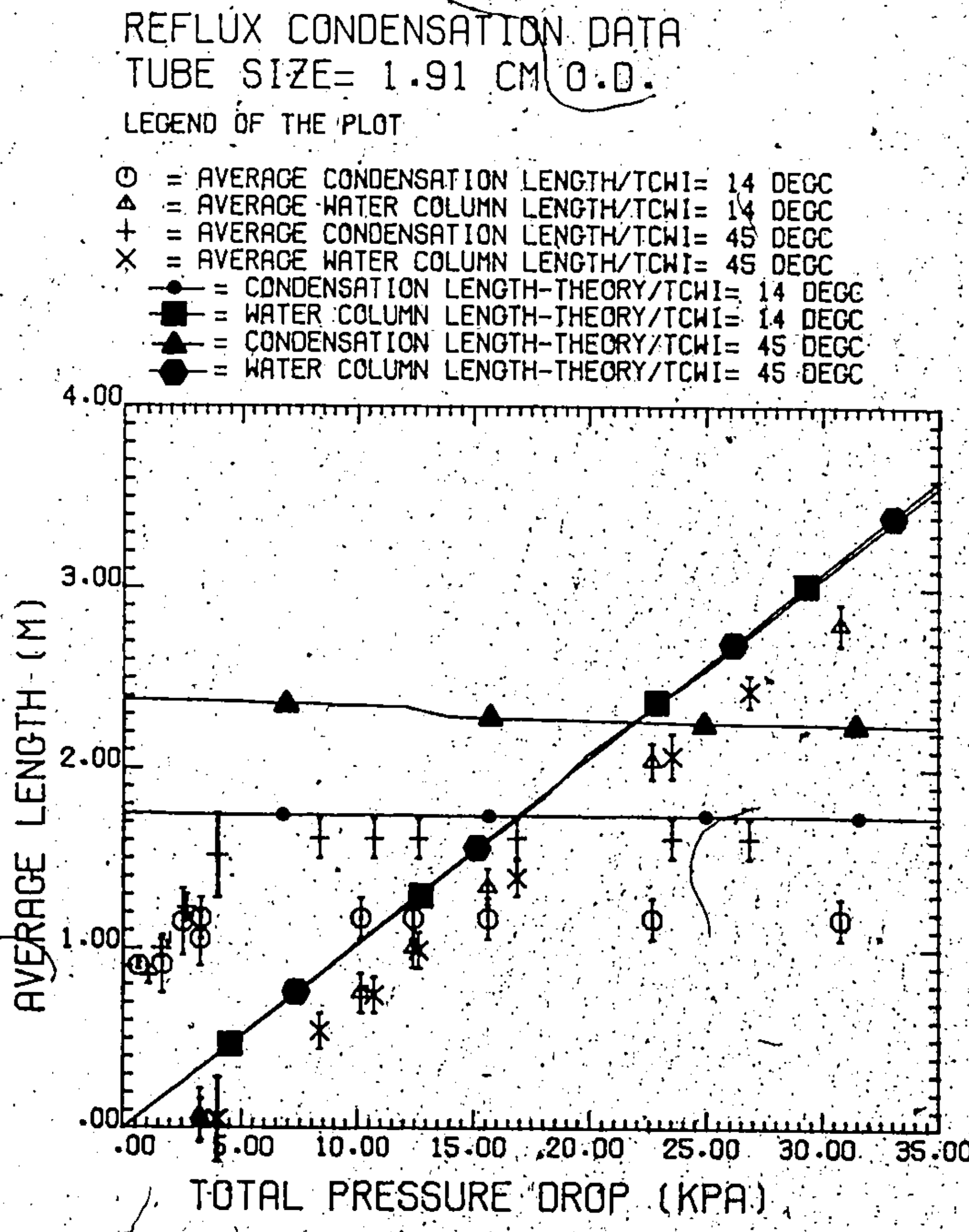

FIGURE 4.9b Variations of Average Condensation Length and Water-Column Length as a Function of Total Pressure Drop Across the Tube for 1.91 cm O.D. Tube

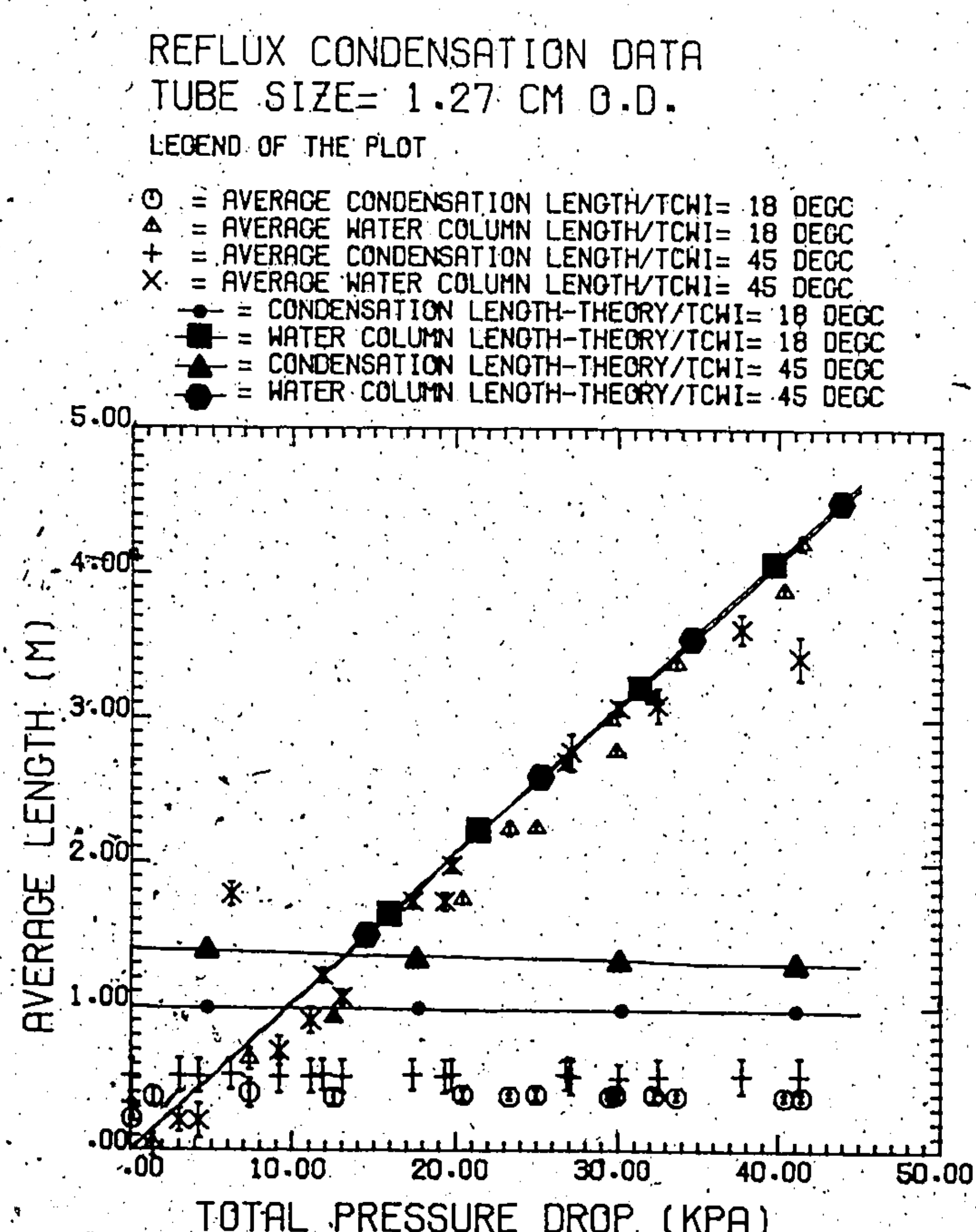

FIGURE 4.9c Variations of Average Condensation Length and Water-Column Length as a Function of Total Pressure Drop Across the Tube for 1.27 cm O.D. Tube

TABLE 4.1a Measured and Calculated Single-Phase Region Lengths for 2.54 cm O.D. Tube, TCWI equal to 10°C and the Upper Plenum Pressurized

RUN NO.	PBP (kPa)	PUP (kPa)	SPL(m) (measured)	SPL(m) (calculated)
D05051	138.138	111.327	2.21	2.73
D05052	135.658	111.029	1.97	2.51
D05053	129.325	111.193	1.28	1.85
D09051	155.423	129.651	2.24	2.62
D09052	150.895	129.214	1.80	2.21
D09053	144.274	129.274	1.15	1.53
D09054	135.044	128.925	0.30	0.62
D10051	165.614	139.563	2.39	2.65
D10052	159.688	137.673	1.80	2.24
D10054	155.389	138.046	0.54	1.76

TABLE 4.1b Measured and Calculated Single-Phase Region Lengths for 2.54 cm O.D. Tube, TCWI equal to 45°C and the Upper Plenum Pressurized

RUN NO.	PBP (kPa)	PUP (kPa)	SPL(m) (measured)	SPL(m) (calculated)
D24061	164.146	138.348	1.60	2.69
D24062	158.007	136.227	1.22	2.27
D24063	154.497	136.254	0.91	1.91
D24064	147.700	135.098	0.27	1.33
D25061	153.682	134.711	1.50	1.98
D25062	149.850	134.625	0.63	1.60
D25063	145.847	134.679	0.97	1.18
D25064	142.694	135.465	0.25	0.78
D26061	144.027	124.457	1.65	2.04
D26062	140.321	123.397	1.36	1.76
D26063	138.240	123.448	1.10	1.54
D26064	133.932	122.937	0.61	1.15
D27061	135.482	114.380	1.59	2.19
D27062	132.044	114.040	1.04	1.87
D27063	129.184	113.921	0.83	1.58
D27064	121.990	113.760	0.05	0.86

TABLE 4.1c Measured and Calculated Single-Phase Region Lengths for 1.91 cm O.D. Tube, TCWI equal to 14°C and the Upper Plenum Pressurized

RUN NO.	PBP (kPa)	PUP (kPa)	SPL(m) (measured)	SPL(m) (calculated)
D09107	161.601	127.979	3.15	3.42
D09108	155.167	126.273	2.47	2.94
D09109	149.647	126.179	2.01	2.39
D091010	141.931	126.618	1.35	1.56
D091011	135.745	125.647	0.73	1.03
D091012	130.825	126.587	0.19	0.43

TABLE 4.1d Measured and Calculated Single-Phase Region Lengths for 1.91 cm O.D. Tube, TCWI equal to 45°C and the Upper Plenum Pressurized

RUN NO.	PBP (kPa)	PUP (kPa)	SPL(m) (measured)	SPL(m) (calculated)
D10107	151.484	125.830	2.73	2.61
D10108	148.479	125.548	2.05	2.33
D10109	143.002	125.826	1.51	1.75
D101010	139.248	125.749	1.19	1.37
D101011	134.160	125.279	0.64	0.90
D101012	131.613	124.547	0.36	0.72

TABLE 4.1e Measured and Calculated Single-Phase Region Lengths for 1.27 cm O.D. Tube, TCWI equal to 10°C and the Upper Plenum Pressurized

RUN NO.	PBP (kPa)	PUP (kPa)	SPL(m) (measured)	SPL(m) (calculated)
D14081	158.512	121.647	3.73	3.76
D14082	149.846	120.778	2.80	2.96
D14083	143.126	120.543	2.24	2.30
D14084	124.993	120.745	1.06	0.43

TABLE 4.1f Measured and Calculated Single-Phase Region Lengths for 1.27 cm O.D. Tube, TCWI equal to 45°C and the Upper Plenum Pressurized

RUN NO.	PBP (kPa)	PUP (kPa)	SPL(m) (measured)	SPL(m) (calculated)
D04081	144.036	118.833	3.97	2.61
D04082	165.855	118.889	3.47	4.85
D04083	161.031	118.840	3.44	4.36
D04086	151.269	118.637	1.57	3.38
D11088	159.853	123.869	3.77	3.73
D11089	149.058	122.744	2.69	2.73
D110810	136.383	123.014	1.41	1.40

is clearly shown in Figure 4.9a,b and c. Tne "error bars" shown are simply indicating the maximum amplitude of oscillations of the two-phase region length which in turn correspond to the oscillations of the single-phase top. The experimental results show the little influence of the inlet cooling temperature on the magnitude of the oscillations.

The inlet cooling water temperature appears to have an opposite effect on the single-phase region lengths than the one on the two-phase region length. The single-phase lengths measured with the coldest inlet cooling water temperature appear to be longer than for the hottest inlet cooling water temperature. This may be due to smaller pressure drops for the cases with the coldest inlet cooling water temperature than for the cases with the hottest one. The present model overpredicts slightly the lengths of the single-phase region because it cannot predict well the pressure drop in the two-phase region and consequently it does not show the observed effect of the inlet cooling water temperature on the lengths of the single-phase region.

4.1.4 Local Measurements

Measurements of pressure, void fraction, and temperature axial distributions have been carried out along with the measurement of heat removal by each individual cooling jacket. A typical set of axial profiles is presented in Figures 4.10 where the results of the present model for the given experimental conditions is also given. In the figure the nomenclature used is as follow: "PBP" means the absolute pressure in the bottom plenum, "STMFLW" stands for the injected steam flow rate (condensation rate), "PUP" is for the absolute pressure in the upper plenum, and "QRMV" stands for the total heat removal. Other sets of axial profile and measurements of local heat removals are shown in Appendix G where no comparison between the model and the experimental data is made. The comparisons shown in Figures 4.10 were seen to be fairly representative of what would be obtained.

From Figures 4.10a and b, the measured pressure drop in the two-phase region is shown to be much smaller than the total system pressure drop (from the bottom plenum to the top plenum). The void fraction profile is shown to decrease as the end of the two-phase region is approached. The present model is seen the underpredict the pressure drop and the liquid holdup in the two-phase region. This discrepancy may be due to the absence of an entrainment mechanism in the present model. A crude estimate of the average amount of liquid holdup entrained can be obtained by assuming the void fraction profile predicted by the present model to be correct. Then it can be seen that a large

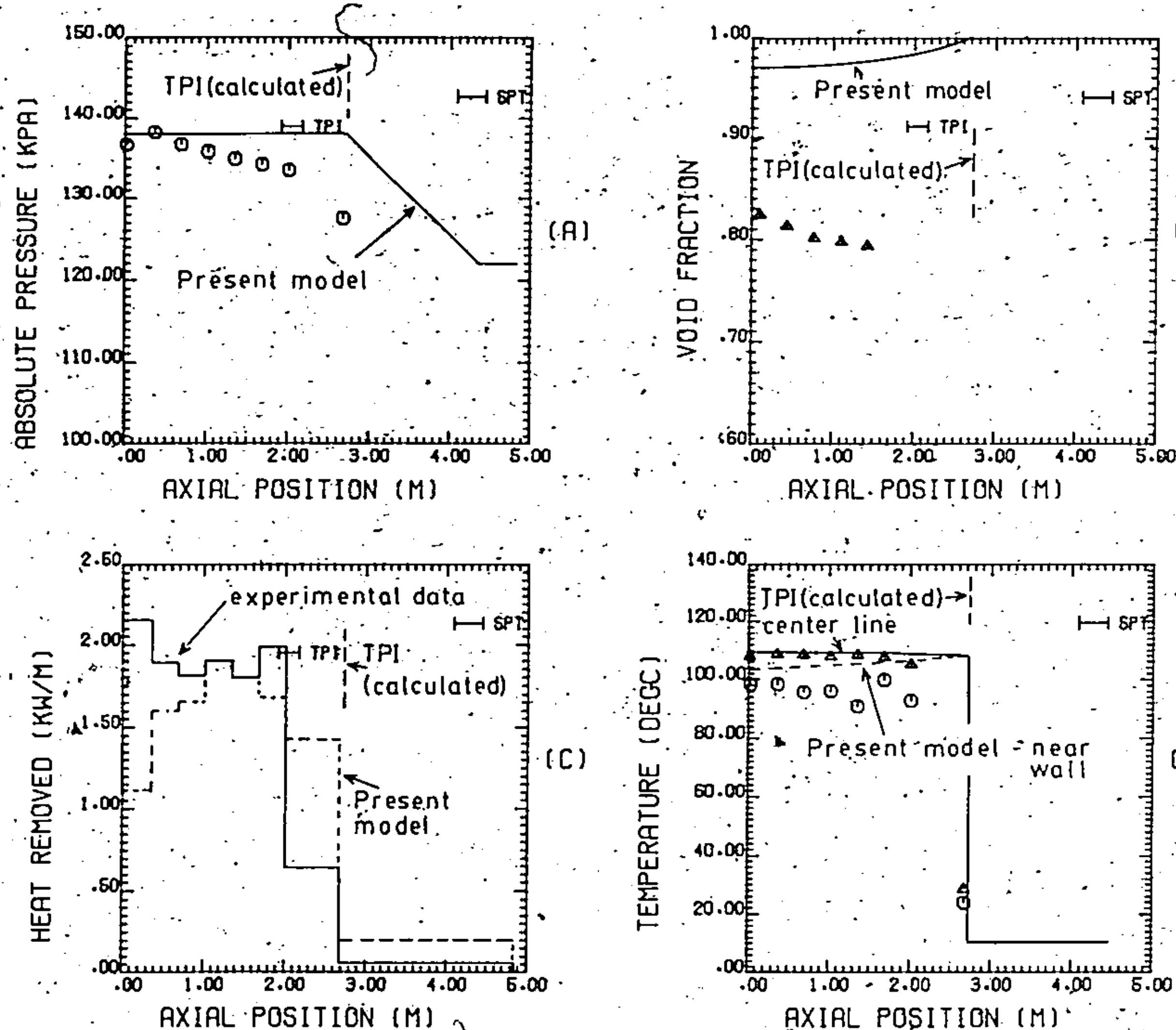

FIGURE 4.10
EXPERIMENTAL DATA OF
RUN NO. D05051

TCWI=10 DEGC
TUBE DIA= 2.54 CM O.D.
PBP= 138.138 KPA
PUP= 111.217 KPA
STMFLW= 122.34 G/MIN
QRMV= 4.350 KW
SINGLE-PHASE TOP= 4.08/ 4.44 M
(ABBREVIATED AS SPT IN THE PLOTS)

TWO-PHASE INTERFACE= 1.92/ 2.18 M
(ABBREVIATED AS TPI IN THE PLOTS)

LEGEND OF TEMPERATURE PLOT
⊙ = NEAR WALL
▲ = CENTER LINE

AVERAGE VOID FRACTIONS

MEASURED = .8059
CALCULATED = .8434

FIGURE 4.10 Local Measurements of Run No. D05051 part of the liquid holdup is in the form of the observed entrainment.

The agreement between the results of the present model and the center-line temperature profile is good; however, the prediction of the condensate temperature near the wall is higher than measured. This could be due to the prediction by the model of a heat flux smaller than what it is actually. This fact is reflected in the prediction of the two-phase region lengths longer than measured and in heat removal profile as illustrated in Figure 4.10c. In Figure 4.10d, the temperature profile exhibit a sharp temperature gradient at the two-phase interface. This experimental observation gives some support to the presence of heat transport at that interface.

Overall the trends in the experimental data are qualitatively well predicted by the model except for the void fraction profile. To a first order of approximation the pressure drop in the two-phase region could be consider to be due to gravity alone where the frictional and accelerational pressure drops are assumed to cancel each other as it could be the case for laminar film condensation in a tube with upward steam flow [15]. This approximation combined with the assumption that the flow in the two-phase region is homogeneous give a mean to verify the void fraction measurements. This is done using the measured pressure drop and two-phase region length to compute an average void fraction that can be compared to the average of the void fraction profile. As indicated in the figure caption (see also in Appendix G) the agreement is fairly good, giving support to the method of void fraction measurement; however, the agreement for the 1.27 cm O.D. tube is not as good as for the other tube sizes. This may be due to the oscillating single-phase region near the void meter which was found to have a strong influence on the measurements.

It is interesting to examine the changes in the shape of the axial pressure profiles as the imposed pressure drop across the tube increases. For instance, typical changes are illustrated in the series of plots of local measurements for the 2.54 cm O.D. tube and for an inlet cooling water temperature of 10°C (see Appendix G, Figures G.4 to G.11). For small imposed pressure drops, the axial profile is shown to be fairly flat, and as the imposed pressure drop increases the curvature of the profile increases. For the range of imposed pressure drops corresponding to steam flow rates smaller than the steam flow rate at flooding, the changes in the curvature of the profile are significant; however, after the flooding condition has been reached the subsequent increases in the imposed pressure drop do not cause any significant change in the curvature of the profile in the two-phase region. In other words, the system reaches a limit: the total pressure drop in the two-phase region does not change significantly after the flooding condition has been reached, and the increase in the imposed pressure drop across the tube is reflected in the length of the single-phase region.

The heat removal profile appears to become fairly uniform, suggesting a constant heat flux at the wall, giving support to that assumption made in the development of the model in Chapter 3. Since the heat transfer and the pressure drop depend mainly on the flow regime and since the local measurements plus the visual observations reported in Chapter 3 indicate no significant changes in this flow regime after the flooding condition has been reached, it can be concluded again that flooding at the tube inlet is the controlling process and the system operates at the flooding point. This gives additional support to the truthfulness of the postulate stated in Section 3.2.3 and confirmed by the comparison between the present model and the global measurements given in Section 4.1.2.

4.1.5 Oscillations of the Single-Phase Region

In Chapter 3, it is mentioned that self-sustained oscillations of the single-phase region were observed for a given imposed pressure drop across the tube. A simple analytical model has been derived to analyse the self-sustained oscillations of the single-phase region. The detailed derivations have been already presented [108] and will be omitted here. It suffices to say that under certain assumptions, valid for the present situation, the whole system can be assimilated to the classical Helmholtz resonator [109, p.170-172] yielding the following expression for the frequency of oscillations:

$$f_{sp} = \frac{1}{2\pi} \left[\frac{p_{bp} \; n \; A}{V \; \rho_\ell \; L_{sp}}\right]^{1/2} \tag{4.3}$$

where

f_{sp}: frequency of oscillations (Hz)

p_{bp}: absolute pressure in the bottom plenum (N/m^2)

n: ratio of the saturated steam specific heats ($= c_{pg}/c_{vg}$, evaluated at p_{bp})

V: total volume of steam below the water column including the bottom plenum (m^3)

ρ_ℓ: density of the single-phase region (m^3)

L_{sp}: length of the single-phase region (m)

A: cross-sectionnal area of the tube (m^2)

In the present study the frequencies of oscillations of the single-phase region have been obtained in the 2.54 cm O.D. tube only. They were obtained from the a power spectrum analysis of the signal from the capacitance level meter (see Section 2.1.2.6). To see the effect of tube size, the frequencies of oscillations obtained in a previous study [73,86] are used to complete the above set of data. The experimental set-up used in that previous study had a tube inner diameter of 1.76 cm, and the frequencies were obtained from the analysis of pressure traces.

The frequencies are calculated using the experimental values and the agreement between the mesured and calculated values appear to be reasonable as illustrated in Table 4.2 and in Figures 4.11 a,b, and c. The experimental data for the 1.76 cm I.D. tube can be found in [73]. A close examination of the experimental data shows a small influence of the tube inner diameter.

The oscillations of the single-phase region mentioned above and in Section 3.1 define a continuously periodic and quasi-static state that could be associated to a limit cycle [111,p.225]. The possible physical

TABLE 4.2: COMPARISON BETWEEN MEASURED AND COMPUTED FREQUENCIES OF OSCILLATIONS OF THE SINGLE-PHASE REGION IN THE 2.54 cm O.D. TUBE

RUN NO.	P_{bp} (kPa)	TCWI (^oC)	L_{sp} (m)	$V \times 10^2$ (m^3)	f_{sp} (Hz) (measured)	f_{sp} (Hz) (calculated)
D05051	138.138	10	2.21	4.86	0.125	0.120
D05052	135.658	10	1.97	4.72	0.130	0.127
D09051	155.423	10	2.24	4.79	0.110	0.127
D09052	150.895	10	1.80	4.88	0.120	0.138
D10051	165.614	10	2.39	4.71	0.100	0.128
D10052	159.688	10	1.85	4.72	0.130	0.142
D17031	127.738	20	1.98	4.59	0.127	0.125
D18031	125.283	30	2.18	4.67	0.120	0.117
D21031	118.391	45	1.15	4.69	0.100	0.160
D21032	115.252	45	0.85	4.69	0.120	0.180
D22031	130.004	10	2.25	4.70	0.124	0.120

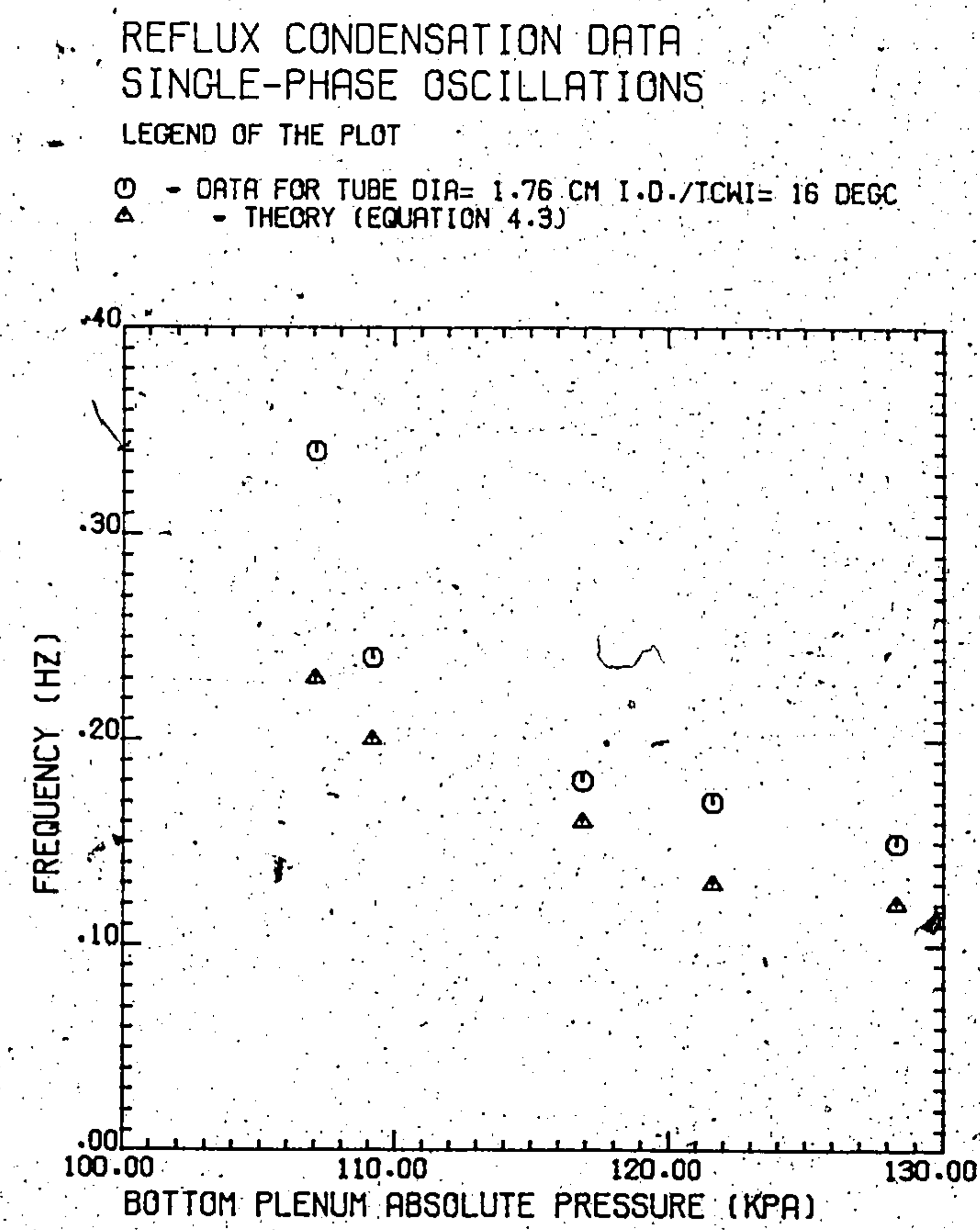

FIGURE 4.11a Variation of Oscillation Frequency of Single-Phase Region as a Function of Bottom Plenum Absolute Pressure for 1.76 cm I.D. Tube and TCWI = 16°C

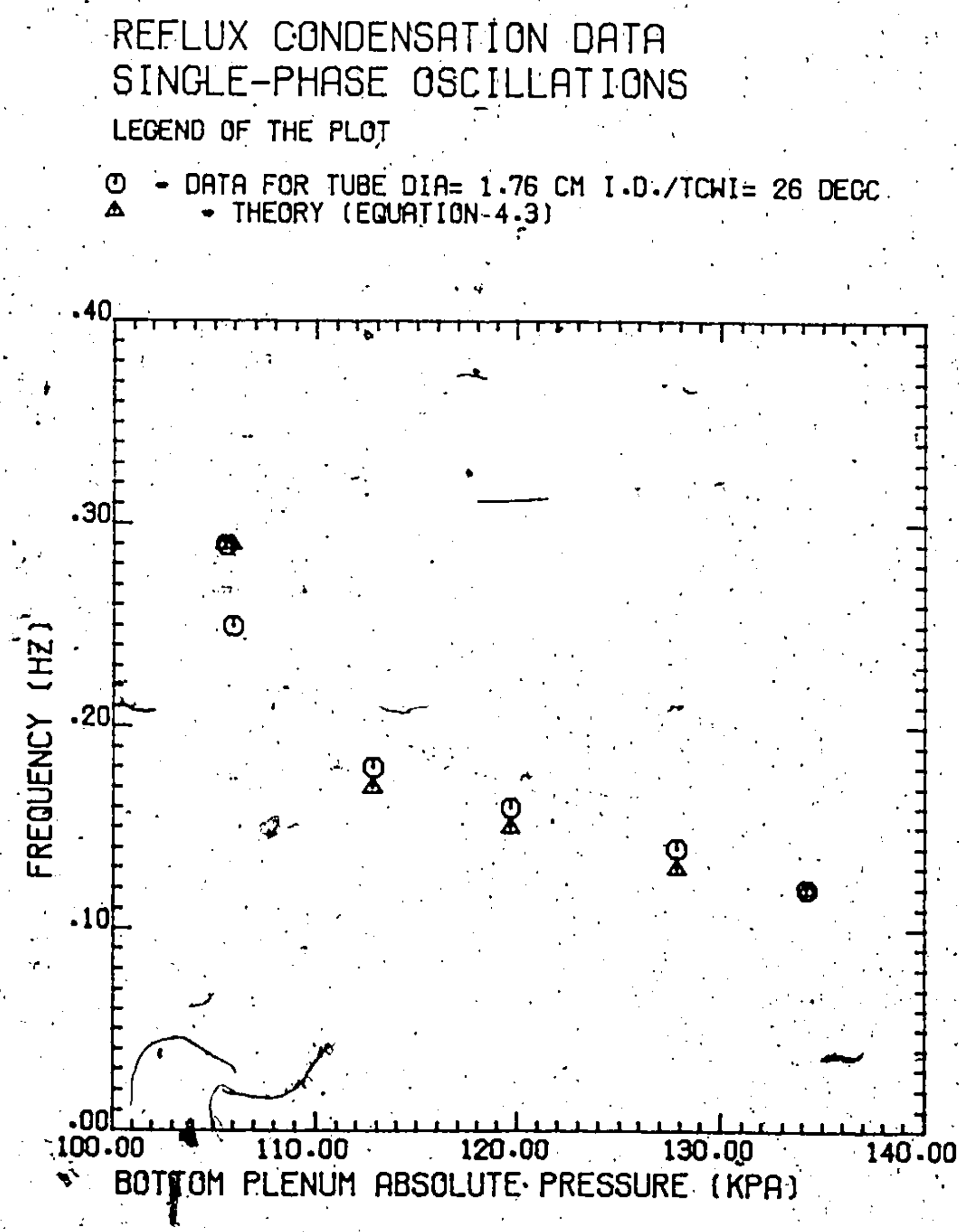

FIGURE 4.11b Variation of Oscillation Frequency of Single-Phase Region as a Function of Bottom Plenum Absolute Pressure for 1.76 cm I.D. Tube and TCWI = 26°C

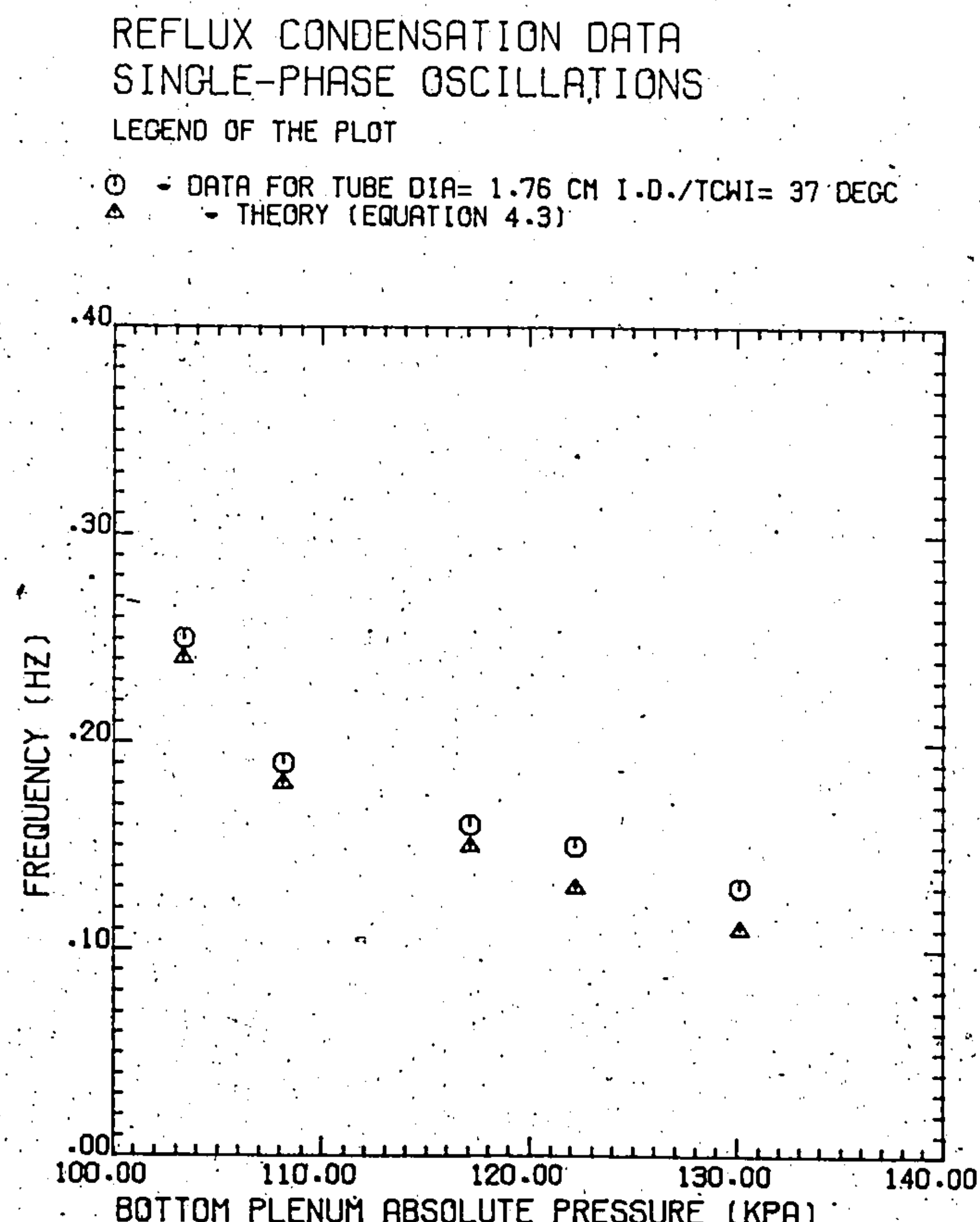

FIGURE 4.11c Variation of Oscillation Frequency of Single-Phase Region as a Function of Bottom Plenum Absolute Pressure for 1.76 cm I.D. Tube and TCWI = 37°C

mechanisms responsible for the limit cycle oscillations could be explained as follow [108,110]. For the case of total reflux condensation with a single-phase region oscillating over the two-phase region, tube inlet and outlet pressures are constant and the flow resistances of the system are concentrated at the system inlet (see Section 4.1.1) and in the friction of the single-phase region on the tube inner wall. Let us initially assumed a slight increase in pressure occuring within the two-phase region. This action has two primary consequences. First, it may tend to reduce the flow rate coming into the tube from the bottom plenum and to increase, because of the flooding condition at the tube inlet, the condensate drainage. Second, the slight pressure increase will push up the single-phase region. This will cause the point of complete condensation to move upward, thus increasing the heat transfer area for condensation. Then, the rate of condensation would temporarily be greater than the inlet steam flow rate and it would result in a depressurization within the two-phase region, a momentary increase in the steam flow rate at the tube inlet, a decreased drainage of the condensate and the downfall of the single-phase region by gravity. This will tend to increase the pressure within the two-phase region and the entire process would be repeated in a cyclical manner.

An unstable linear system would give unbounded flow oscillations, but non-linear effects such as the friction of the single-phase region on the tube inner wall would be responsible for limiting the amplitude of the oscillations. In other words, the resulting force destabilizing the system is counter-balanced by the viscous dissipation in the system. The reasonable agreement between the experimental data and equation (4.3) suggests that the frequency of the oscillations is strongly dependent upon the volume of steam (bottom plenum included) below the single-phase region and they cannot originate from density wave propagation. This is because density waves are encountered mostly in evaporating systems and they are related to the fluid transport time through the evaporator.

4.2 Results for Imposed Steam Flow Rate

For an imposed steam flow rate the reflux condenser exhibits a cyclical operation where, during one cycle, the length of the single-phase region increases at the expense of the two-phase region until a point where the system becomes unstable and the single-phase region is ejected. The bottom plenum pressure variations in time reflect very well the cycling characteristic of the flow regime observed as illustrated in Figures 4.12a,b and c. Each figure shows two bottom plenum traces with

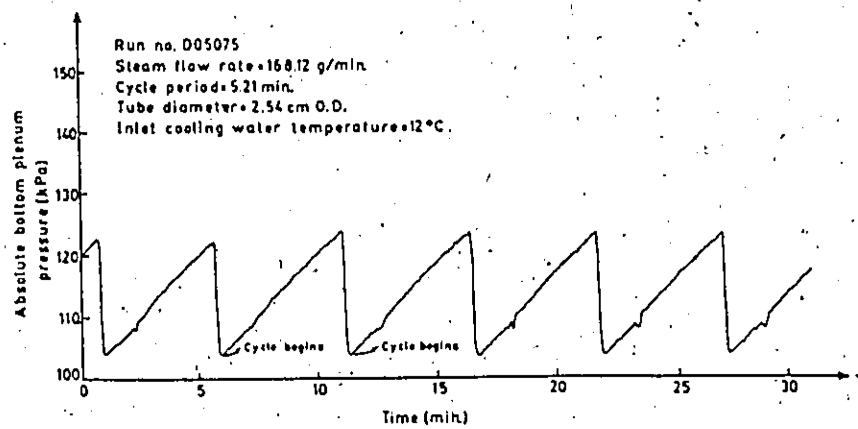

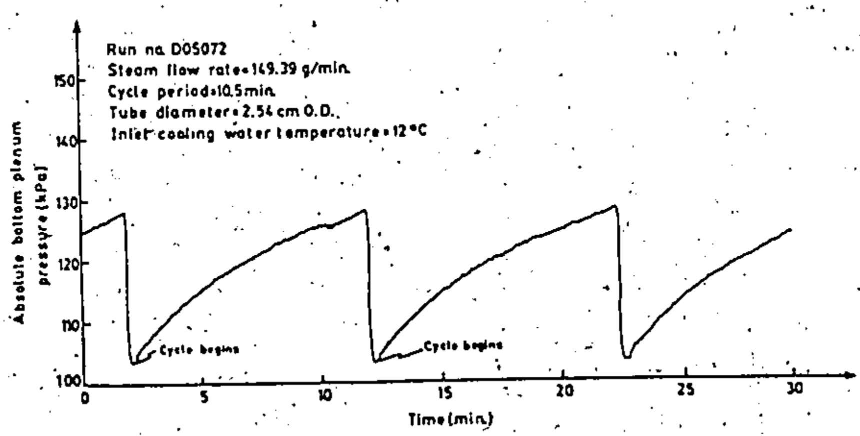

FIGURE 4.12a Variations of Absolute Bottom Plenum Pressure as a Function of Time in Fill and Dump Cycling for 2.54 cm O.D. Tube

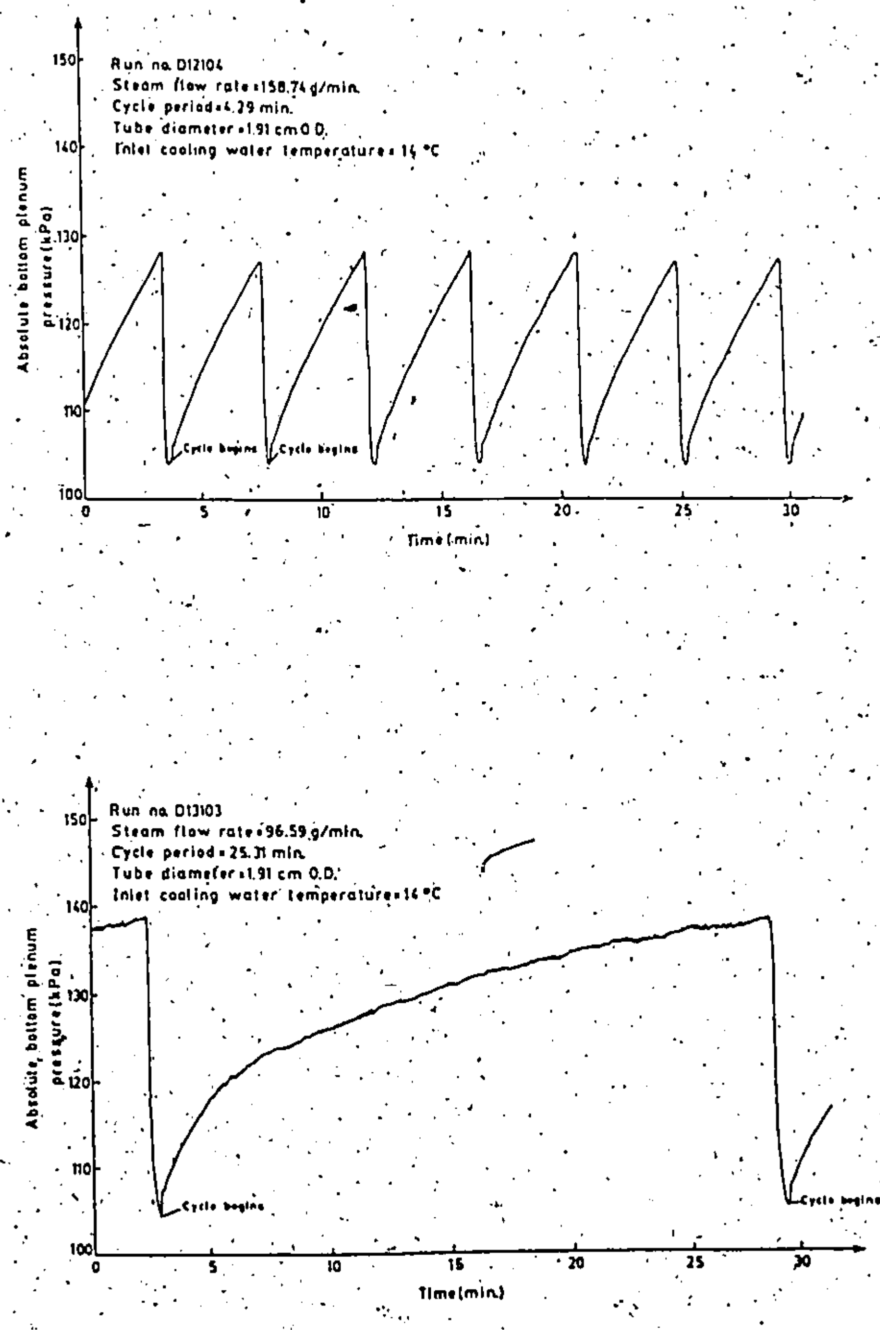

FIGURE 4.12b Variations of Absolute Bottom Plenum Pressure as a Function of Time in Fill and Dump Cycling for 1.91 cm O.D. Tube

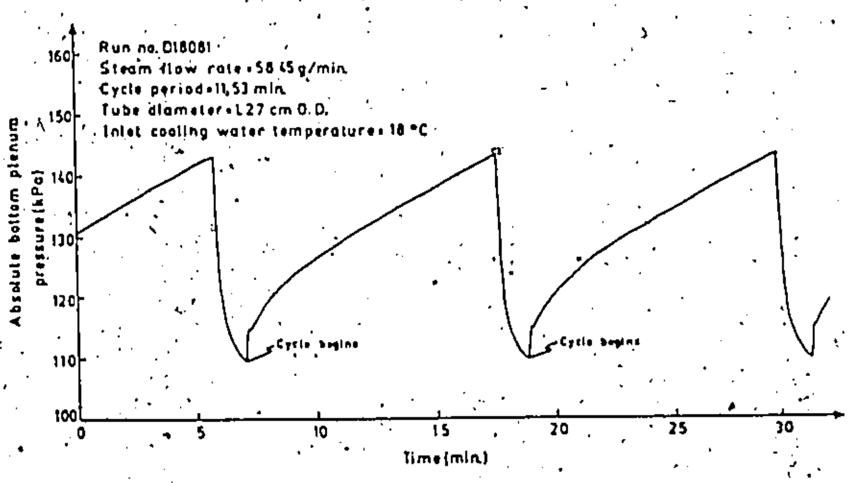

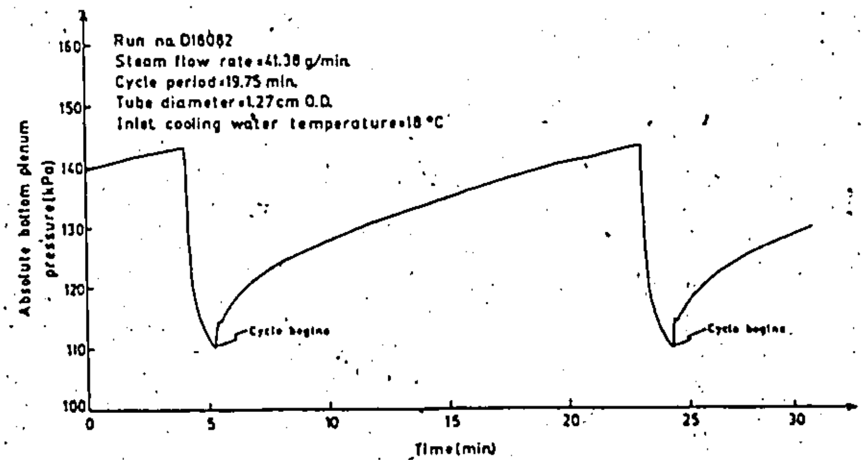

FIGURE 4.12c Variations of Absolute Bottom Plenum Pressure as a Function of Time in Fill and Dump Cycling for 1.27 cm O.D. Tube

different cycle periods. In a typical cycle, it can be seen that as the single-phase region increases the bottom plenum pressure increases, it reaches a maximum value indicating that the tube cannot holdup more condensate and it suddenly decreases when the single-phase region is ejected (see Figure 3.2), ending the cycle.

The bulk of the experimental data is separated in three interrelated aspects: flooding, heat removal and local measurements. The present flow regime does not allowed the measurements of the single-phase and two-phase region lengths. Then, what can be mentioned about condensate holdup in the tube is that most part of it is in the form of a growing single-phase region and it is obviously trapped in the system for a certain period only. In the analysis of a small-break LOCA, the particulars of the hypothetical scenario could lead to a condition where fill and dump cycling is most likely to be the heat rejection mechanisms in the steam-generators. This accident condition would be less severe than what it would be if total reflux condensation was the assumed heat rejection mechanism. This is because in the case of fill and dump cycling the coolant would accumulate in the steam generators and contrary to what occurs in total reflux condensation, the coolant would end up circulating to the reactor core.

4.2.1 Flooding

As mentioned in Section 3.1.2, the behavior of the system for a steam flow rate less than the one at the flooding point is the same for both boundary conditions. This is illustrated in Figures 4.13a,b and c where total reflux condensation data for increasing imposed steam flow rates are shown to follow the ideal complete condensation line before reaching the flooding line defined by the present model (point A to point B on Figure 4.13a).

At any instant in the ascending part of a fill and dump cycle, part of the condensate flows back to the tube inlet and the other part is carried over the existing two-phase region to form the growing single-phase region. From conservation of mass, the sum of the carry-over flow rate and the reflux rate is equal to the total steam flow injected. These three flow rates, averaged over several cycles, are plotted in the $K_g^{1/2}$-$K_\ell^{1/2}$ plane in Figures 4.13a,b and c. It was observed that fill and dump cycling starts after the flooding point has been reached. This causes the reflux rates to change path, i.e. from path AB to path CD as the imposed steam flow rate increases.

For all three tube sizes, the experimental data show that as the imposed steam flow rate increases,

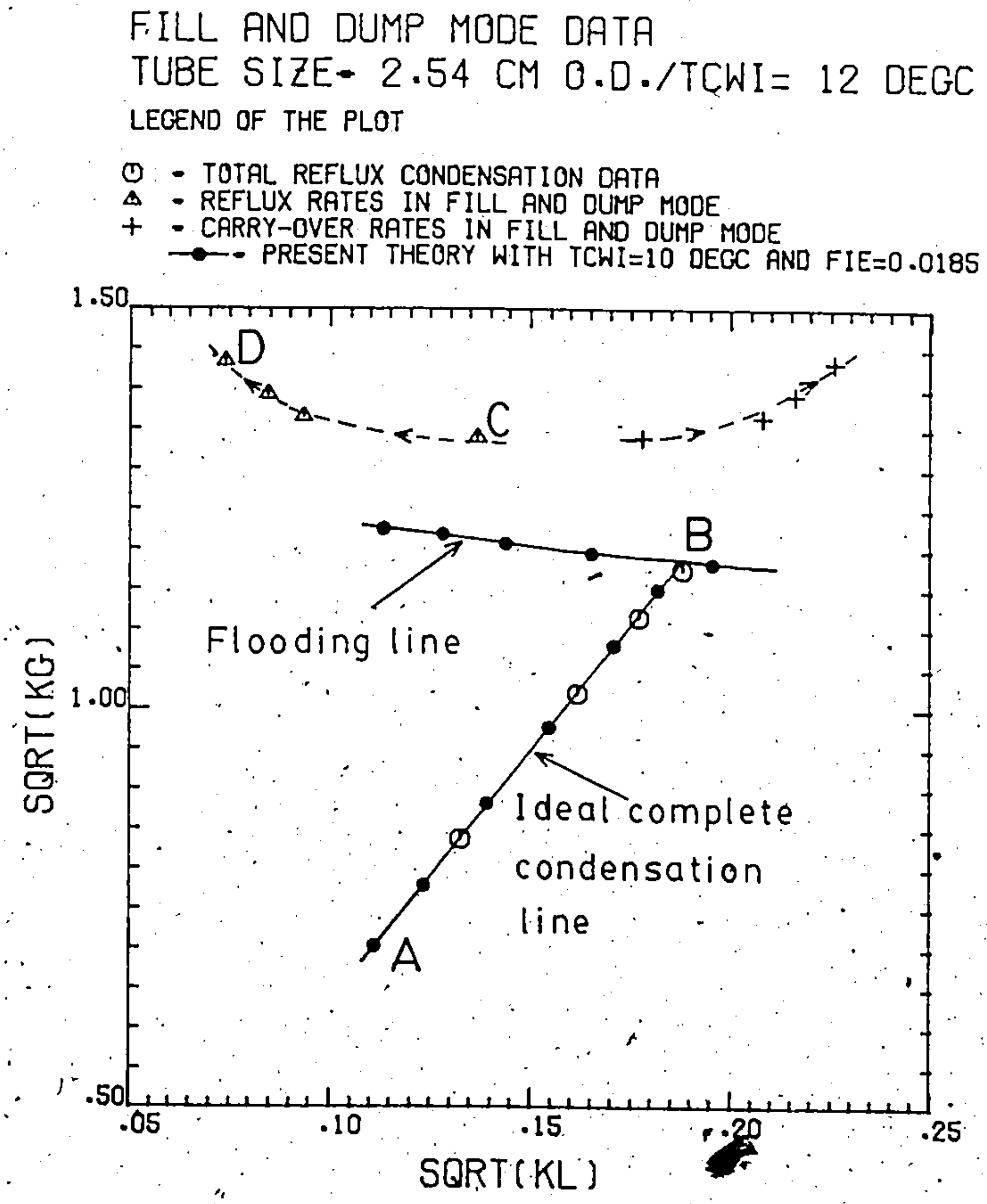

FIGURE 4.13a Fill and Dump Cycling Data in $K_g^{1/2}$-$K_\ell^{1/2}$ Plane for 2.54 O.D. Tube

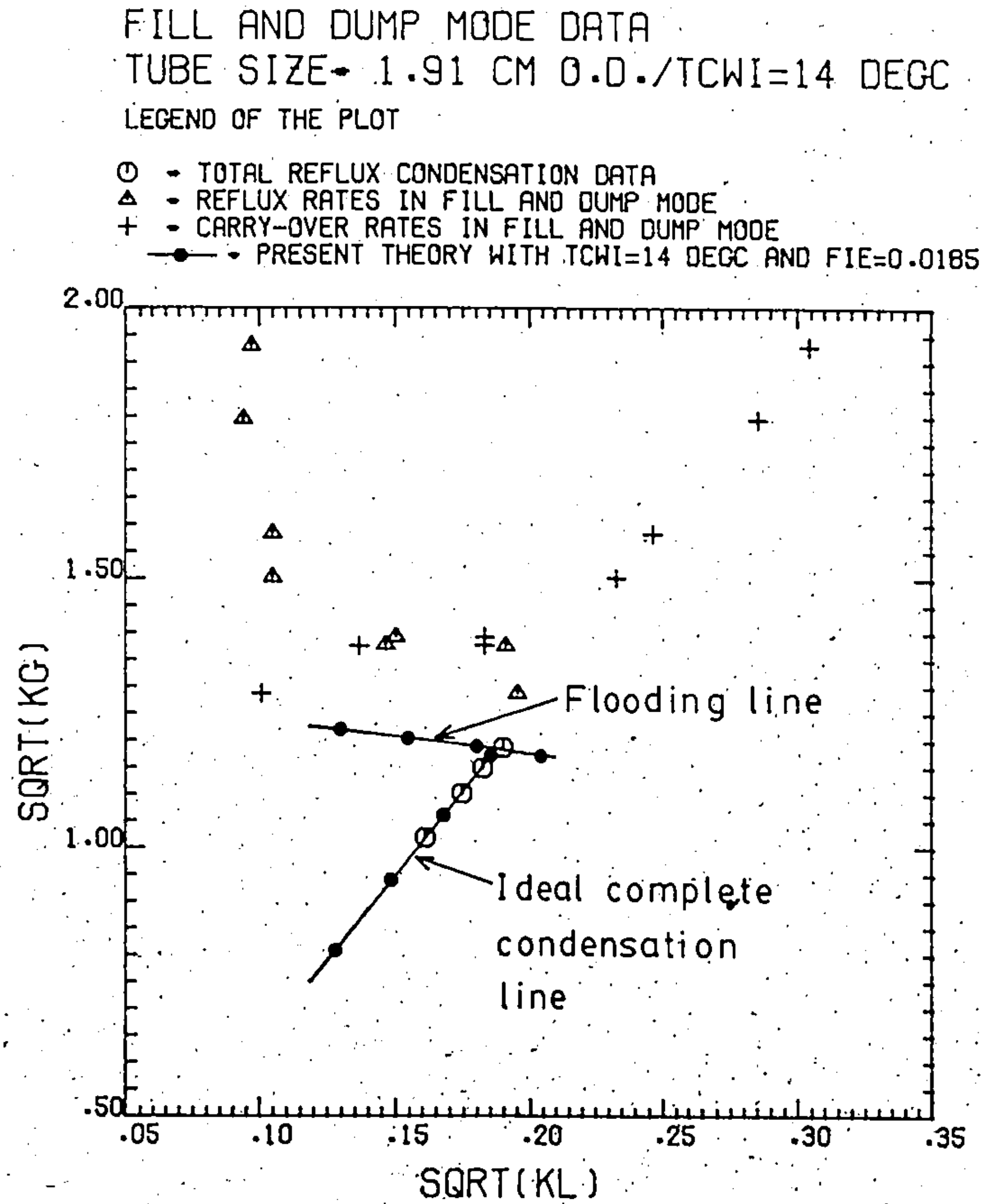

FIGURE 4.13b Fill and Dump Cycling Data in $K_g^{1/2}-K_\ell^{1/2}$ Plane for 1.91 O.D. Tube

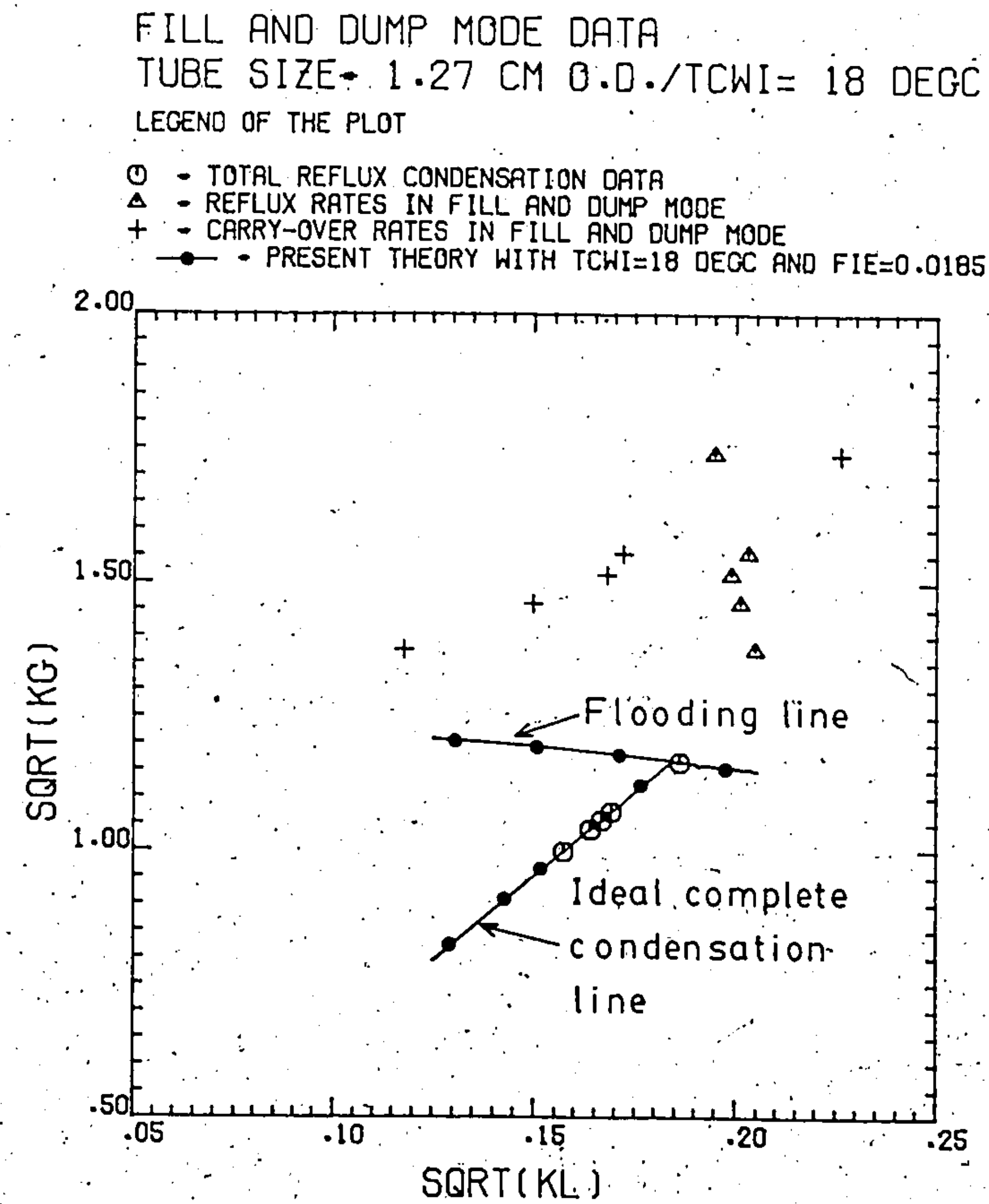

FIGURE 4.13c Fill and Dump Cycling Data in $K_g^{1/2}$-$K_\ell^{1/2}$ Plane for 1.27 O.D. Tube

the reflux rates decreases while the carry-over rates increases. Although each variation in the reflux flow rates does not follow the predicted flooding curve, it nevertheless follows qualitatively the general trend of a flooding curve. The discrepancy between the reflux data and the present model could be due to the formulation of the flooding used in the model, that appears to be more adequate for a flow regime that is quasi-static rather than dynamic . Thus, it can be suggested that flooding could play a key role in the determination of the fractions of the total flow rate that will be carried over and will flow back to the tube inlet which in turn have a great influence , on a time average basis, on the heat removal and the liquid holdup. The same sets of experimental data are plotted with the cycle period as the independent variable in Figures 4.14a,b and c. In each plot, a line has been drawn at the level of the flooding flow rate evaluated from total reflux condensation data at the maximum bottom plenum pressure reached in the ascending part of the cycle with the longest period. It can be seen that as the cycle period increases, the reflux rate increases to level off at the line corresponding to the flooding flow rate in total reflux condensation, the carry-over rate decreases up to a point much lower than the same line and the injected steam flow rate decreases but remains above that line. Here we must emphasize that all the steam injected in the system was condensed. The trends in

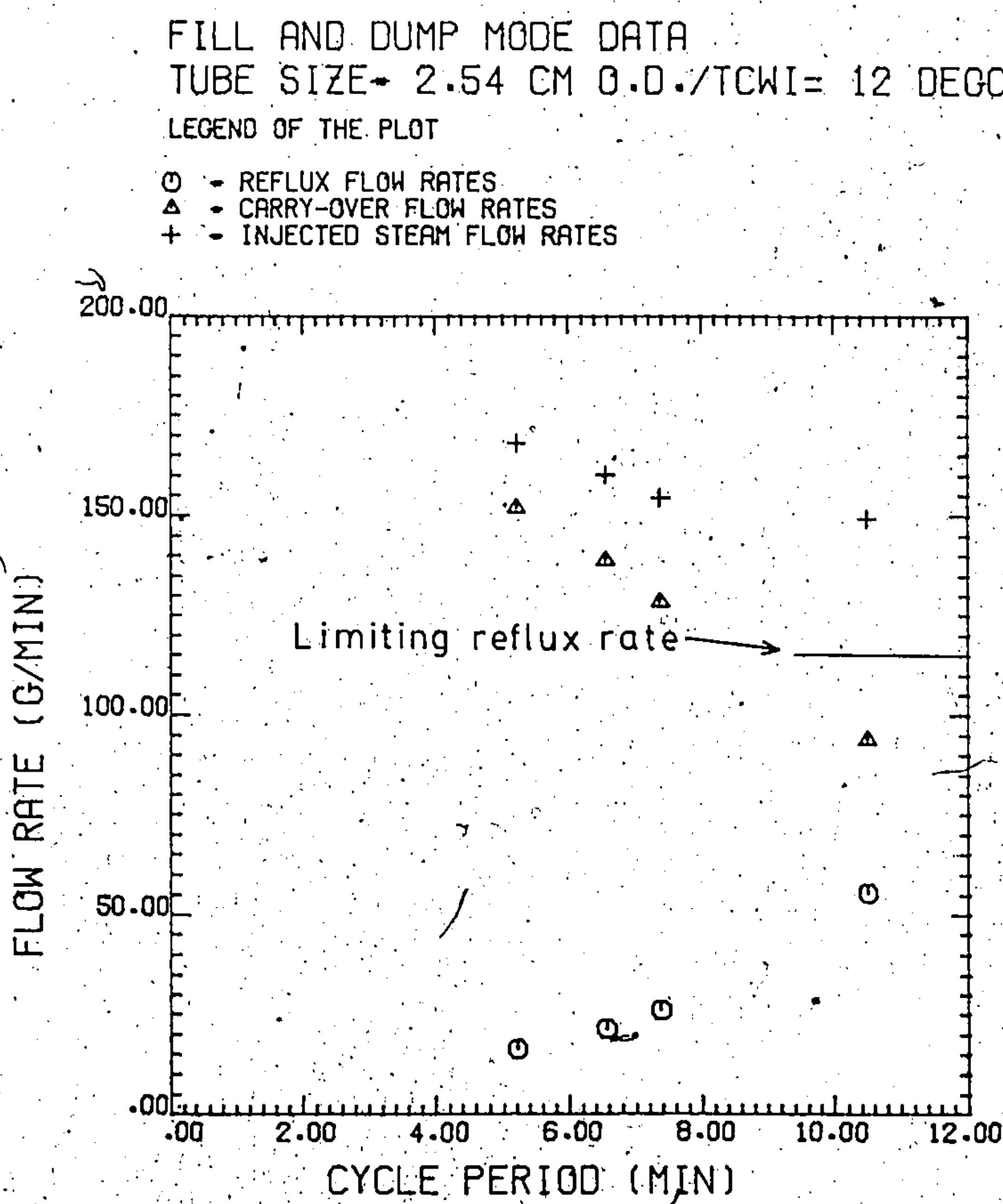

FIGURE 4.14a Variations of Reflux, Carry-over and Injected Steam Flow Rates as a Function of Cycle Period for 2.54 cm O.D. Tube

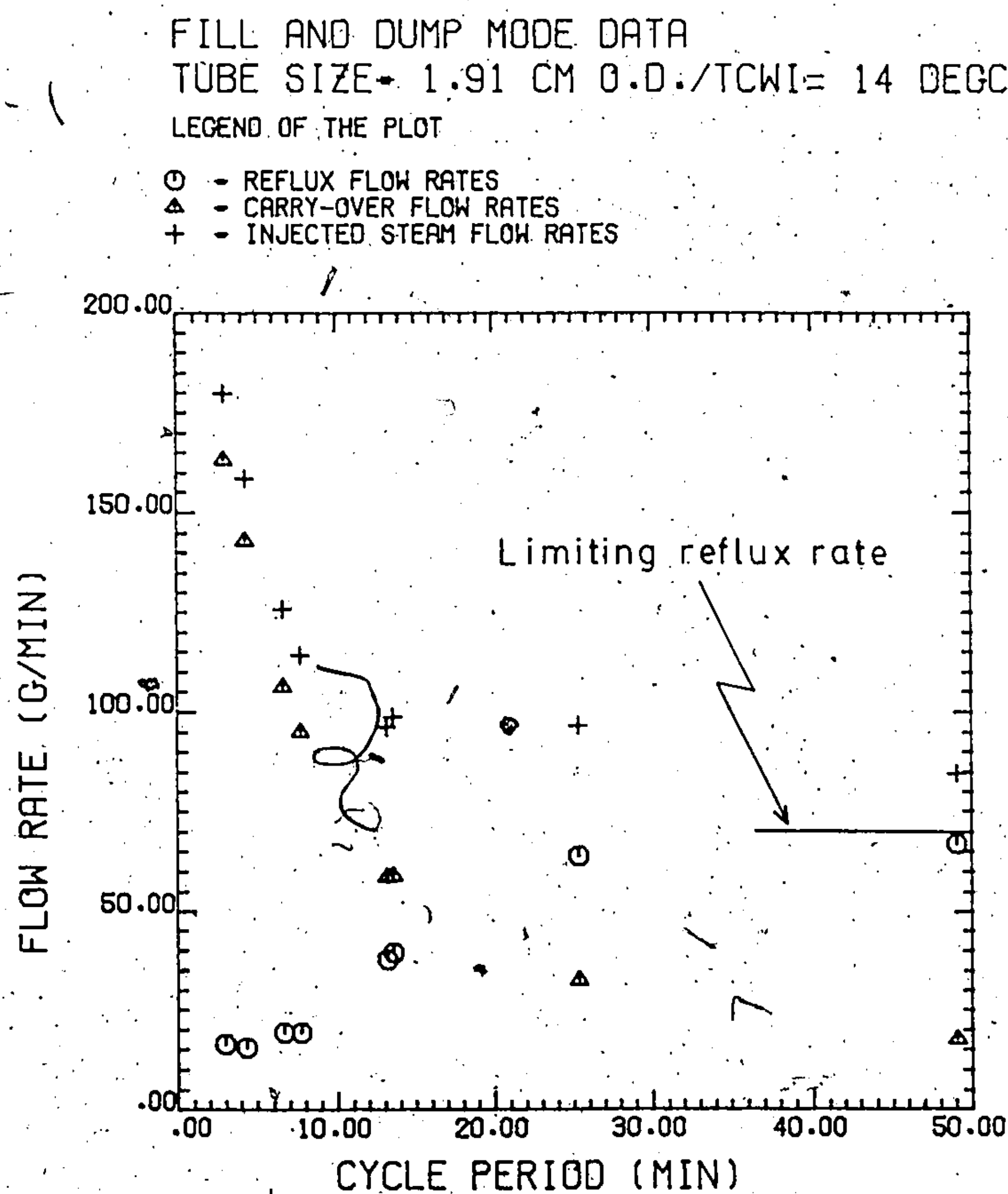

FIGURE 4.14b Variations of Reflux, Carry-over and Injected Steam Flow Rates as a Function of Cycle Period for 1.91 cm O.D. Tube

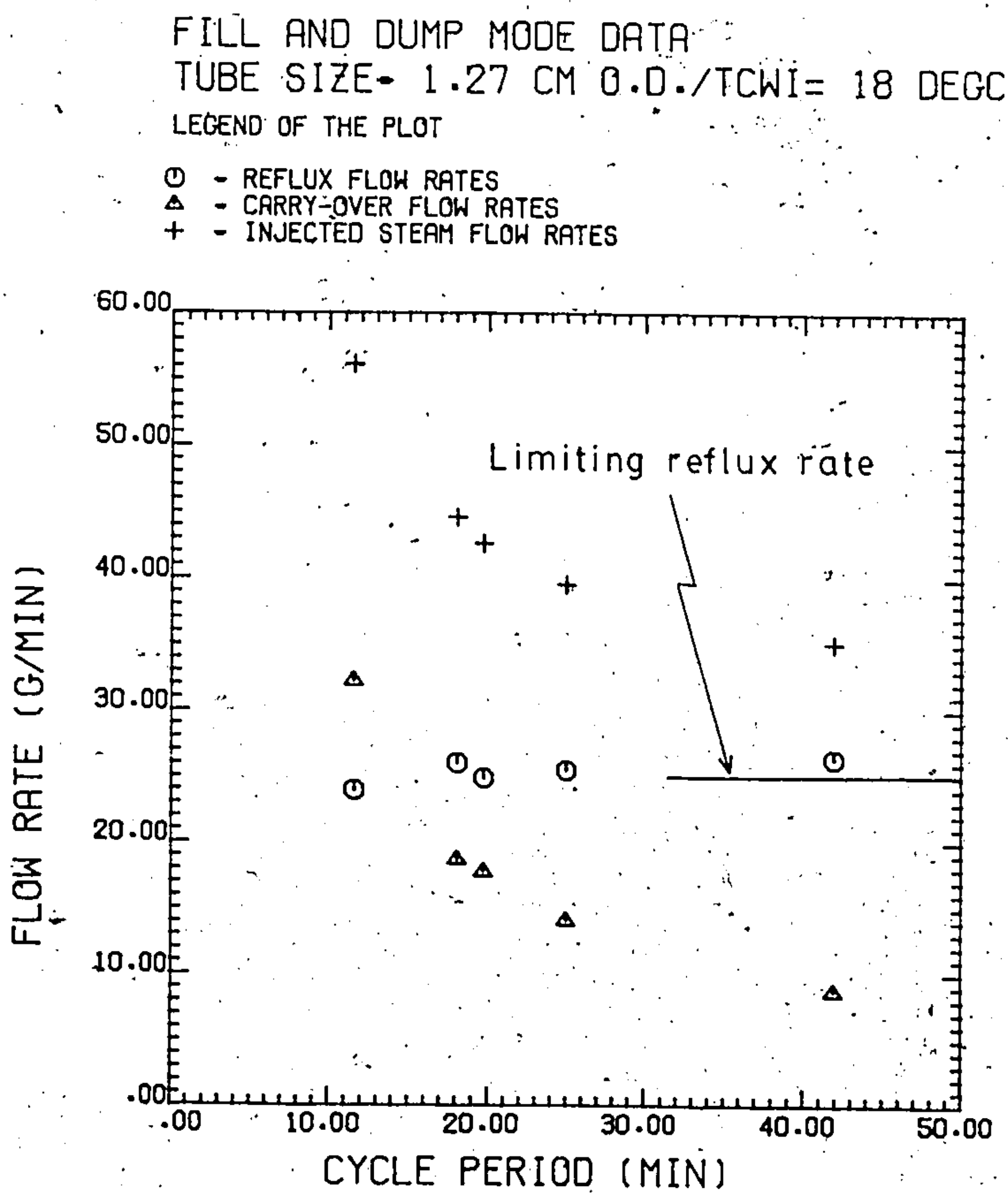

FIGURE 4.14c Variations of Reflux, Carry-over and Injected Steam Flow Rates as a Function of Cycle Period for 1.27 cm O.D. Tube

the experimental data suggest that if the cycle period was infinitely long, the flow regime would resemble more to one observed for imposed pressure drops, because the pressure in the bottom plenum would be nearly constant. Therefore, total reflux condensation is, to a certain extend, the limit case of fill and dump cycling.

Reflux rates as a function of the cycle period for the three tube sizes are shown in Figure 4.15a. They appear to level off at the same value of K_{ℓ} (approximately at $K_{\ell}=.20$) as the cycle period increases. In other words, the tube size does not influence the value at which these variations are leveling off. This behavior is quite similar to what has been observed in total reflux condensation in the sense that the tube diameter does not influence the non-dimensional value of the flooding flow rate. In Figure 4.15b, the variations of the carry-over flow rates appear to join each other as the cycle period increases; on the other hand, the variations of the total flow rate do not show a similar behavior as illustrated in Figure 4.15c.

4.2.2 Heat Removal

The variations of the total heat removal averaged over several cycles of the same period are shown in Figure 4.16 where the tube size is the main parameter. It can

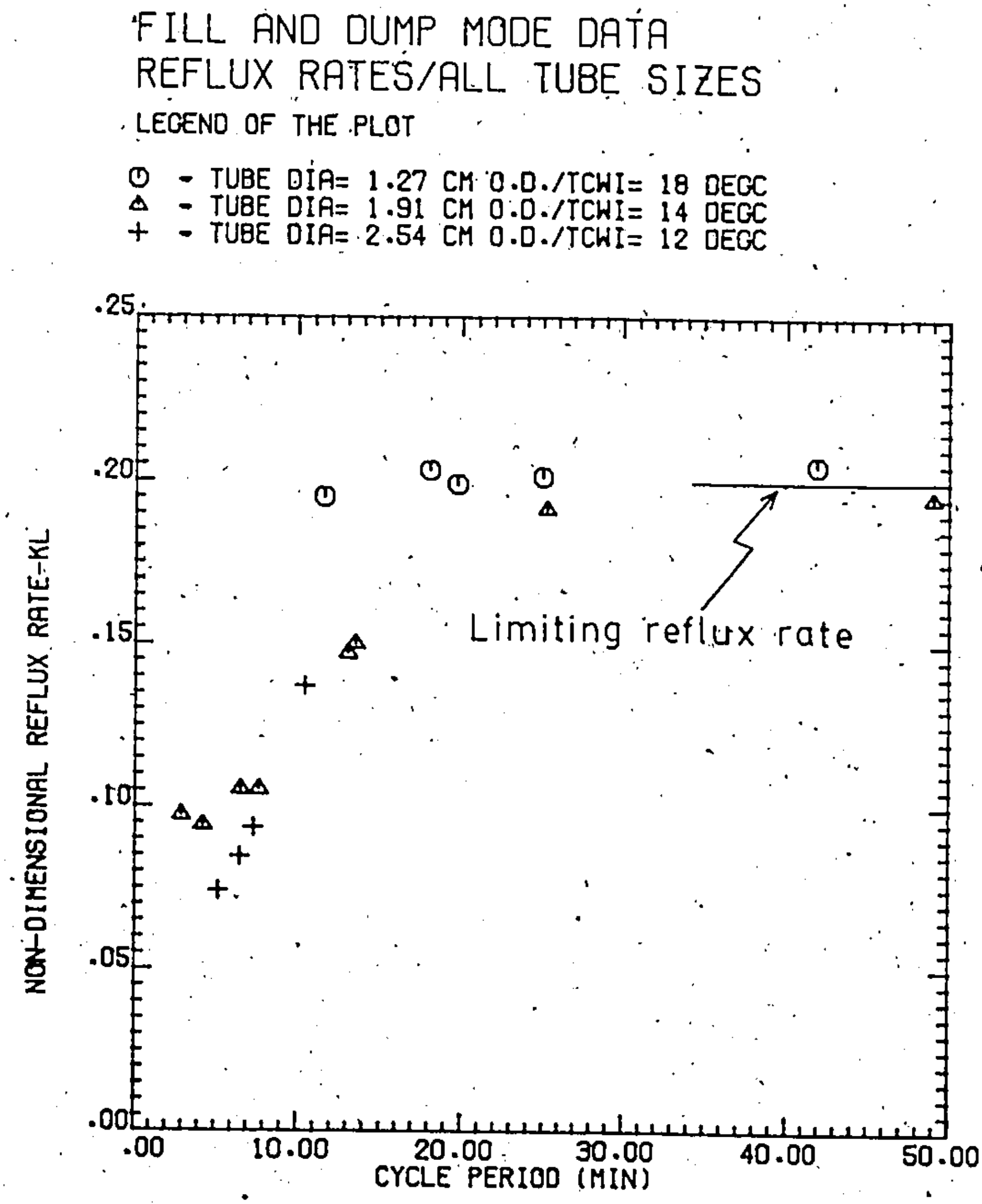

FIGURE 4.15a Variations of Reflux Rates as a Function of Cycle Period for All Tube Sizes

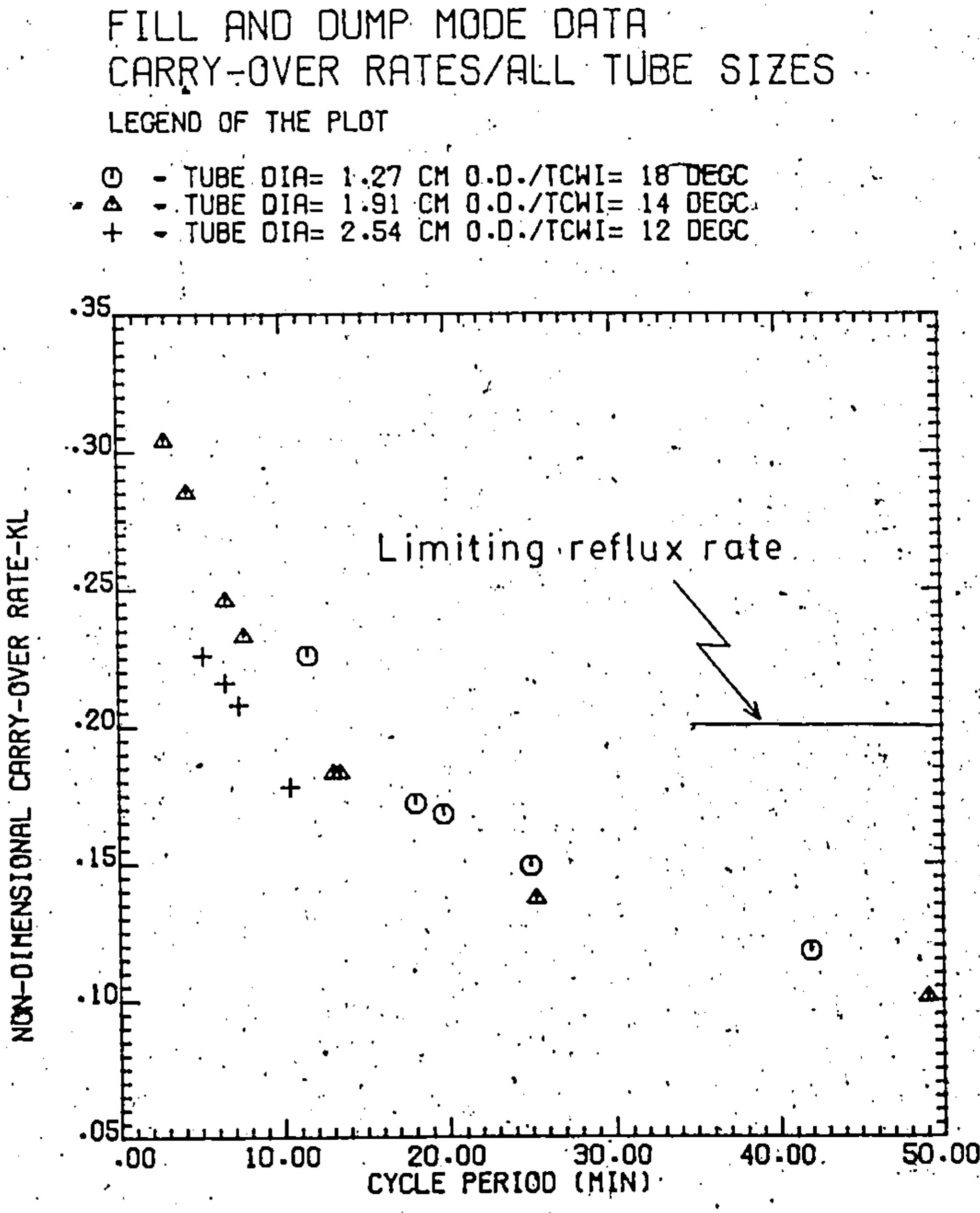

FIGURE 4.15b Variations of Carry-over Rates as a Function of Cycle Period of All Tube Sizes

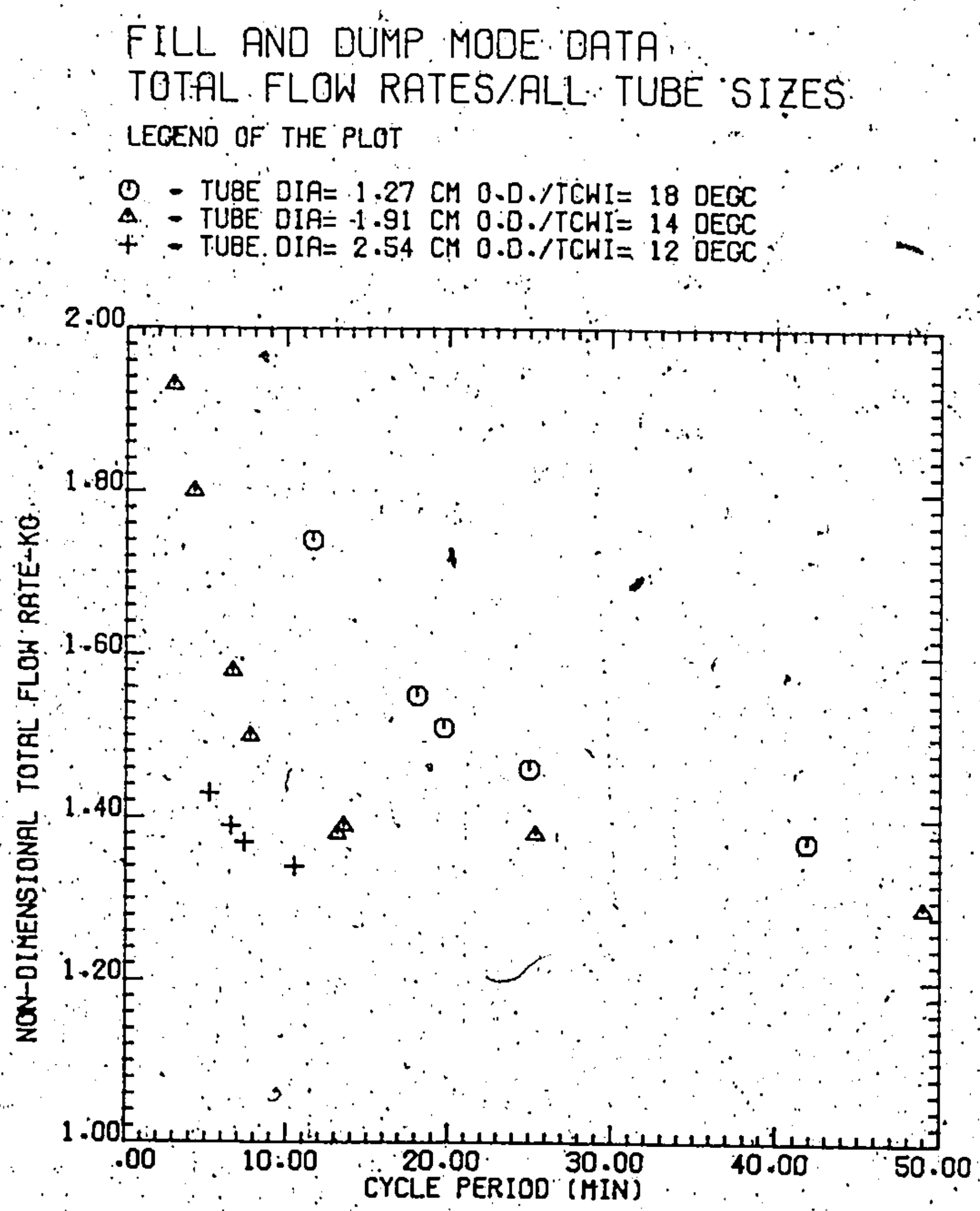

FIGURE 4.15c Variations of Total Flow Rates as a Function of Cycle Period for All Tube Sizes

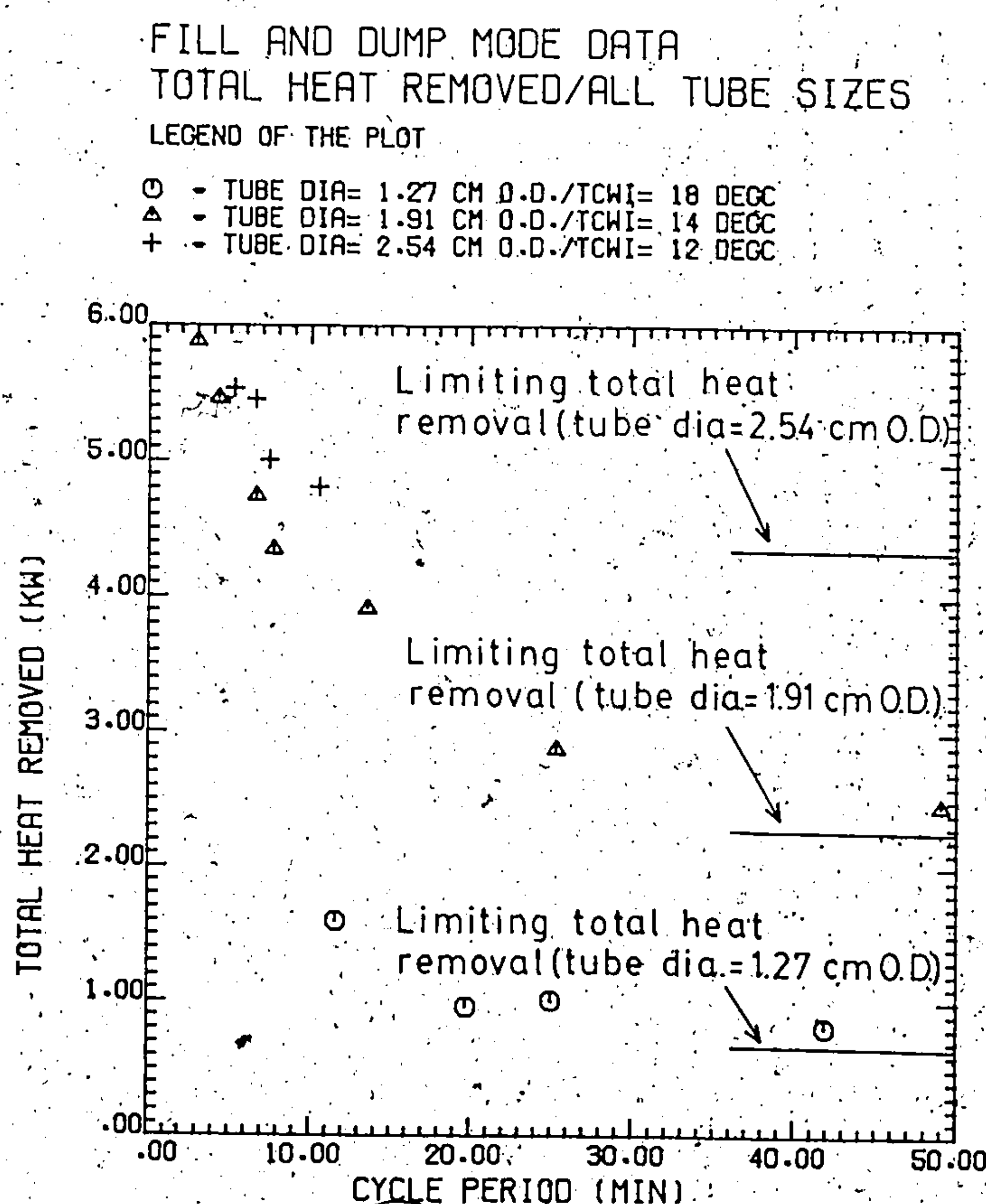

FIGURE 4.16 Variations of Total Heat Removed During One Cycle of Fill and Dump Cycling for All Tube Sizes

be seen that, as in total reflux condensation, the heat removal strongly depends on the tube diameter. In the plot, three lines are drawn at levels of heat removal corresponding to the flooding flow rate evaluated from total reflux condensation data at the maximum bottom plenum pressure reached in the ascending part of the cycle with the longest period. For each tube size the total heat removal appears to converge at a level slightly above the line corresponding to the heat removal in total reflux condensation. In other words, fill and dump cycling is more efficient heat rejection mechanism than total reflux condensation. Moreover, as the cycle period increases the heat removal decreases and tends to reach the total reflux condensation value.

4.2.3 Local Measurements

The main purpose of performing local measurements under fill and dump cycling is to see how the shape of the pressure and temperature axial profiles are changing with time and to see the region where most of the heat removal occurs.

A typical set of axial profiles is given in Figures 4.17, 4.18 and 4.19. It can be seen in Figure 4.17 that the curvature of the axial pressure profiles increases as time increases. This is equivalent to say that the

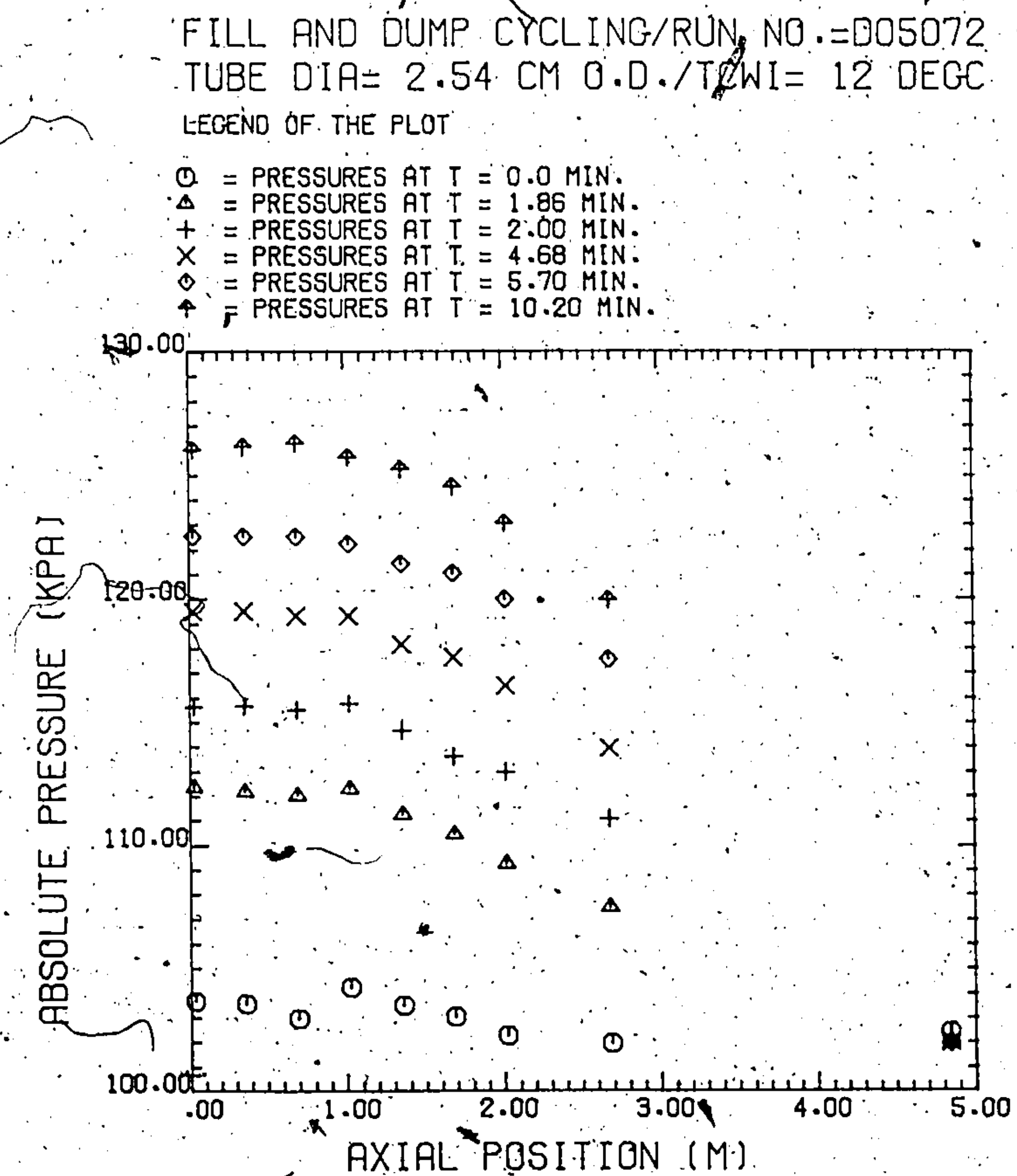

FIGURE 4.17 Axial Pressure Profiles During One Cycle of Fill and Dump Cycling for 2.54 cm O.D. Tube

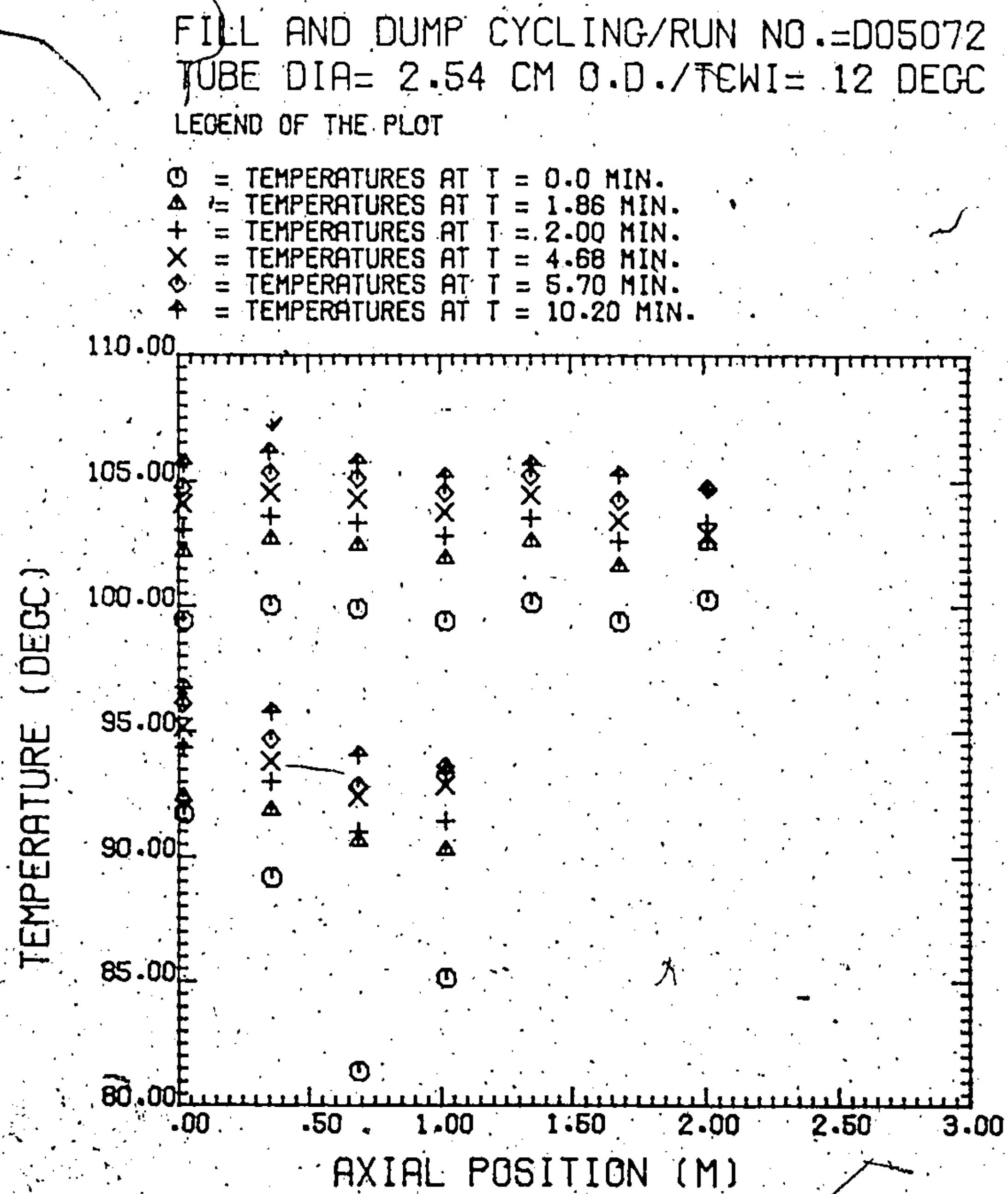

FIGURE 4.18 Axial Temperature Profiles During One Cycle of Fill and Dump Cycling for 2.54 cm O.D. Tube

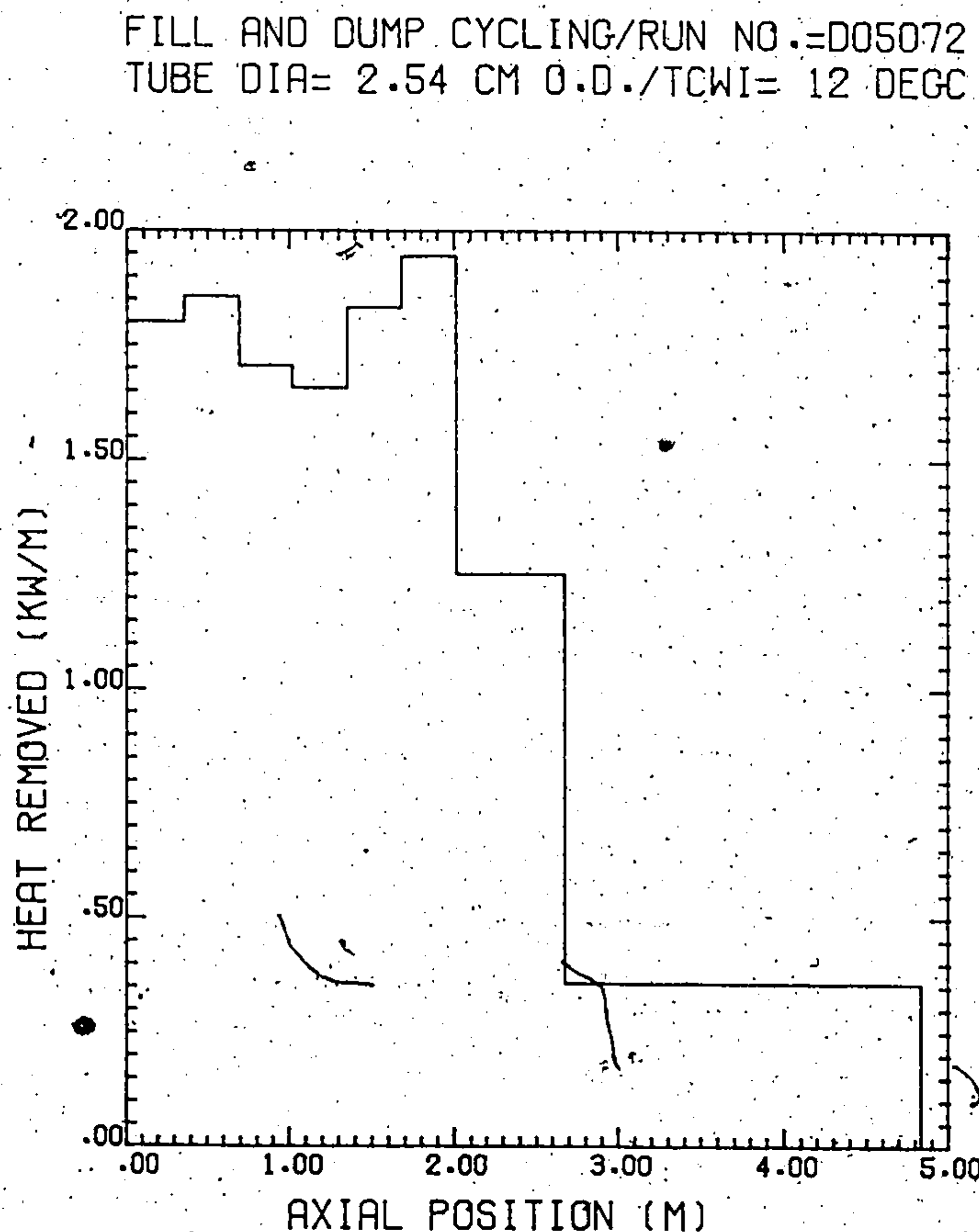

FIGURE 4.19 Axial Heat Removal Profile Averaged over Several Cycle Fill and Dump Cycling for 2.54 cm O.D. Tube

curvature of the profiles increases as the bottom plenum pressure increases, which is similar to what has been observed in total reflux condensation. In Figure 4.18, the temperature axial profiles are shown to follow the evolution of the pressure axial profiles. In Figure 4.19, the heat removal axial profile, averaged several cycles, indicates a notable amount of heat is removed in the upper section of the reflux condenser when compared to total reflux condensation data (see Figure 4.108). This is to be expected since the condensation length is for a significant part of the cycle much longer than what has been observed in total reflux condensation for the same inlet cooling water temperature. This gives additional support to the experimental fact that fill and dump cycling is a more efficient heat rejection mechanism than total reflux condensation.

4.3. Remarks on the Experimental Data and the Present Theory

In the Semiscale MOD-2A Natural Circulation experiments [5] an inverted U-tube of the steam generators was instrumented with differential pressure cells: one on the upflow side and the other on the downflow side of the tube. In these reflux condensation experiments, the upflow side is the side by which the steam from the core enters the tube and where counter-current steam-condensate flow occurs; the downflow side is the side by which part of the condensate flow leaves the tube. The shortest straight length of the U-tubes in their loop has a length-diameter ratio (ℓ/D) greater than 450, thus each of the tubes can be considered as a long reflux condenser.

Figure 4.20 shows the time variations of the pressure drop across the tube on both upflow and downflow sides, observed in MOD-2A experiments, due to an increase in core power. It can be seen that after the core power has been increased, the pressure drop variation shows a cycling behavior as it was observed with the present set-up. Note that the absolute pressure traces in Figure 4.11a,b and c could be put in terms of pressure drop traces, since in the present study the upper plenum was open to atmosphere. This pressure drop on the upflow-side tube reaches values that are much higher than that expected for frictional drop alone. From that result, Loomis and Soda suggests that flooding played an important role in the behavior of the system [5]. They attributed this increased pressure drop to a constriction of the tube flow area due to increased condensation and they did not explained the origin of the observed decrease in the pressure drop. However, in the light of the flow regime observed and the experimental data obtained in the present study, the cyclical pressure

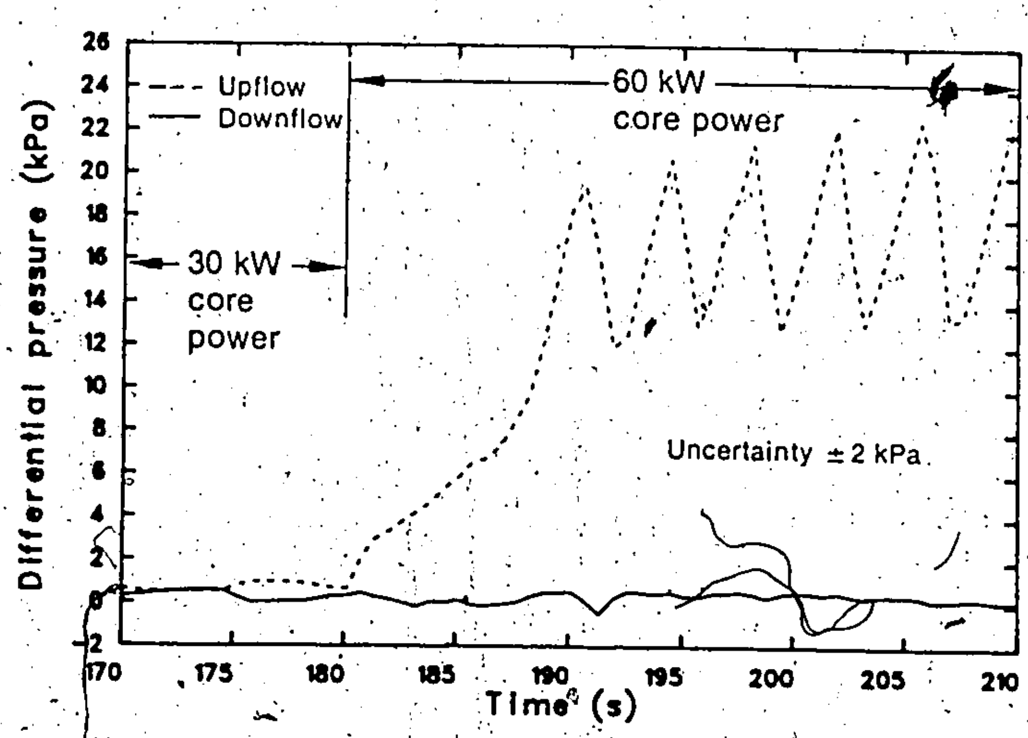

FIGURE 4.20 Results from the MOD-2A Natural Circulation Experiments (After Loomis and Soda [5])

drop could rather be attributed to the build up of a single-phase region of the top of a two-phase region (pressure drop increase) and the evacuation of this single-phase region (pressure drop decrease). Moreover, the cyclical pressure drop observed suggests that their boundary condition at the tube inlet could be similar to the imposed steam flow rate boundary condition used in the present study.

The instrumentation of the Semiscale MOD-2A loop provided means to measure a reflux/carry-over flow split of about one to one. This flow split was observed to remain constant even for an increase in the core power which results in an increase in steam flow from the core to the steam generators; however, that situation may not occurs in actual reactor system. This possibility is suggested by the experimental data presented in Section 4.2.1 where as the cycle period increases the flow split goes, in general, from a value less than one to a value greater than one.

The comparison between the pressure drop characteristic curves, each obtained with their respective boundary conditions, are shown in Figures 4.21a,b and c. For increasing steam flow rate, the experimental data show that for the imposed pressure drop boundary condition the reflux condenser can either operate in total reflux condensation mode or with a continuous upward annular flow. For the imposed constant steam flow boundary condition, the

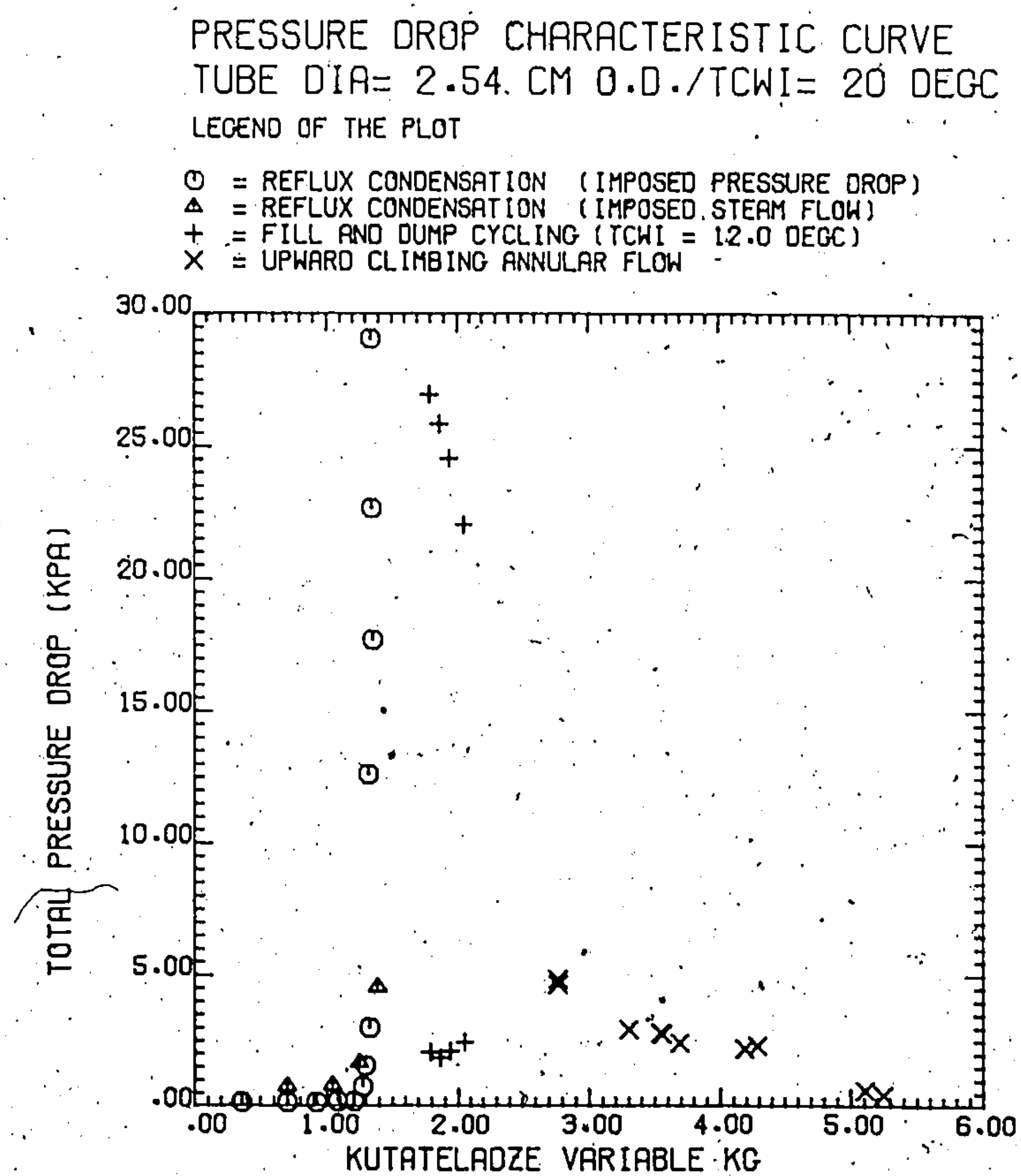

FIGURE 4.21a Pressure Drop Characteristic Curves for 2.54 cm O.D. Tube

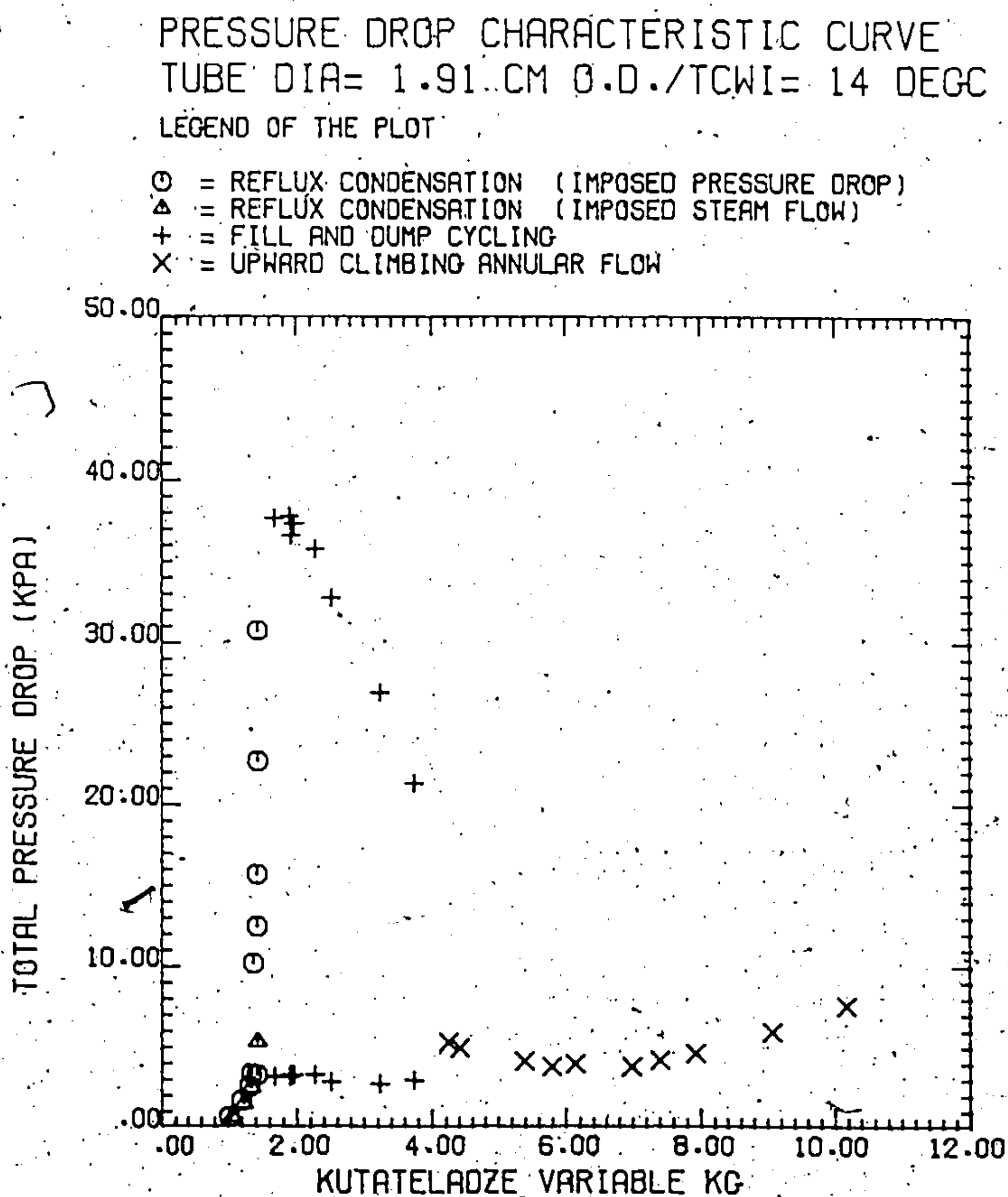

FIGURE 4.21b. Pressure Drop Characteristic Curves for 1.91 cm O.D. Tube

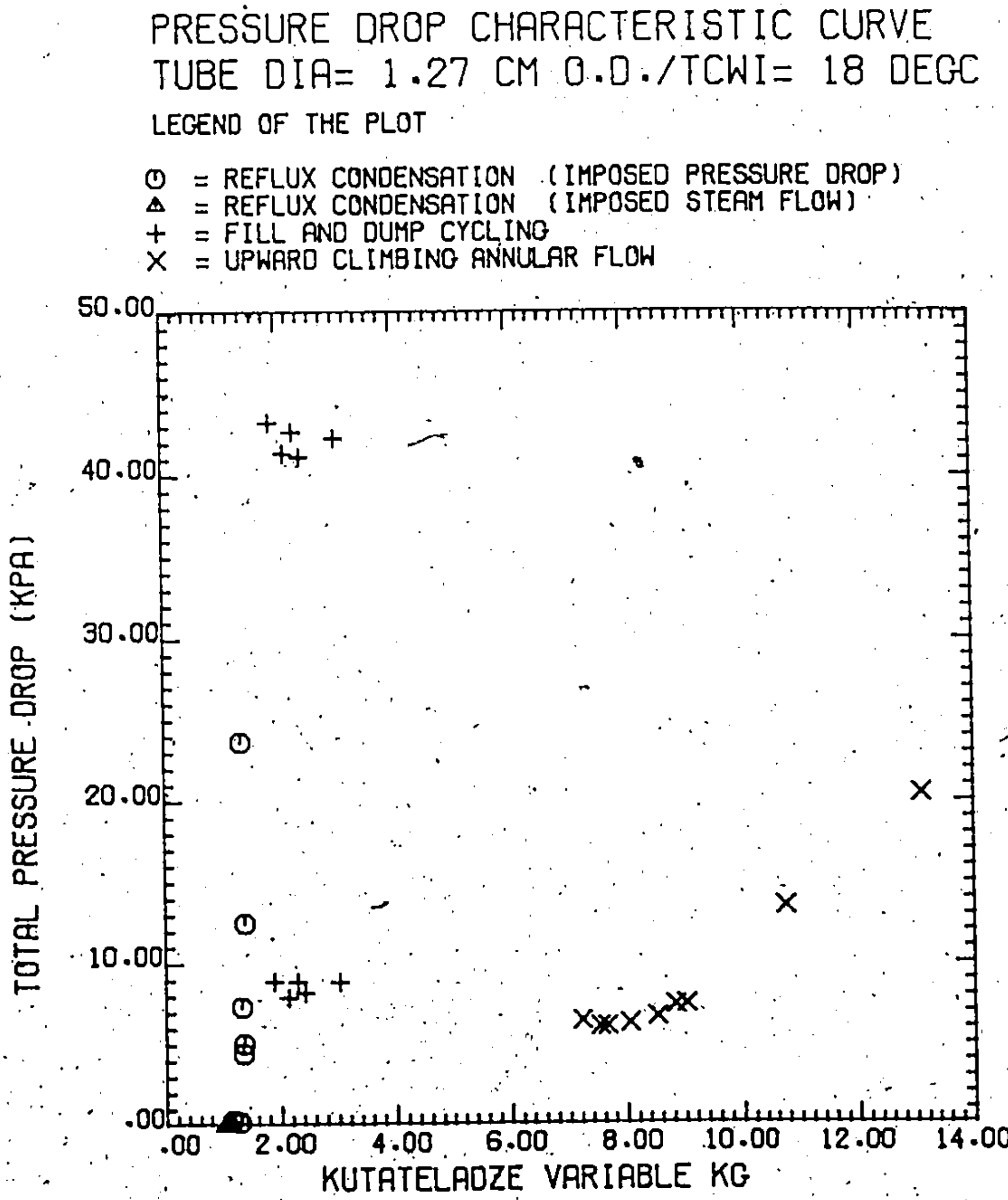

FIGURE 4.21c Pressure Drop Characteristic Curves for 1.27 cm O.D. Tube

reflux condenser can operate in total reflux condensation mode, in fill and dump cycling or with a continuous upward co-current annular flow. It can be seen from the figures that no transition flow regime was observed for the imposed pressure drop boundary condition whereas, for the imposed steam flow rate boundary condition, the fill and dump cycling could be considered as transition flow regime betwen total reflux condensation and upward co-current annular flow. Russell [14] observed a characteristic curve with fill and dump cycling as the flow regime that is similar to the present results; however, no correspondance was made betwen a boundary condition and the observed flow regime as it is done in the present study.

From a reactor safety point of view, the prediction by the present model of the single-phase region lengths, although slightly longer than measured, is acceptable. Because, in the case where the particulars of an accident scenario are such that total reflux condensation is the heat rejection mechanism in the steam generators, the present model would predict that more coolant inventory is trapped in the primary side of the steam generators than there would be actually. This could lead to a conservative accident analysis when compared to the results that could be obtained if the prediction by the model of the single-phase region lengths was more, since the coolant trapped in the steam generators would not be available for core cooling. Moreover, the experimental data in Figures 4.21a,b and c, show the system to be able to condensed more steam when it operates in the fill and dump cycling mode or with a con-tinuous upward co-current annular flow, where in the later case the steam leaving the reflux condenser was condensed by a heat exchanger at its outlet (see Figure 2.3b) and that heat exchanger replaces, to a certain extent, the outlet leg of an actual U-tube. This gives support to the statement that total reflux condensation is the heat rejection mechanism that defines flow regime characteristics to es-timate conservative lower bounds of heat removal capabilities of steam generators in small-break LOCAs analysis.

The condensation of steam implies mainly the transfer of its latent heat to a heat sink, the multiplica-tion of a condensation rate by the latent heat would give a very good estimate of the amount of heat removal by the secondary side of the reflux condenser at that given condi-tion. The good agreement achieved betwen the experimental data and the present model show that heat removal (via the condensation rate) and liquid holdup in the system can be well predicted. Therefore, the present model could be used as a tool in the analysis of a small-break LOCA where, to be conservative, the assumed heat rejection mechanism in the steam generator is total reflux condensation.

CHAPTER 5

CONCLUSIONS AND RECOMMENDATIONS

5.1 Conclusions

Reflux condensation phenomena in vertical tubes were studied for two well defined boundary conditions. Standard methods were used to measure pressures, temperatures and flow rates in the reflux condenser. A ring type capacitance void fraction meter was developed and implemented in the reflux condenser.

A correspondence between an imposed boundary condition and its resulting flow regime has been made where total reflux condensation occurs for an imposed pressure drop across the tube and fill and dump cycling occurs for an imposed steam flow rate at tube inlet. A phenomenological model for total reflux condensation has been derived based on an extended Nusselt's model of film-wise condensation, a linearized stability analysis of the condensate film flow and on the use of three concepts: critical layer, maximum mechanical energy transfer and film instability.

For total reflux condensation, the good prediction of measured rates of condensation by the present model shows that flooding occurs at the tube inlet and plays a key role in defining the maximum heat removal and the distribution of the condensate holdup in the tube. For the present tube entrance conditions, representative of what is found in actual steam generator, the flooding flow rate, in terms of the non-dimensional Kutateladze variable K_g, is not a function of the tube diameter and the system pressure. The inlet cooling water temperature has a notable influence on the definition of the flooding flow rate as for the hottest cooling water, flooding occurs at a lower point than for the coldest cooling water.

The heat removal, in absolute terms, is strongly dependent on the tube diameter and the inlet cooling water temperature. The present model does not take into account the heat losses to the surroundings; consequently, it overpredicts the measured heat removal. However, the general trends in the experimental data is followed as to an increase in tube diameter corresponds an increase in heat removal and to an increase in inlet cooling water temperature corresponds a decrease in heat removal.

The average length of the two-phase region is also a strong function of the tube diameter and the inlet cooling water temperature. The model overpredicts the measured average two-phase region; on the other hand, it follows the general trends in the experimental data as to an increase in tube diameter and inlet cooling water temperature corresponds an increase in the average two-phase region lengths. Entrainment was observed in the form of droplet aggregates pulsating upward towards the end of the two-phase region. For a given imposed pressure drop the lengths of the single-phase and two-phase regions remain, on a time average basis, fairly constant and it is shown that all the steam injected in the system is condensed with all the condensate flowing back to the tube inlet. Then, from the principle of mass conservation no <u>net</u> flow must occur at both ends of the two-phase region. Based, on that statement, it is argued that part of the condensate holdup in the two-phase region could be <u>recirculated</u>. The presence of entrainment, could have a beneficial influence on the effectiveness of the reflux condensation process as it promotes direct contact condensation in the vapor core and reduces the average length necessary for condensation.

In total reflux condensation a significant amount of condensate can be trapped in the tube in the form of a single-phase region. The agreement between the experimental data and the present model is satisfactorily as the model overpredicts slightly the single-phase region length which is conservative from a reactor safety point of view. In regards of the oscillations of the single-phase region, the present study shows that under certain assumptions, valid for the present situation, the whole system can be assimilated to an Helmholtz resonator. The agreement betwen the prediction and the experimental frequencies is shown to be satisfactory and no tube size dependency was noted.

For fill and dump cycling, the experimental data show that the condensate flow is separated in two parts: a reflux flow and a carry-over flow. As the cycle period increases, the reflux rate increases and the carry-over rate decreases, and the amount of total heat removal decreases; thus, the flow split is not always one to one. The variations of the reflux rate and the total heat removal for an increasing cycle period, indicate that fill and dump cycling is more efficient in removing heat than total reflux condensation. For an infinitely long cycle, total reflux condensation appears to define the lower bounds for the values of total heat removal that fill and dump cycling could reached.

The improved understanding developed in the present study of the mechanisms governing heat removal and liquid holdup in total reflux condensation in vertical tubes in reflected in the good agreement between the experimental data and the present model in regard of the condensation rate and liquid holdup. The results of the present work could be used in a small-break LOCA analysis where the present model could estimate the heat removal capabilities (via the condensation rates) and the amount of coolant trapped in the steam generators, if, to be conservative, total reflux condensation is the assumed flow regime on the primary side of the steam generators. The heat removal capability of steam generator defined with total reflux condensation as the flow regime is a lower bound, because it corresponds in some cases to the maximum amount of heat that can be transferred to the secondary side with total reflux condensation as the heat rejection mechanism and it is smaller than what could be achieved with fill and dump cycling and upward co-current annular flow.

5.2 Recommendations

From the results of present study, here are some recommendations on the work that could be undertook:

(i) A similar set of experiments should be done with the inner tube made of metal. This would allow the system to go to higher pressure and it would show the influence of thermal conductivity of the tube wall.

(ii) Reflux condensation should be studied in a metal system at high pressure and temperature, possibly in the range of the postulated conditions in small-break LOCA analyses, where the secondary side would be allow to boil. That system would be fairly different than the present system as the resistance to heat flow would be smaller than the one in the present system.

(iii) The effect of the liquid level on the secondary side with the coolant in single phase and/or in two phase should be investigated as it may have as influence on the global stability of total reflux condensation.

APPENDIX A

DESIGN DETAILS, CALIBRATION AND ERROR ANALYSIS OF STEAM FLOW RATE INSTRUMENTATION

A.1 STEAM ORIFICE METER

A.1.1 Mechanical Design Details

In preliminary reflux condensation experiments [73,74], it was observed that for a 1.94 cm and 2.54 cm O.D. tubes, the rates of condensation were of the order of 70 g/min. and 100 g/min. respectively. It was concluded that the steam flow meter should cover a range of 0 to 150 g/min., then the question was to look for an instrument that will enable us to measure such low steam flow rates accurately at a minimum cost.

We found that an orifice meter installed in a 0.64 cm (1/4") nominal pipe enable us to cover the whole range of flow rates. Orifice meters installed in pipe less than 2.54 cm (1") in nominal diameter have been studied in the past [75-78]. The conclusions in the paper of Marxman and Burlage [75] are particularly interesting for the present case; they are:

(i) that individual calibration of orifice installations in pipes about 2.54 cm (1") in diameter or smaller is essential, unless relatively poor accuracy is acceptable. This requirement arises from the practical difficulties in reproducing exactly small orifices.

(ii) The empirical equation for the expansion coefficient

$$Y_1 = 1 - [0.41 + 0.35\ (A_2 / A_1)^2]\ \ (p_1 - p_2)\ /\ \gamma\ p_1 \qquad (A.1)$$

where

p_1 : pressure upstream of the orifice plate (N/m^2)
p_2 : pressure downstream of the orifice plate (N/m^2)
γ : ratio of the specific heat for the steam
A_1 : cross-sectional area of the pipe (m^2)
A_2 : cross-sectional area of the orifice (m^2)

as published in the ASME Fluid Meters Report [79], can be used for calculating expansion coefficients for almost any orifice-metering applications ordinarily encountered.

Then, our problem was to calibrate the orifice meter for each orifice plate and to check if actually if equation (A.1) could be used to calculate the expansion coefficient . We can verify this by doing the comparison between the steam orifice meter reading and the measured value of the steam flow.

A.1.2 Method of Calibration

In the general case, an orifice meter gives the mass flow rate according to the following equation [80, p.220].

$$\dot{m}_{act} = Y_1 \; A_2 \; K \; [2\rho \; (p_1 - p_2)]^{1/2} \tag{A.2}$$

where

m_{act} : is the actual mass flow rate (kg/s)

Y_1 : the expansion coefficient

K : the flow coefficient = CM

C : discharge coefficient

M : velocity of approach factor = $[1 - (A_2/A_1)^2]^{-1/2}$

ρ : density of the fluid evaluated at the upstream condition (kg/m^3)

In Figure A.1, we show a sketch of the arrangement used in our orifice meter. The inner diameter of the pipe is D = 0.925 cm and the dimensions of the three orifice plates used in the experiment are given in Table A.1. The thickness of the orifice plates is 1.59 mm. As recommended [80] the pressure tap connections are as shown in Figure A.1: at one diameter upstream and half a diameter downstream of the orifice plate.

It is well known that the flow coefficient is a function of the Reynolds number Re and the geometry of the orifice meter arrangement. Since it does not depend on the fluid being metered, we have simply to find a function that relates to Re for each orifice plate.

A series of tests was conducted using tap water as the fluid. The tap water pressure was around 4 bars (g) and at a temperature less than 20^{o}C; these conditions make the assumption of considering the tap water as an incompressible fluid realistic. During a typical run, the water was collected for a certain time giving the mass flow rate. The pressure drop across the orifice plate was recorded and averaged by a NOVA III mini-computer. Then, equation (A.2) for the incompressible flow case can be solved for the flow coefficient, because all the other variables are either defined or measured. This procedure was repeated for a range

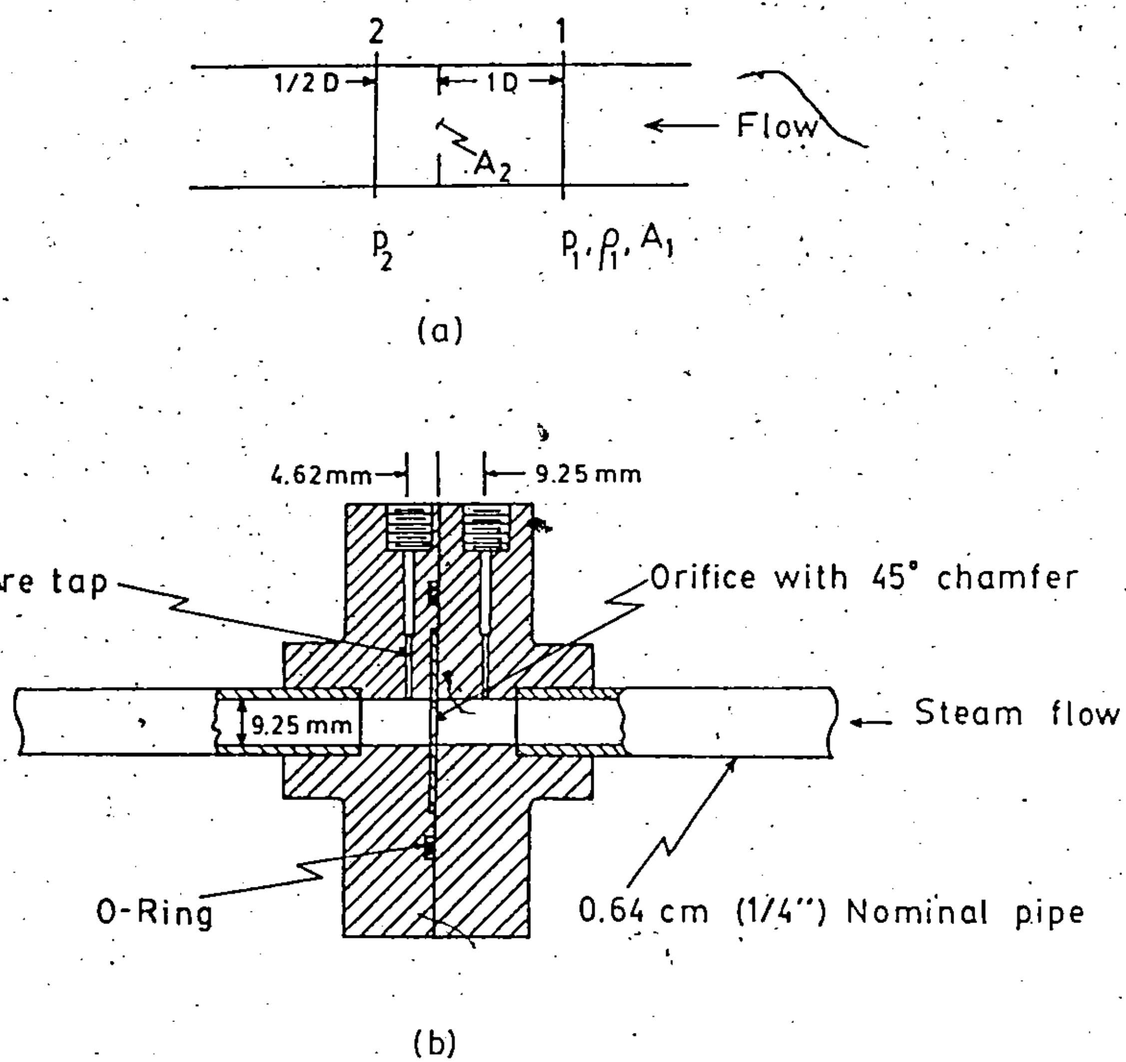

FIGURE A-1 Schematic of the Steam Orifice Meter Arrangement of mass flow rates and for the three orifice plates. The results are shown in Figure A.2a,b,c. A least square fit was done for each data set and the coefficents are given in Table A.2.

A.1.3 Error Analysis

The error analysis on the data for the determination of the function K=K(Re), consists of looking at the propagation of errors on looking at the propagation of errors on the the independent variables into the error on the dependent variable. Using equation (A.2) for the case of an incompressible fluid, we have:

$$K = \frac{\dot{m}_{act}}{A_2 \, [2 \rho \, (p_1 - p_2)]^{1/2}} \qquad (A.3)$$

where K is the dependent variable. As shown in Bevington [69, p.56-60] error propagation for the total error in K can be written as:

$$\sigma_K^2 = K^2 \left[\frac{\sigma^2_{\dot{m}_{act}}}{\dot{m}^2_{act}} + \frac{\sigma^2_{A_2}}{A_2^2} + \frac{\sigma^2_{\Delta p}}{4 \Delta p^2} \right] \qquad (A.4)$$

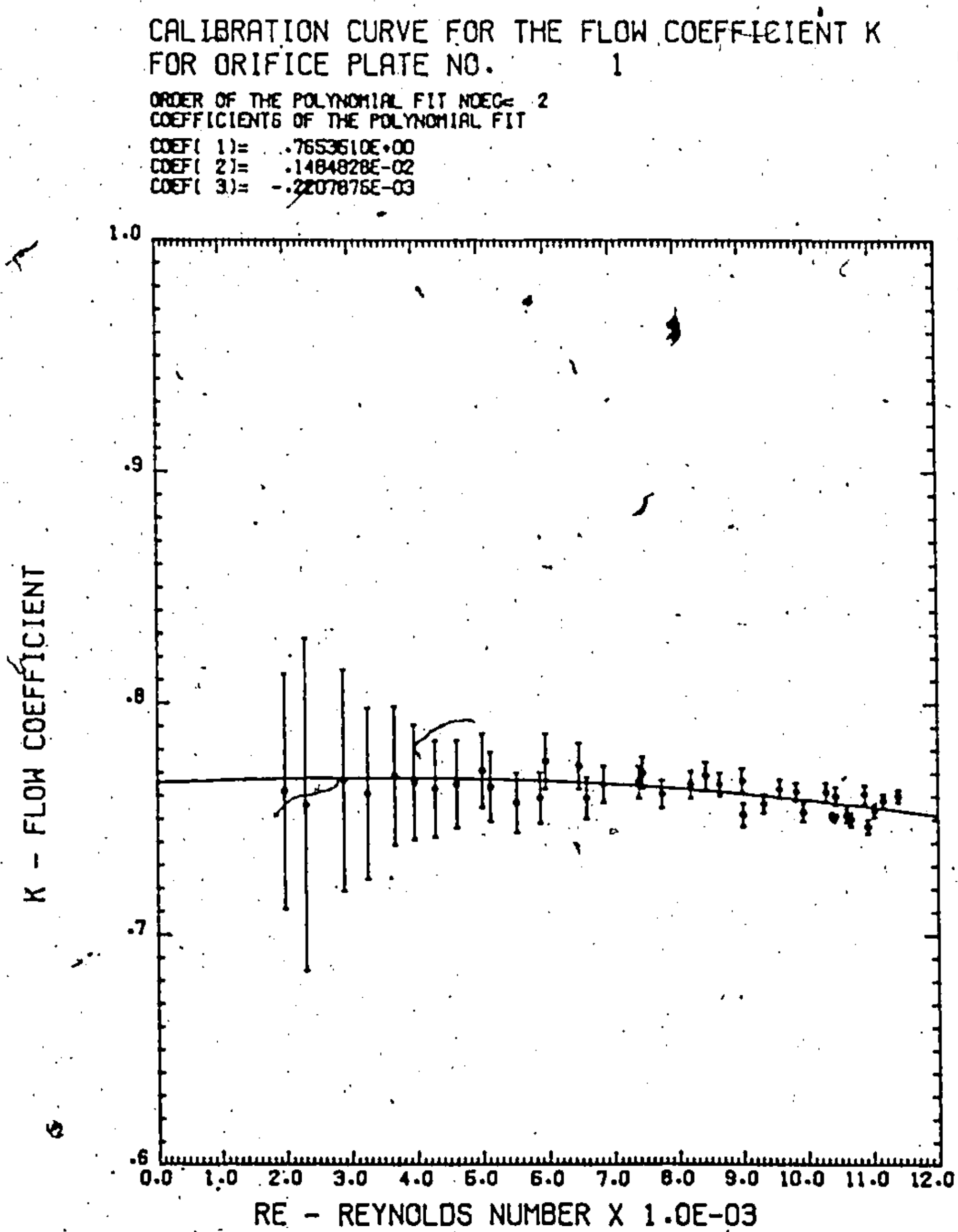

FIGURE A-2a Calibration Curve for the Flow Coefficient K for Orifice Plate No. 1

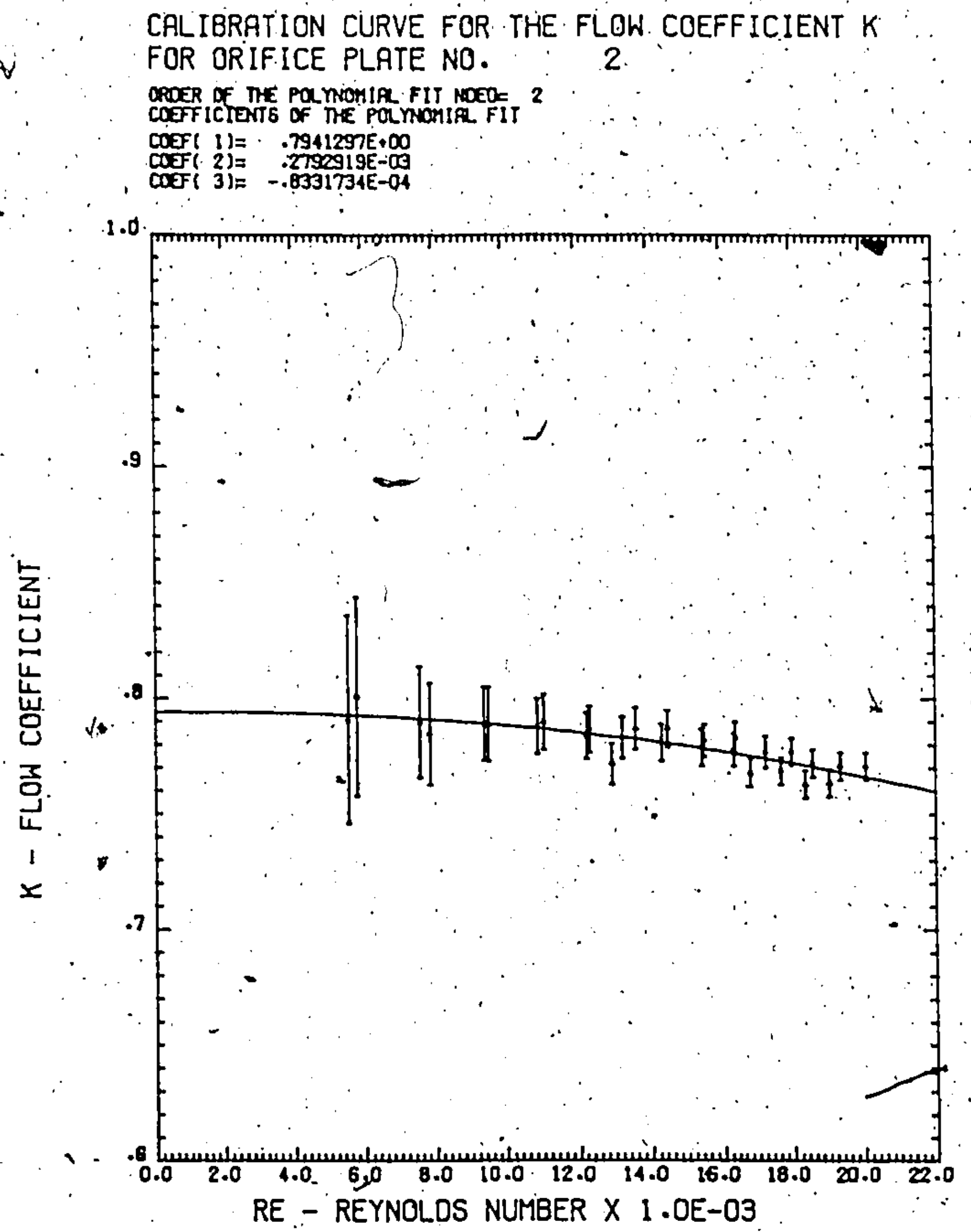

FIGURE A-2b Calibration Curve for the Flow Coefficient K for Orifice Plate No. 2

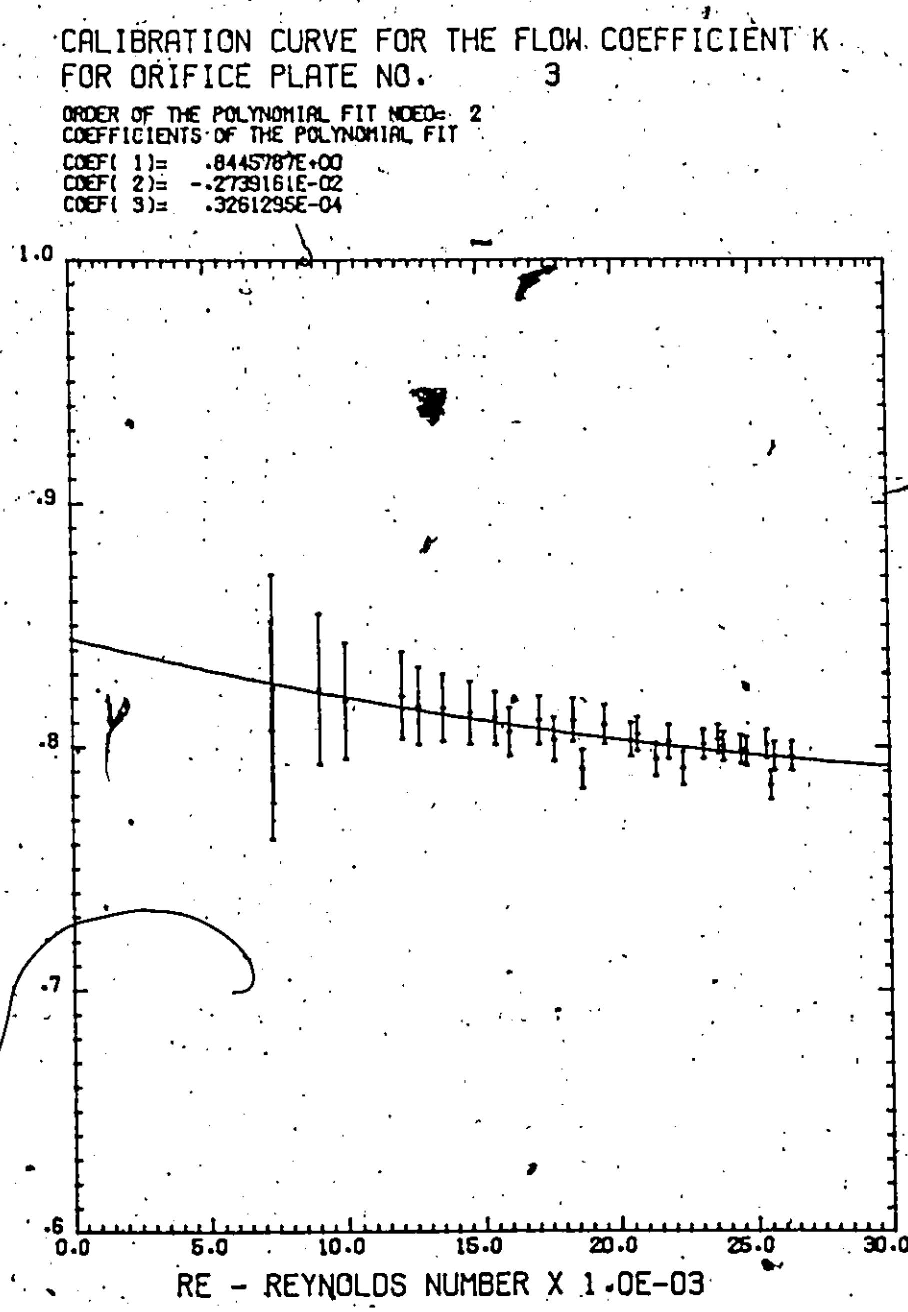

FIGURE A-2c Calibration Curve for the Flow Coefficient K for Orifice Plate No. 3

where

σ_i: is the standard deviation on variable "i",

i: $k, \dot{m}_{act}$, A_2 and Δp

and $\Delta p = p_1 - p_2$

It should be noted that if we cannot calculate a standard deviation on an independent variable, for example "A_2", we simply take the maximum error made in the measurement as the standard deviation. This can be justified by the following considerations: if the independent variable is assumed to be distributed like a Gaussian then the maximum error corresponds to at least two standard deviations from the mean; however, if the standard deviation is taken to be the maximum error, then the total extent of the distribution will be larger. This will correspond to an overestimated uncertainty in the value of the variable; but we can consider that we are conservative in our evaluation of the standard deviation.

A.1.3.1 Error Estimate in the Pressure Difference Measurement

The standard deviation in the pressure difference Δp is given by the following error propagation equation:

$$\sigma_{\Delta p} = \left(\sigma_{f_1}^2 + \sigma_{p_2}^2 + \sigma_{\Delta p,f}^2\right)^{1/2} \tag{A.5}$$

We assume here that $\sigma_{p1} = \sigma_{p2}$ because of the similarity in the tap hole. The error in the measurement of the pressure p_1 and p_2 comes from the accuracy of the pressure transducer (1/2% full scale) and the size of the tap hole. The range of the diaphragm (0-35 kPa) gives an accuracy of ±175 N/m^2. Benedict [56, p.346-348] gives a method to estimate the pressure tap error, for our case the maximum error made is ±8.51 N/m^2. The pressure difference signal was taken by computer, a sufficient number of points (1000) were taken to minimize $\sigma_{\Delta p,f}$, the standard deviation on the mean due to the fluctuations, the maximum standard deviation observed was less that ±60 N/m^2. Then we have that $\sigma_{\Delta p}$ = ±266 N/m^2.

A.1.3.2 Error Estimate in the Orifice Area

We have that:

$$\frac{\sigma_{A_2}^2}{A_2^2} = \frac{\sigma_{D_2}^2}{D_2^2} \tag{A.6}$$

which can be evaluated for each orifice plate, the error (standard deviation) taken for the orifice diameter is 2.54 x 10^{-5}m.

A.1.3.3 Error Estimate in the Mass Flow Rate Measurement

The mass flow rate was determined by collecting the water for a period of time, the error made was dependent on the amount collected. The maximum error observed was less than 3.2%.

A.1.3.4 Error Estimate in the Flow Coefficient

The error in each flow coefficient K was evaluated using equation (A.4), as shown in Figures A.2a, b, and c. The standard deviation of the fit, which is related to the spread of the data, can be estimated from the following equation from Bevington [69, p.187].

$$s^2 = \frac{1}{(N - n - 1)} \frac{\sum_i \frac{1}{\sigma_i^2} [y_i - y(x_i)]^2}{\frac{1}{N} \sum_i \frac{1}{\sigma_i^2}} \tag{A.7}$$

where

s : standard deviation of the data

N : number of points

n : order of the polynomial fit $y(x_i)$ (here, n = 2)

x_i : independent variable (here, x_i = Reynolds number)

y_i : dependent variable (here, y_i = flow coefficient)

σ_i : standard deviation (error) in y_i

Each polynomial fits the data to the standard deviation given in the last column of Table A.2.

A.1.4 Test and Final Design

As mentioned before the central problem in the present design lies in the validity of the empirical equation for the expansion coefficient Y_1, Equation (A.1), for the present orifice meter. To check the validity of the expression for Y_1, a series of experiments were conducted for various conditions. Also, these experiments gave an operating experience that was necessary to finalize the design.

The set-up used in the test consists simply in the orifice meter connected to a small heat exchanger, as shown in Figure A.3. In a typical test the steam is injected in the orifice meter and it is condensed in the heat exchanger. The condensate is collected for a certain period of time to

TABLE A.1: DIMENSIONS OF ORIFICES

ORIFICE PLATE NUMBER	ORIFICE DIAMETER (cm)
1	0.422
2	0.561
3	0.635

TABLE A.2: COEFFICIENTS OF THE LEAST SQUARE FITS

	$K = a_o + a_1x + a_2x^2$			
PLATE NO.	a_o	a_1	a_2	s
1	0.7653510E+00	0.1484828E-02	- 0.2207875E-03	0.177591E-03
2	0.7941297E+00	0.2792912E-03	- 0.8331734E-04	0.209259E-03
3	0.8445787E+00	- 0.2739161E-02	0.3261295E-04	0.270623E-03

where $x = \frac{Re}{1000}$

s : standard deviation of the fit (see Equation A.7)

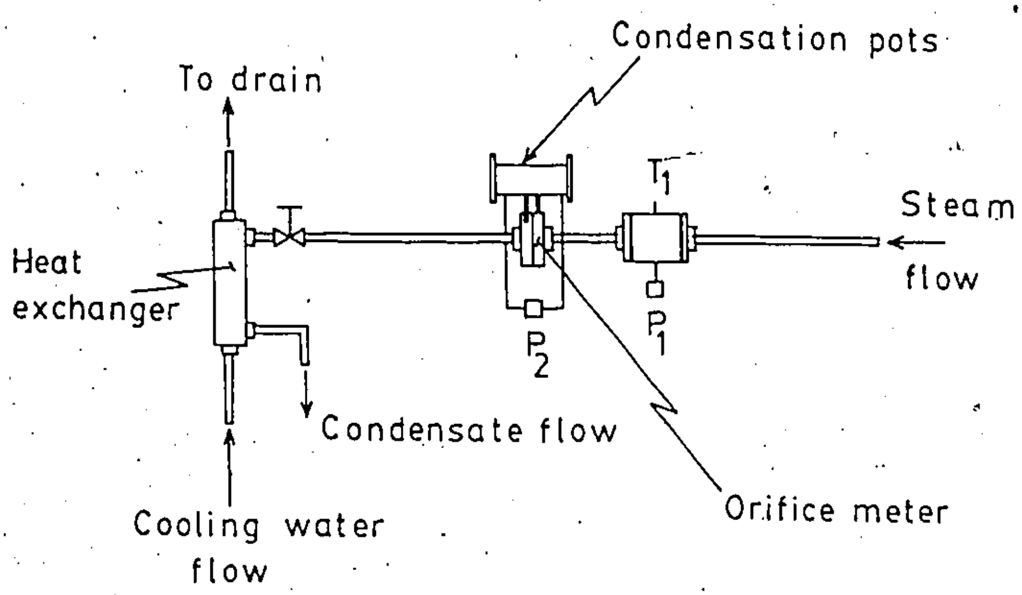

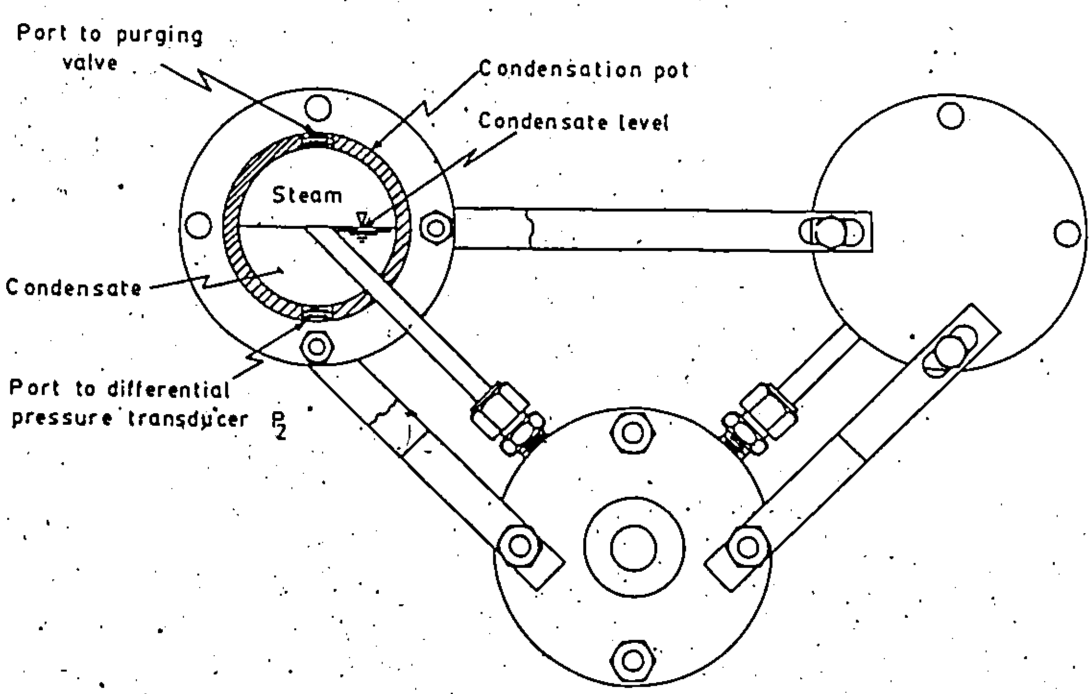

FIGURE A-3 Physical Arrangement of the Steam Orifice Meter for the Experimental Test give the measured steam flow rate: besides, the thermodynamic conditions and the pressure drop across the orifice are measured and processed by the NOVAC III computer.

A.1.4.1 Operating Experience

In operating the set-up, drifts and oscillations were observed in the measured pressure drop across the orifice. This phenomenon is due to the condensation of steam at the pressure taps. To eliminate the drifts and reduce the oscillations as much as possible, condensation pots were installed in the way indicated in Figure A.3 as suggested by Masek [81]. This final design results in no sensible drift and much reduced oscillations, as shown in Figure A.4. The validity of the use of the expression for Y_1, was studied with this final design.

A.1.4.2 Experimental Tests

The experimental tests were conducted with orifice plate no. 2, as it appears at that time to be the one that will be used the most in the experimental program on reflux condensation. The flow range covered was from 55 g/min. to 145 g/min. for various thermodynamic conditions defined in the following classes:

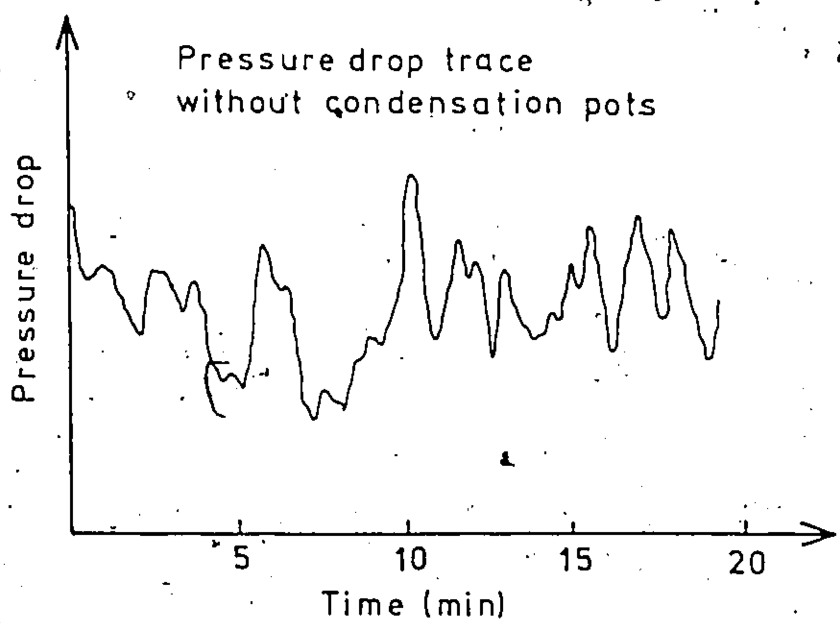

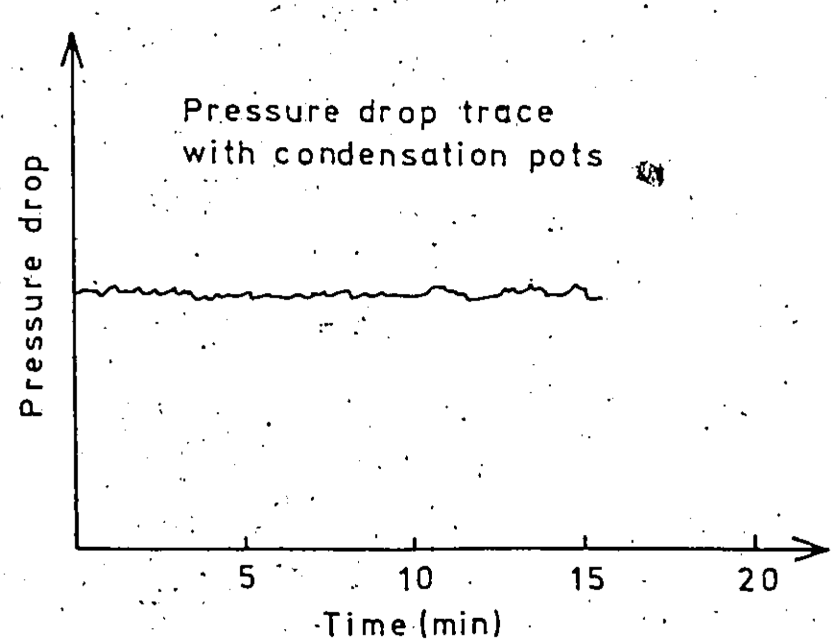

FIGURE A-4 Effect of the Use of Condensation Pots

(i) reading from pressure transducer P1 less than 20 kPa(g) (corresponding to a reading from thermocouple T1 less than 104^{o}C) but most of the readings are between 10 kPa(g) and 15 kPa(g);

(ii) reading from pressure transducer P1 between 20 kPa(g) and 60 kPa(g) (equivalent to a reading from thermocouple T1 between 104^{o}C and 111^{o}C) but most of the readings are between 30 kPa(g) and 45 kPa(g);

(iii) reading from pressure transducer P1 greater than 60 kPa(g) (corresponding to a reading from thermocouple T1 greater than 111^{o}C) but most of the readings are between 70 kPa(g) and 75 kPa(g). The maximum pressure condition was 76.25 kPa(g).

A total of 55 run were conducted, each taking about 15 minutes. Before every series of tests the system was properly warmed up by running it for an 1 1/2 hour. During a typical run, 500 points of digitalized output voltages from pressure transducers P1 and P2 and from thermocouple T1 are recorded every one or two minuted enough times to cover the 14 minutes time of the run. The averages and the standard deviations of the data are computed and recorded for further usage. At the same time the condensate dripping out of the heat exchanger is collected for a certain time giving the measured steam mass flow rate.

The calculated steam mass flow rate is obtained by solving Equation (A.2) by iteration, K being a function of Reynold number. Two calculations are performed one is based on the pressure measured by P1 being considered to be at saturation and the other basec on the temperature measured by T1 being considered to be at saturation. The thermal-hydraulic parameters are evaluated using "POLSAW" a package of subprograms based on the canonical functions of the 1967 ASME Steam Tables [82], to obtain a high accuracy values. This subprogram package is attached to a main program ORICAL1 that performs the solution of Equation (A.2) using Equation (A.1) to evaluation Y_1, where the measured pressure drop is used for the value of "(p_1-p_2)".

The results of the calculations are shown in Figure A.5. For the "pressure based" calculations (Figure A.5a) a fairly good agreement between the measured and calculated is shown as most of the data points have a deviation less than 5%, in fact the actual average deviation is 3.69%. However, the comparison line on the gaph (the middle line) is not the best fit through the data points;

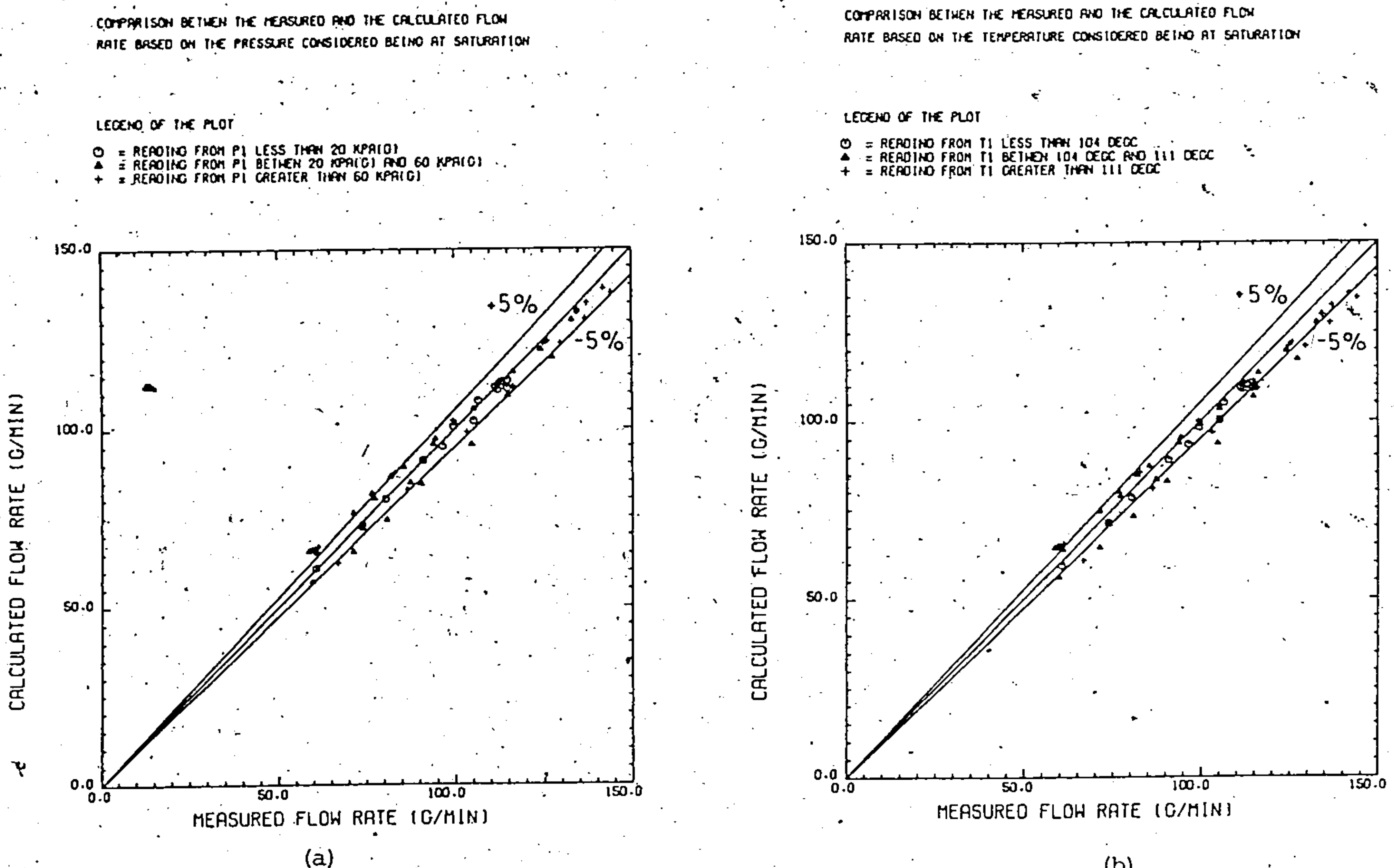

FIGURE A-5 Comparison Between the Measured and Calculated Flow Rates for the Steam Orifice Meter With Plate No. 2

nevertheless, the standard deviation of the data based on that line is equal to 3.97 g/min. It indicated that the spread of the data around this comparison line is small and the deviation from measured values could be for flows around 55 g/min. (lower and of the experimental test range) about 7.2% and for flow around 145 g/min. (upper end of the experimental test range) about 2.7%, giving an average deviation of 4.95%.

For the "temperature based" calculations (Figure A.5b), the agreement is good, but the average deviation of 4.57% and the standard deviation of 5.15 g/min. indicate a greater spread of the data around the comparison line than in the case of the "pressure based" calculations.

From the above considerations, two main conclusions arise:

(i) the empirical equation (A.1) for the evaluation of the expansion coefficient Y_1 is adequate for all present practical purposes as a good agreement between the calculated and the measured steam flow rates is obtained;

(ii) the combined usage of Equation (A.1) for Y_1 and the calibration curve for K in the solution of

Equation (A.2) for the calculated value of the steam mass flow, leads to an average deviation from the measured value of less than ±5%. This is taken as being the maximum of the inaccuracy of the steam mass flow rates calculated from the readings from P1, P2 and T1 in the reflux condensation experiments.

In the case of the other orifice plates, the adequacy of the expression for Y_1 (Equation A.1) will be checked by comparing the steam mass flow rate measured by the orifice meter to the rate of condensation measured by bottom plenum condensate level meter, where in reflux condensation experiments they should be equal to each other.

A.2. BOTTOM PLENUM LEVEL MEASUREMENT

The level of the condensate in the bottom plenum is measured by the use of a reluctance differential pressure transducer, as shown in Figure A.6. The calibration of the level meter was done at atmospheric pressure with 20°C tap water ($\rho_1 = 998.3$ kg/m^3) by using one of two following static methods: record the pressure transducer output (volt) for the mass of water either added, when the initial level is just above the level of the lower threaded bosses,

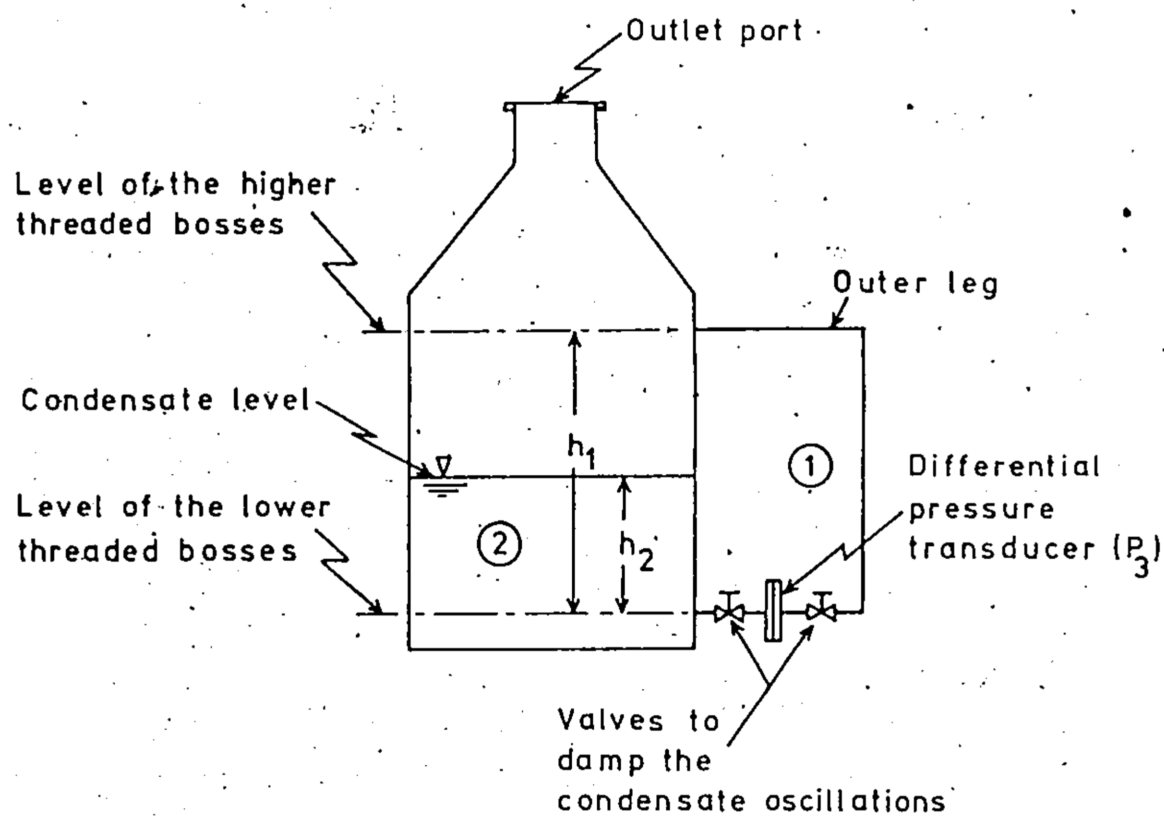

FIGURE A-6 Schematic of the Arrangement of the Bottom Plénum Condensate Level Meter or removed, when the initial level is just below the level of the higher threaded bosses. The later method was found more practical than the first, especially when the reflux condenser is installed at the outlet port of the plenum, and thus adopted in doing the calibration. The calibration curve used in all the experiments in shown in Figure A.7.

The pressure transducer must be protected from the heat of the condensate and the steam in the plenum, this consideration leads to the fact that the liquid in the outer leg of the level meter will be at room temperature (20°C) but the condensate inside the plenum is at a near saturation temperature, then it has a different density. Thus a correction must be applied to the condensation rate derived from the readings of the level meter.

For an actual experimental condition, the correction that can be applied is derived as follow:

(i) for the situation in Figure A.6, the actual differential pressure measured by the transducer is given for any time by:

$$\Delta p = (\rho_1 - \rho_2)\, g h_1 + \rho_2 g\, \Delta h \qquad (A.8)$$

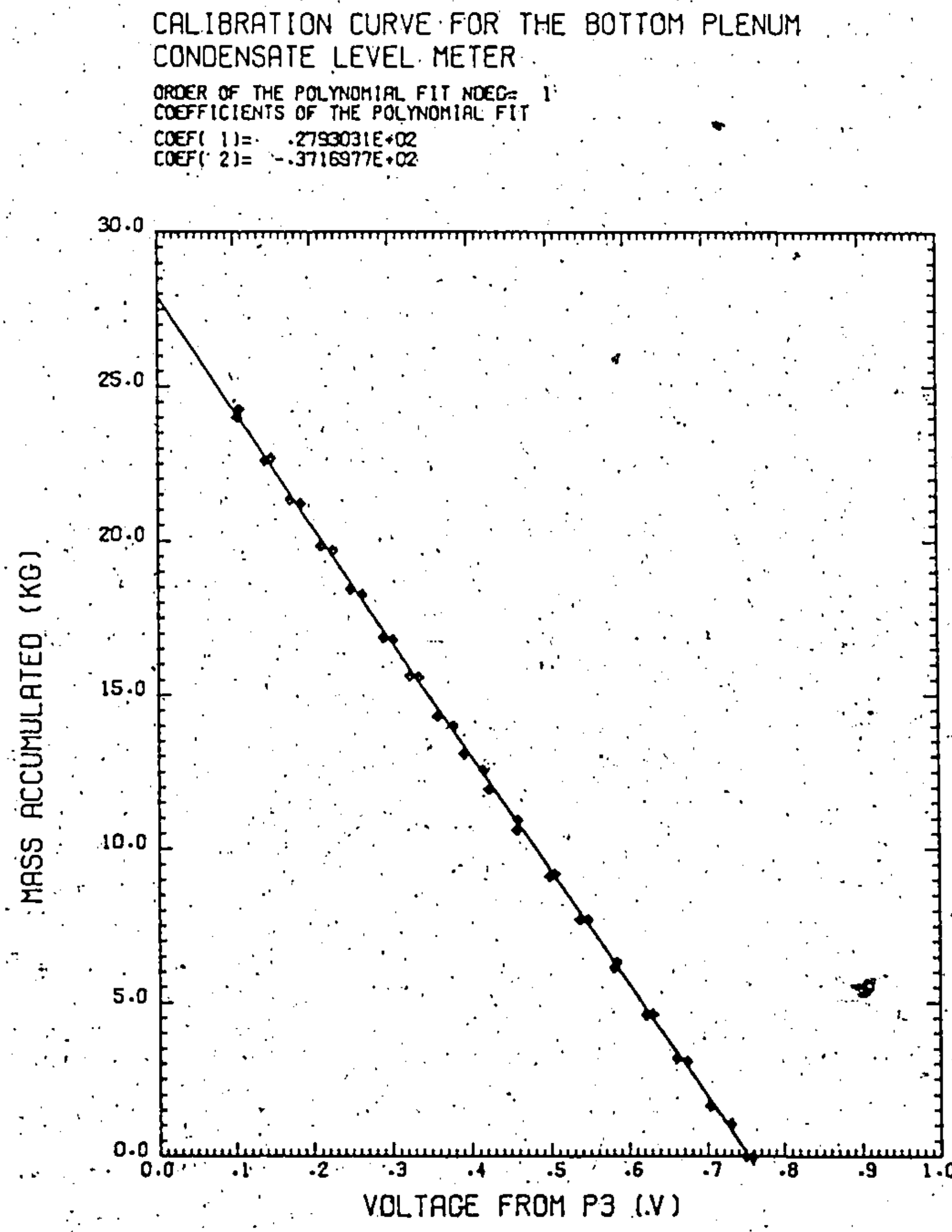

FIGURE A-7 Calibration Curve for the Bottom Plenum Condensate Level Meter (Mass Accumulated vs Output Voltage from P3)

where

Δp : actual differential pressure (N/m^2)

h_1 : distance between the threaded bosses (m)

h_2 : height of the condensate level in the plenum (m)

ρ_1 : density of water at atmospheric pressure and room temperature (20^oC) (kg/m^3)

ρ_2 : density of the condensate in the plenum (kg/m^3)

g : gravitational constant ($9.81\ m/s^2$)

Δh : $h_1 - h_2$ (m)

(ii) during an experiment the condensate accumulates in the plenum, thus for two different times $t_a < t_b$ we can write:

at $t = t_a$

$$\Delta p_a = (\rho_1 - \rho_2)\ gh_1 + \rho_2 g\ \Delta h_a \tag{A.9}$$

and at $t = t_b$

$$\Delta p_b = (\rho_1 - \rho_2)\ gh_1 + \rho_2 g\ \Delta h_b \tag{A.10}$$

the linear response of the pressure transducer enable us to put Equations (A.9) and (A.10) in the following form:

$$V_a = \frac{1}{K_1} (\rho_1 - \rho_2) \quad gh_1 + \frac{\rho_2 g}{K_1} \Delta h_a \tag{A.11}$$

$$V_b = \frac{1}{K_1} (\rho_1 - \rho_2) \, gh_1 + \frac{\rho_2 g}{K_1} \Delta h_b \tag{A.12}$$

where

V_a, V_b : DC output voltage from the pressure transducer (volt)

K_1: proportionality constant ($\Delta p = K_1 V$)

(iii) the calibration curve is a first order polynomial:

$$m = a_0 + a_1 V \tag{A.13}$$

where

m : mass accumulated (kg)

a_o, a_1: coefficients of the calibration curve

Using Equation (A.13), Equations (A.11) and (A.12) can be written as:

$$m_a = a_0 + \frac{a_1}{K_1} (\rho_1 - \rho_2)\, gh_1 + \frac{a_1}{K_1} \rho_2 g\, \Delta h_a \qquad (A.14)$$

$$m_b = a_0 + \frac{a_1}{K_1} (\rho_1 - \rho_2)\, gh_1 + \frac{a_1}{K_1} \rho_2 g\, \Delta h_b \qquad (A.15)$$

(iv) the actual rate of condensation is given by:

$$\dot{m}_2 = \frac{(m_b - m_a)}{(t_b - t_a)} = \frac{1}{(t_b - t_a)} \frac{a_1}{K_1} \rho_2\, g\, [\Delta h_b - \Delta h_a] \qquad (A.16)$$

in the case where $\rho_2 = \rho_1$, i.e. same conditions on each side of the pressure transducer, Equation (A.16) becomes:

$$\dot{m}_\ell = \frac{1}{(t_b - t_a)} \frac{a_1}{K_1} \rho_\ell g \, [\Delta h_b - \Delta h_a] \qquad (A.17)$$

Dividing Equation (A.16) by (A.17) we have

$$\dot{m}_2 = \frac{\rho_2}{\rho_\ell} \dot{m}_\ell \qquad (A.18)$$

(v) the direct use of the output voltage of pressure transducer in Equation (A.13) implies the assumption that the conditions are the same on each side i.e. $\rho_2 = \rho_1$; however, this introduce an error that can be corrected by using Equation (A.18).

Another source of error is the oscillations of the condensate level, that have been damped by putting a valve in each leg of the level meter.

In general, the level meter was not chosen as a basis to measure the condensation rate in most cases, because of the uncertainty in the correction equation (Equation A.18) and the oscillations of the condensate level even though the condensation rate from the level meter is often quite close of the one given by the steam orifice meter. In conclusion, these are the two reasons for the use of the level meter as a mean of comparison.

A piece of information that could prove to be very useful in the mathematical modeling of the system is the volume occupied by the steam. The total volume of the plenum including the inlet port is 54.4 liters and the instantaneous volume occupied by the steam is given by:

$$V_s(t) = V_{tot} - M_c(t)/\rho_\ell \tag{A.19}$$

where

$V_s(t)$: volume occupied by the steam at time "t" (m^3)

V_{tot} : total volume of the plenum ($54.4 \times 10^{-3}\ m^3$)

$M_c(t)$: mass accumulated at time "t" (kg)

ρ_ℓ : density of the condensate evaluated at the thermodynamic state given by the readings of T2 and P4 (kg/m^3)

APPENDIX B

CALIBRATION OF THE COOLING WATER ORIFICE METERS

In this appendix we give briefly the mechanical design details, the method of calibration and the error analysis for the cooling water orifice meter and its relation to errors in heat balances.

B.1 MECHANICAL DESIGN DETAILS

The physical arrangement of the cooling water orifice meters is basically the same one used for the steam orifice meter, but some changes have been made as illustrated in Figure B-1.

The pressure taps are 1 D upstream and 1/2 D downstream of the orifice plate, the sharp edge orifice has also a chamfer of 45^{o}. The inner inner diameter of the pipe is 1.27 cm, the diameter of the orifice is 2.26 mm and the thickness of the orifice plate is 3.175 mm.

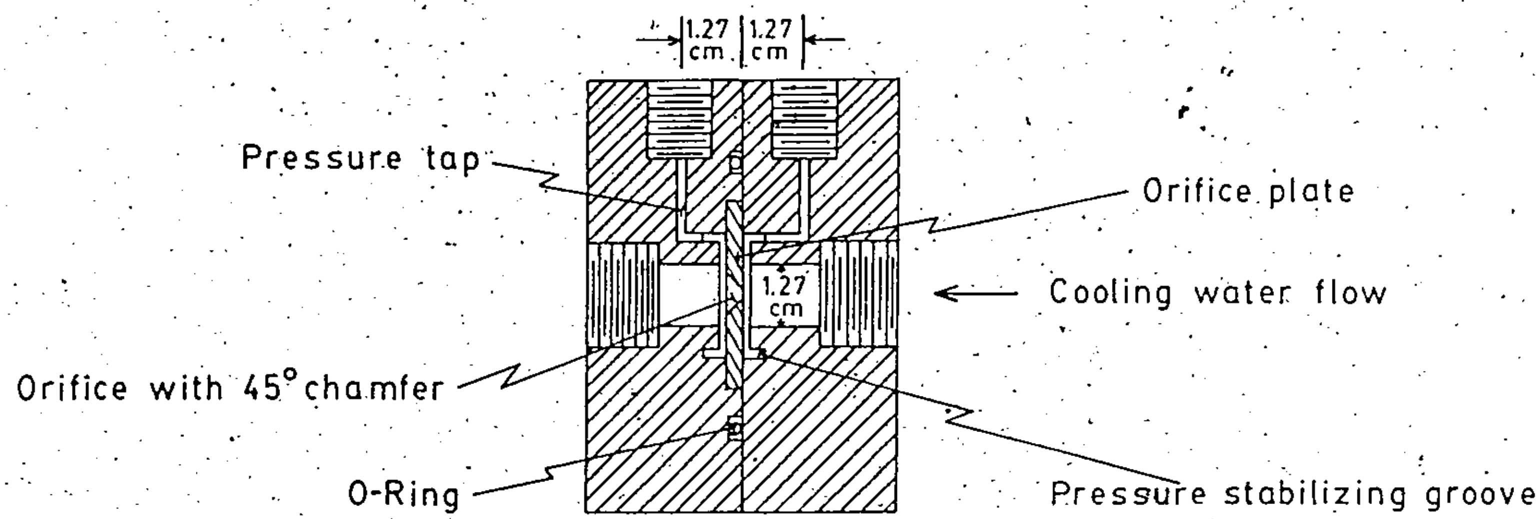

FIGURE B-1 Schematic of the Cooling Water Orifice Meter Arrangement

The pressure drop across the orifice plate is measured by a U-tube manometer with Meriam Blue Fluid as the differential pressure indication. The Meriam Blue Fluid has a specific gravity of 1.75 at 12.8°C compared with water at 4°C and it is not missible with the water filling up the rest of the manometer branches and the tubing connecting the manometer to the flange pressure taps. At a certain flow rate, the pressure drop across the orifice plate can be expressed as:

$$\Delta p = g \; \Delta h \; \rho_\ell \; (S.G. - 1) \tag{B.1}$$

where

Δp : pressure drop across the orifice plate (N/m^2)
g : constant of gravity ($9.81 \; m/s^2$)
Δh : difference of the Meriam Blue Fluid levels (m)
S.G. : specific gravity of the Meriam Blue Fluid (1.75)
ρ_ℓ : density of water ($998.3 \; kg/m^3$)

The Meriam Blue Fluid has been chosen as a manometer fluid because it gives a sufficient sensitivity; indeed, we have for $h = 1$ m, corresponding to a defined maximum flow rate, a pressure drop of $7.34 \; kN/m^2$, which is quite reasonable [83].

B.2 METHOD OF CALIBRATION

All the orifice meter were calibrated in-situ by a series of tests using tap water at 4.13 bars(g) and at a temperature less than 15 ^{o}C; these conditions make the assumption of considering the tap water as an incompressible fluid realistic. The fluctuations of the pressure in the domestic water line induce some fluctuations of the differential pressure indicated by the manometer. To determine an average pressure drop with a known error the minimum and maximum levels in each branches of the U-tube manometer have to be measured. During a typical run, the water was collected for a certain time giving the mass flow rate and the minimum and maximum levels in each manometer branch were observed for a minimum of 2 minutes and recorded.

B.3 ERROR ANALYSIS.

The results of the calibration tests give eight sets of data with both variables having uncertainties. The standard multiple linear regression analysis cannot be applied alone to these sets of data; instead, it must be applied along with the effective variance method [63], where, as mentioned in the main text, a fourth order polynomial is used to correlate the pressure drop across the orifice and the mass flow rate. A FORTRAN V program called EVMFIT(*) was developed to perform the analysis on the calibration data. The flow chart of the program is shown in Figure B-2 and the listing can be found in [72]. The results are shown in Figure B-3a to B-3h, inclusively and Table B-1 gives the standard deviation of each fit, calculated using equation (A-7) from Appendix A.

The fourth order polynomial fit was not used to do the error analysis, in fact it is only a convenient way for data reduction, it avoids the iteration process in the solution of the standard flow meter equation (Equation A-2, Appendix A); which is necessary when the values of the thermal- hydraulic properties change form one experiments to another. In the present case, the inlet cooling water temperature varies from $10^{\circ}C$ to $45^{\circ}C$ (p = 4 bars), this implies a maximum variations in the density of 1.1% and in the mass flow rate of 0.6% (the mass flow rate being proportional to the square root of the density), these variations are small enough to be neglected.

The standard flow meter equation was used, along

(*) EVMFIT: Effective Variance Method FIT with the propagation of error formula [3, p.59], to perform the error analysis. The procedure is as follow:

(i) for each flow meter, the calibration data is reduced to correlate the flow coefficient K as a function of the Reynolds number, using Equation (A-2). The standard deviation of the fit is used as an estimate of the error in the flow coefficient;

(ii) the error in the flow measurement is computed by using the following propagation of error equation:

$$\frac{\sigma_{\dot{m}}^2}{\dot{m}^2} = \frac{\sigma_K^2}{K^2} + \frac{\sigma_{\Delta p}^2}{4\ \Delta p^2} \qquad (B.2)$$

The results of this procedure maximum error that can be expected in metering the cooling water flow for each orifice meter is given in Table B-2. It can be seen that the maximum error made in using these orifice meter will be less than 2%, even when the temperature effect on the density is included.

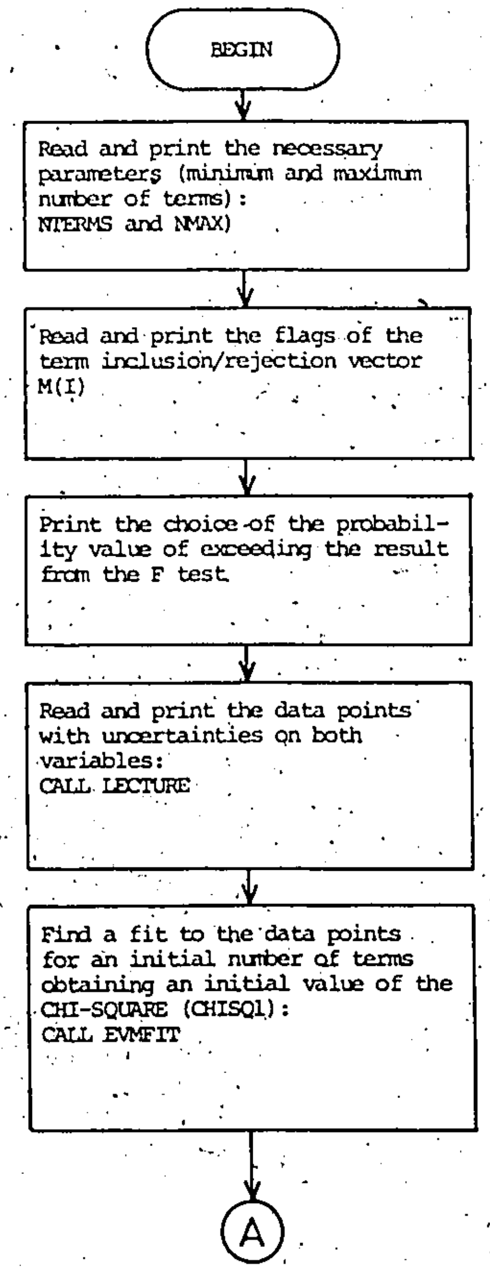

FIGURE B.2 Flow Chart of Program EVMFIT

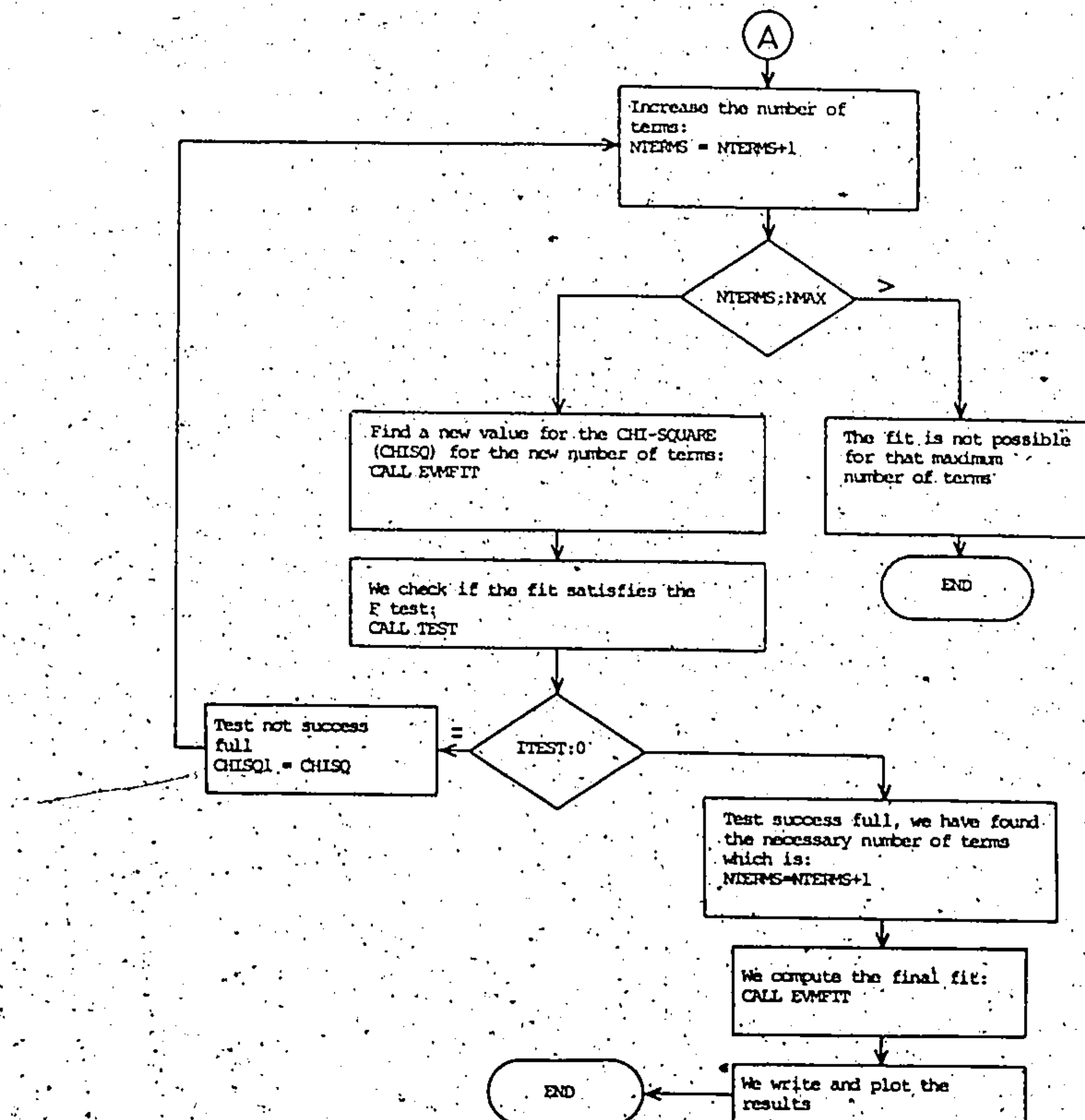

FIGURE B.2 (continued)

```
CALIBRATION CURVE FOR THE COOLING WATER
ORIFICE METER NO. 1

NUMBER OF TERMS IN THE FIT NTERMS=  4
COEFFICIENTS OF THE STANDARD POLYNOMIAL FIT
COEF( 0)=   .1443574E+01
COEF( 1)=   .2611468E+02
COEF( 2)=  -.4654773E+02
COEF( 3)=   .5356338E+02
COEF( 4)=  -.2353918E+02
FLAG IN THE TERM INCLUSION/REJECTION VECTOR M
M( 1)= 1  M( 2)= 1  M( 3)= 1  M( 4)= 1  M( 5)= 1
M( 6)= 1  M( 7)= 1  M( 8)= 1  M( 9)= 1  M(10)= 1
```

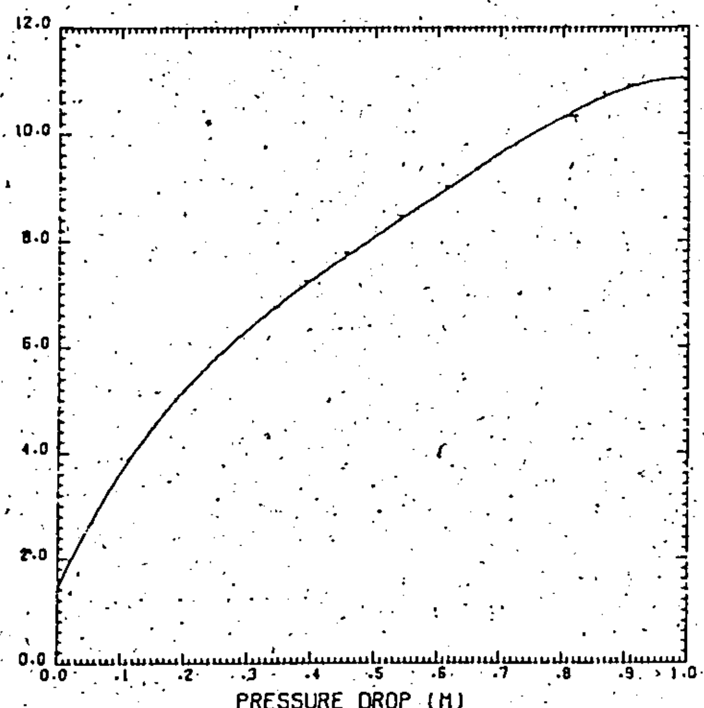


```
CALIBRATION CURVE FOR THE COOLING WATER
ORIFICE METER NO. 2

NUMBER OF TERMS IN THE FIT NTERMS=  4
COEFFICIENTS OF THE STANDARD POLYNOMIAL FIT
COEF( 0)=   .1380776E+01
COEF( 1)=   .2533337E+02
COEF( 2)=  -.4756282E+02
COEF( 3)=   .5576803E+02
COEF( 4)=  -.2486728E+02
FLAG IN THE TERM INCLUSION/REJECTION VECTOR M
M( 1)= 1  M( 2)= 1  M( 3)= 1  M( 4)= 1  M( 5)= 1
M( 6)= 1  M( 7)= 1  M( 8)= 1  M( 9)= 1  M(10)= 1
```

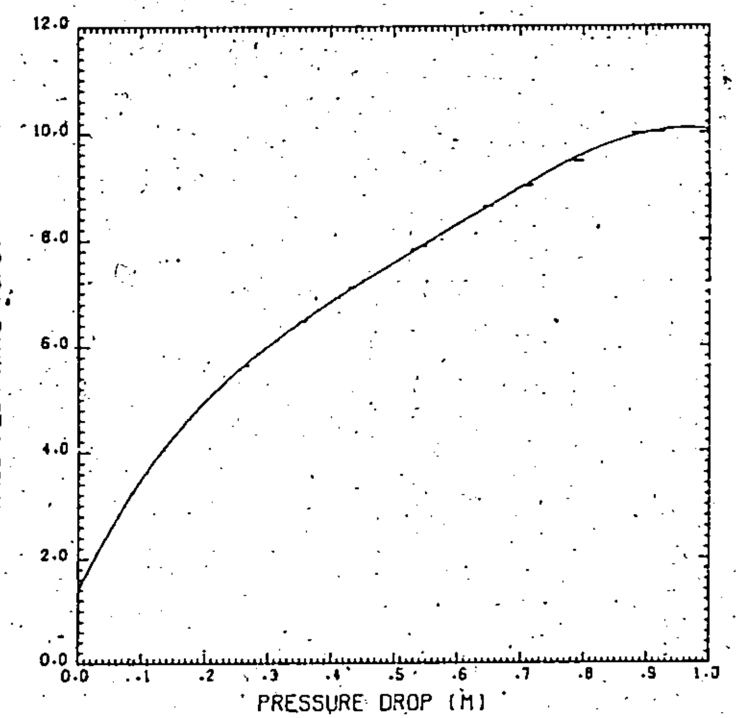

FIGURE B-3a,b Calibration for Cooling Water Orifice Meters No. 1 and 2

CALIBRATION CURVE FOR THE COOLING WATER
ORIFICE METER NO. 3

NUMBER OF TERMS IN THE FIT NTERMS= 4
COEFFICIENTS OF THE STANDARD POLYNOMIAL FIT
COEF(0)= .1859884E+01
COEF(1)= .2204860E+02
COEF(2)= -.2919486E+02
COEF(3)= .2652305E+02
COEF(4)= -.9742708E+01
FLAG IN THE TERM INCLUSION/REJECTION VECTOR M
M(1)= 1 M(2)= 1 M(3)= 1 M(4)= 1 M(5)= 1
M(6)= 1 M(7)= 1 M(8)= 1 M(9)= 1 M(10)= 1

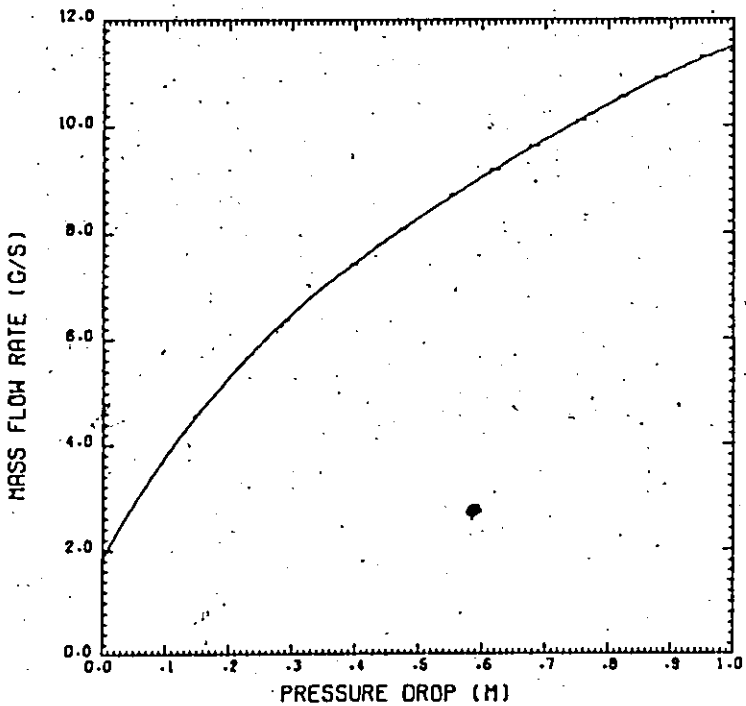

CALIBRATION CURVE FOR THE COOLING WATER
ORIFICE METER NO. 4

NUMBER OF TERMS IN THE FIT NTERMS= 4
COEFFICIENTS OF THE STANDARD POLYNOMIAL FIT
COEF(0)= .1916983E+01
COEF(1)= .2368784E+02
COEF(2)= -.3307739E+02
COEF(3)= .3179658E+02
COEF(4)= -.1241670E+02
FLAG IN THE TERM INCLUSION/REJECTION VECTOR M
M(1)= 1 M(2)= 1 M(3)= 1 M(4)= 1 M(5)= 1
M(6)= 1 M(7)= 1 M(8)= 1 M(9)= 1 M(10)= 1

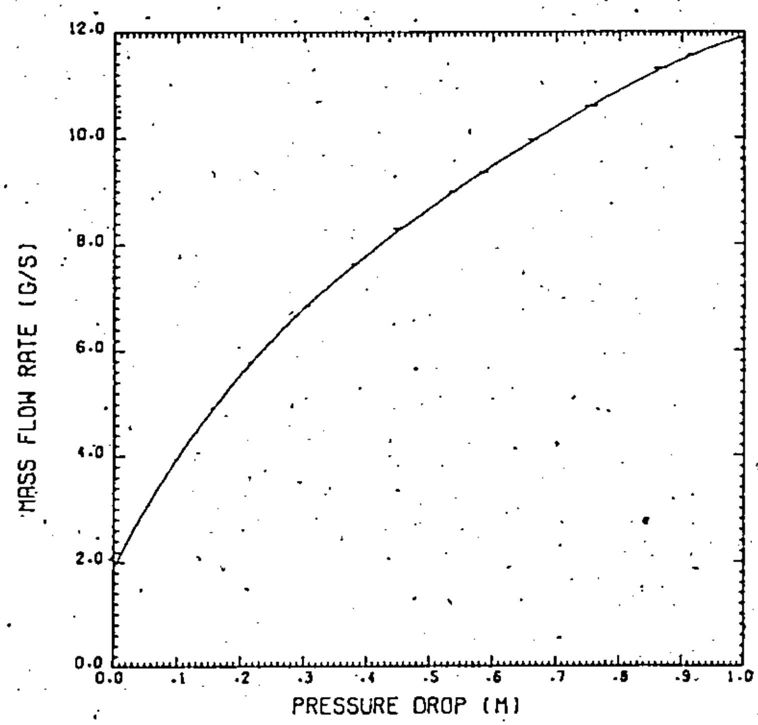

FIGURE B-3c,d . Calibration Curves for Cooling Water Orifice Meters No. 3 and 4

CALIBRATION CURVE FOR THE COOLING WATER
ORIFICE METER NO. 5

NUMBER OF TERMS IN THE FIT NTERMS= 4
COEFFICIENTS OF THE STANDARD POLYNOMIAL FIT
COEF(0)= .1507644E+01
COEF(1)= .2315597E+02
COEF(2)= -.3917604E+02
COEF(3)= .4474486E+02
COEF(4)= -.2014856E+02
FLAG IN THE TERM INCLUSION/REJECTION VECTOR M
M(1)= 1 M(2)= 1 M(3)= 1 M(4)= 1 M(5)= 1
M(6)= 1 M(7)= 1 M(8)= 1 M(9)= 1 M(10)= 1

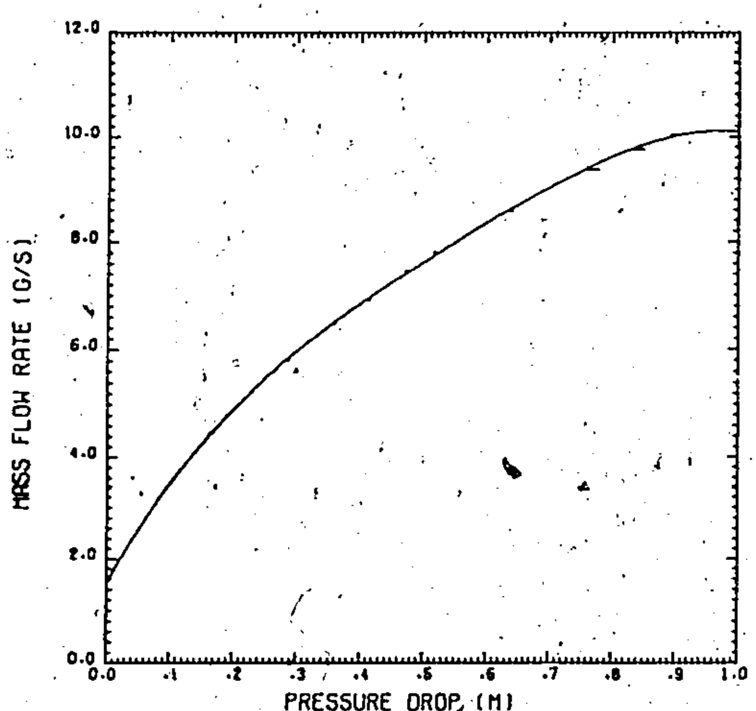

CALIBRATION CURVE FOR THE COOLING WATER
ORIFICE METER NO. 6

NUMBER OF TERMS IN THE FIT NTERMS= 4
COEFFICIENTS OF THE STANDARD POLYNOMIAL FIT
COEF(0)= .1654683E+01
COEF(1)= .2258625E+02
COEF(2)= -.3354196E+02
COEF(3)= .3348666E+02
COEF(4)= -.1323298E+02
FLAG IN THE TERM INCLUSION/REJECTION VECTOR M
M(1)= 1 M(2)= 1 M(3)= 1 M(4)= 1 M(5)= 1
M(6)= 1 M(7)= 1 M(8)= 1 M(9)= 1 M(10)= 1

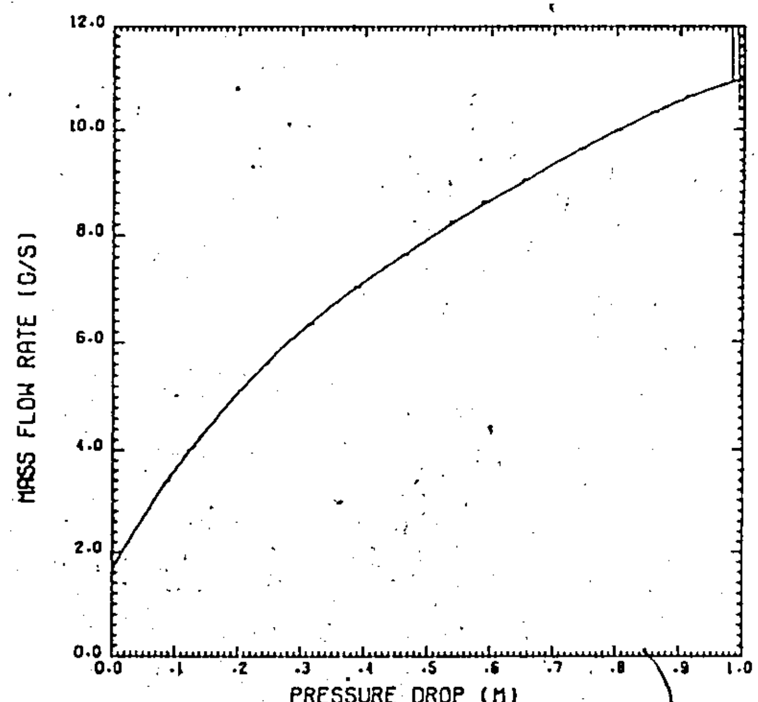

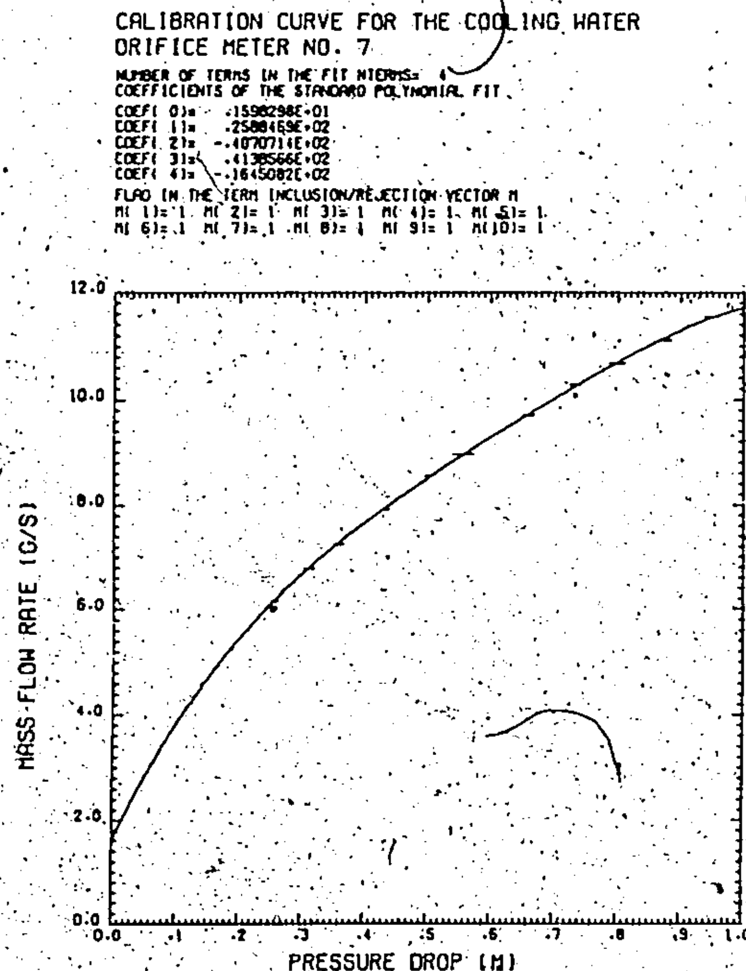

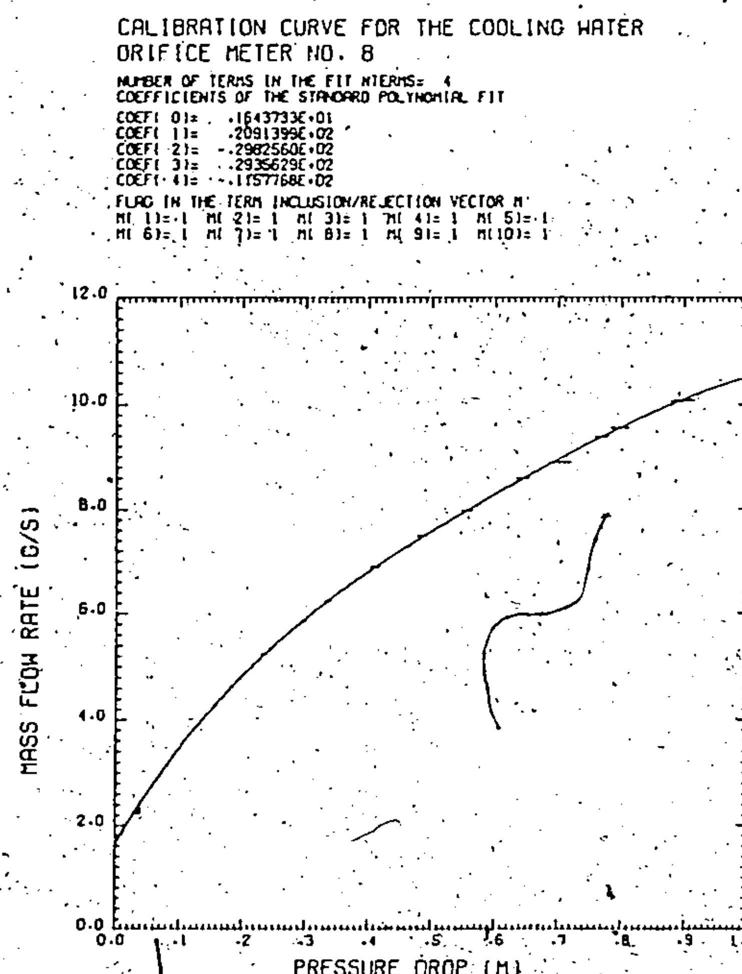

FIGURE B.3g,h Calibration Curves for Cooling Water Orifice meters No. 7 and 8

TABLE B.1: STANDARD DEVIATIONS OF THE FITS

ORIFICE METER NUMBER	S: STANDARD DEVIATION
1	0.8503334E-02
2	0.8196557E-02
3	0.4924494E-02
4	0.2166692E-02
5	0.8147370E-02
6	0.3239999E-02
7	0.9834489E-02
8	0.1748613E-02

TABLE B.2: MAXIMUM ERROR ESTIMATE

ORIFICE METER NO.	MAXIMUM ERROR ESTIMATE (%)
1	1.13
2	1.00
3	0.77
4	0.87
5	0.97
6	0.79
7	1.12
8	1.82

B.4 REMARK

To ensure a better heat transfer from the primary side to the secondary side one should have the cooling water flowing in the turbulent flow regime; however, this will give large errors on the heat balances done for each cooling jacket, the temperature differene between the outlet and the inlet being very small. This fact is illustrated by an error propagation analysis done on the heat balance equation:

$$Q = \dot{m}\ c_p\ \Delta T \qquad (B.3)$$

$$\frac{\sigma_Q^2}{Q^2} = \frac{\sigma_{\dot{m}}^2}{\dot{m}^2} + \frac{\sigma_{T_i}^2 + \sigma_{T_o}^2}{\Delta T^2} \qquad (B.4)$$

where

Q : heat removed (KW)

c_p: specific heat (KJ/kg^{o}C)

ΔT : $(T_o - T_i)$ = temperature difference between the outlet (T_o) and the inlet (T_i) (^{o}C)

From Equation (B-4) it can be seen that, knowing the error on the mass flow rate (5%, say), only a large temperature difference ($T_o - T_i$) can lead to small errors in the heat balances. This is the reason that motivate the choice of having such low flow on the secondary side. A maximum error of 10% in the heat balances was set as a criteria for the design of the cooling water orifice meters.

APPENDIX C

DESIGN OF THE WATER COLUMN FREQUENCY AND LEVEL METER

This appendix gives the results of a study for the design of the frequency and level meter. The purpose of the study was not to obtain a full understanding of the behavior of the probe, instead the study was limited to the influence of the configuration of the probe on the linearity of the response and the influence of the temperature of the surrounding medium. These were thought to be the two main parameters that could influence the behavior of the probe.

C.1 PHYSICAL SITUATION AND DESIGN DETAILS

The flow regime mentioned in the main text (Section 2.1.2.5) indicated the presence of a water column oscillating over a two-phase region. In adjusting the experimental conditions it is possible to have the top of the water column oscillating in the top section of the reflux condenser, leading to the situation shown in Figure C-1. In the exploded view of the probe we can see the detailed arrangement made of aluminium and electrical tapes: the 9.5 mm aluminium tapes are the capacitance electrodes,

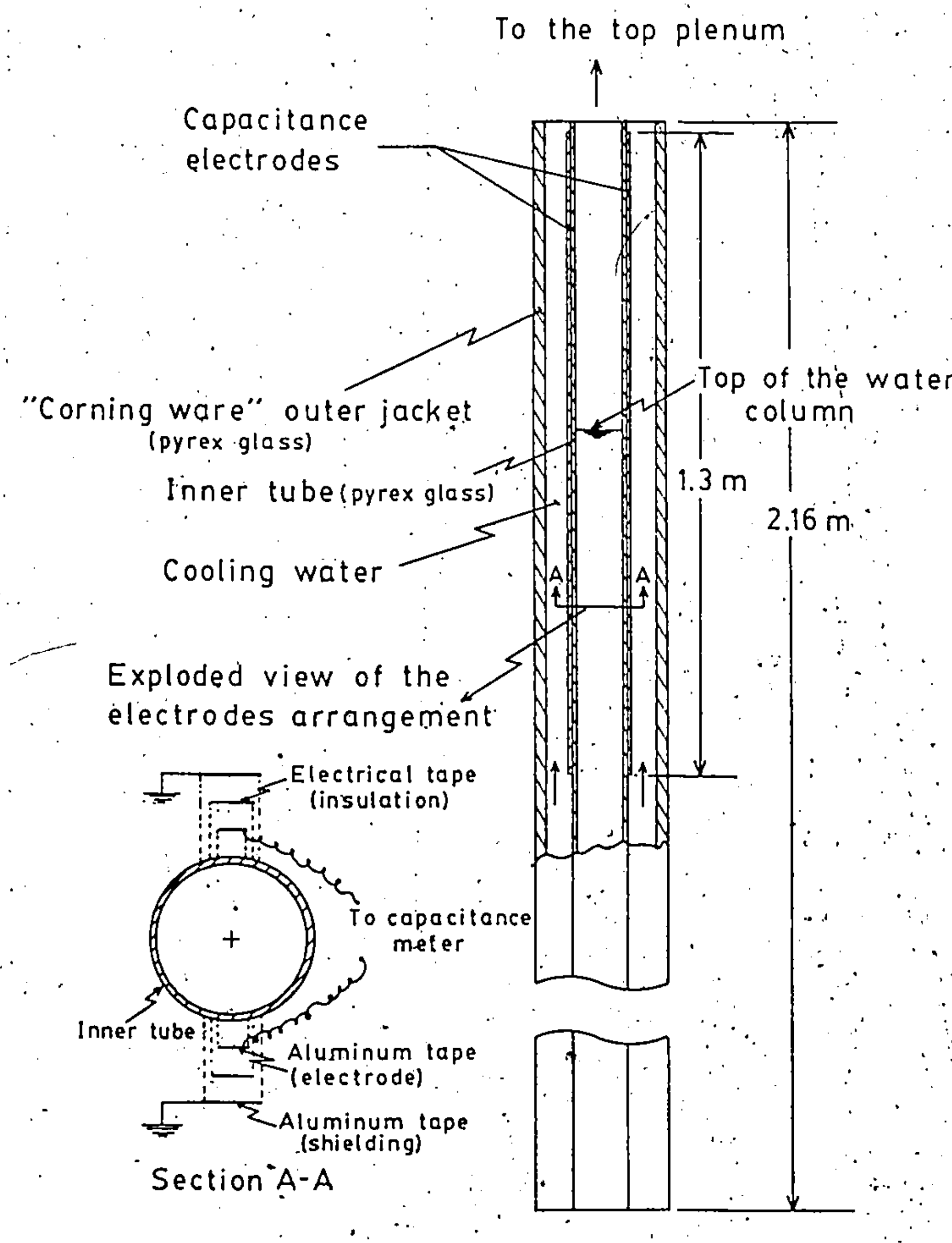

FIGURE C-1 Schematic of the Capacitance Level Meter the 19.05 mm aluminium tapes (electrically linked together) are the shield of the capacitance probe and the electrical tape acts as an insulator between the electrodes and the shields. A heat shrink tubing, painted with marine varnish, is used to waterproof the whole assembly. The width of the electodes and the shields are adjusted such that it is possible to see the top level of the water column for in-situ calibrations and visual observations: at the same time, precautions were taken to see if the chosen width of the electrodes ensure a sufficient sensitivity.

C.2 METHOD OF CALIBRATION

The change in capacitance from the water level below the beginning of the probe to a tube full of water is of the order of 40 pF with the probe configuration chosen. This implies a sensitivity of about 3 cm/pF that is enough for all practical purposes

The calibration of the probe is done by a static method. The inner tube is filled up with water at a known temperature and recording the value of the capacitance meter analog output on a digital voltmeter and the level of the liquid measured with a meter stick. This calibration procedure was done for various combination of temperature of the cooling water and the water used to fill the inner tube.

Very stable values of the analog output by the capacitance meter was observed during all the calibration tests.

C.3 RESULTS

The results of the calibration tests are shown in Figure C-2 for all the condition studied. It can be seen that the response of the probe is linear and the spread of the data is small, showing a small sensitivity to the temperature of the surroundings. In fact, most of the data points deviate by less than 2.5% of the fit and the standard deviation of the fit is 0.045 m. The nondimensional voltage in the preceeding graph (Figure C-2) is calculated as follow:

$$\bar{V}_{nd} = \frac{\bar{V} - \bar{V}_1}{\bar{V}_2 - \bar{V}_1} \qquad (C.1)$$

where

$\bar{V}_{nd}$: nondimensional voltage

CALIBRATION CURVE FOR THE CAPACITANCE LEVEL METER
FOR TUBE O.D. OF 2.54 CM

ORDER OF THE POLYNOMIAL FIT NDEG= 1
COEFFICIENTS OF THE POLYNOMIAL FIT
COEF(1)= .3507894E+01
COEF(2)= .1180800E+01
LEGEND OF THE PLOT

ʘ = COLD JACKET(18 DEGC). COLD INNER TUBE(18 DEGC)
▲ = COLD JACKET(18 DEGC). HOT INNER TUBE(80 DEGC)
\+ = HOT JACKET(45 DEGC). COLD INNER TUBE(18 DEGC)
× = HOT JACKET(35 DEGC). HOT INNER TUBE(80 DEGC)
◈ = COLD JACKET(18 DEGC). COLD INNER TUBE(18 DEGC)
↑ = HOT JACKET(41.5 DEGC). COLD INNER TUBE(18 DEGC)
⊼ = HOT JACKET(45 DEGC). HOT INNER TUBE(80 DEGC)

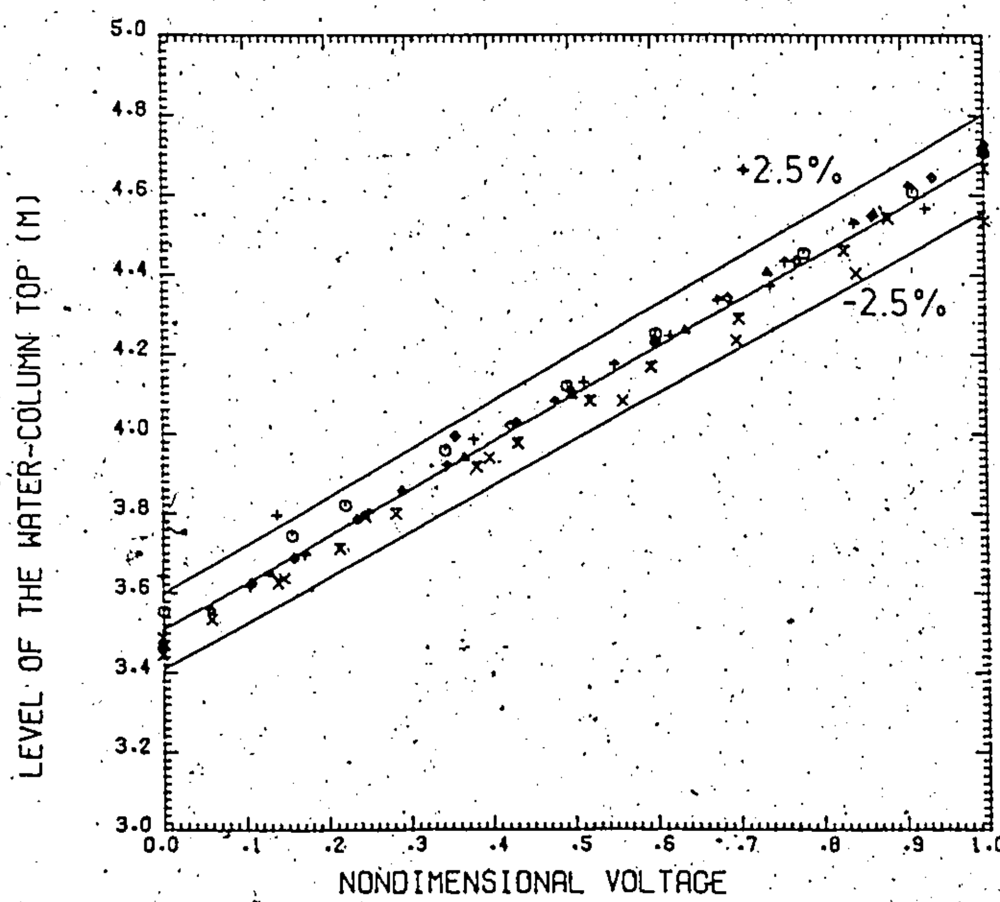

FIGURE C-2 Calibration Curve of the Capacitance Level Meter

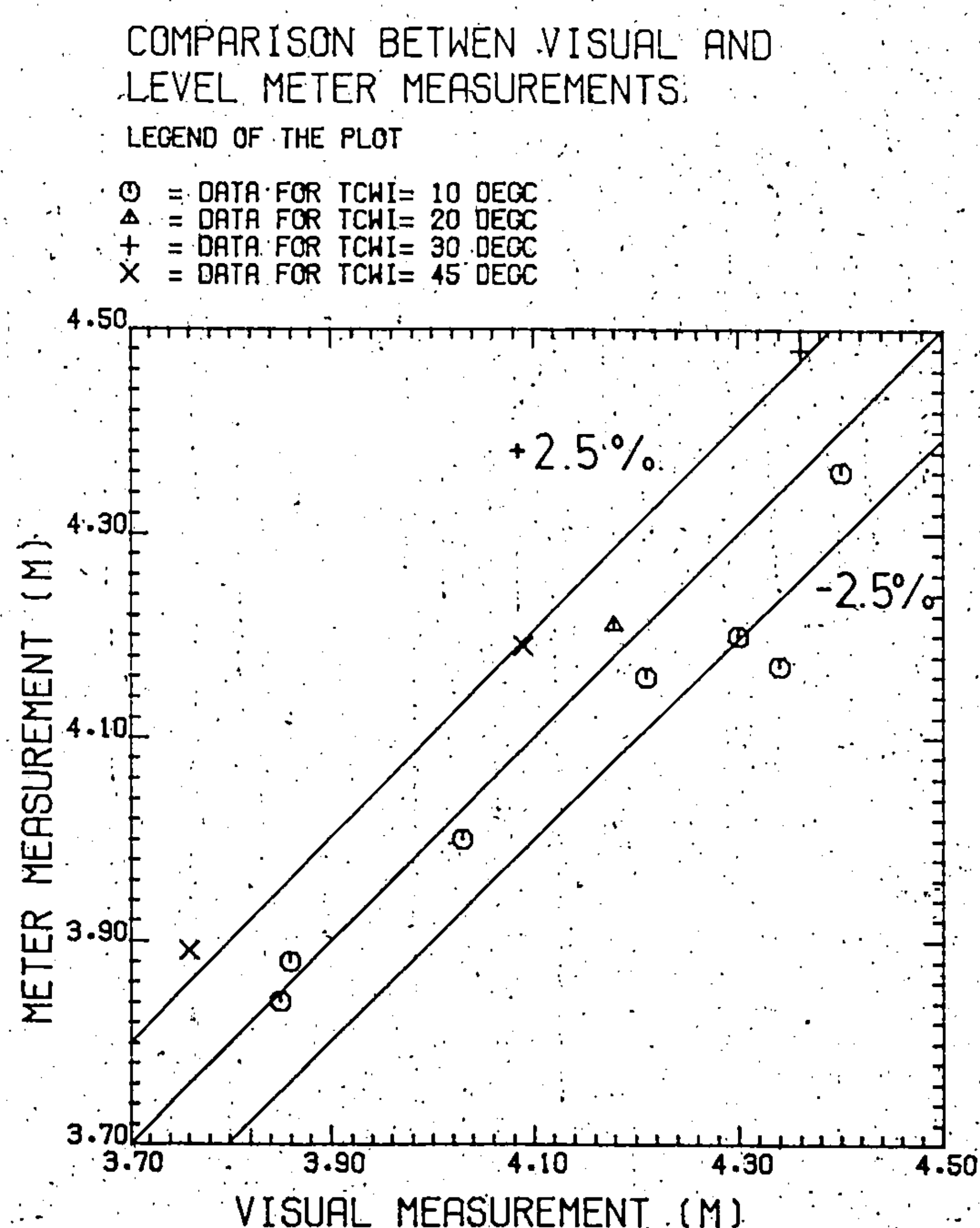

FIGURE C.3 Comparison Between Visual Observations and Meter Measurements for 2.54 cm O.D. Tube

$\bar{V}_1$: average output voltage from the Boonton Capacitance Meter for the level just above the beginning of the sensor (V)

$\bar{V}_2$: average output voltage from the Boonton Capacitance Meter for the level just below the end of the sensor (V)

$\bar{V}$: average output voltage from the Boonton Capacitance Meter for the present measured level (V)

The linear response of the capacitance level meter to changes in the inner tube water level indicates that a calibration curve could be generated for each experimental conditions, in other words for each day of experimentation. This is done by fixing the cooling water temperature for that experiment and reading the outputs of the capacitance meter by the NOVAC III computer for two inner tube meter levels: one just above the beginning of the sensor and the other just before the end of the sensor. This procedure was tested with success in actual experiments as shown in Figure C-3, where average levels of the water column top measured by the capacitance level meter are compared to visual observations.

APPENDIX D

CALIBRATION OF THE CAPACITANCE VOID METER

This appendix gives some mechanical design details of the calibration unit, the method of calibration used and the multiple linear regression analysis done on the data. This will result in the tree calibration curves, one for each tube size studied, that relate the void fraction "ε_g" to the dimensionless voltage "$\overline{V}_{nd}$", along with the associated error analysis.

D.1 THE CALIBRATION UNIT

The main design characteristic of the calibration unit is the physical arrangement of the second section (glass section) and the mechanical elements surrounding it. To obtain meaningful calibration curves, the whole assembly should represent a situation as close as possible to the actual experimental conditions. Figure D-1 gives a layout of the test section and the assembly of the quick-closing valves, brass spacers and Teflon spacers. A 30.5 cm pyrex glass section was chosen because it represents very well a reflux condenser section of the same lenght with

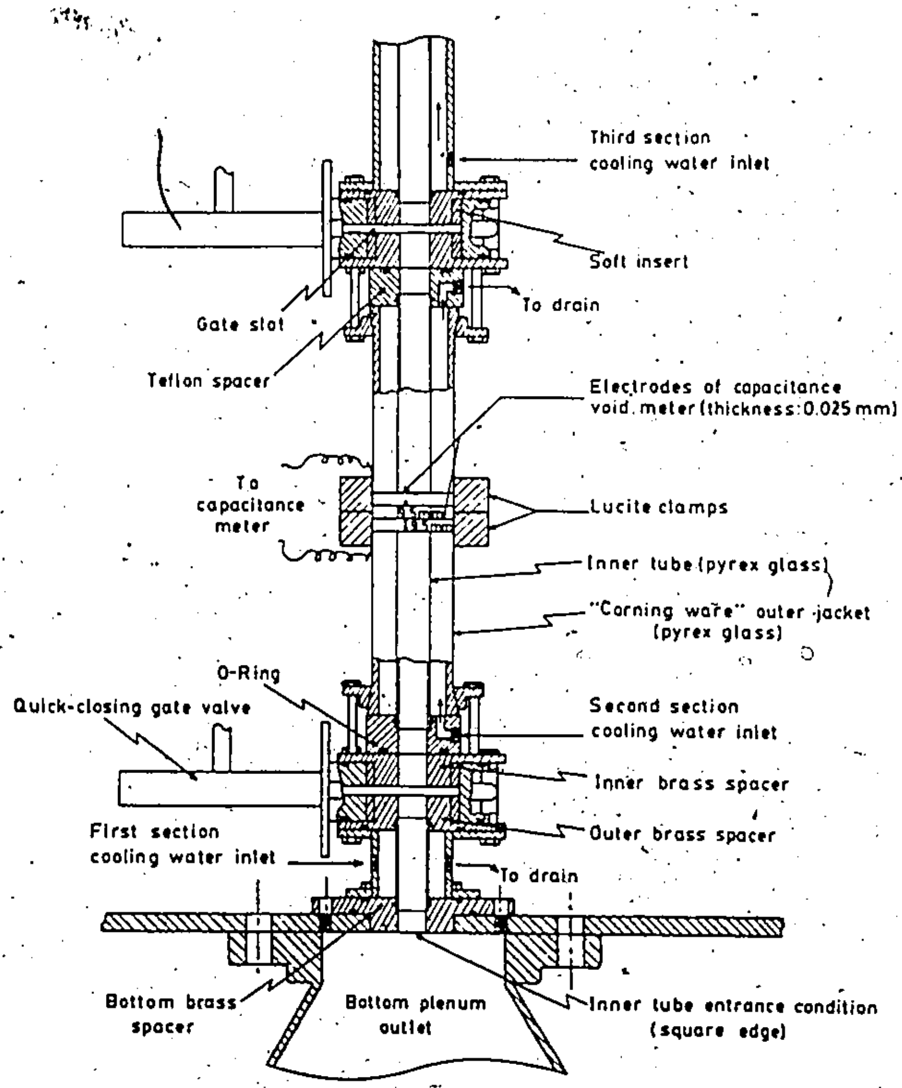

FIGURE D.1 Quick Closing Valves Arrangement in the Calibration Unit its ports in the Teflon for the flow of cooling water and the inner tube pressure and temperature measurements.

The geometry of the inlet at the bottom of the inner tube is exactly the same as in the reflux condenser. In all the tests both plenums were opened to atmosphere allowing the air in the bottom plenum to escapes as the water, coming from the top, fills it. The distance between the outlet at the top of the inner tube and the position of the capacitance void meter is about 3.5 m. This distance allows the falling film flow to establish itself and to tend as much as possible to reach a fully developed flow, knowing that two-phase flows are never fully developed [46, p.37]. The apparatus is designed to allow the user to change the inner tube diameter but all the Teflon and brass spacers must be changed or machined again to meet the new inner tube diameter.

D.2 THE CALIBRATION METHOD

The method used in the calibration tests to obtain one ensemble (time-volume) average void fraction and a corresponding time average dimensionless voltage is given as follow:

(i) at the beginning the values of the capacitance for the inner tube full and empty of water are recorded;

(ii) a falling film flow (annular flow) is established in the inner tube by injecting water in the top plenum. The rate of injection remains constant during the whole test;

(iii) the NOVA computer is set such that it records 6000 data points form the capacitance. The data is averaged and the standard deviation is calculated assuming a normal distribution;

(iv) the two-phase mixture is trapped by actuating the quick-acting valves;

(v) the trapped water is extracted and its volume measured. This volume is feed the NOVA computer to compute the void fraction from a prior knowledge of the total volume enclosed between the gates of the two quick-acting valves.

This procedure gives only an instantaneous values of the measured void fraction and dimensionless voltage. To obtain the time average values, this procedure is repeated until the cumulative average does not change much. Typical results of a test is shown in Figure D-2 and D-3. It should be noted that step (i) is not repeated for each instantaneous values, it is done only at the beginning and at the end of a test.

D.3 ERROR ANALYSIS

The dimensionless voltage "$\bar{V}_{nd}$" is calculated by:

$$\bar{V}_{nd} = \frac{\bar{V}_{act} - \bar{V}_1}{\bar{V}_2 - \bar{V}_1} \tag{D.1}$$

where

$\bar{V}_{nd}$: time average dimensionless voltage

$$\bar{V}_1 = \frac{\bar{V}_{i1} + \bar{V}_{f1}}{2} \quad \text{and} \quad \bar{V}_2 = \frac{\bar{V}_{i2} + \bar{V}_{f2}}{2}$$

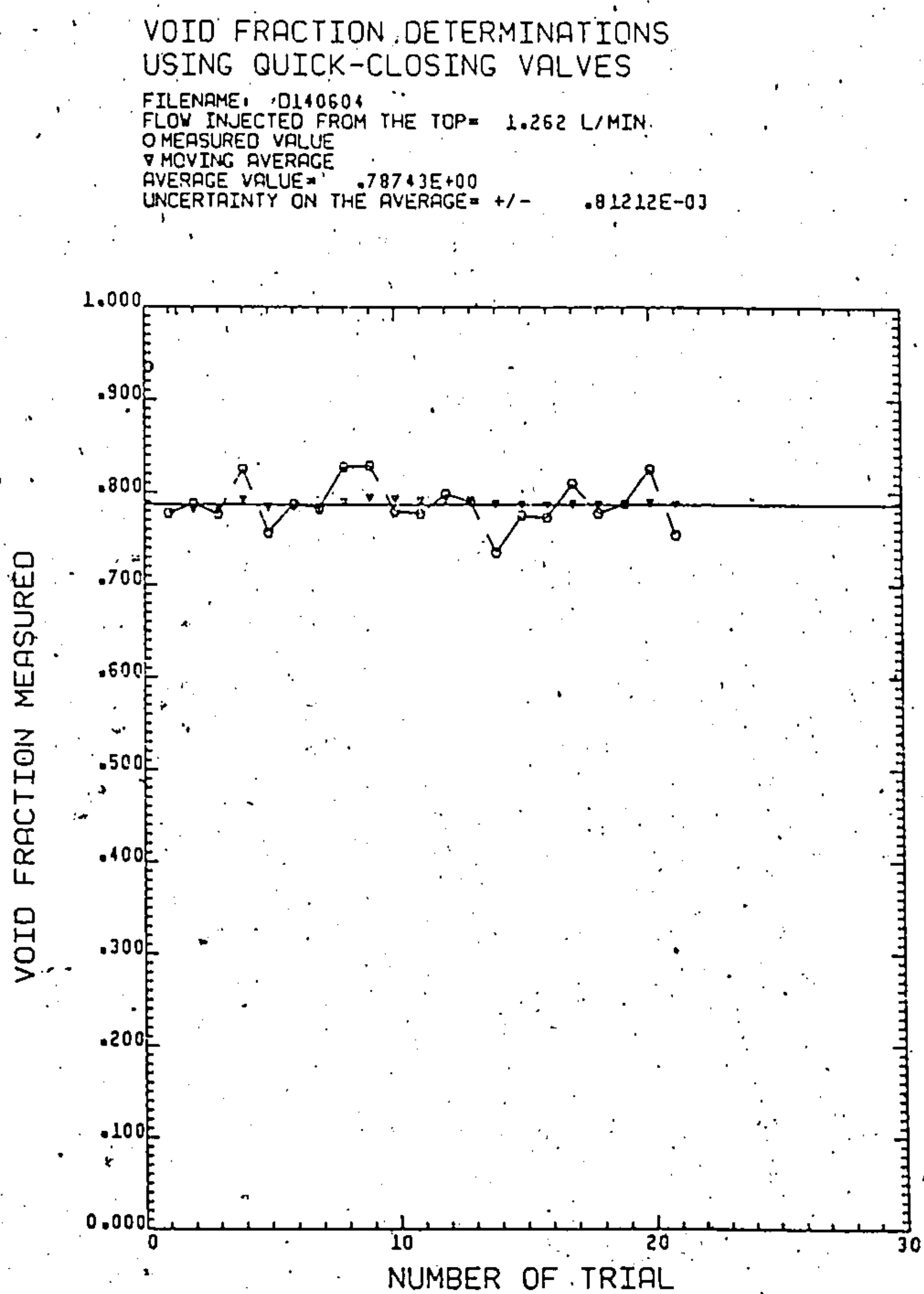

FIGURE D-2 Time-Volume Average Void Fraction Determination

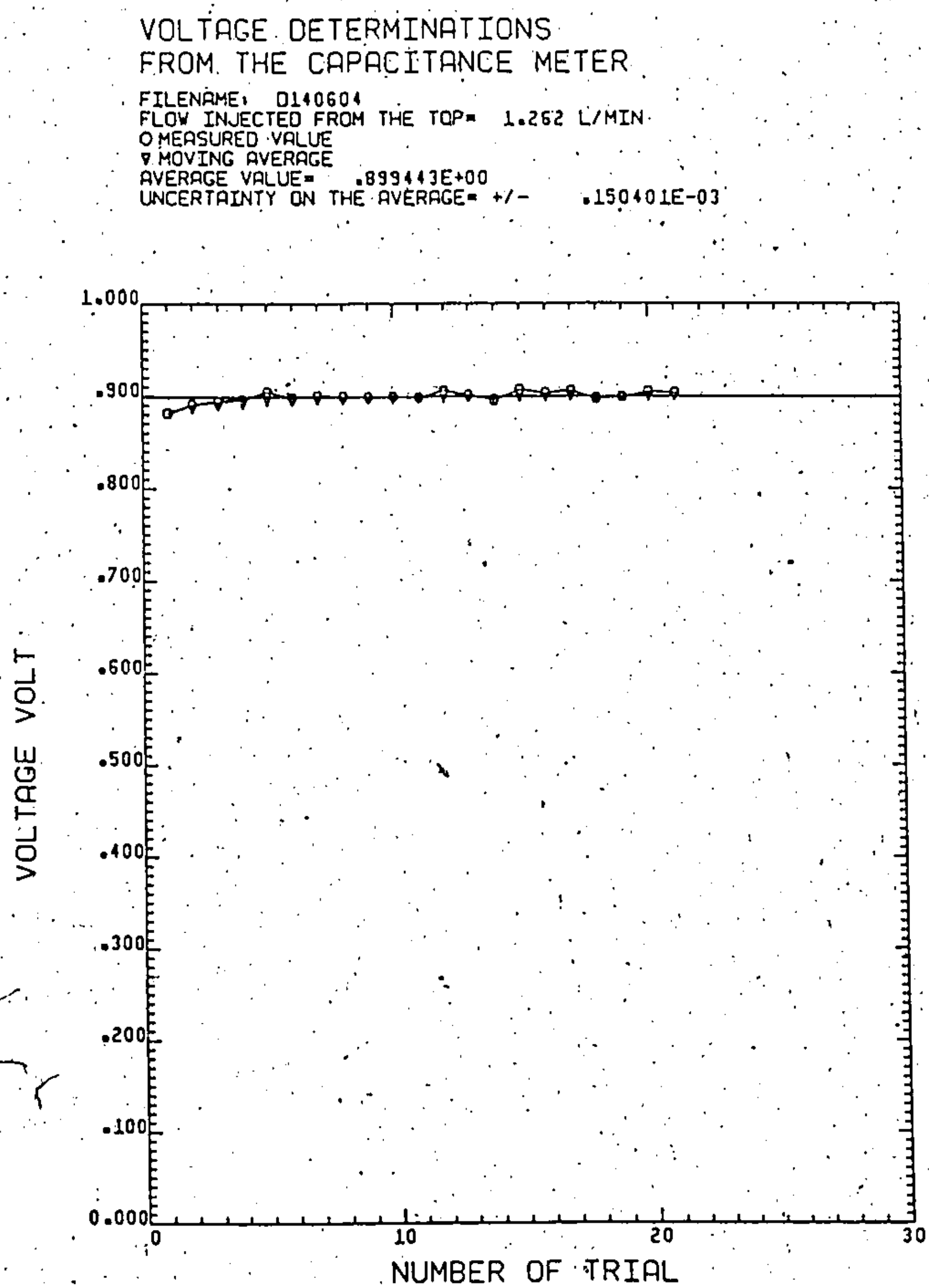

FIGURE D-3 Time Averaged Voltage Determination

$\bar{V}_{act}$: time average dimensionless voltage

$\bar{V}_{i1}$: average voltage at the beginning of the series of tests for the inner tube full of water (V)

$\bar{V}_{i2}$: average voltage at the beginning of the series of tests for the inner tube empty (V)

$\bar{V}_{f1}$: average voltage at the end of the series of tests for the inner tube full of water (V)

$\bar{V}_{f2}$: average voltage at the end of the series of tests for the inner tube empty (V)

It should be noted that all the voltage measured have a known error equal to the standard deviation of the signal. The expression for the propagation of errors for the dimensionless voltage is given by [2, p.59]:

$$\sigma^2_{\bar{V}_{nd}} = \frac{\sigma^2_{act}}{(\bar{V}_2 - \bar{V}_1)^2} + \sigma^2_{\bar{V}_1} \frac{(\bar{V}_2 - \bar{V}_{act})^2}{(\bar{V}_2 - \bar{V}_1)^4} + \sigma^2_{\bar{V}_2} \frac{(\bar{V}_{act} - \bar{V}_1)^2}{(\bar{V}_2 - \bar{V}_1)^4} \tag{D.2}$$

where:

$\sigma^2_{\bar{V}_{act}}$:variance of $\bar{V}_{act}$

$\sigma^2_{\bar{V}_1}$:variance of $\bar{V}_1$

$\sigma^2_{\bar{V}_2}$:variance of $\bar{V}_2$

and

$$\sigma^2_{\bar{V}_1} = \frac{1}{2}(\sigma^2_{\bar{V}_{i1}} + \sigma^2_{\bar{V}_{f1}}) \quad \text{and} \quad \sigma^2_{\bar{V}_2} = \frac{1}{2}(\sigma^2_{\bar{V}_{i2}} + \sigma^2_{\bar{V}_{f2}})$$

The variances on $\bar{V}_{act}$, $\bar{V}_1$, $\bar{V}_2$ and the void fraction are calculated using standard formula [69, p.72-73], but it should be noted that each instantaneous voltage signal $\bar{V}_{act}$ has its particular standard deviation. The time-volume average void fraction and its error (standard deviation) are also calculated using standard formula.

The above calculations results in a set of data with both variables having uncertainties, as mentioned in the text, the multiple regression analysis along with the effective variance method [68] must be applied to obtain the coefficients of the best fit calibration curves, which are shown in the main text. The coefficients of the polynomial fits are obtained by using the computer program EVMFIT(*).

In general, the expression for the calibration curve takes the following form:

$$\varepsilon_g = a_o + \sum_{i=1}^{n} a_i M_i X_i (\overline{V}_{nd}) \tag{D.3}$$

where

ε_g: void fraction

$a_o, a_1, a_2, \ldots, a_n$: coefficients of the fit

M_i: inclusion or rejection variable equal to 1 or 0

$X_i(\overline{V}_{nd})$: Chebychev or Legendre polynomial of order "i"

$\overline{V}_{nd}$: nondimensional voltage ($0 < \overline{V}_{nd} < 1$)

(*) EVMFIT : Effective Variance Method FIT (see Appendix B, Section B.3)

The variable M_i is used to include or reject terms in Equation (D-3), as an example the calibration curve for the 1.27 cm O.D. tube we have:

$$\epsilon_g = a_o + a_2 T_2(\bar{V}_{nd}) + a_4 T_4(\bar{V}_{nd}) + a_6 T_6(\bar{V}_{nd}) + a_8 T_8(\bar{V}_{nd}) \qquad (D.4)$$

where

a_o : COEF(0)

a_2 : COEF(1) $\quad$ a_4 : COEF(2)

a_6 : COEF(3) $\quad$ a_8 : COEF(4)

and

T_2, T_4, T_6, and T_8 are respectively the second, fourth, sixth and eighth order Chebychev or Legendre polynomials.

The choice of the polynomial type and the number of terms is based on the F test as presented in Bevington [69, p.187-202]. The standard deviation of each fit is presented in Table D-1. The standard deviation is taken as being the accuracy of the fit.

TABLE D.1: STANDARD DEVIATION OF THE CAPACITANCE VOID METERS CALIBRATION CURVES

INNER TUBE SIZE (O.D.) (cm)	STANDARD DEVIATION σ_{fit}
1.27	0.754E-01
1.91	0.808E-02
2.54	0.136E-02

APPENDIX E

ESTIMATION OF THE NON-CONDENSIBLE GAS CONCENTRATION IN STEAM

In Chapter 2, Figure 2.4 shows a typical situation of non-condensible gas flow rate measurements. The height of the water level in the sample tube determines the volume of the non-condensible gas accumulated and the pressure in the non-condensible gas volume. It was necessary to calibrate the sample tube and a linear fit was obtained.

In the computation of the mass of gas accumulated over a period of time (in general 30 min.) the perfect gas law was assumed to be valid. In Table E-1 we present the results obtained for the cases of total reflux condensation under an imposed constant pressure drop condition with a water column oscillating over a two-phase region as the observed flow pattern.

From the results in Table E-1, we can infer that an average of one part in 10900 (0.009%) was present in the steam. The maximum amount found was one part in 6141

TABLE E.1: RESULTS OF NON CONDENSIBLE GAS CONCENTRATION MEASUREMENTS IN STEAM

RUN NO.	STEAM FLOW RATE (g/min)	NON-COND. GAS FLOW RATE (g/min) x 10^3	PERCENTAGE PER WEIGHT x 10^3	CONCENTRATION BY PART
NC22031	119.74	6.78	5.66	17670
NC22032	111.44	7.00	6.28	15295
NC23031	119.92	11.63	9.70	10310
NC23032	102.99	0.703	0.68	146557
NC18041	109.49	15.64	14.28	7000
NC19041	105.18	15.38	14.60	6839
NC20041	110.78	14.04	12.70	7888
NC21041	105.02	13.78	13.10	7617
NC22041	104.43	16.73	16.00	6242
NC26041	106.14	16.52	15.50	6426
NC27041	109.49	17.83	16.30	6141
NC05051	122.14	13.53	11.10	9032
NC09051	111.42	4.79	4.30	23277
NC10051	111.25	3.86	3.50	28849
NC24061	96.85	6.28	6.50	15418
NC25061	100.57	6.60	6.60	15238
NC26061	102.95	4.47	4.30	23031
NC27061	101.50	4.20	4.10	24167

(0.0163%). The results presented are only for the 2.54 O.D. tube. Experiments with the other tubes did not show significant presence of non-condensible gas; however, to be conservative, the amounts measured for the 2.54 cm O.D. were assumed to be valid for these two tubes sizes.

APPENDIX F

F.1. EXPRESSIONS FOR THE VARIABLES IN EQUATIONS (3.69) AND (3.70)

The expressions for β_1, β_2, β_3, L_1, N_1, and N_2 are:

$$\beta_1 = \left\{ -\bar{k}^2 - \frac{i\bar{k}Re_o}{2}(\bar{u}_{\ell i} - \bar{c}) + \left[-i\bar{k}Re_o \frac{\partial^2 \bar{u}_\ell^{(0)}}{\partial \bar{y}^2} - \frac{\bar{k}^2}{4} Re_o^2 (\bar{u}_{\ell i}^{(0)} - \bar{c}^{(0)})^2 \right]^{1/2} \right\}^{1/2} \tag{F.1}$$

$$\beta_2 = \left\{ -\bar{k}^2 - \frac{i\bar{k}Re_o}{2}(\bar{u}_{\ell i}^{(0)} - \bar{c}) - \left[-i\bar{k}Re_o \frac{\partial^2 \bar{u}_\ell^{(0)}}{\partial \bar{y}^2} - \frac{\bar{k}^2}{4} Re_o^2 (\bar{u}_{\ell i}^{(0)} - \bar{c}^{(0)})^2 \right]^{1/2} \right\}^{1/2} \tag{F.2}$$

$$\beta_3 = [- \bar{k}^2 - i\bar{k}\ Pe\ (\bar{u}_{\ell i}^{(0)} - \bar{c}^{(0)})] \qquad (F.3)$$

$$L_1 = i\bar{k}\ Pe\ \frac{\partial \bar{T}_{\ell}^{(0)}}{\partial \bar{y}} \qquad (F.4)$$

$$N_1 = \beta_1^2 + \bar{k}^2 + i\bar{k}\ Pe\ (\bar{u}_{\ell i}^{(0)} - \bar{c}^{(0)}) \qquad (F.5)$$

$$N_2 = \beta_2^2 + \bar{k}^2 + i\bar{k}\ Pe\ (\bar{u}_{\ell i}^{(0)} - \bar{c}^{(0)}) \qquad (F.6)$$

F.2. EXPRESSIONS FOR THE VARIABLES IN THE DETERMINANT OF FIGURE 3.5

The expressions for the variables in the determinant of Figure 3-5 not already defined in the main text are given here:

$$\hat{c} = (\bar{u}_{\ell i}^{(0)} - \hat{\bar{c}}^{(0)}) \qquad \text{(F.7)}$$

$$b_{10} = -\beta_1^2 \cos\beta_1 + \beta_2^2 \cos\beta_2 \qquad \text{(F.8)}$$

$$b_{11} = \cos\beta_1 - \cos\beta_2 \qquad \text{(F.9)}$$

$$b_{12} = \sin\beta_1 - \frac{\beta_1}{\beta_2} \sin\beta_2 \qquad \text{(F.10)}$$

$$b_{13} = \frac{\cos\beta_1}{N_1} - \frac{\cos\beta_2}{N_2} \qquad \text{(F.11)}$$

$$b_{20} = \beta_1^2 \sin\beta_1 - \frac{\beta_2^3}{\beta_1} \sin\beta_1 \qquad (F.12)$$

$$b_{21} = -\sin\beta_1 + \frac{\beta_2}{\beta_1} \sin\beta_2 \qquad (F.13)$$

$$b_{22} = -\frac{\sin\beta_1}{N_1} + \frac{\beta_2}{\beta_1} \frac{\sin\beta_2}{N_2} \qquad (F.14)$$

$$c_{10} = -\beta_1 \sin\beta_1 + \beta_2 \sin\beta_2 \qquad (F.15)$$

$$c_{20} = -\beta_1 \cos\beta_1 + \frac{\beta_2^2}{\beta_1} \cos\beta_2 \qquad (F.16)$$

$$d_{10} = \frac{\sin\beta_1}{N_1} - \frac{\beta_1}{\beta_2} \frac{\sin\beta_2}{N_2} \qquad (F.17)$$

$$a_1 = \frac{i}{\bar{k}} \frac{Ku}{Pe} \frac{\partial \bar{T}_\ell^{(0)}}{\partial \bar{y}} \tag{F.18}$$

$$a_2 = \frac{\partial \bar{T}_\ell^{(0)}}{\partial \bar{y}} \tag{F.19}$$

$$a_4 = - E \text{ (see Equation (F.26))} \tag{F.20}$$

$$a_5 = \frac{i}{\bar{k}} \frac{Ku}{Pe} E \text{ (see Equation (F.26) for "E")} \tag{F.21}$$

$$a_6 = 2 \bar{k} \frac{(1 - \gamma)}{\gamma} \frac{Ku^2}{Re_o Pr^2} \frac{\partial \bar{T}_\ell^{(0)}}{\partial \bar{y}} \tag{F.22}$$

$$a_7 = \frac{i}{\bar{k}} \frac{Ku}{Pe} \tag{F.23}$$

F.3. EXPRESSIONS FOR THE VARIABLES IN EQUATION (3-71)

The expressions for the variables in equation (3.71) not already defined in the main text are given here:

$$D_1 = -\bar{k}\,Re_o\hat{c} - (3\,\bar{k}^2 + \beta_1^2)i \tag{F.24}$$

$$D_2 = -\bar{k}\,Re_o\hat{c} - (3\,\bar{k}^2 + \beta_2^2)i \tag{F.25}$$

$$E = \bar{k}\,P_s - \bar{k}^3\,We\,Re_o - 2\,\bar{k}^3\,\frac{M_r}{\Upsilon}\,\frac{Ku}{Pe}\,\frac{\partial\bar{T}_\ell^{(0)}}{\partial\bar{y}} \tag{F.26}$$

$$G_1 = \left(T_s - \frac{\partial^2\bar{u}_\ell^{(0)}}{\partial\bar{y}^2}\right) + \hat{c}\,(\bar{k}^2 - \beta_1^2) \tag{F.27}$$

$$G_2 = \left(T_s - \frac{\partial^2\bar{u}_\ell^{(0)}}{\partial\bar{y}^2}\right) + \hat{c}\,(\bar{k}^2 - \beta_2^2) \tag{F.28}$$

$$F_{ht}^{(1)} = \left(\bar{T}_s - \frac{\partial^2 \bar{u}_\ell^{(0)}}{\partial \bar{y}^2}\right)\left\{\beta_1^2\ \beta_2\left(\frac{D_1}{N_2} - \frac{D_2}{N_1}\right)\right.$$

$$\left(\frac{\beta_2}{\beta_1} \sin\beta_2 \cos\beta_1 - \sin\beta_1 \cos\beta_2\right)$$

$$+ \beta_1\beta_1\beta_3\left[\left(\frac{D_1}{N_1} + \frac{D_2}{N_2}\right) - \left(\frac{D_2\beta_2}{N_1\beta_1} + \frac{D_1\beta_1}{N_2\beta_2}\right)\sin\beta_1 \sin\beta_2\right. \tag{F.29}$$

$$\left.\left. - \left(\frac{D_2}{N_1} + \frac{D_1}{N_2}\right)\cos\beta_1 \cos\beta_2\right] \tan\beta_3\right\}$$

$$F_{ht}^{(2)} = \beta_1\beta_2\beta_3\ \left\{\beta_1\beta_2(D_1 + D_2) \sin\beta_1 \sin\beta_2\right.$$

$$+ (\beta_1^2 D_2 + \beta_2^2 D_1) \cos\beta_1 \cos\beta_2 - (\beta_1^2 D_1 + \beta_2^2 D_2) \tag{F.30}$$

$$+ \bar{k}\ \left[(D_1 + D_2)\ (1 - \cos\beta_1 \cos\beta_2)\right.$$

$$\left.\left. - \left(\frac{D_1\beta_1}{\beta_2} + \frac{D_2\beta_2}{\beta_1}\right) \sin\beta_1 \sin\beta_2\right]\right\} \tan\beta_3$$

$$F_{nt}^{(3)} = -\beta_1\beta_2\beta_3\left[\left(\frac{G_1}{N_1} + \frac{G_2}{N_2}\right) - \left(\frac{G_1}{N_1}\,\frac{\beta_2}{\beta_1} + \frac{G_2}{N_2}\,\frac{\beta_1}{\beta_2}\right)\sin\beta_1\,\sin\beta_2 \right.$$
$$\left. - \left(\frac{G_2}{N_1} + \frac{G_1}{N_2}\right)\cos\beta_1\,\cos\beta_2\right] \qquad (F.31)$$

$$F_{ht}^{(4)} = -\beta_2\beta_3\left[\frac{G_2}{N_1}\sin\beta_1\,\cos\beta_2 + \frac{G_1\beta_1}{N_2\beta_2}\sin\beta_2\,\cos\beta_1\right]\tan\beta_3 \qquad (F.32)$$

$$F_{ht}^{(5)} = \beta_1\beta_2\left[\beta_1(c_{20}b_{13} - c_{11}b_{22}) + \bar{k}^2(b_{11}b_{13} - b_{12}b_{22})\right]$$
$$+ \beta_1\beta_2\beta_3\left[\beta_1(c_{20}d_{10} - c_{10}b_{13}) + \bar{k}^2(d_{10}b_{11} - b_{12}b_{13})\right]\tan\beta_3 \qquad (F.33)$$

$$F_{ht}^{(6)} = \beta_1\beta_2\beta_3\ \hat{c}\ (c_{10}b_{11} - c_{20}b_{12})$$

$$\left[2\bar{k}\ \frac{(1-\gamma)}{\gamma}\ \frac{Ku}{Re_o Pr^2}\ \frac{\partial \bar{T}_\ell^{(0)}}{\partial \bar{y}} + \frac{iRe_o}{Pe}\ \frac{\partial \bar{u}_\ell^{(0)}}{\partial \bar{y}}\right]\tan\beta_3 \tag{F.34}$$

$$F_{ht}^{(7)} = \bar{k}\ \frac{\partial \bar{u}_\ell^{(0)}}{\partial \bar{y}}\left(T_s - \frac{\partial^2 \bar{u}_\ell^{(0)}}{\partial \bar{y}}\right)\Big[(b_{11}b_{13} - b_{12}b_{22})$$

$$+ \beta_2\beta_3(b_{11}d_{10} - b_{12}b_{13})\ \tan\beta_3\Big] \tag{F.35}$$

$$F_{ht}^{(8)} = \Bigg\{ - \beta_1\beta_2\left(\frac{1}{N_1} - \frac{i}{N_2}\right)\left(T_s - \frac{\partial^2 \bar{u}_\ell^{(0)}}{\partial \bar{y}^2}\right)$$

$$(D_1\beta_1\ \sin\beta_1 - D_2\beta_2\ \sin\beta_2)$$

$$+ 2\ i\bar{k}^2\ \frac{(1-\gamma)}{\gamma}\ \frac{Ku}{Pr}\ \frac{\partial \bar{T}_\ell^{(0)}}{\partial \bar{y}}\ (G_2\ \cos\beta_2 - G_1\ \cos\beta_1) \tag{F.36}$$

$$- E\ \left[\left(\bar{k}^2 - \beta_2^2\right)\ \cos\beta_2 - (\bar{k}^2 - \beta_1^2)\ \cos\beta_1\right]\Bigg\}\frac{1}{\cos\beta_3}$$

APPENDIX G

G.1 : COMPARISON BETWEEN THE READINGS FROM THE CONDENSATE LEVEL METERS AND THE STEAM ORIFICE METER FOR ALL TUBE SIZES

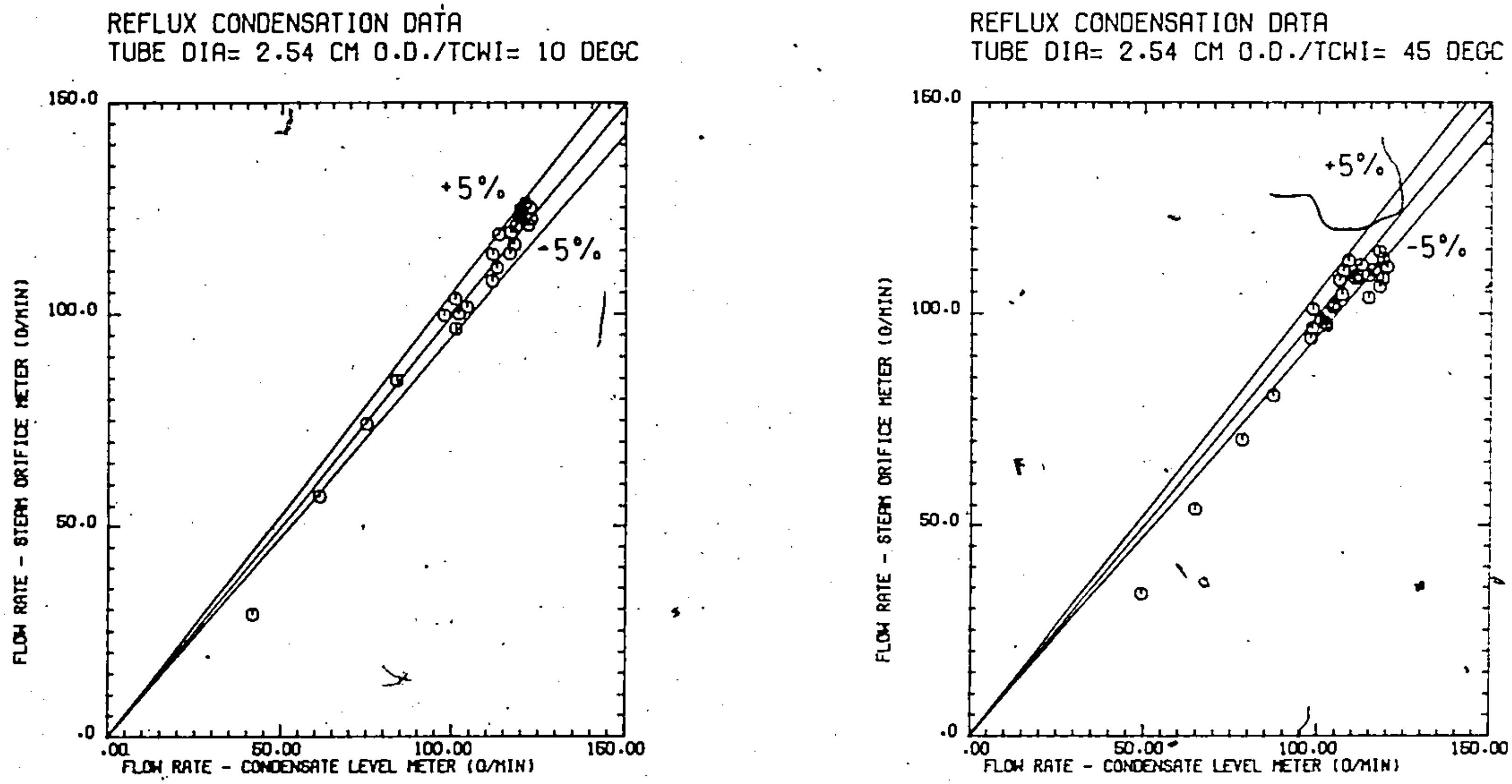

FIGURE G.1 Comparison Between Flow Rates Measured by the Condensate Level Meter and the Steam Orifice Meter for 2.54 cm O.D. Tube

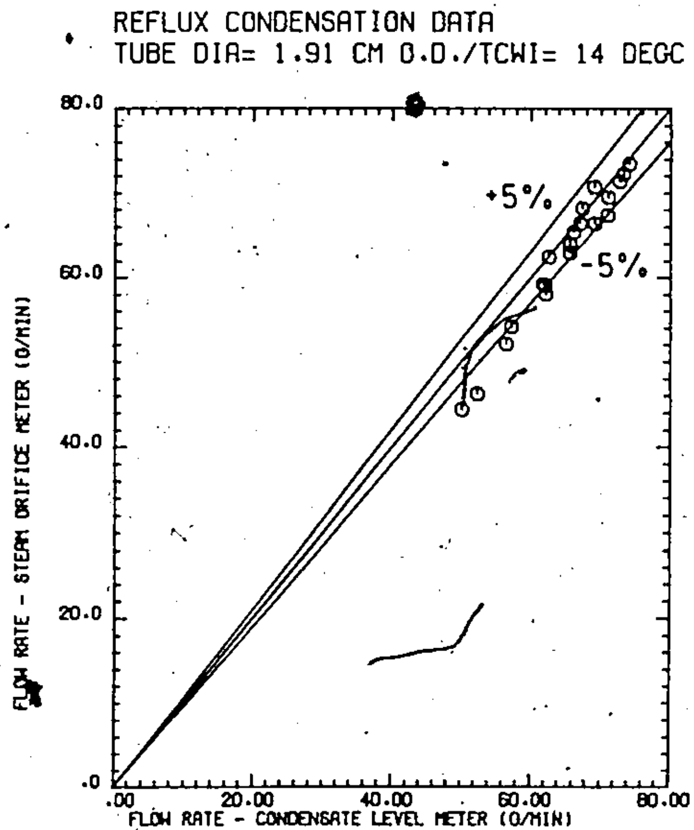

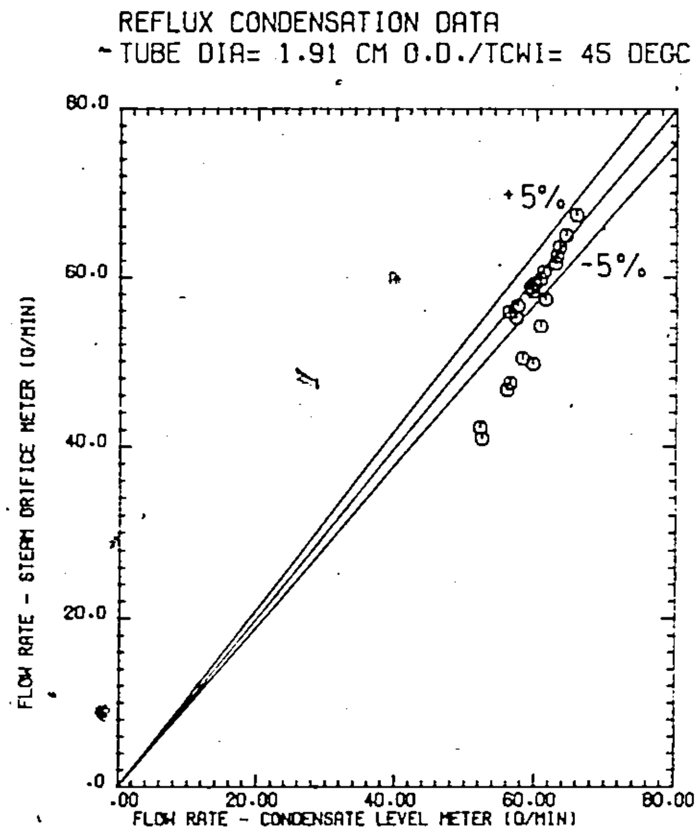

FIGURE G.2 Comparison Between Flow Rates Measured by the Condensate Level Meter and the Steam Orifice Meter for 1.91 cm O.D. Tube

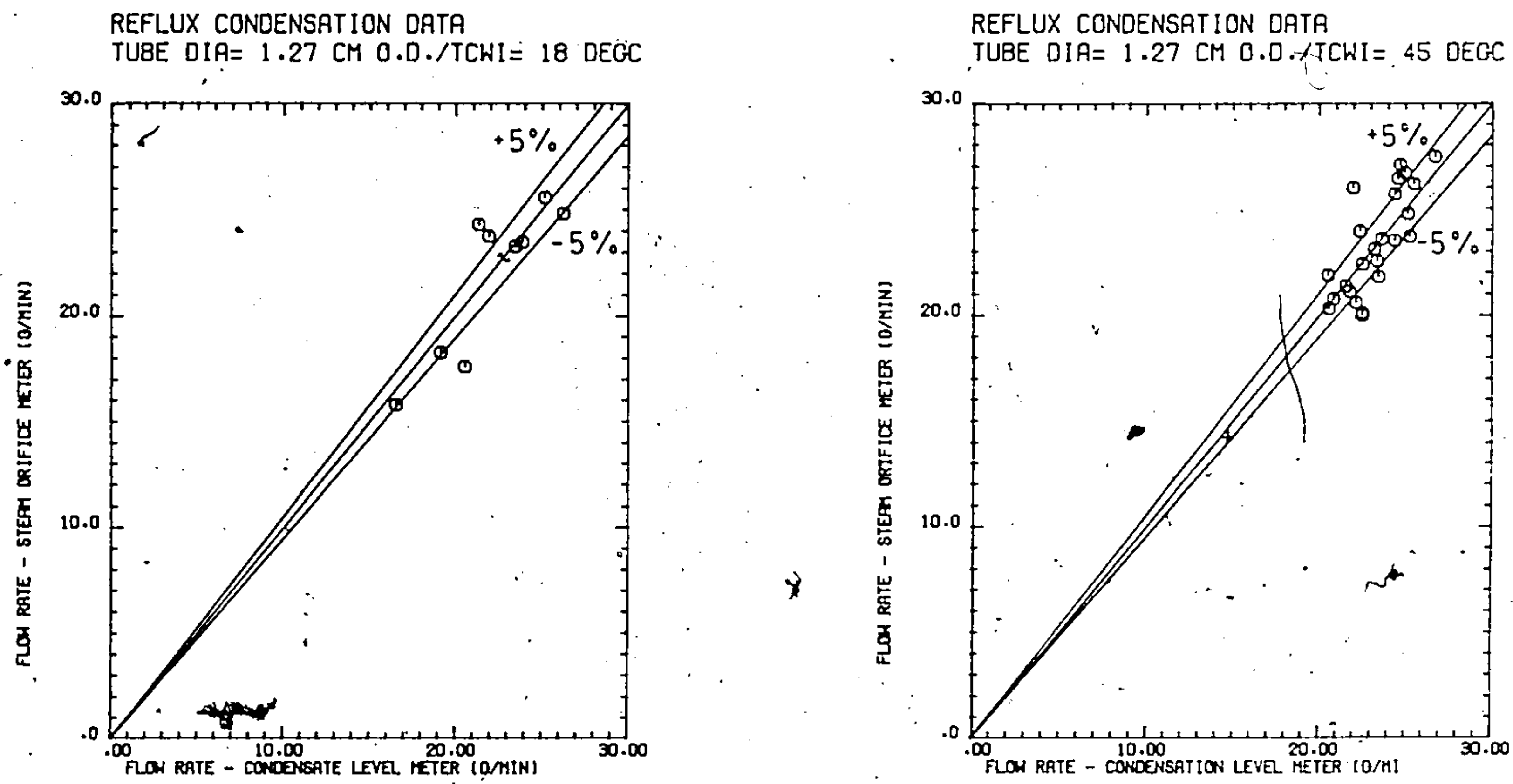

FIGURE G.3 Comparison Between Flow Rates Measured by the Condensate Level Meter and the Steam Orifice Meter for 1.27 cm O.D. Tube

G.2 : LOCAL MEASUREMENTS IN TOTAL REFLUX CONDENSATION

FIGURE G.2.1 : LOCAL MEASUREMENTS IN 2.54 CM O.D. TUBE WITH TCWI = $10^{o}C$

FIGURES G.4 TO G.11 : LOCAL MEASUREMENTS IN 2.54 CM O.D. TUBE WITH TCWI = $10^{o}C$

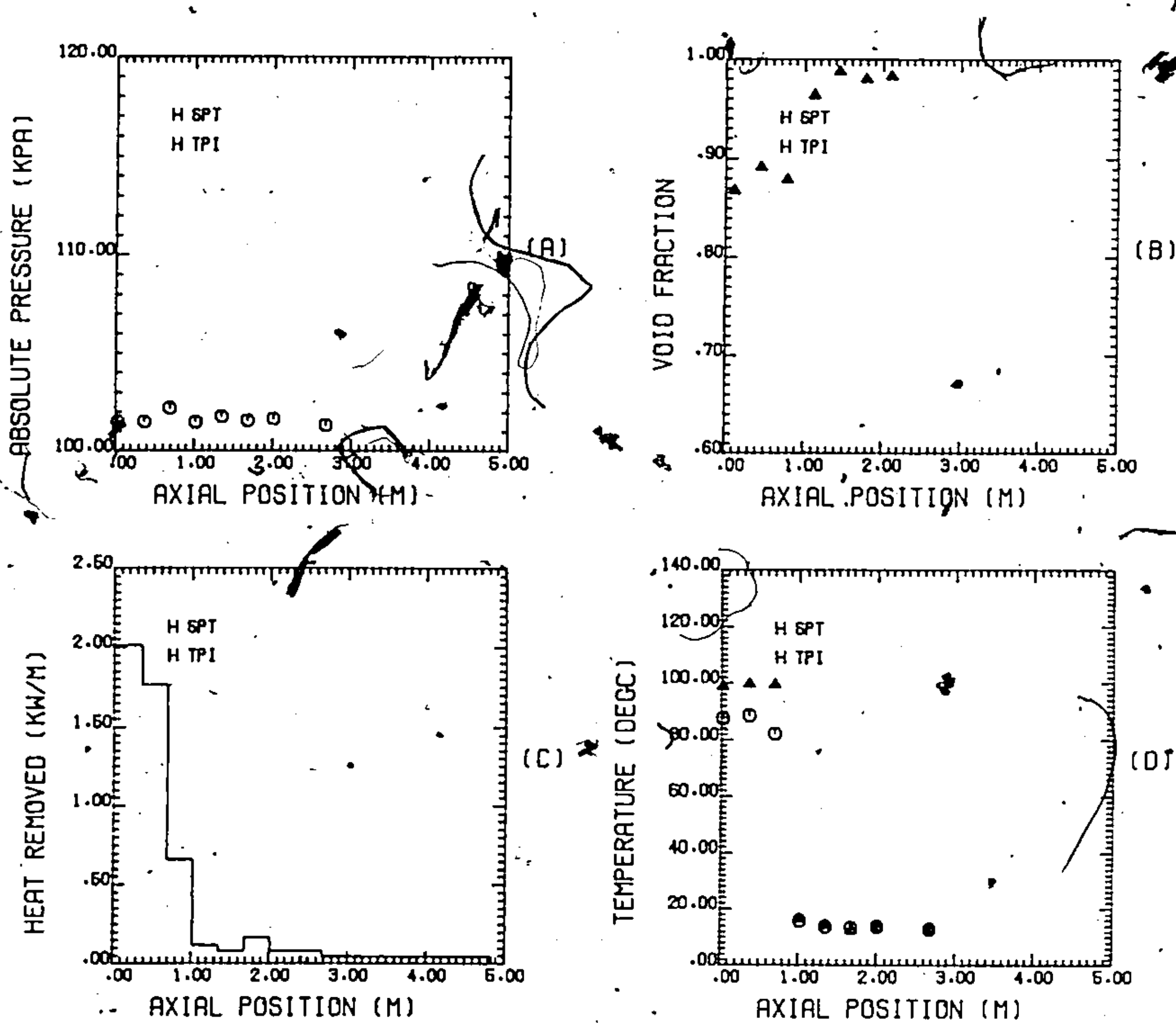

FIGURE G.4
EXPERIMENTAL DATA OF
RUN NO. D20APR4

TCHI=10 DEGC
TUBE DIA= 2.54 CM O.D.
PBP= 101.491 KPA
PUP= 101.325 KPA
STMFLW= 41.88 G/MIN
QRMV= 1.740 KW
SINGLE-PHASE TOP- .70/ .80 M
(ABBREVIATED AS SPT IN THE PLOTS)

TWO-PHASE INTERFACE- .70/ .80 M
(ABBREVIATED AS TPI IN THE PLOTS)

LEGEND OF TEMPERATURE PLOT
⊙ = NEAR WALL
▲ = CENTER LINE

AVERAGE VOID FRACTIONS

MEASURED = .9359
CALCULATED = NOT AVAILABLE

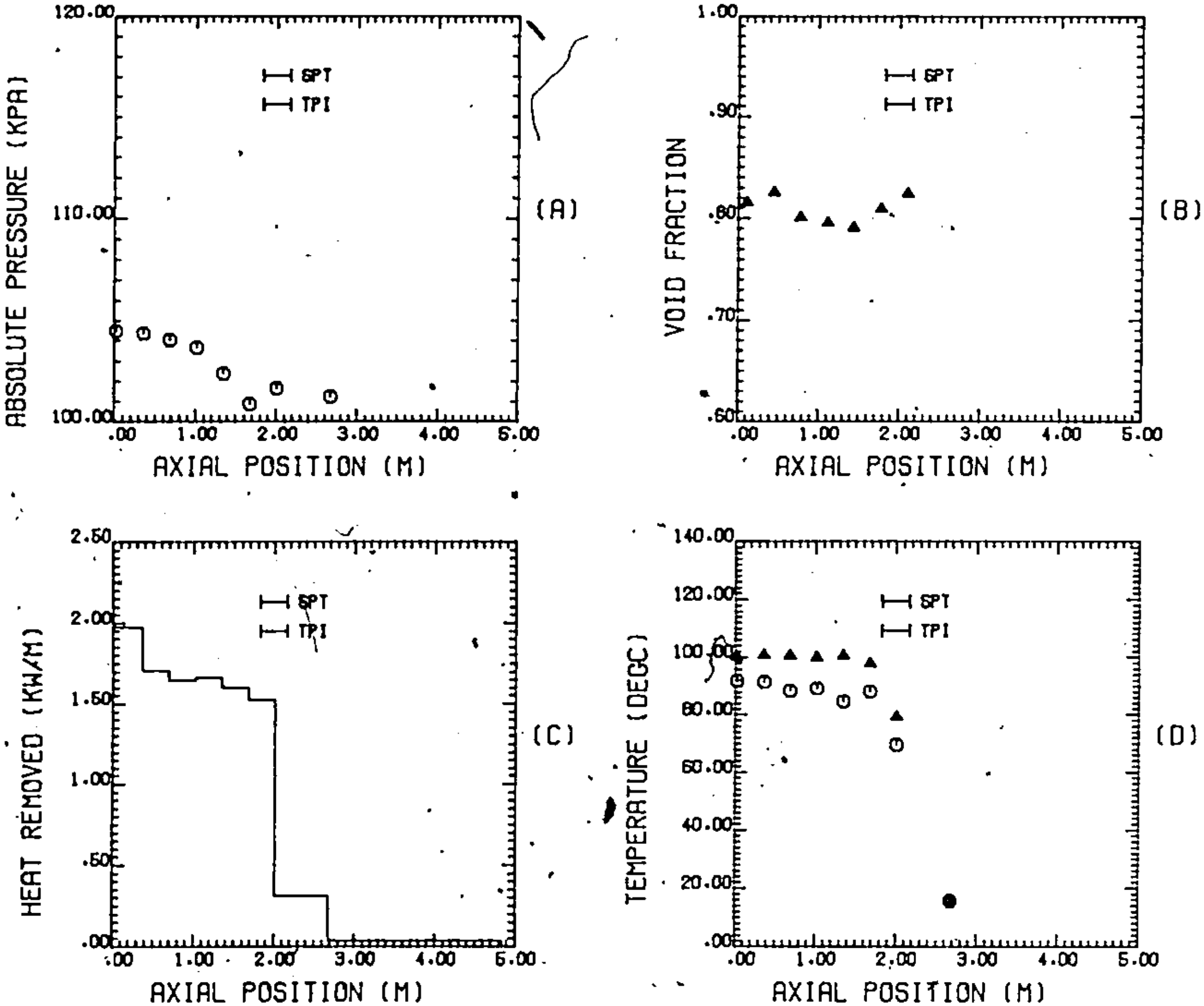

FIGURE G.5
EXPERIMENTAL DATA OF
RUN NO. D23032

TCWI=10 DEGC
TUBE DIA= 2.54 CM O.D.
PBP= 104.507 KPA
PUP= 101.325 KPA
STMFLW= 100.09 G/MIN
QRMV= 3.620 KW
SINGLE-PHASE TOP= 1.82/ 2.16 M
(ABBREVIATED AS SPT IN THE PLOTS)

TWO-PHASE INTERFACE= 1.82/ 2.16 M
(ABBREVIATED AS TPI IN THE PLOTS)

LEGEND OF TEMPERATURE PLOT
⊙ = NEAR WALL
▲ = CENTER LINE

AVERAGE VOID FRACTIONS

MEASURED = .8086
CALCULATED = .8504

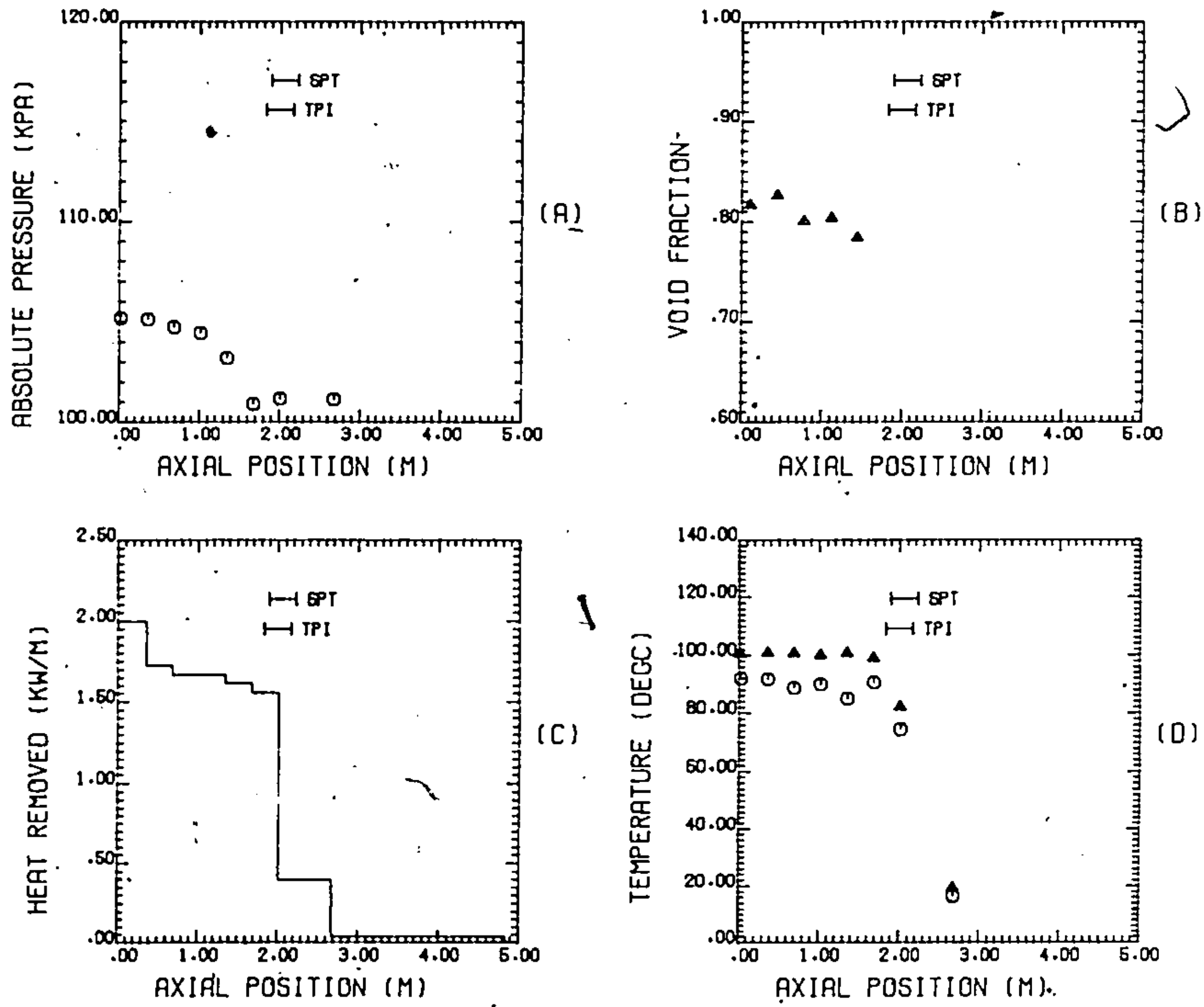

FIGURE G.6
EXPERIMENTAL DATA OF
RUN NO. D23031

TCWI=10 DEGC
TUBE DIA= 2.54 CM O.D.
PBP= 105.259 KPA
PUP= 101.325 KPA
STMFLW= 101.59 G/MIN
QRMV= 3.710 KW
SINGLE-PHASE TOP- 1.89/ 2.23 M
(ABBREVIATED AS SPT IN THE PLOTS)

TWO-PHASE INTERFACE- 1.82/ 2.16 M
(ABBREVIATED AS TPI IN THE PLOTS)

LEGEND OF TEMPERATURE PLOT
⊙ = NEAR WALL
▲ = CENTER LINE

AVERAGE VOID FRACTIONS

MEASURED = .8061
CALCULATED = .8100

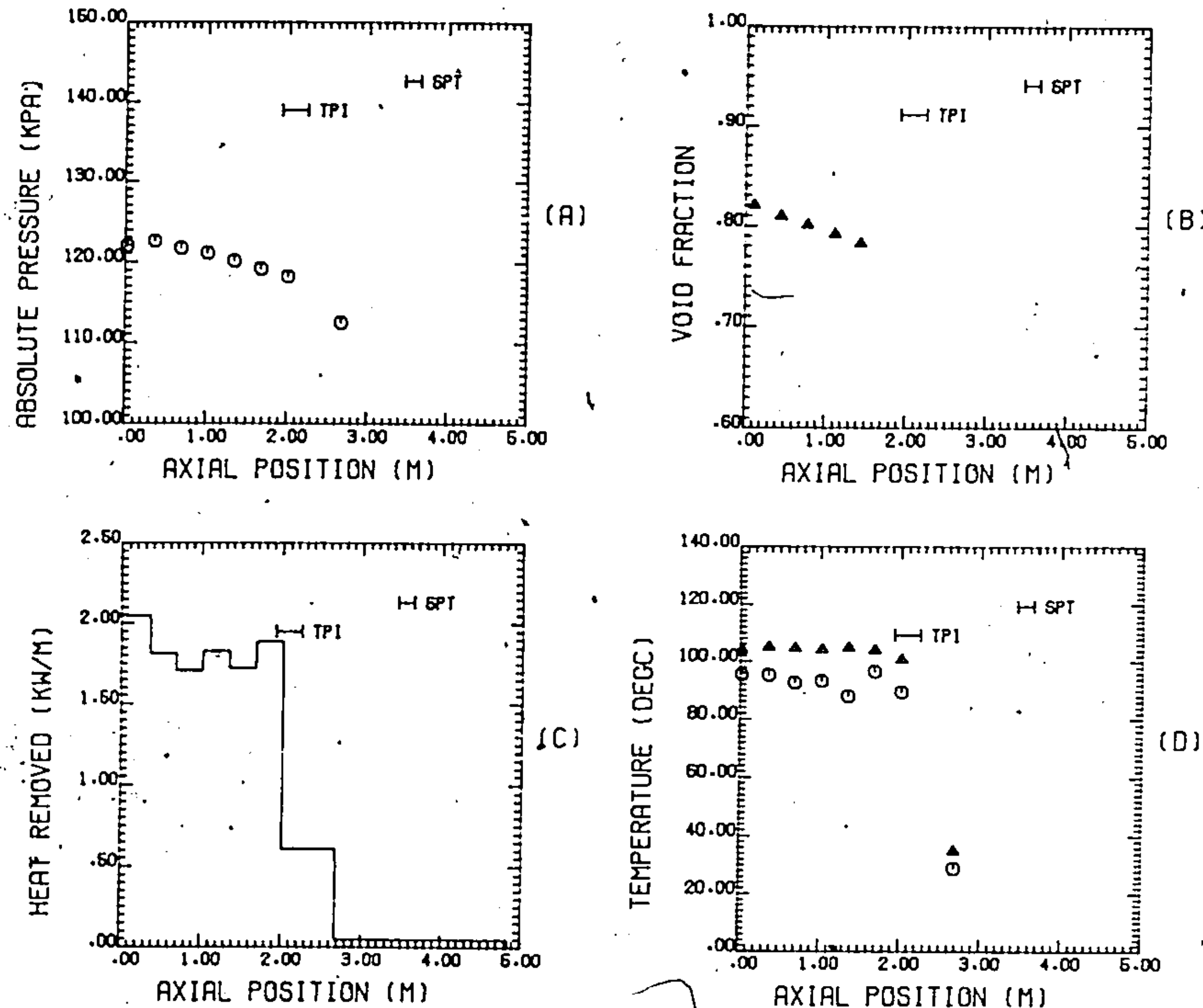

FIGURE G.7
EXPERIMENTAL DATA OF
RUN NO. D05054

TCHI=10 DEGC
TUBE DIA= 2.54 CM O.D.
PBP= 122.945 KPA
PUP= 111.215 KPA
STMFLW= 116.31 G/MIN
QRMV= 4.120 KW
SINGLE-PHASE TOP- 3.45/ 3.65 M
(ABBREVIATED AS SPT IN THE PLOTS)

TWO-PHASE INTERFACE- 1.92/ 2.24 M
(ABBREVIATED AS TPI IN THE PLOTS)

LEGEND OF TEMPERATURE PLOT
⊙ = NEAR WALL
▲ = CENTER LINE

AVERAGE VOID FRACTIONS

MEASURED = .8009
CALCULATED = .8062

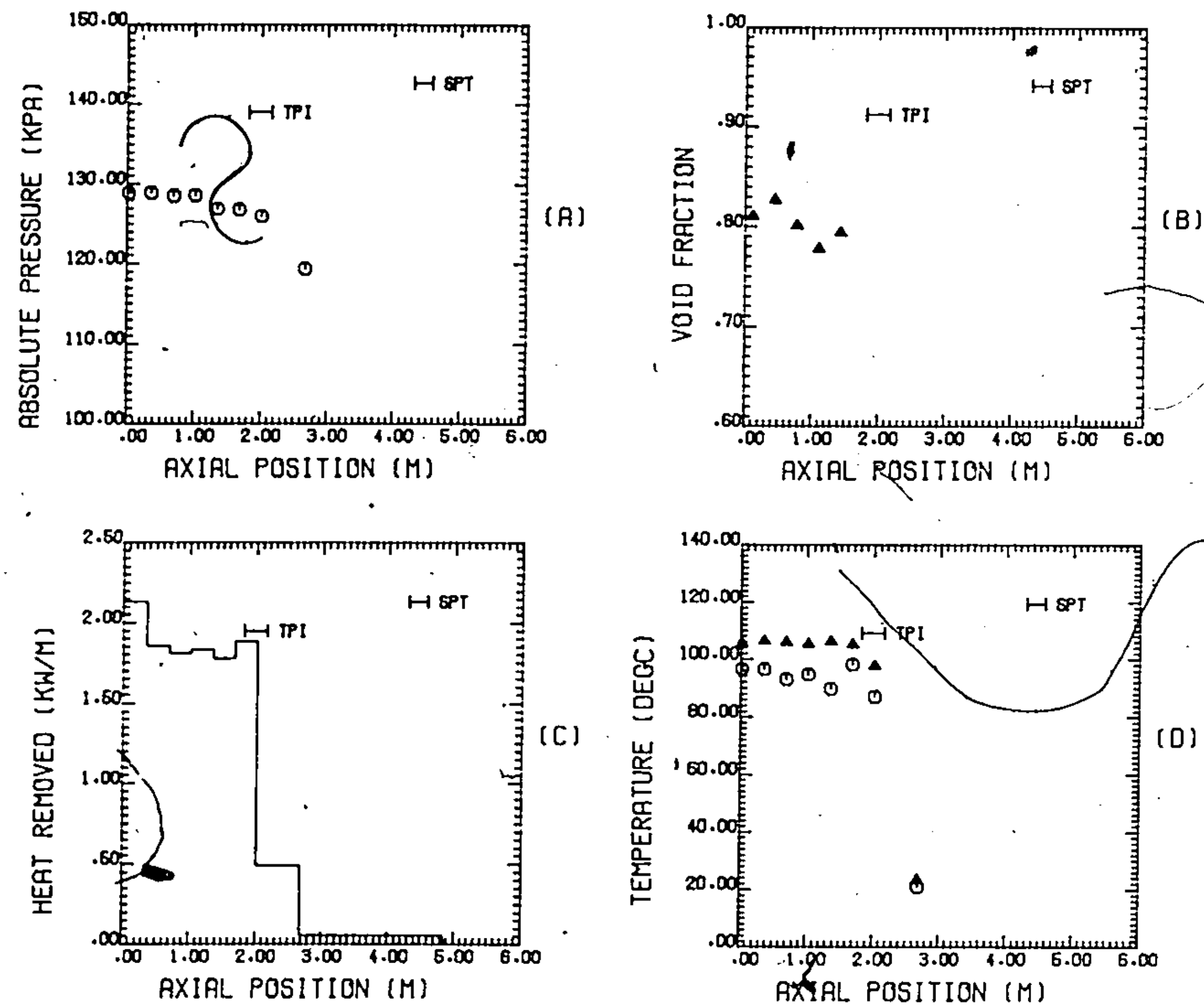

FIGURE G.8
EXPERIMENTAL DATA OF
RUN NO. D22031

TCWI=10 DEGC
TUBE DIA= 2.54 CM O.D.
PBP= 130.004 KPA
PUP= 101.325 KPA
STMFLW= 114.20 G/MIN
QRMV= 4.160 KW
SINGLE-PHASE TOP- 4.30/ 4.58 M
(ABBREVIATED AS SPT IN THE PLOTS)

TWO-PHASE INTERFACE- 1.82/ 2.16 M
(ABBREVIATED AS TPI IN THE PLOTS).

LEGEND OF TEMPERATURE PLOT
⊙ = NEAR WALL
▲ = CENTER LINE

AVERAGE VOID FRACTIONS

MEASURED = .8022
CALCULATED = .8482

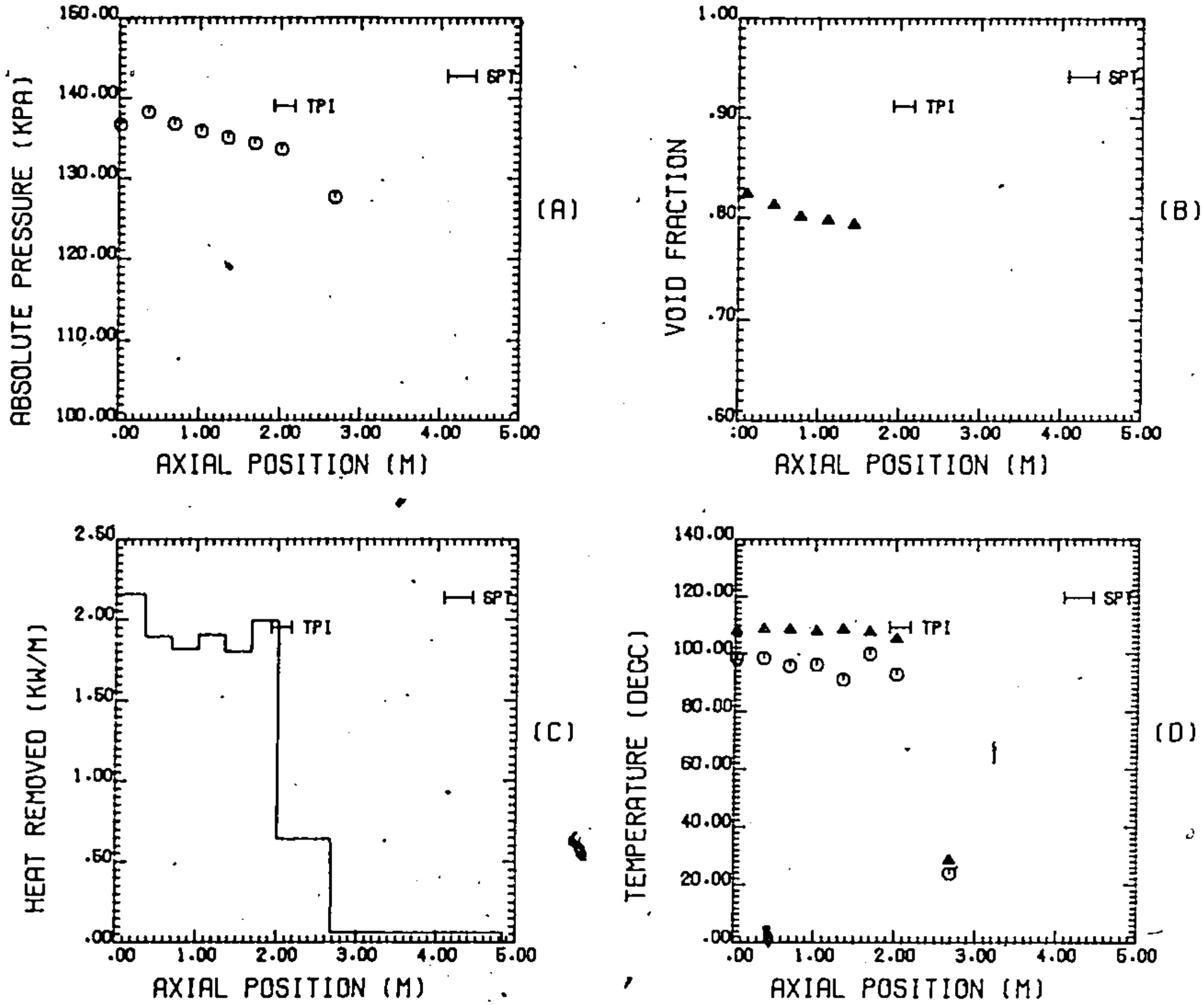

FIGURE G.9
EXPERIMENTAL DATA OF
RUN NO. D05051

TCWI=10 DEGC
TUBE DIA= 2.54 CM O.D.
PBP= 138.138 KPA
PUP= 111.217 KPA
STMFLW= 122.34 G/MIN
QRMV= 4.350 KW
SINGLE-PHASE TOP- 4.08/ 4.44 M
(ABBREVIATED AS SPT IN THE PLOTS)

TWO-PHASE INTERFACE- 1.92/ 2.18 M
(ABBREVIATED AS TPI IN THE PLOTS)

LEGEND OF TEMPERATURE PLOT
ʘ = NEAR WALL
▲ = CENTER LINE

AVERAGE VOID FRACTIONS

MEASURED = .8059
CALCULATED = .8434

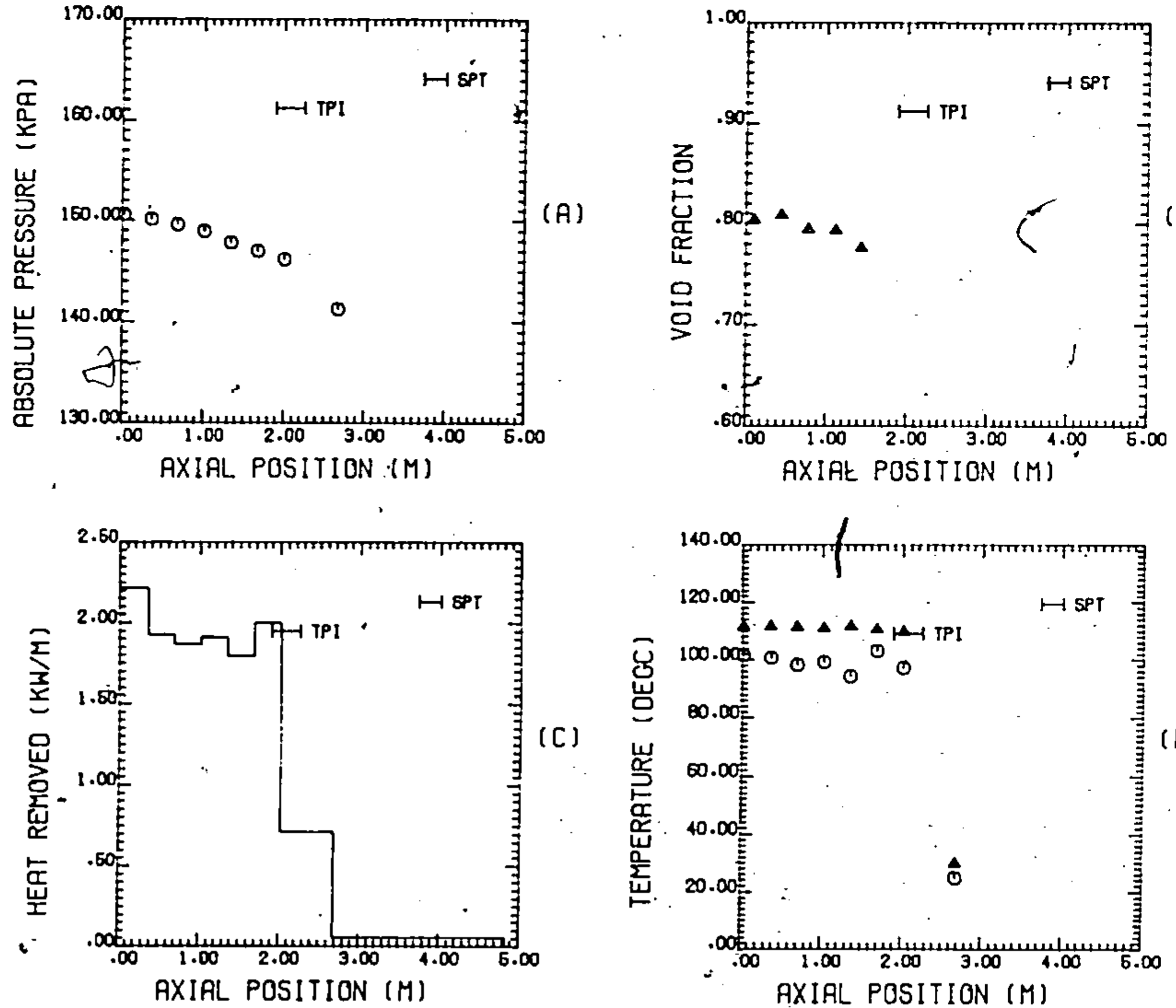

FIGURE G.10
EXPERIMENTAL DATA OF
RUN NO. D09052

TCWI=10 DEGC
TUBE DIA= 2.54 CM O.D.
PBP= 150.895 KPA
PUP= 129.214 KPA
STMFLW= 122.63 G/MIN
QRMV= 4.440 KW
SINGLE-PHASE TOP- 3.73/ 4.01 M
(ABBREVIATED AS SPT IN THE PLOTS)

TWO-PHASE INTERFACE- 1.89/ 2.25 M
(ABBREVIATED AS TPI IN THE PLOTS)

LEGEND OF TEMPERATURE PLOT
⊙ = NEAR WALL
▲ = CENTER LINE

AVERAGE VOID FRACTIONS

MEASURED = .7950
CALCULATED = .7704

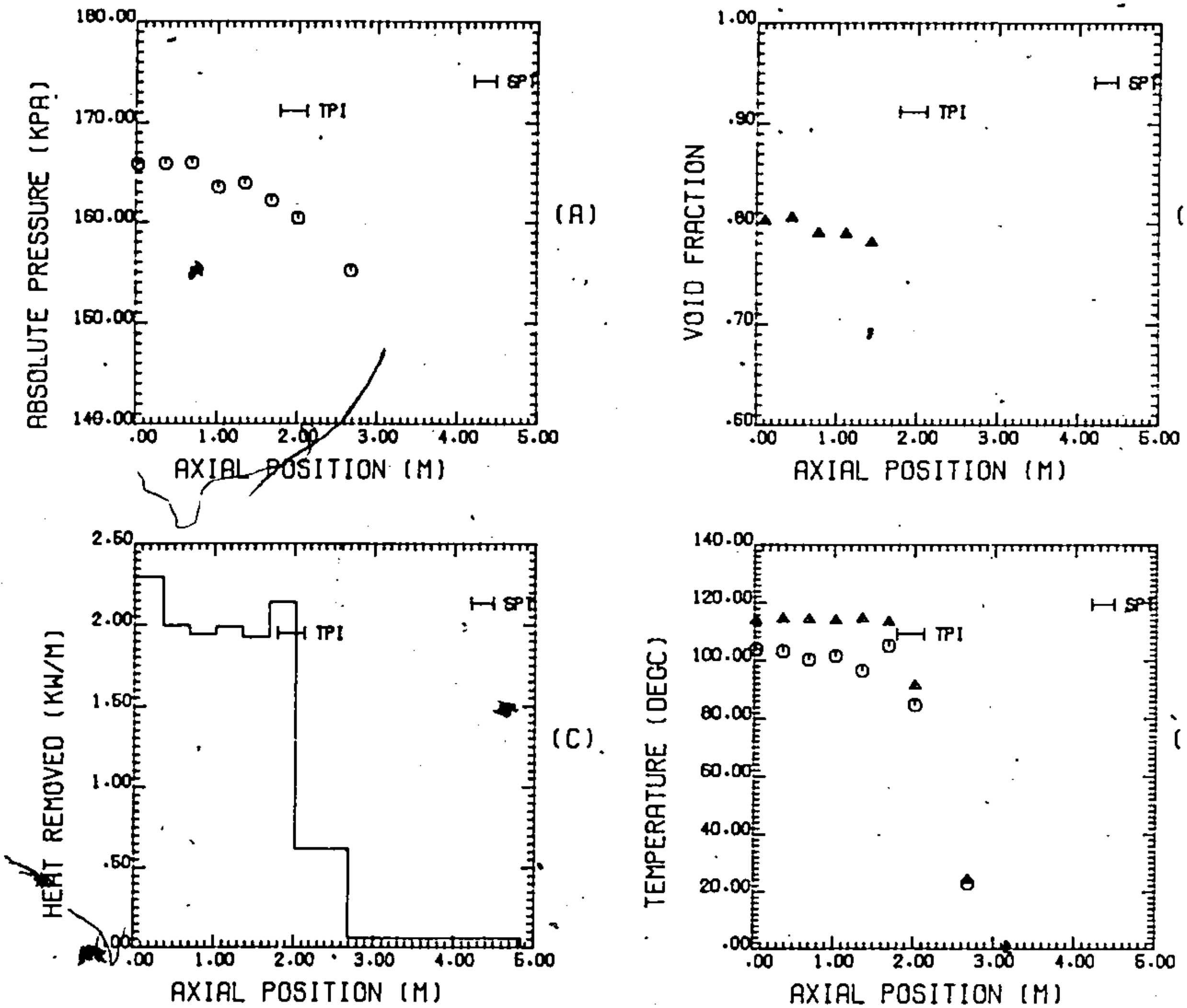

FIGURE G.11
EXPERIMENTAL DATA OF
RUN NO. D10051

TCWI=10 DEGC
TUBE DIA= 2.54 CM O.D.
PBP= 165.907 KPA
PUP= 126:010 KPA
STMFLW= 126.01 G/MIN
QRMV= 4.580 KW

SINGLE-PHASE TOP- 4.20/ 4.48 M
(ABBREVIATED AS SPT IN THE PLOTS)

TWO-PHASE INTERFACE- 1.78/ 2.12 M
(ABBREVIATED AS TPI IN THE PLOTS)

LEGEND OF TEMPERATURE PLOT
Θ = NEAR WALL
▲ = CENTER LINE

AVERAGE VOID FRACTIONS

MEASURED = .7935
CALCULATED = .7135

FIGURE G.2.2 : LOCAL MEASUREMENTS IN 2.54 CM O.D. TUBE WITH TCWI = 45^{o}C

FIGURES G.12 TO G.19 : LOCAL MEASUREMENTS IN 2.54 CM O.D. TUBE WITH TCWI = 45^{o}C

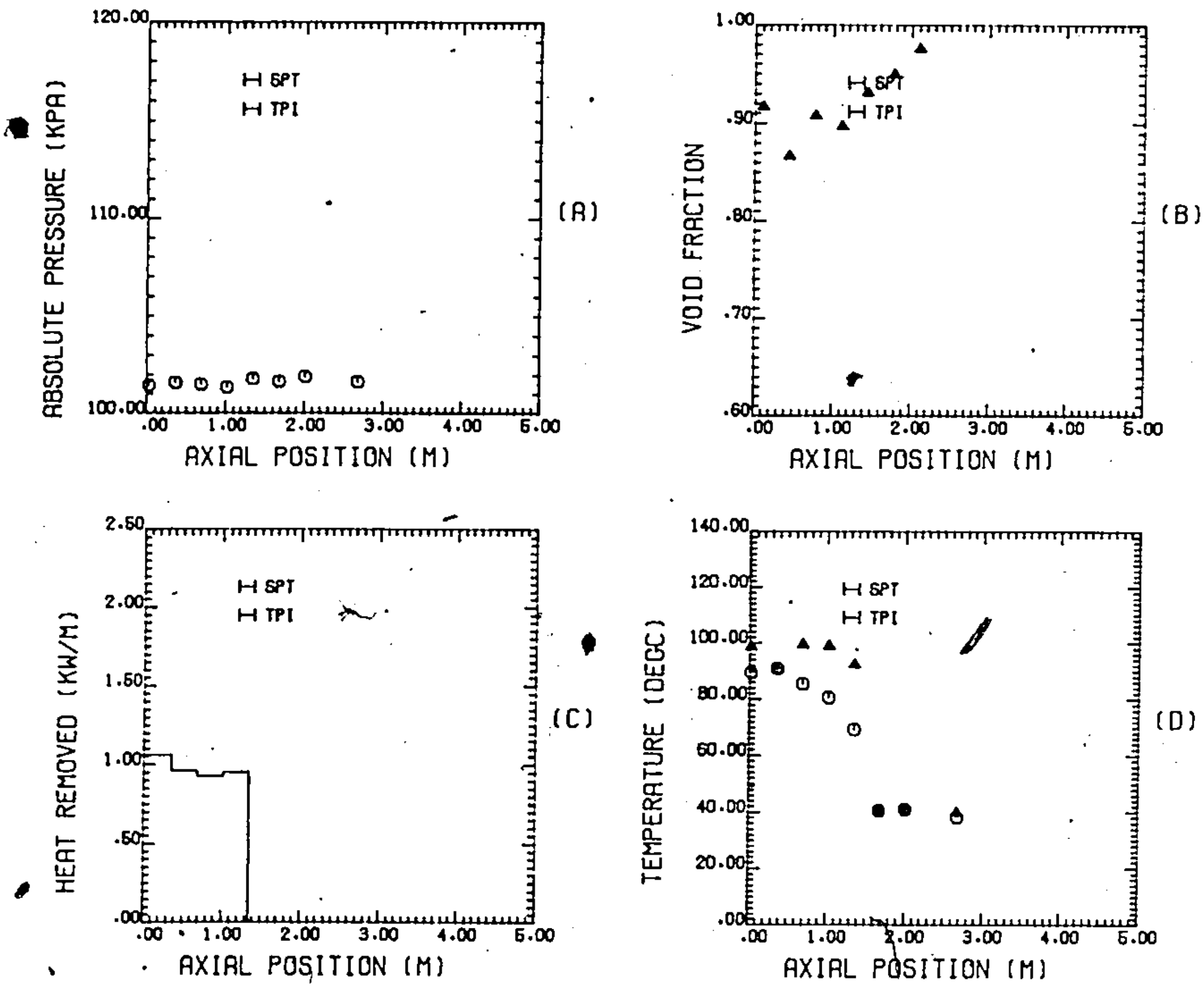

FIGURE G.12
EXPERIMENTAL DATA OF
RUN NO. D27044

TCWI= 45 DEGC
TUBE DIA= 2.54 CM O.D.
PBP= 101.449 KPA
PUP= 101.325 KPA
STMFLW= 49.36 G/MIN
QRMV= 1.060 KW
SINGLE-PHASE TOP- 1.20/ 1.40 M
(ABBREVIATED AS SPT IN THE PLOTS)

TWO-PHASE INTERFACE- 1.20/ 1.40 M
(ABBREVIATED AS TPI IN THE PLOTS)

LEGEND OF TEMPERATURE PLOT
⊙ = NEAR WALL
▲ = CENTER LINE

AVERAGE VOID FRACTIONS

MEASURED = .9205
CALCULATED = NOT AVAILABLE

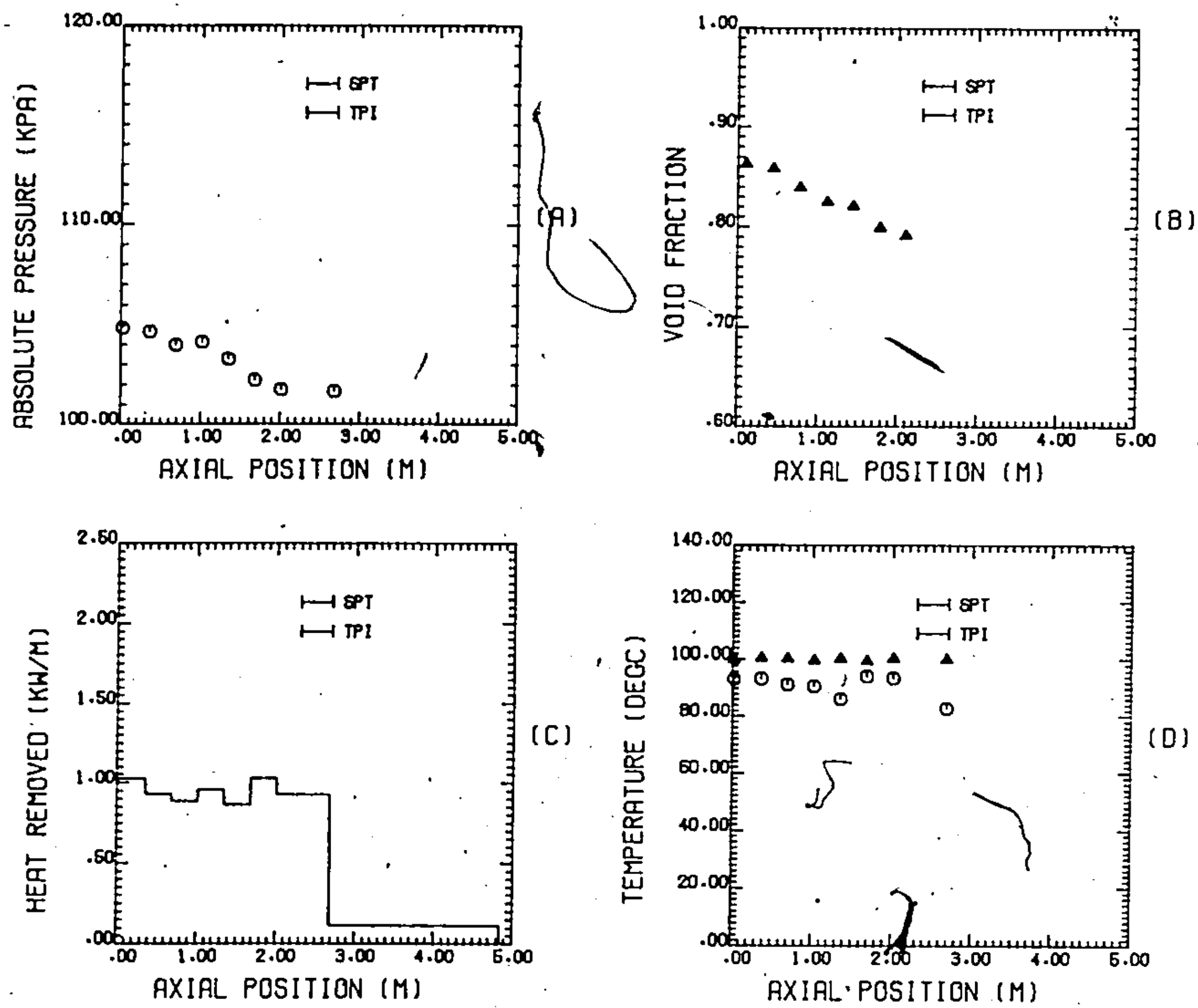

FIGURE G.13
EXPERIMENTAL DATA OF
RUN NO. D26041

TCWI= 45 DEGC
TUBE DIA= 2.54 CM O.D.
PBP= 104.988 KPA
PUP= 101.325 KPA
STMFLW= 97.06 G/MIN
QRMV= 2.70 KW
SINGLE-PHASE TOP- 2.30/ 2.70 M
(ABBREVIATED AS SPT IN THE PLOTS)

TWO-PHASE INTERFACE- 2.30/ 2.70 M
(ABBREVIATED AS TPI IN THE PLOTS)

LEGEND OF TEMPERATURE PLOT
⊙ = NEAR WALL
▲ = CENTER LINE

AVERAGE VOID FRACTIONS

MEASURED = .8280
CALCULATED = .8644

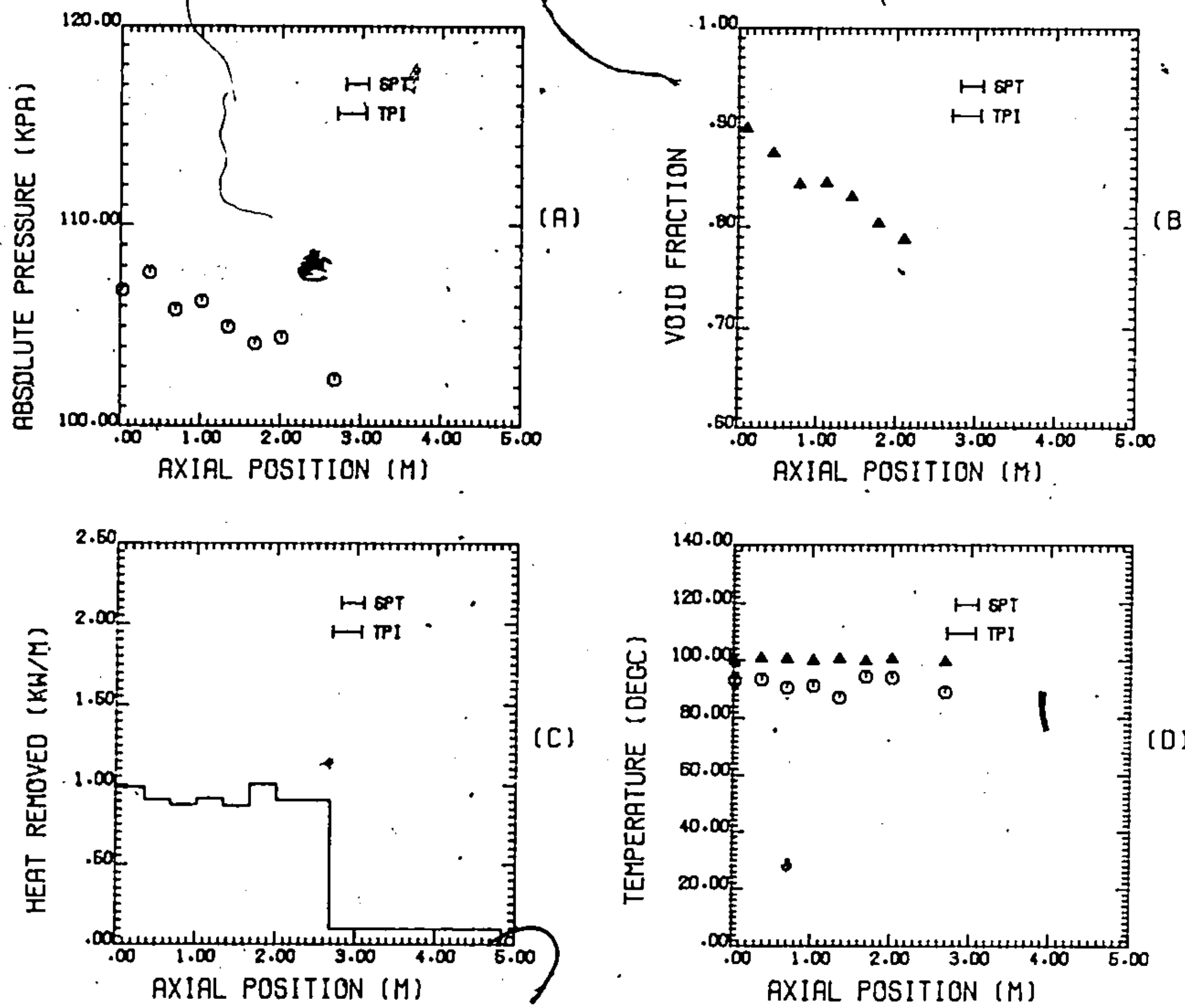

FIGURE G.14
EXPERIMENTAL DATA OF
RUN NO. D21034

TCWI= 45 DEGC
TUBE DIA= 2.54 CM O.D.
PBP= 106.784 KPA
PUP= 101.325 KPA
STMFLW= 98.54 G/MIN
QRMV= 2.610 KW
SINGLE-PHASE TOP- 2.83/ 3.08 M
(ABBREVIATED AS SPT IN THE PLOTS)

TWO-PHASE INTERFACE- 2.70/ 3.06 M
(ABBREVIATED AS TPI IN THE PLOTS)

LEGEND OF TEMPERATURE PLOT
⊙ = NEAR WALL
▲ = CENTER LINE

AVERAGE VOID FRACTIONS

MEASURED = .8403
CALCULATED = .9141

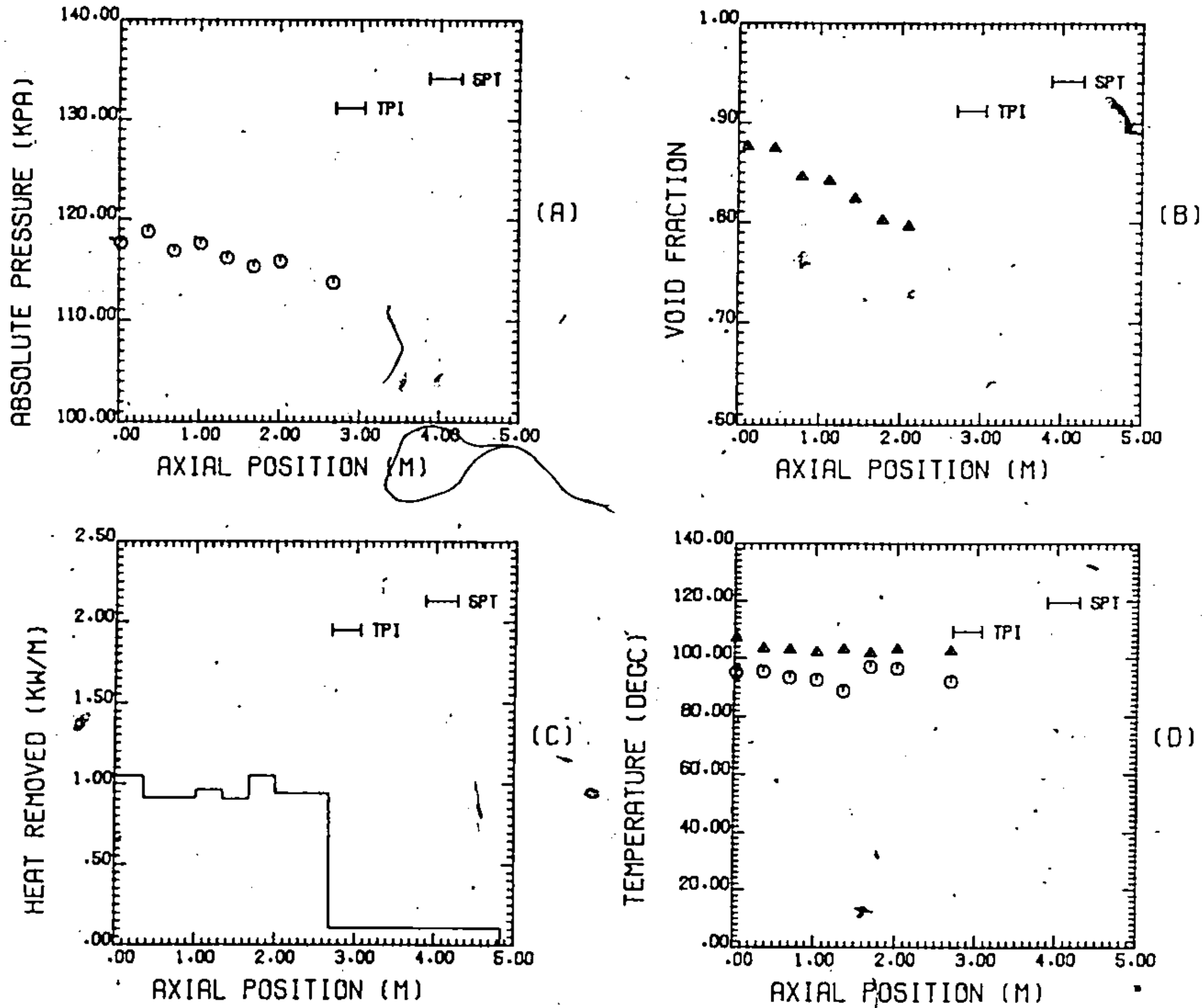

FIGURE G.15
EXPERIMENTAL DATA OF
RUN NO. D21031

TCWI= 45 DEGC
TUBE DIA= 2.54 CM O.D.
PBP= 118.391 KPA
PUP= 101.325 KPA
STMFLW= 102.15 G/MIN
QRMV= 2.740 KW
SINGLE-PHASE TOP- 3.87/ 4.27 M
(ABBREVIATED AS SPT IN THE PLOTS)

TWO-PHASE INTERFACE- 2.70/ 3.06 M
(ABBREVIATED AS TPI IN THE PLOTS)

LEGEND OF TEMPERATURE PLOT
⊙ = NEAR WALL
▲ = CENTER LINE

AVERAGE VOID FRACTIONS

MEASURED = .8365
CALCULATED = .8557

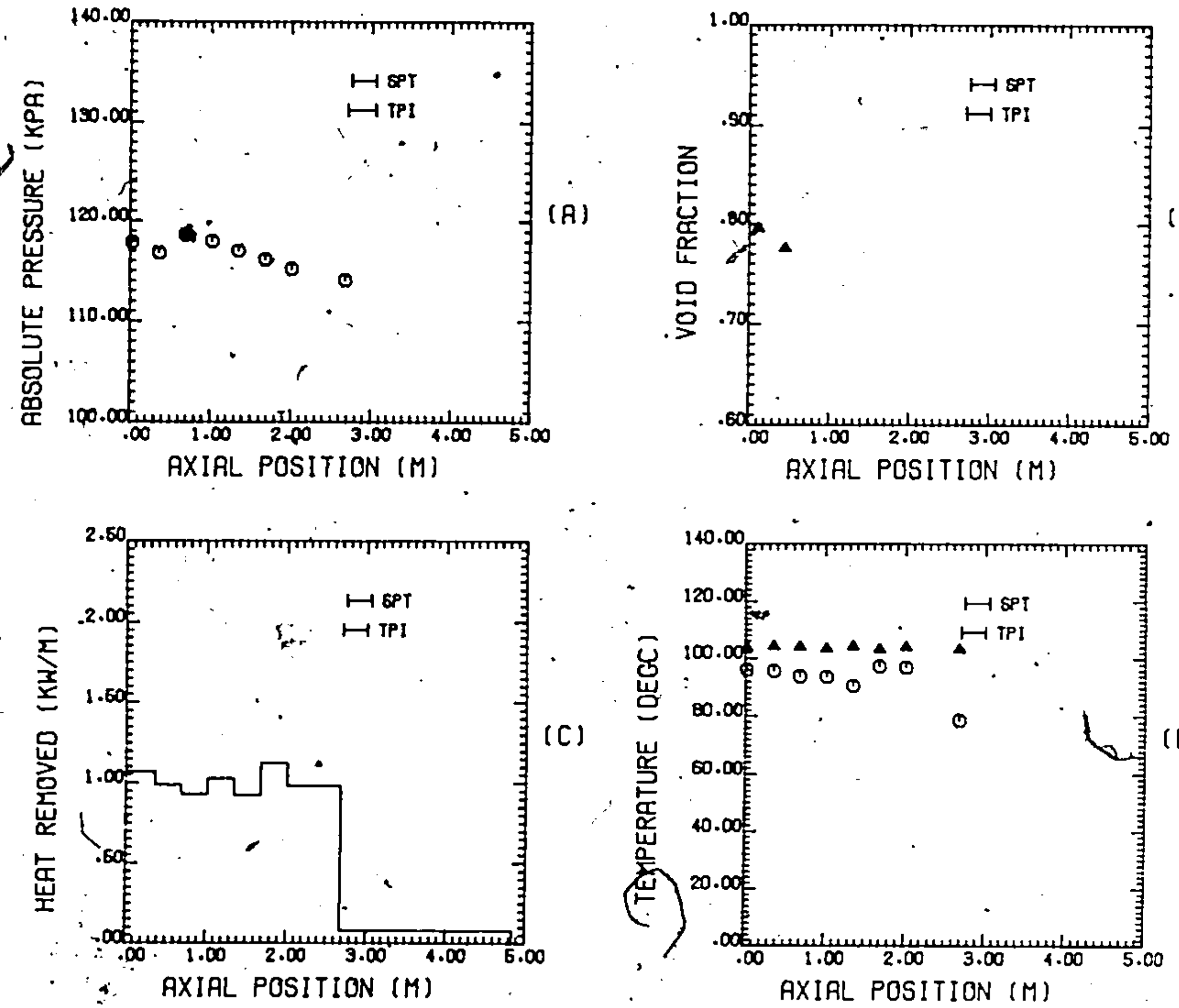

FIGURE G.16
EXPERIMENTAL DATA OF
RUN NO. D270

TCWI= 45 DEGC
TUBE DIA= 2.54 CM O.D.
PBP= 121.990 KPA
PUP= 113.760 KPA
STMFLW= 104.39 G/MIN
QRMV= 2.790 KW

SINGLE-PHASE TOP- 2.75/ 3.05 M
(ABBREVIATED AS SPT IN THE PLOTS)

TWO-PHASE INTERFACE- 2.70/ 3.00 M
(ABBREVIATED AS TPI IN THE PLOTS)

LEGEND OF TEMPERATURE PLOT
⊙ = NEAR WALL
▲ = CENTER LINE

AVERAGE VOID FRACTIONS

MEASURED = .7860
CALCULATED = .8553

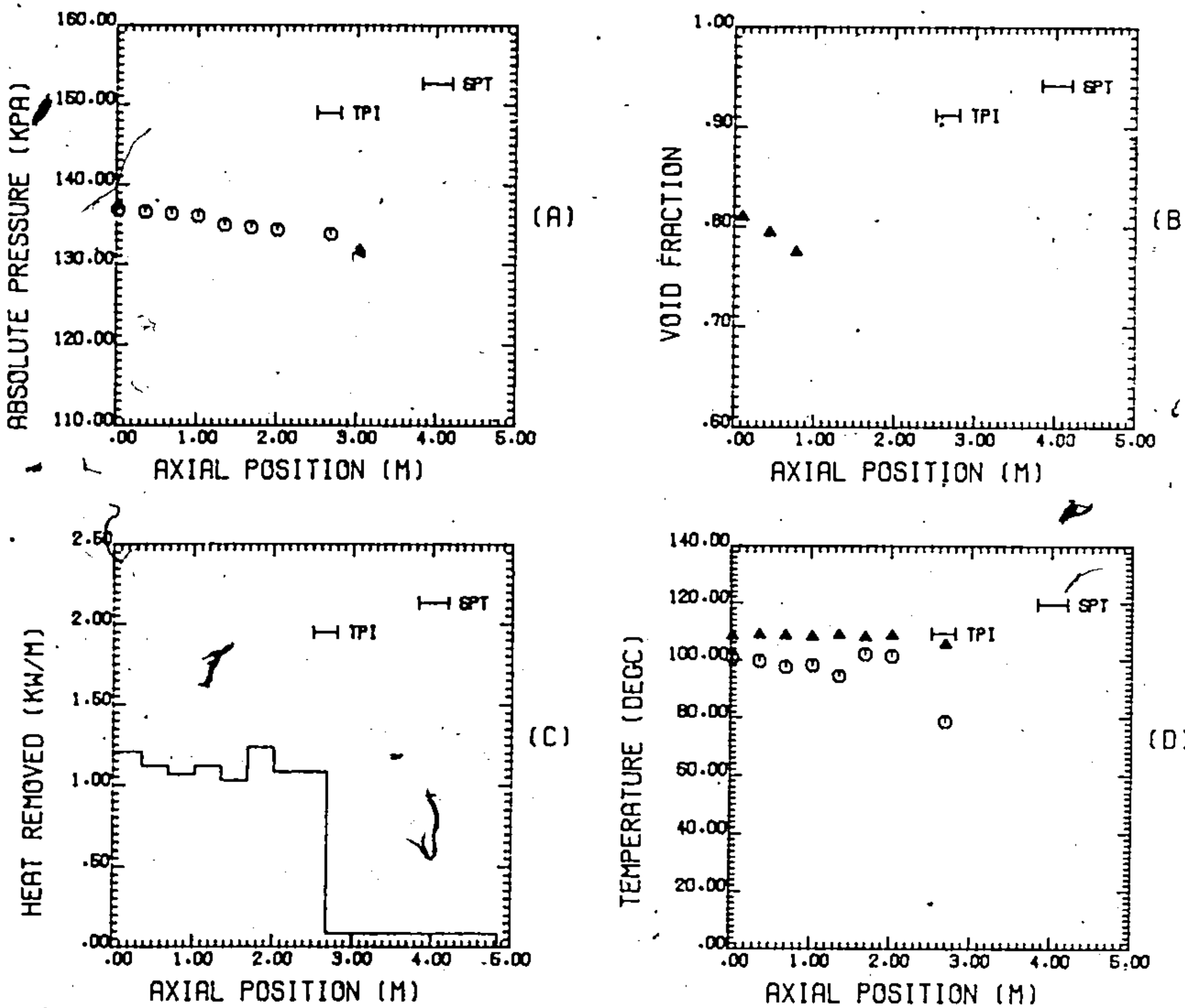

FIGURE G.17
EXPERIMENTAL DATA OF
RUN NO. D26063

TCWI= 45 DEGC
TUBE DIA= 2.54 CM O.D.
PBP= 138.240 KPA
PUP= 123.448 KPA
STMFLW= 109.86 G/MIN
QRMV= 3.110 KW
SINGLE-PHASE TOP- 3.82/ 4.20 M
(ABBREVIATED AS SPT IN THE PLOTS)

TWO-PHASE INTERFACE- 2.50/ 2.80 M
(ABBREVIATED AS TPI IN THE PLOTS)

LEGEND OF TEMPERATURE PLOT
⊙ = NEAR WALL
▲ = CENTER LINE

AVERAGE VOID FRACTIONS

MEASURED = .7927

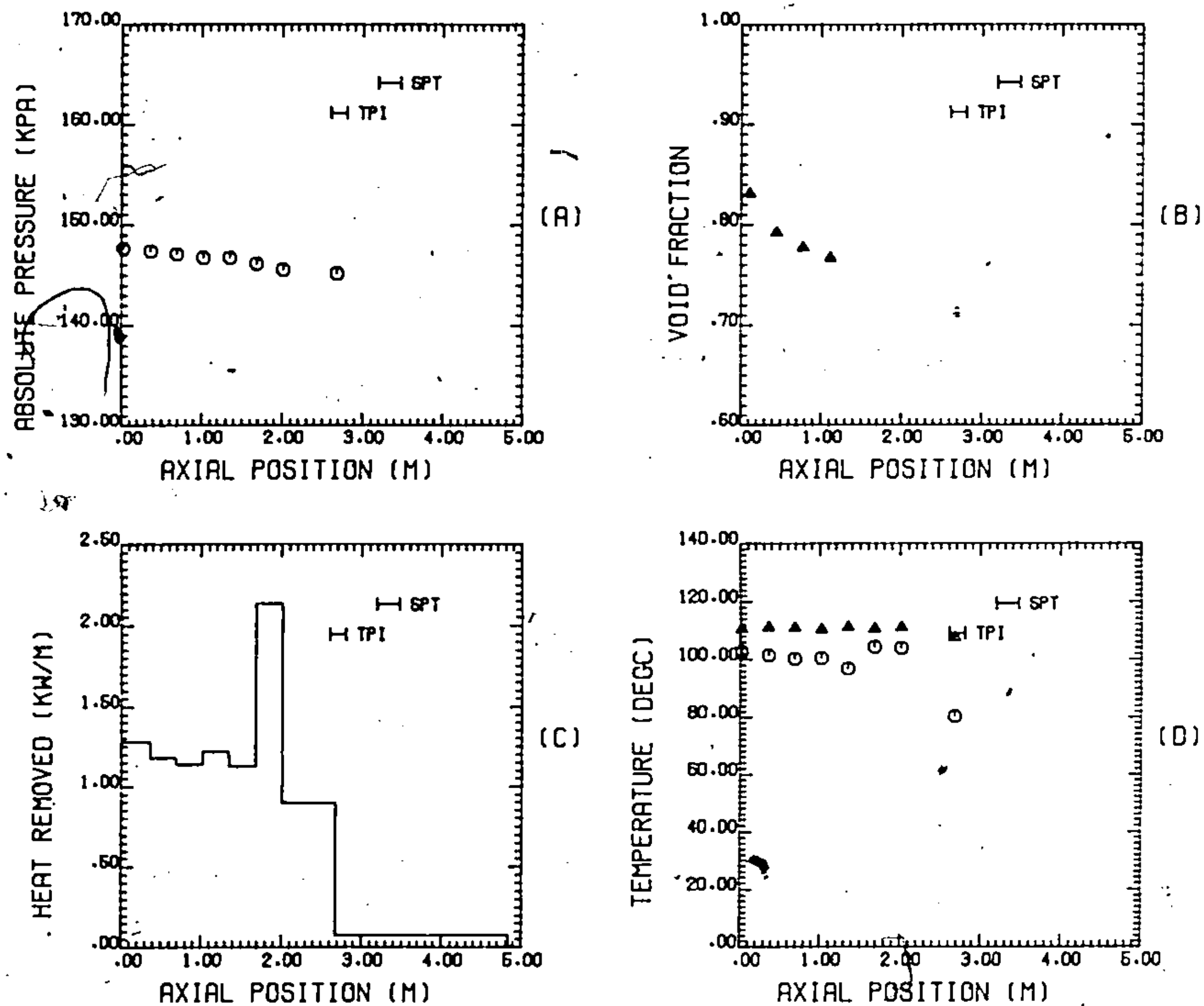

FIGURE G.18
EXPERIMENTAL DATA OF
RUN NO. D25062

TCWI=45 DEGC
TUBE DIA= 2.54 CM O.D.
PBP= 149.850 KPA
PUP= 134.625 KPA
STMFLW= 112.77 G/MIN
QRMV= 3.390 KW
SINGLE-PHASE TOP- 3.19/ 3.47 M
(ABBREVIATED AS SPT IN THE PLOTS)

TWO-PHASE INTERFACE- 2.60/ 2.80 M
(ABBREVIATED AS TPI IN THE PLOTS)

LEGEND OF TEMPERATURE PLOT
⊙ = NEAR WALL
▲ = CENTER LINE

AVERAGE VOID FRACTIONS

MEASURED = .7916
CALCULATED = .8869

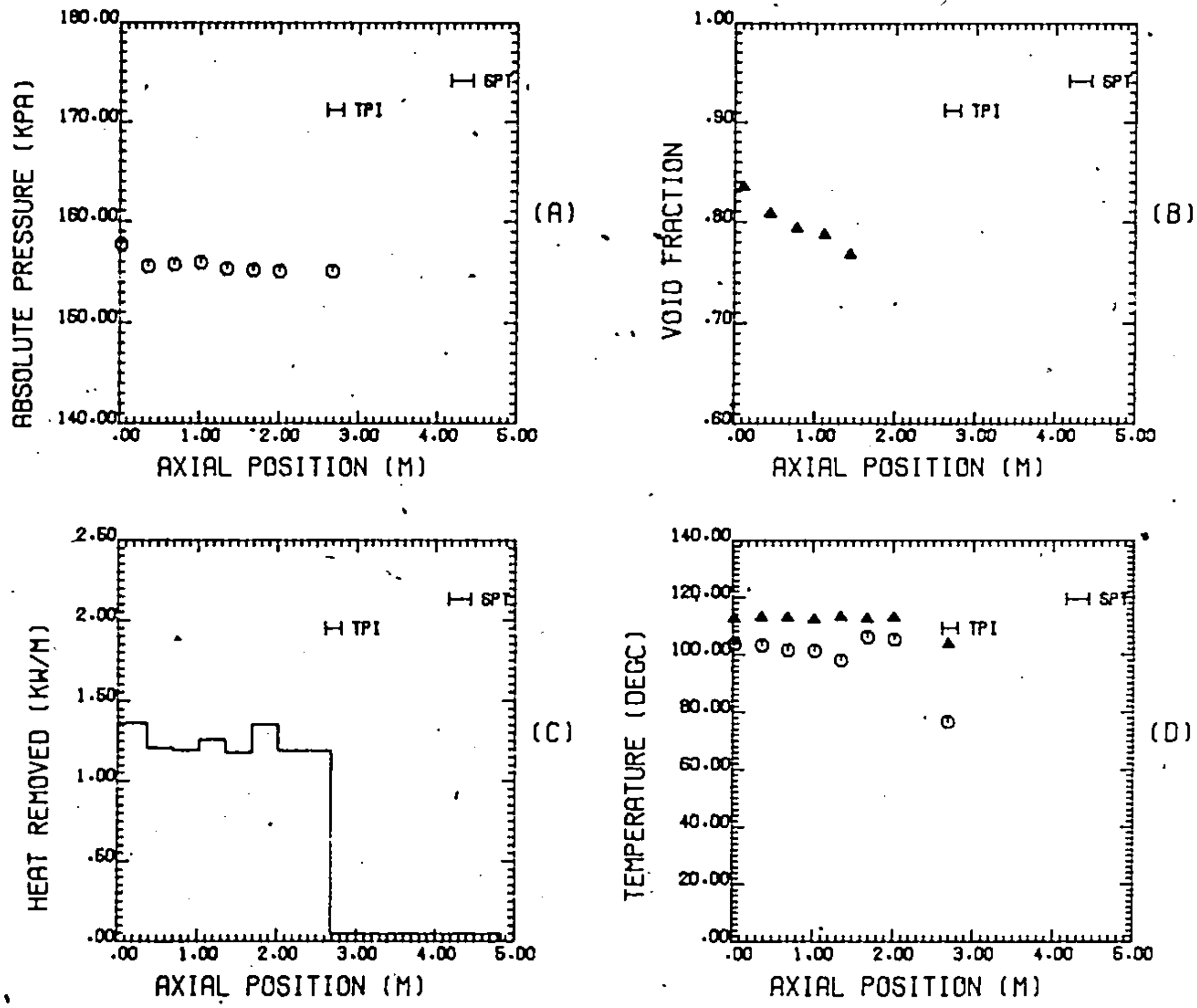

FIGURE G.19
EXPERIMENTAL DATA OF
RUN NO. D24061

TCWI= 45 DEGC
TUBE DIA= 2.54 CM O.D.
PBP= 164.146 KPA
PUP= 138.348 KPA
STMFLW= 110.89 G/MIN
QRMV= 3.340 KW
SINGLE-PHASE TOP= 4.16/ 4.44 M
(ABBREVIATED AS SPT IN THE PLOTS)

TWO-PHASE INTERFACE= 2.60/ 2.80 M
(ABBREVIATED AS TPI IN THE PLOTS)

LEGEND OF TEMPERATURE PLOT
⊙ = NEAR WALL
▲ = CENTER LINE

AVERAGE VOID FRACTIONS

MEASURED = .7980
CALCULATED = .8644

FIGURE G.2.3 : LOCAL MEASUREMENTS IN 1.91 CM O.D. TUBE WITH TCWI = 14°C

FIGURES G.20 TO G.27 : LOCAL MEASUREMENTS IN 1.91 CM O.D. TUBE WITH TCWI = 14°C

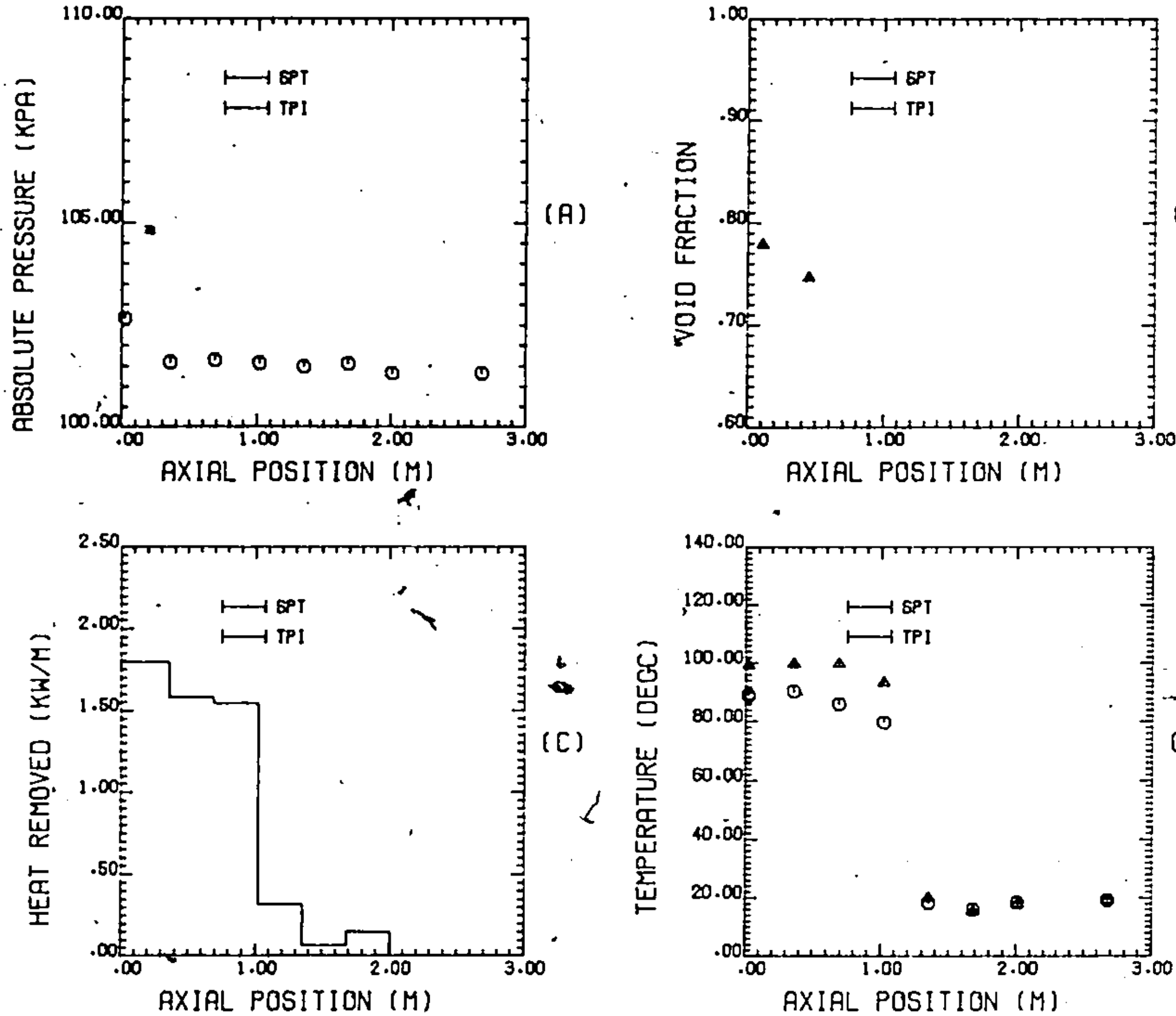

FIGURE G.20
EXPERIMENTAL DATA OF
RUN NO. D14103

TCWI=14 DEGC
TUBE DIA= 1.91 CM O.D.
PBP= 102.668 KPA
PUP= 101.325 KPA
STMFLW= 52.05 G/MIN
QRMV= 1.7944 KW
SINGLE-PHASE TOP- .75/ 1.07 M
(ABBREVIATED AS SPT IN THE PLOTS)

TWO-PHASE INTERFACE- .75/ 1.07 M
(ABBREVIATED AS TPI IN THE PLOTS)

LEGEND OF TEMPERATURE PLOT
O = NEAR WALL
Δ = CENTER LINE

AVERAGE VOID FRACTIONS

MEASURED = .7188
CALCULATED = .7428

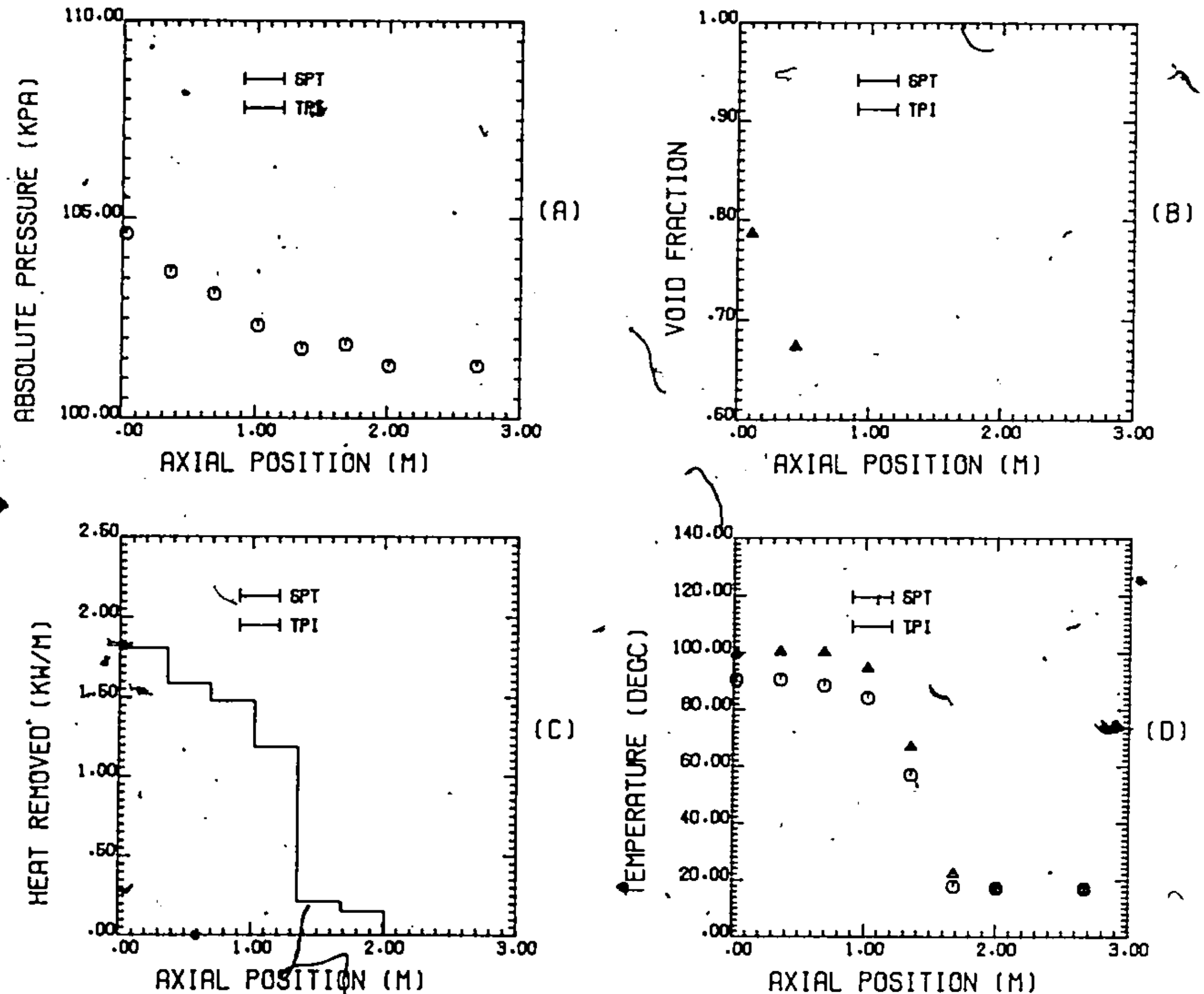

FIGURE G.21
EXPERIMENTAL DATA OF
RUN NO. D14101

TCWI=14 DEGC
TUBE DIA= 1.91 CM O.D.
PBP= 104.603 KPA
PUP= 101.325 KPA
STMFLW= 62.90 G/MIN
QRMV= 2.1164 KW

SINGLE-PHASE TOP- .90/ 1.20 M
(ABBREVIATED AS SPT IN THE PLOTS)

TWO-PHASE INTERFACE- .90/ 1.20 M
(ABBREVIATED AS TPI IN THE PLOTS)

LEGEND OF TEMPERATURE PLOT
⊙ = NEAR WALL
▲ = CENTER LINE

AVERAGE VOID FRACTIONS

MEASURED = .7303
CALCULATED = .7696

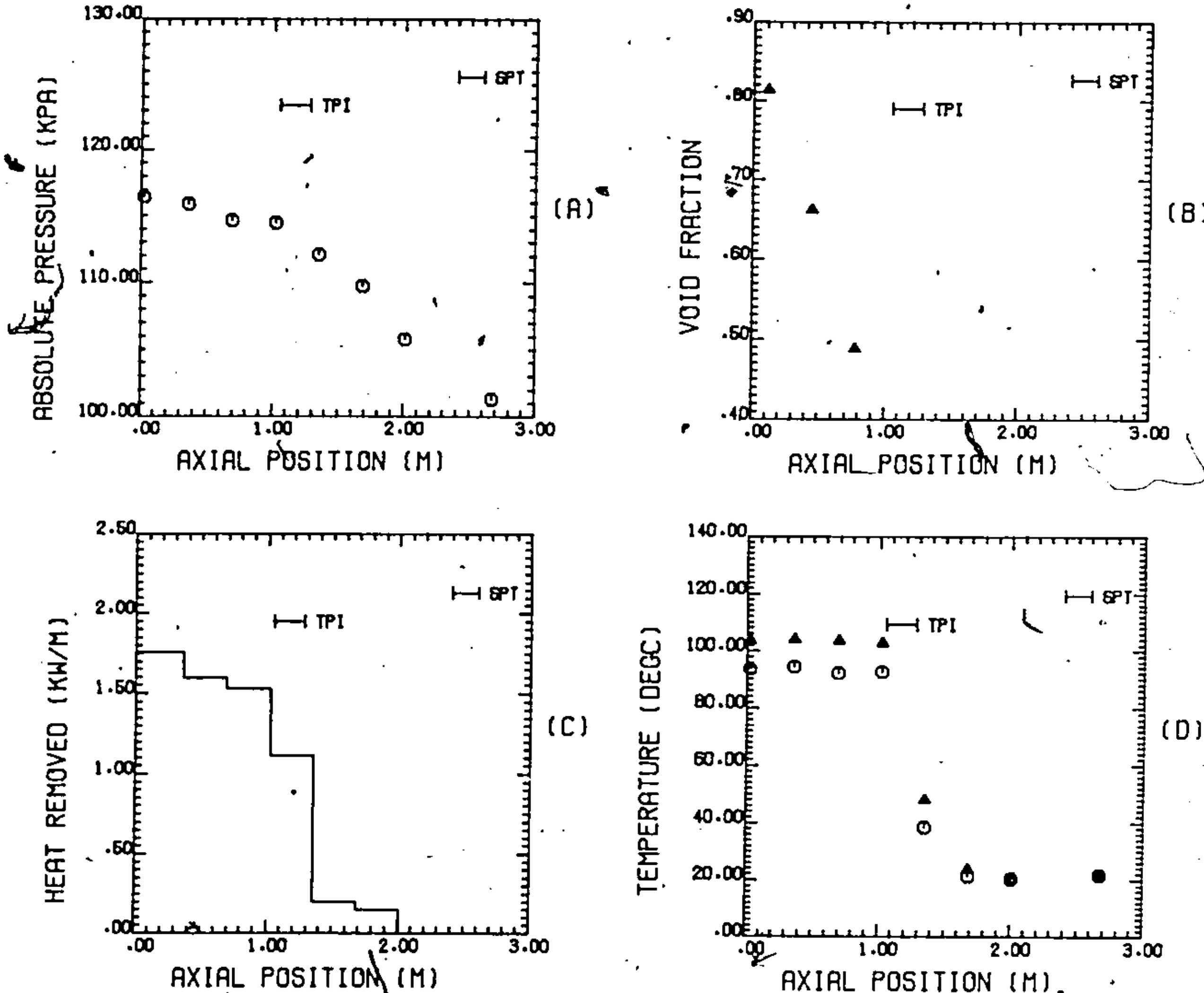

FIGURE G.22
EXPERIMENTAL DATA OF
RUN NO. D09103

TCWI=14 DEGC
TUBE DIA= 1.91 CM O.D.
PBP= 116.966 KPA
PUP= 101.325 KPA
STMFLW= 66.42 G/MIN
QRMV= 2.0914 KW
SINGLE-PHASE TOP. 2.40/ 2.60 M
(ABBREVIATED AS SPT IN THE PLOTS)

TWO-PHASE INTERFACE. 1.05/ 1.28 M
(ABBREVIATED AS TPI IN THE PLOTS)

LEGEND OF TEMPERATURE PLOT
⊙ = NEAR WALL
▲ = CENTER LINE

AVERAGE VOID FRACTIONS

MEASURED = .6550
CALCULATED = .7190

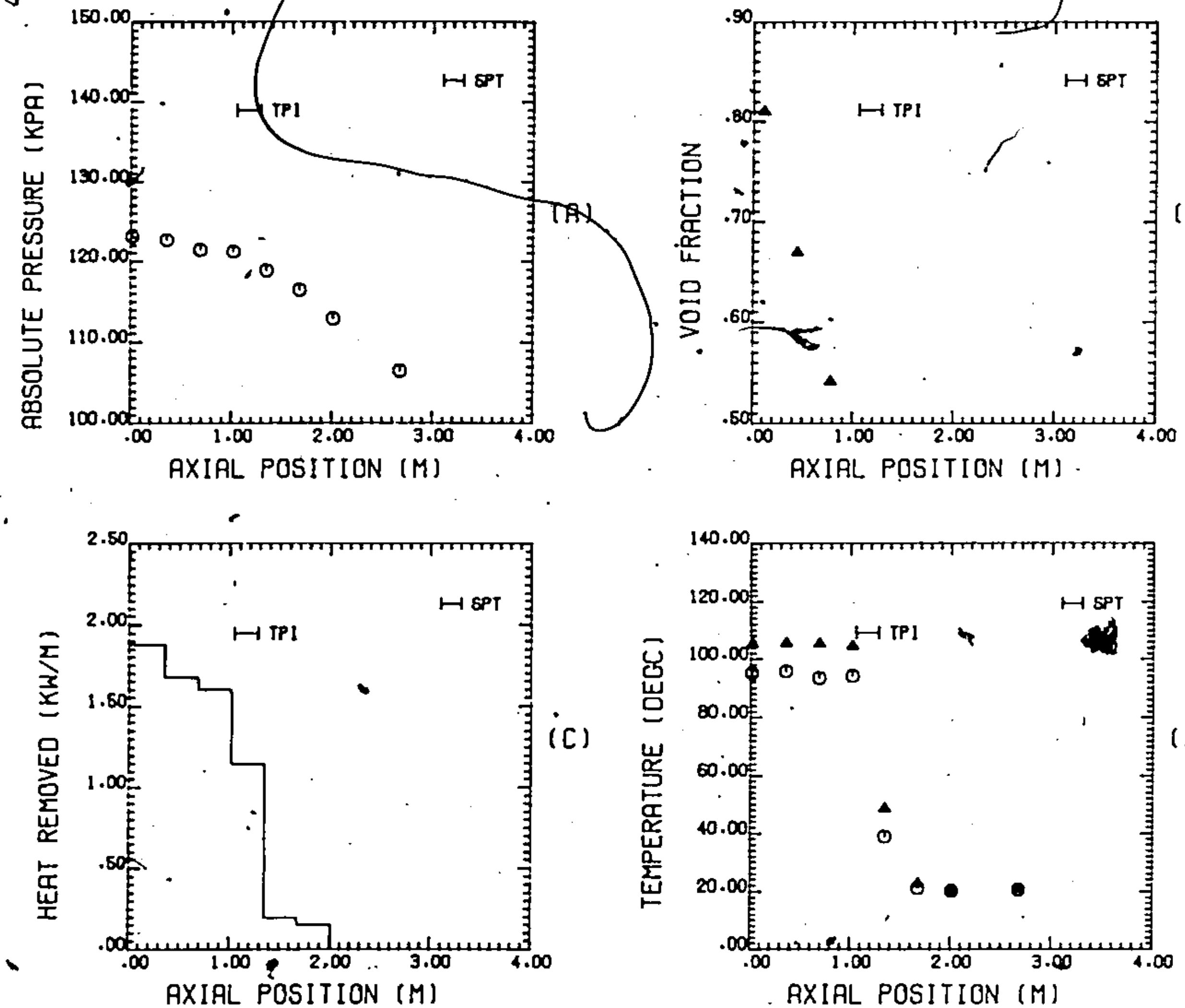

FIGURE G.23
EXPERIMENTAL DATA OF
RUN NO. D09102

TCWI=14 DEGC
TUBE DIA= 1.91 CM O.D.
PBP= 123.997 KPA
PUP= 101.325 KPA
STMFLW= 68.15 G/MIN
QRMV= 2.1951 KW
SINGLE-PHASE TOP- 3.10/ 3.30 M
(ABBREVIATED AS SPT IN THE PLOTS)

TWO-PHASE INTERFACE- 1.05/ 1.28 M
(ABBREVIATED AS TPI IN THE PLOTS)

LEGEND OF TEMPERATURE PLOT
⊙ = NEAR WALL
▲ = CENTER LINE

AVERAGE VOID FRACTIONS

MEASURED = .6739
CALCULATED = .7299

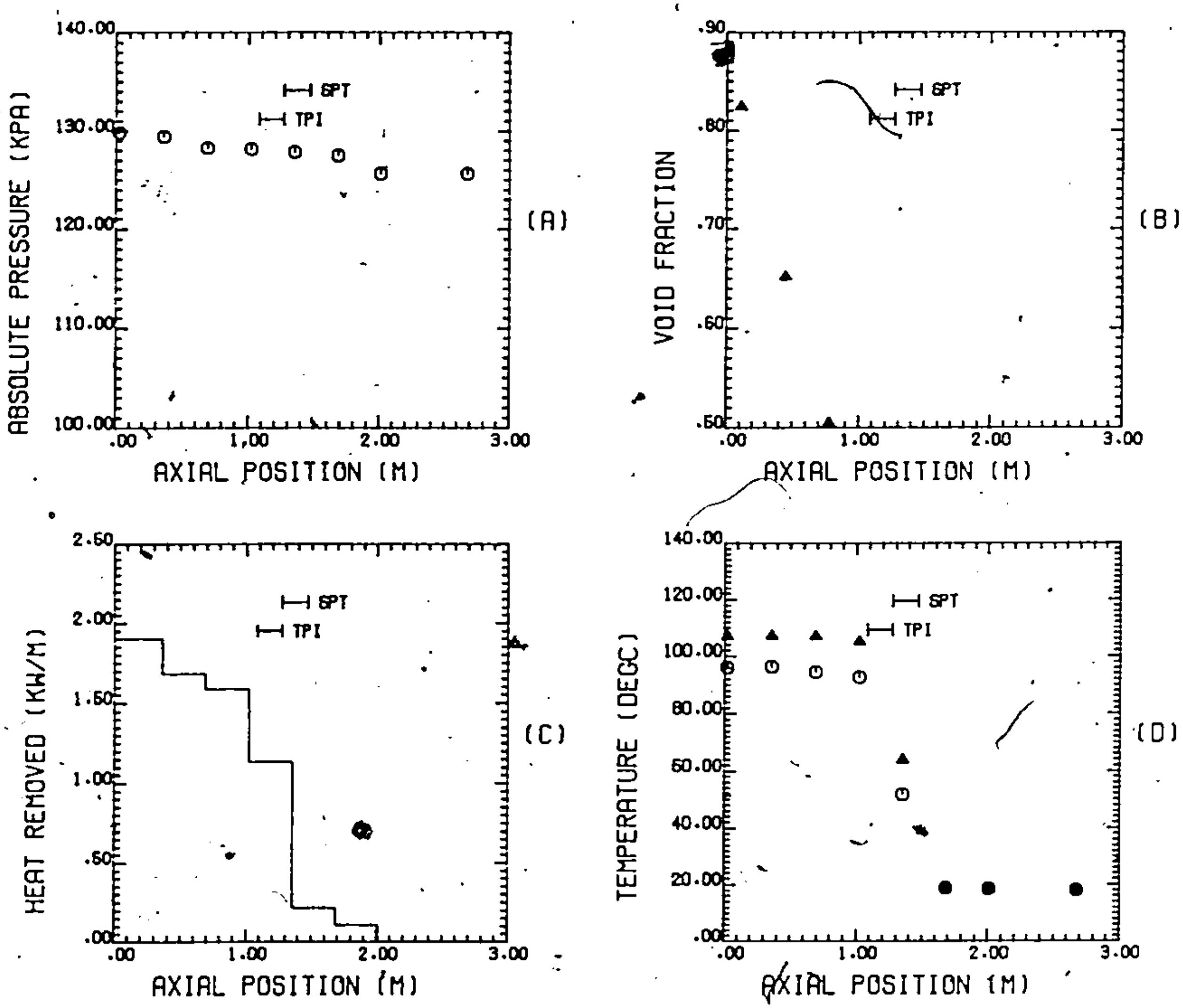

FIGURE G.2
EXPERIMENTAL DATA OF
RUN NO. D091012

TCWI=14 DEGC
TUBE DIA= 1.91 CM O.D.
PBP= 130.825 KPA
PUP= 126.587 KPA
STMFLW= 66.32 G/MIN
QRMV= 2.1846 KW
SINGLE-PHASE TOP- 1.27/ 1.47 M
(ABBREVIATED AS SPT IN THE PLOTS)

TWO-PHASE INTERFACE- 1.09/ 1.27 M
(ABBREVIATED AS TPI IN THE PLOTS)

LEGEND OF TEMPERATURE PLOT
⊖ = NEAR WALL
▲ = CENTER LINE

AVERAGE VOID FRACTIONS

MEASURED = .6603
CALCULATED = .7443

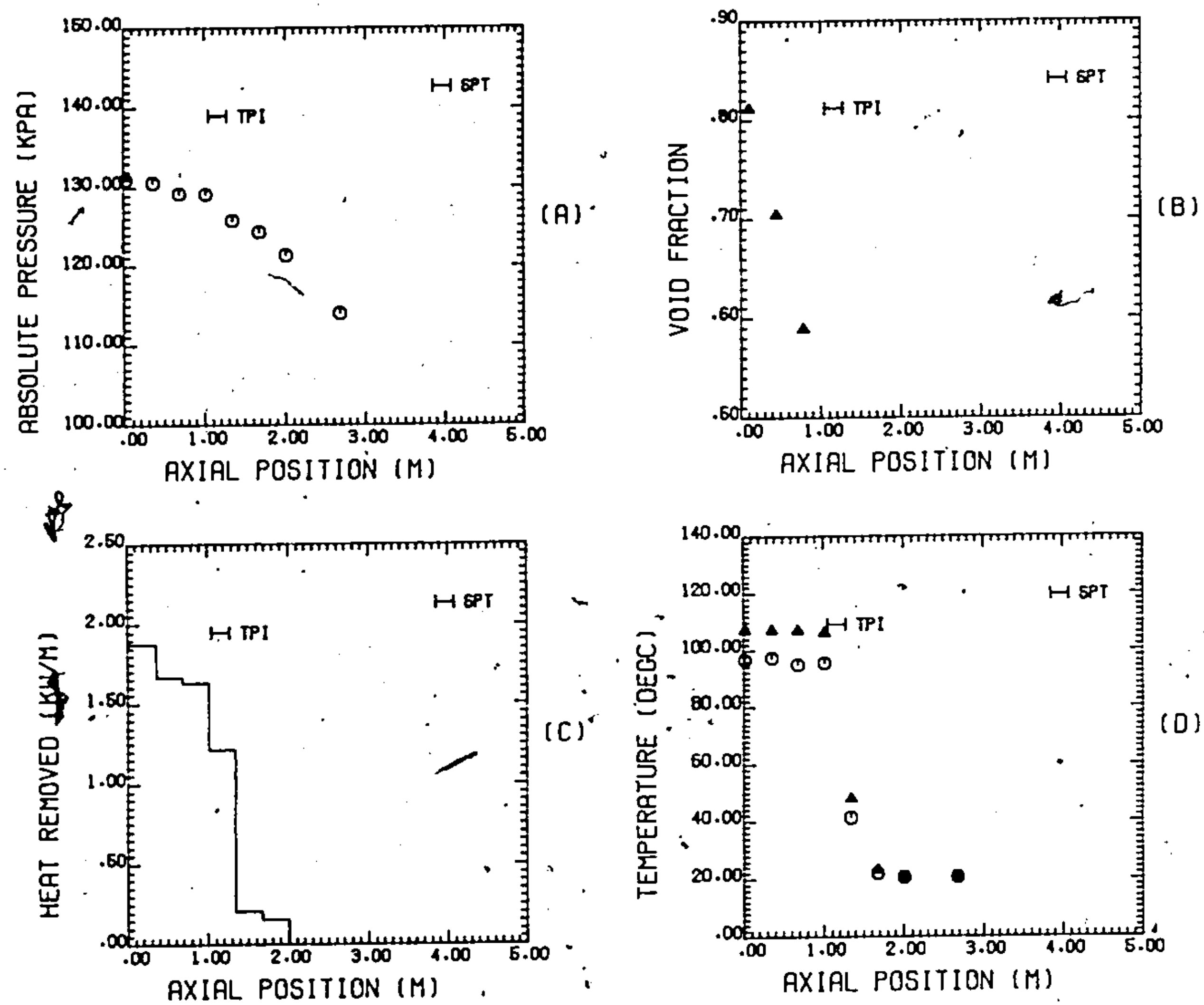

FIGURE G.25
EXPERIMENTAL DATA OF
RUN NO. D09101

TCWI=14 DEGC
TUBE DIA= 1.91 CM O.D.
PBP= 132.072 KPA
PUP= 101.325 KPA
STMFLW= 70.71 G/MIN
QRMV= 2.250 KW
SINGLE-PHASE TOP- 3.85/ 4.08 M
(ABBREVIATED AS SPT IN THE PLOTS)

TWO-PHASE INTERFACE- 1.05/ 1.28 M
(ABBREVIATED AS TPI IN THE PLOTS)

LEGEND OF TEMPERATURE PLOT
⊖ = NEAR WALL
▲ = CENTER LINE

AVERAGE VOID FRACTIONS

MEASURED = .7014
CALCULATED = .7202

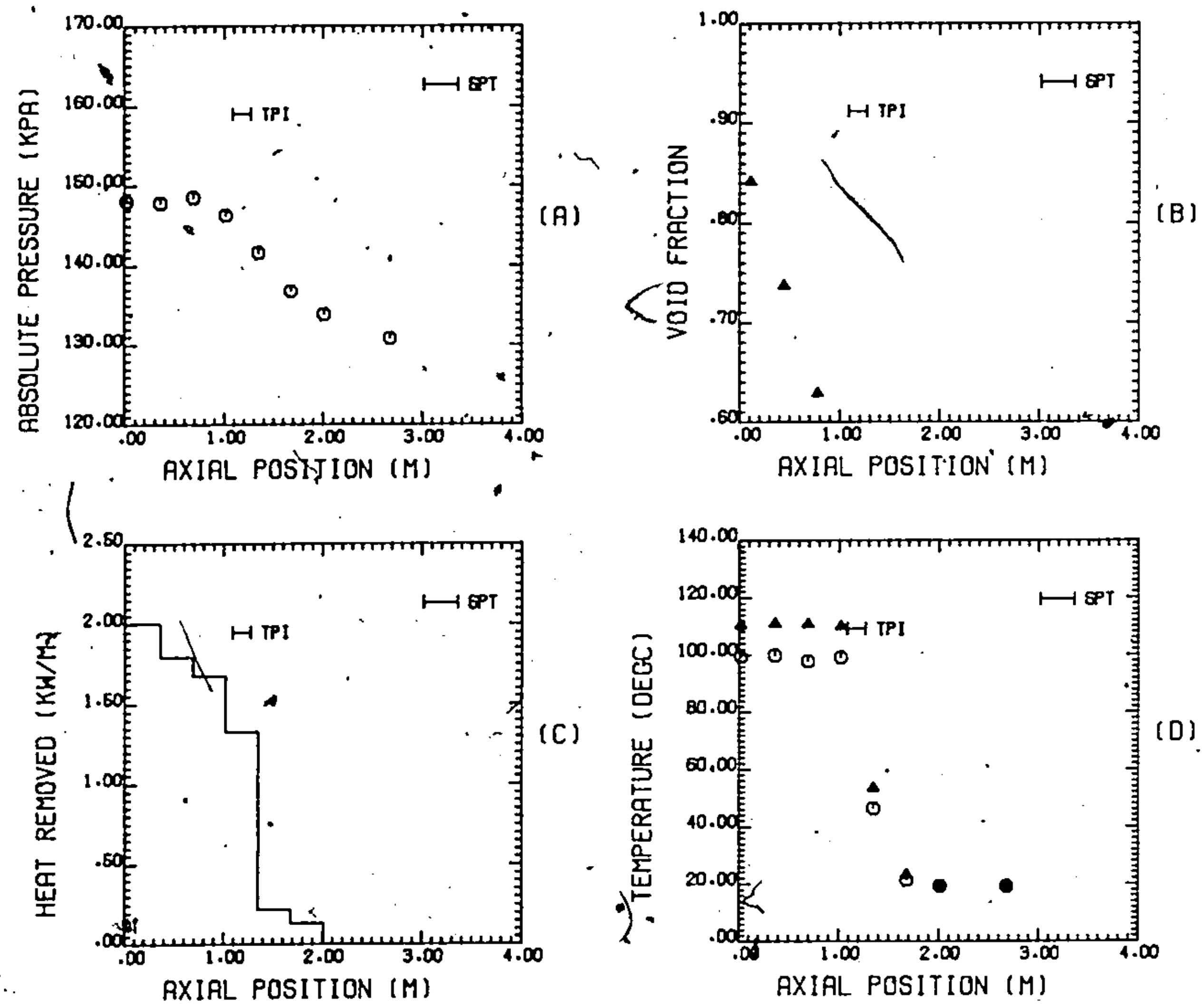

FIGURE G.26
EXPERIMENTAL DATA OF
RUN NO. D09109

TCWI=14 DEGC
TUBE DIA= 1.91 CM O.D.
PBP= 149.647 KPA
PUP= 129.179 KPA
STMFLW= 71.34 G/MIN
QRMV= 2.3631 KW
SINGLE-PHASE TOP- 3.02/ 3.36 M
(ABBREVIATED AS SPT IN THE PLOTS)

TWO-PHASE INTERFACE- 1.09/ 1.27 M
(ABBREVIATED AS TPI IN THE PLOTS)

LEGEND OF TEMPERATURE PLOT
⊖ = NEAR WALL
▲ = CENTER LINE

AVERAGE VOID FRACTIONS

MEASURED = .7357
CALCULATED = .8114

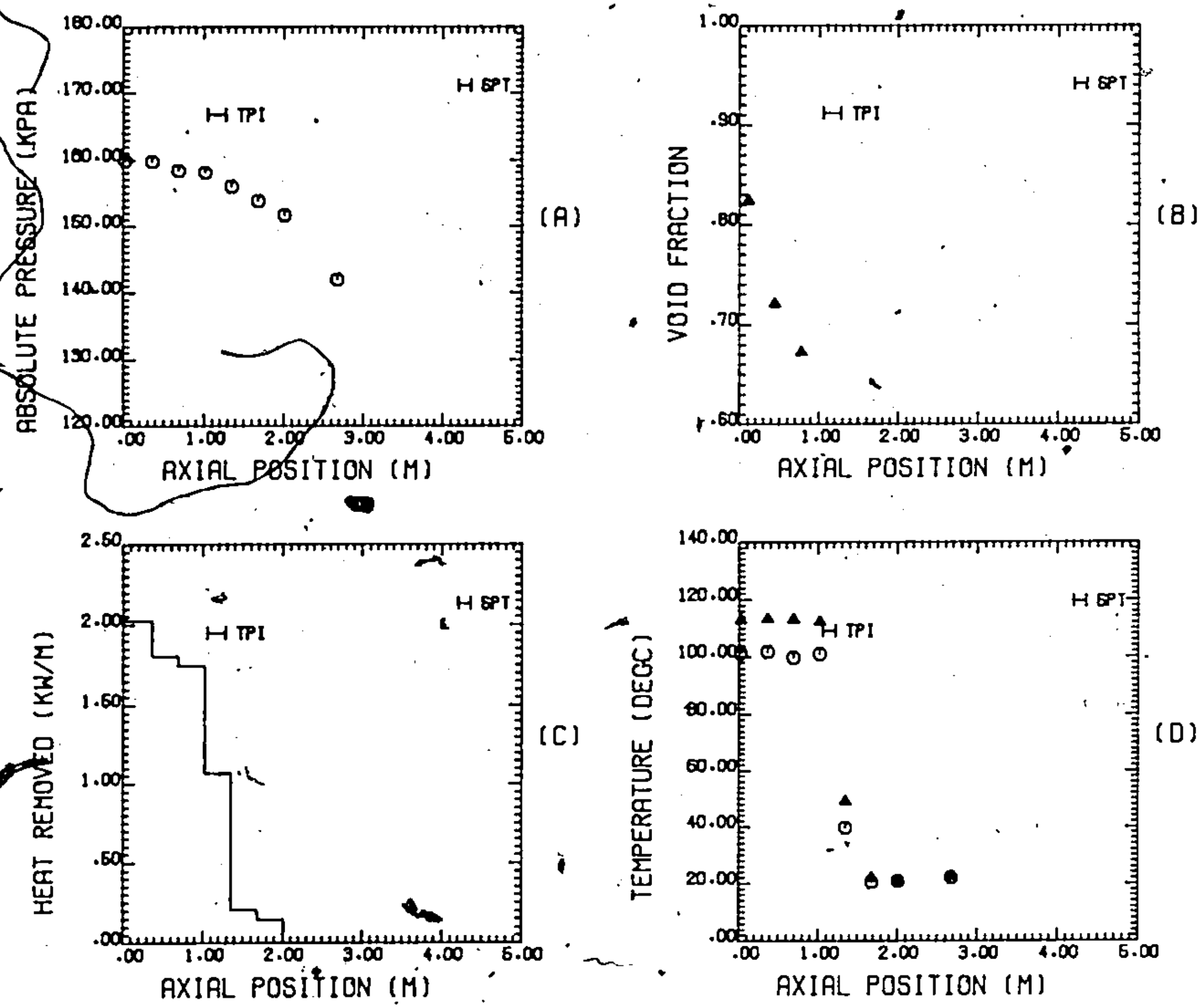

FIGURE G.27
EXPERIMENTAL DATA OF
RUN NO. D09107

TCWI=14 DEGC
TUBE DIA= 1.91 CM O.D.
PBP= 161.601 KPA
PUP= 127.979 KPA
STMFLW= 73.47 G/MIN
QRMV= 2.3092 KW
SINGLE-PHASE TOP= 4.20/ 4.35 M
(ABBREVIATED AS SPT IN THE PLOTS)

TWO-PHASE INTERFACE= 1.05/ 1.21 M
(ABBREVIATED AS TPI IN THE PLOTS)

LEGEND OF TEMPERATURE PLOT
⊙ = NEAR WALL
▲ = CENTER LINE

AVERAGE VOID FRACTIONS

MEASURED = .7389
CALCULATED = .7575

FIGURE G.2.4 : LOCAL MEASUREMENTS IN 1.91 CM O.D. TUBE WITH TCWI = 45°C

FIGURES G.28 TO G.35 : LOCAL MEASUREMENTS IN 1.91 CM O.D. TUBE WITH TCWI = 45°C

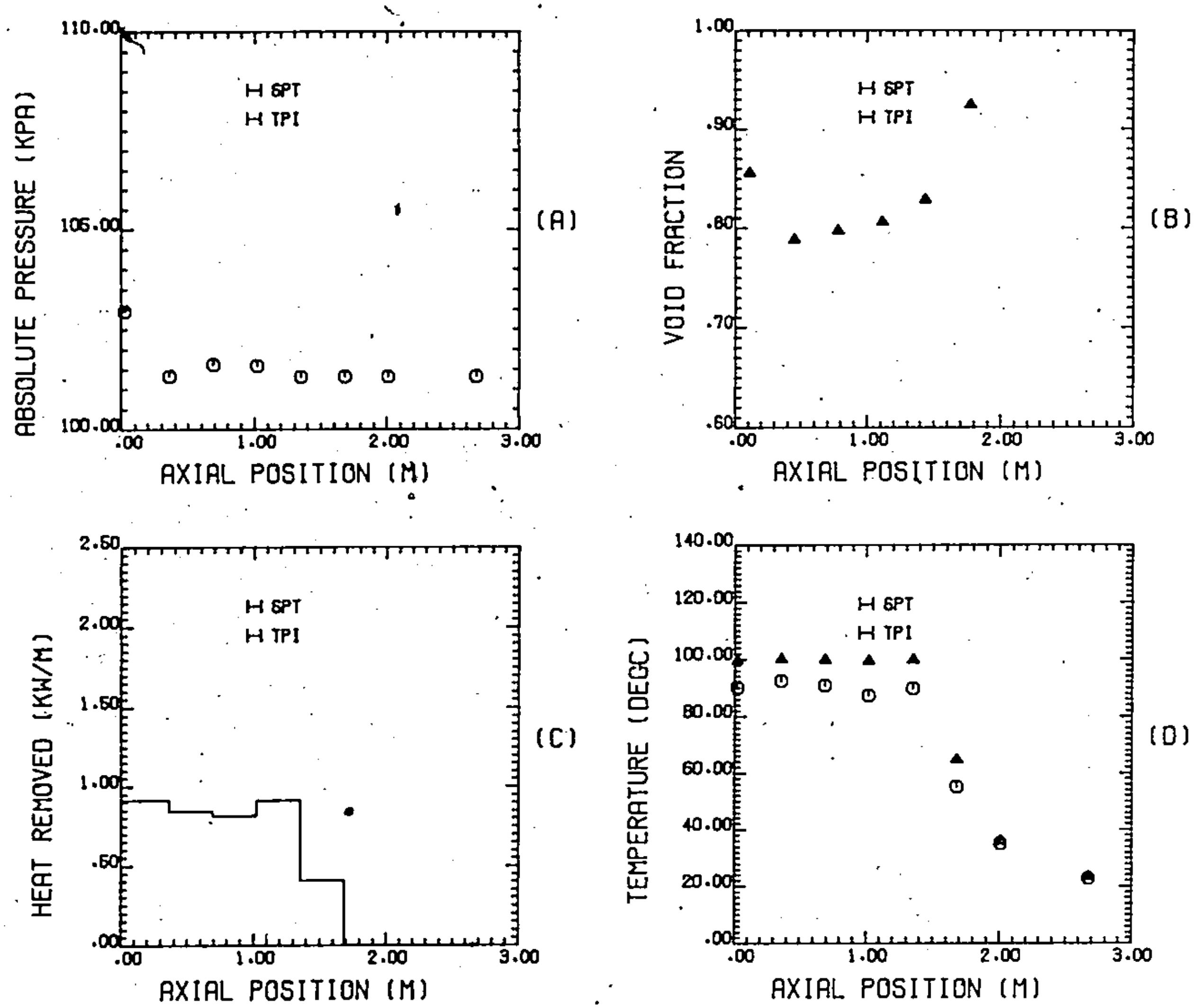

FIGURE G.28
EXPERIMENTAL DATA OF
RUN NO. D16104

TCWI= 45 DEGC
TUBE DIA= 1.91 CM O.D.
PBP= 102.954 KPA
PUP= 101.325 KPA
STMFLW= 46.61 G/MIN
QRMV= 1.2297 KW
SINGLE-PHASE TOP= .95/ 1.05 M
(ABBREVIATED AS SPT IN THE PLOTS)

TWO-PHASE INTERFACE= .95/ 1.05 M
(ABBREVIATED AS TPI IN THE PLOTS)

LEGEND OF TEMPERATURE PLOT
Θ = NEAR WALL
▲ = CENTER LINE

AVERAGE VOID FRACTIONS

MEASURED = .8331
CALCULATED = .8575

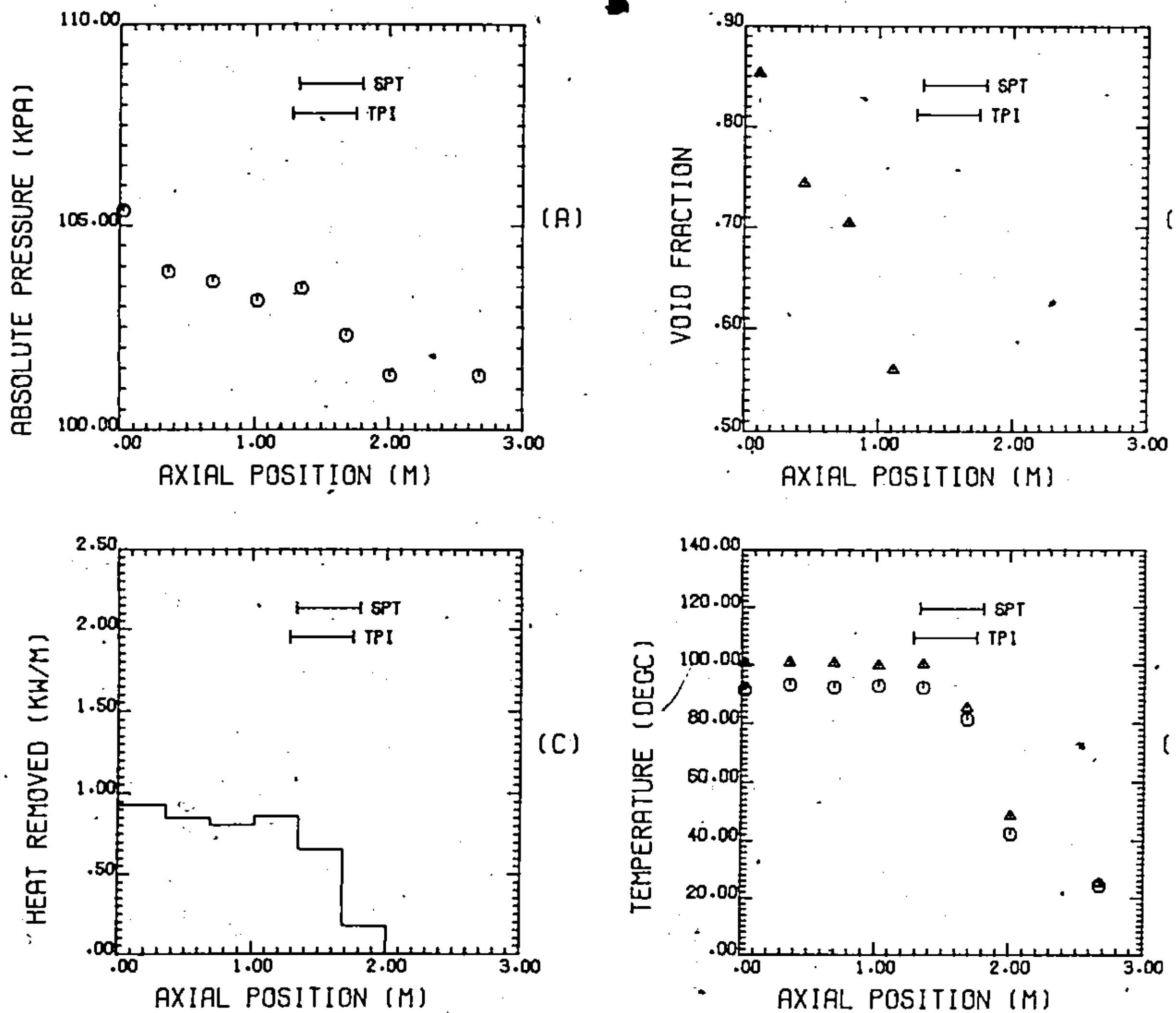

FIGURE G.29
EXPERIMENTAL DATA OF
RUN NO. D16101

TCWI= 45 DEGC
TUBE DIA= 1.91 CM O.D.
PBP= 105.377 KPA
PUP= 101.325 KPA
STMFLW= 54.18 G/MIN
QRMV= 1.4083 KW
SINGLE-PHASE TOP= 1.33/ 1.80 M
(ABBREVIATED AS SPT IN THE PLOTS)

TWO-PHASE INTERFACE= 1.28/ 1.75 M
(ABBREVIATED AS TPI IN THE PLOTS)

LEGEND OF TEMPERATURE PLOT
Θ = NEAR WALL
Δ = CENTER LINE

AVERAGE VOID FRACTIONS

MEASURED = .7153
CALCULATED = .7897

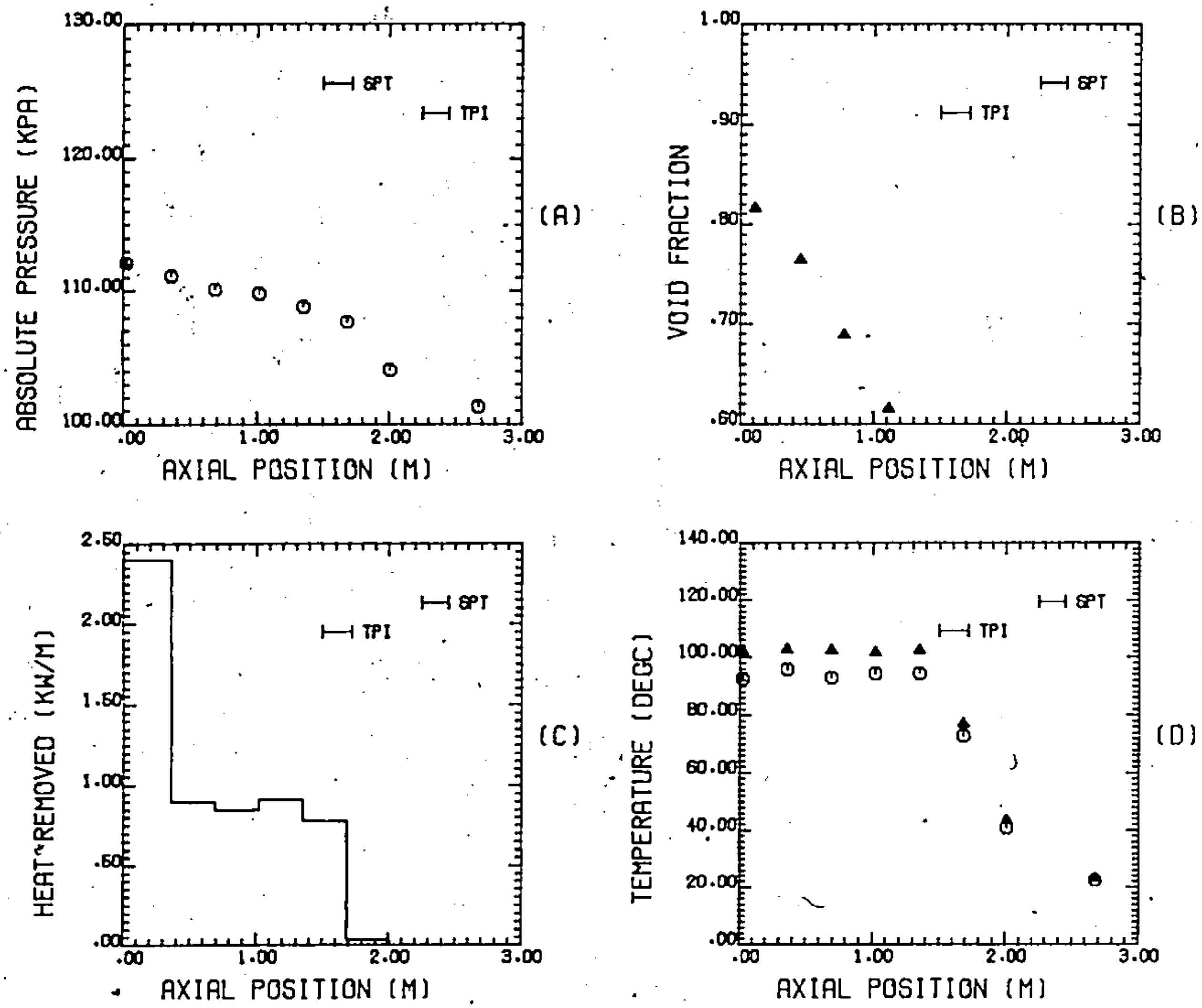

FIGURE G.30
EXPERIMENTAL DATA OF
RUN NO. D10105

TCHI= 45 DEGC
TUBE DIA= 1.91 CM O.D.
PBP= 112.068 KPA
PUP= 101.325 KPA
STMFLW= 55.11 G/MIN
QRMV= 1.9367 KW
SINGLE-PHASE TOP- 2.25/ 2.45 M
(ABBREVIATED AS SPT IN THE PLOTS)

TWO-PHASE INTERFACE- 1.50/ 1.72 M
(ABBREVIATED AS TPI IN THE PLOTS)

LEGEND OF TEMPERATURE PLOT
⊙ = NEAR WALL
▲ = CENTER LINE

AVERAGE VOID FRACTIONS

MEASURED = .7208
CALCULATED = .7087

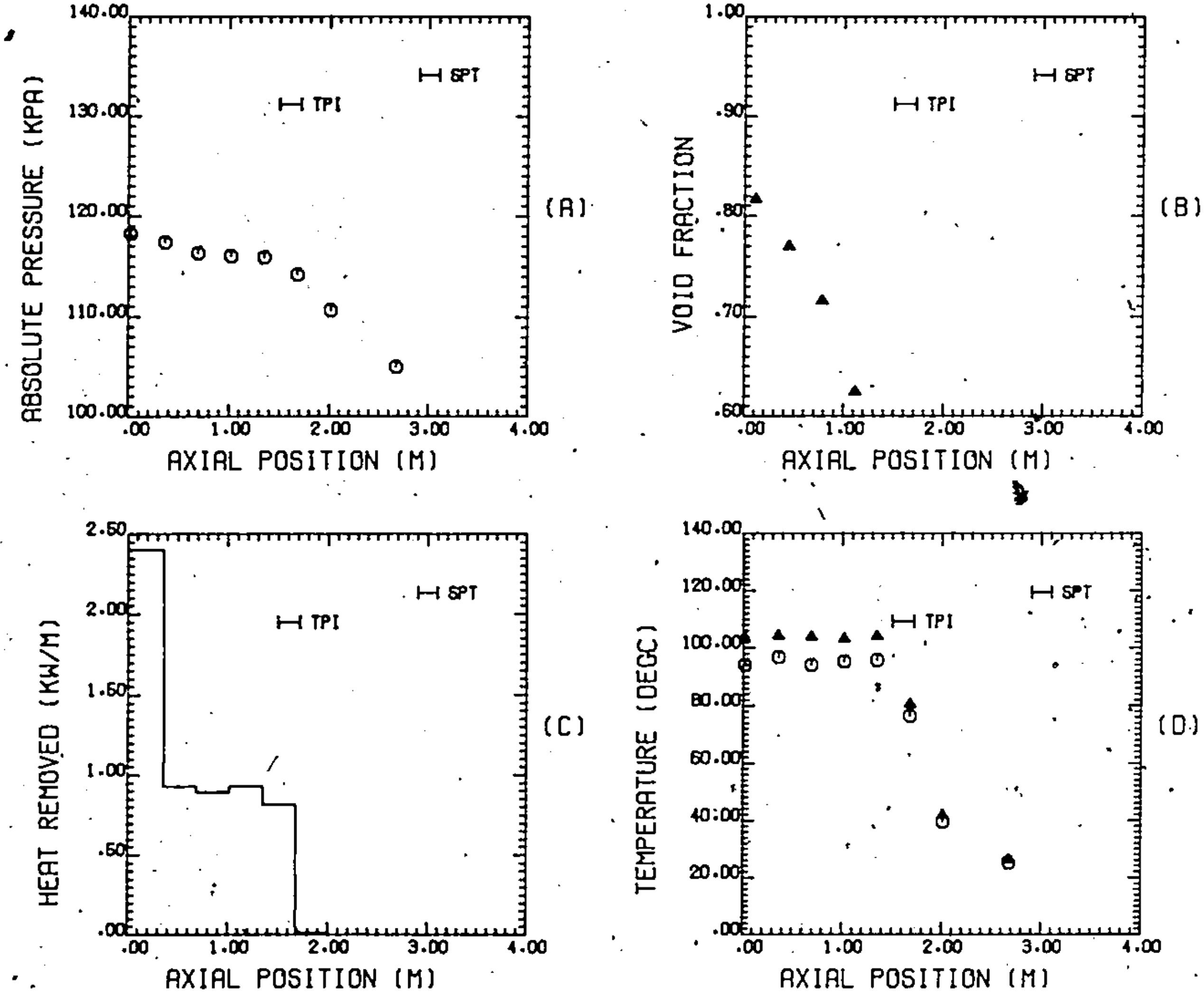

FIGURE G.31
EXPERIMENTAL DATA OF
RUN NO. D10103

TCWI= 45 DEGC
TUBE DIA= 1.91 CM O.D.
PBP= 118.182 KPA
PUP= 101.325 KPA
STMFLW= 58.34 G/MIN
QRMV= 2.0082 KW

SINGLE-PHASE TOP- 2.90/ 3.10 M
(ABBREVIATED AS SPT IN THE PLOTS)

TWO-PHASE INTERFACE- 1.50/ 1.72 M
(ABBREVIATED AS TPI IN THE PLOTS)

LEGEND OF TEMPERATURE PLOT
⊙ = NEAR WALL
▲ = CENTER LINE

AVERAGE VOID FRACTIONS

MEASURED = .7313
CALCULATED = .7344

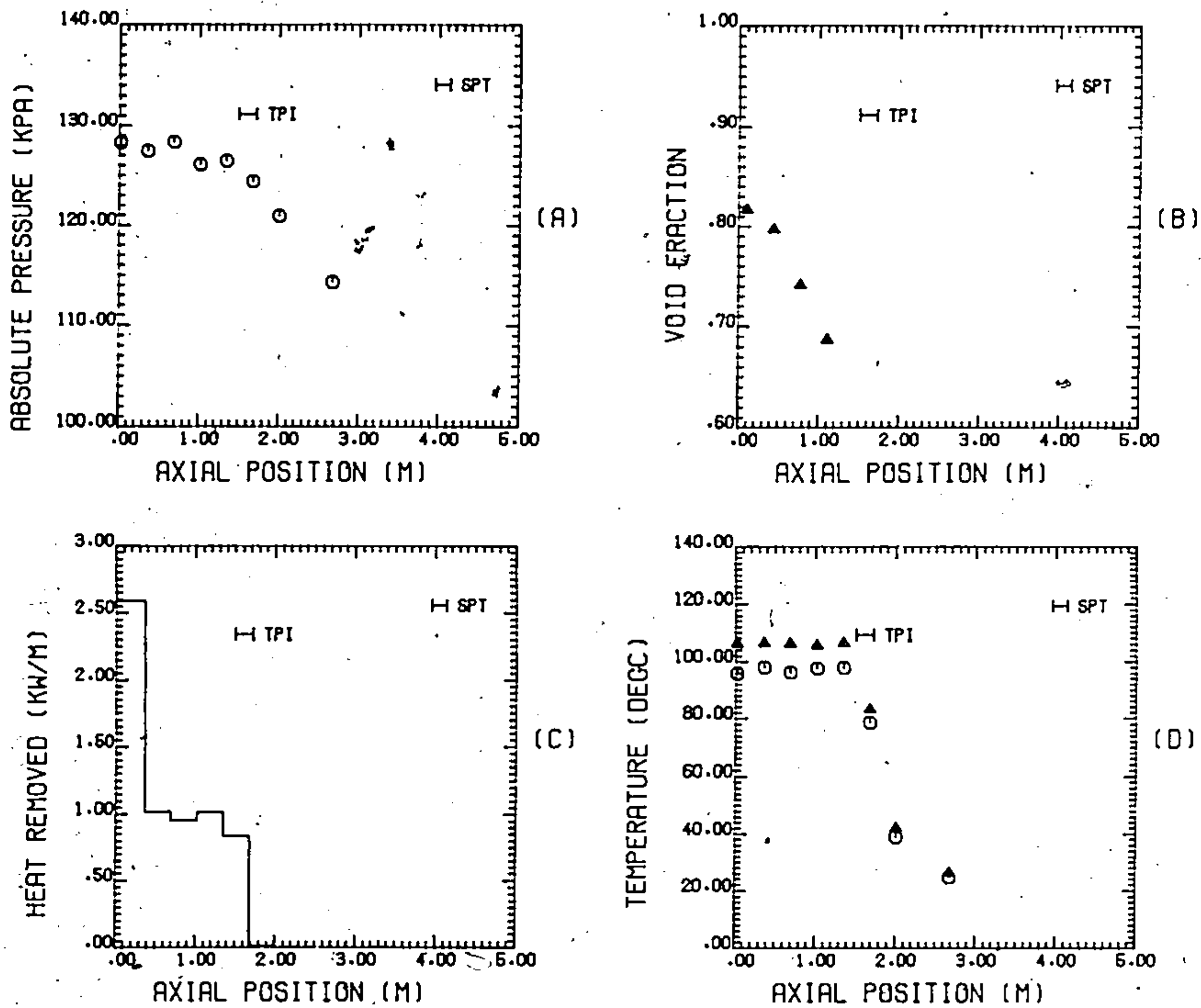

FIGURE G.32
EXPERIMENTAL DATA OF
RUN NO. D10101

TCWI= 45 DEGC
TUBE DIA= 1.91 CM O.D.
PBP= 128.510 KPA
PUP= 101.325 KPA
STMFLW= 59.75 G/MIN
QRMV= 2.1151 KW
SINGLE-PHASE TOP- 3.95/ 4.13 M
(ABBREVIATED AS SPT IN THE PLOTS)

TWO-PHASE INTERFACE- 1.50/ 1.72 M
(ABBREVIATED AS TPI IN THE PLOTS)

LEGEND OF TEMPERATURE PLOT
Θ = NEAR WALL
▲ = CENTER LINE

AVERAGE VOID FRACTIONS

MEASURED = .7603
CALCULATED = .7294

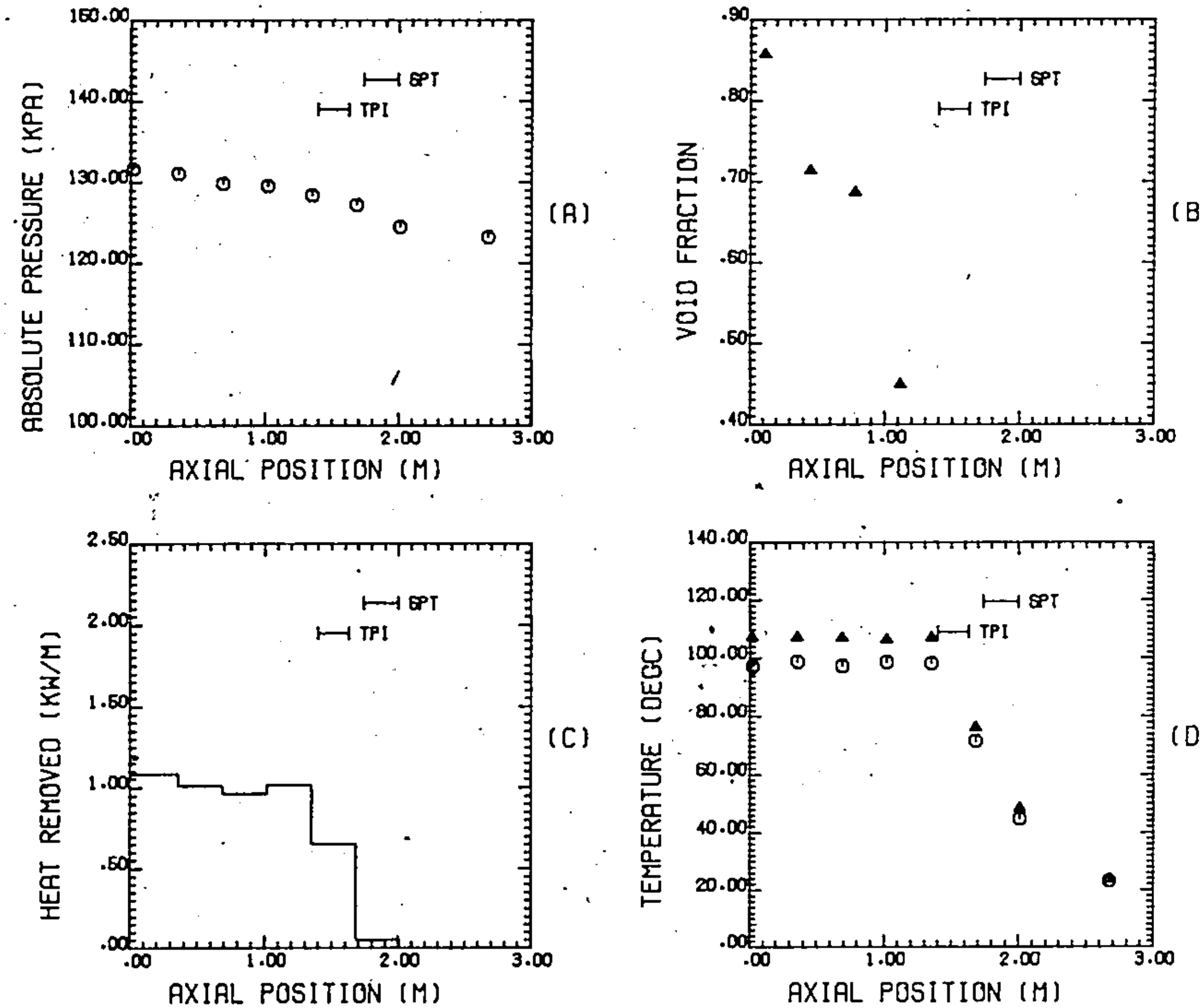

FIGURE G.33
EXPERIMENTAL DATA OF
RUN NO. D101012

TCWI= 45 DEGC
TUBE DIA= 1.91 CM O.D.
PBP= 131.613 KPA
PUP= 124.564 KPA
STMFLW= 60.67 G/MIN
QRMV= 1.5742 KW
SINGLE-PHASE TOP= 1.74/ 2.00 M
(ABBREVIATED AS SPT IN THE PLOTS)

TWO-PHASE INTERFACE= 1.40/ 1.63 M
(ABBREVIATED AS TPI IN THE PLOTS)

LEGEND OF TEMPERATURE PLOT
⊙ = NEAR WALL
▲ = CENTER LINE

AVERAGE VOID FRACTIONS

MEASURED = .6762
CALCULATED = .7264

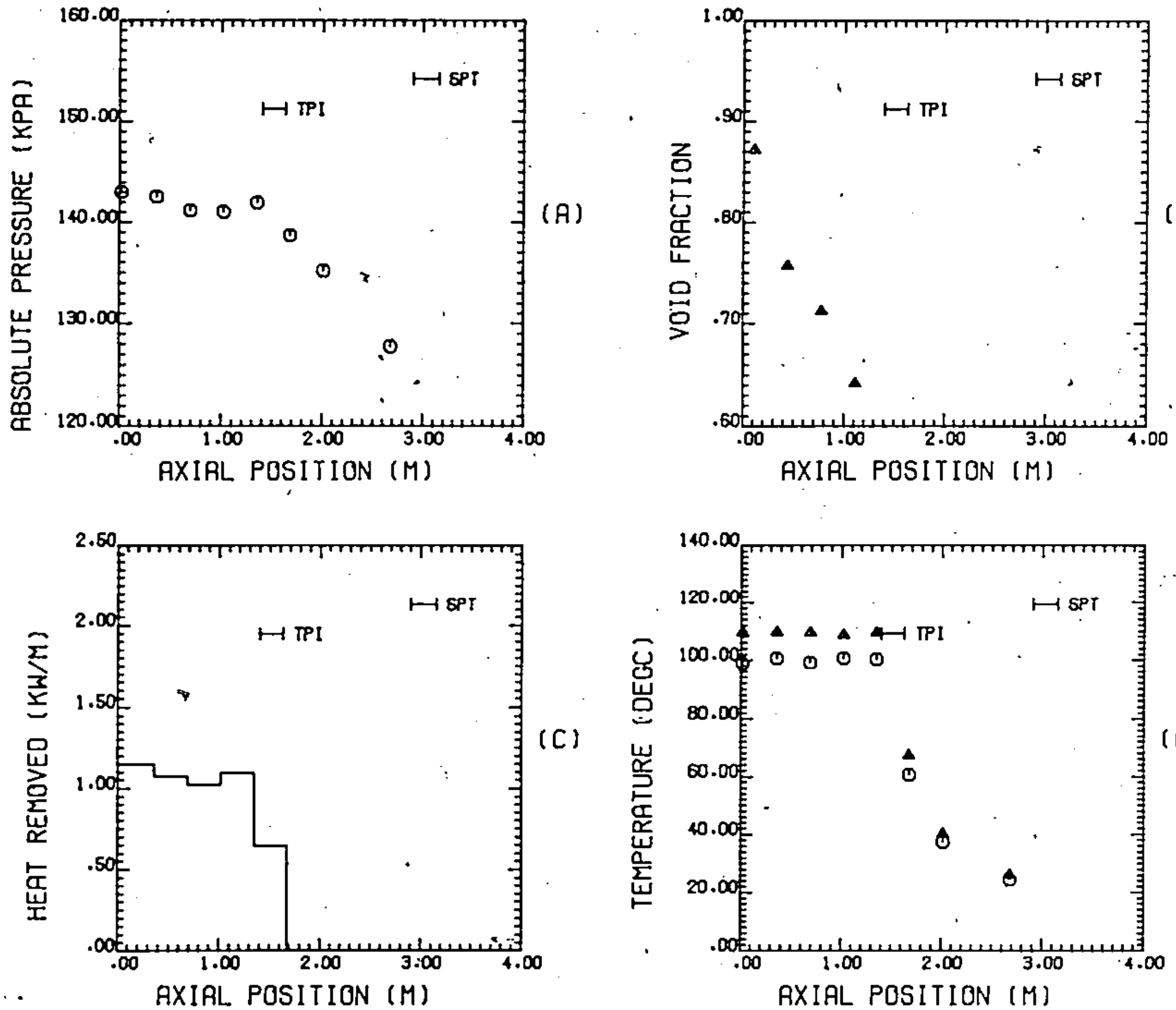

FIGURE G.34
EXPERIMENTAL DATA OF
RUN NO. D10109

TCWI= 45 DEGC
TUBE DIA= 1.91 CM O.D.
PBP= 102.954 KPA
PUP= 101.325 KPA
STMFLW= 46.61 G/MIN
QRMV= 1.2297 KW
SINGLE-PHASE TOP= 2.90/ 3.15 M
(ABBREVIATED AS SPT IN THE PLOTS)

TWO-PHASE INTERFACE= 1.40/ 1.63 M
(ABBREVIATED AS TPI IN THE PLOTS)

LEGEND OF TEMPERATURE PLOT
Θ = NEAR WALL
▲ = CENTER LINE

AVERAGE VOID FRACTIONS

MEASURED = .7457
CALCULATED = .8031

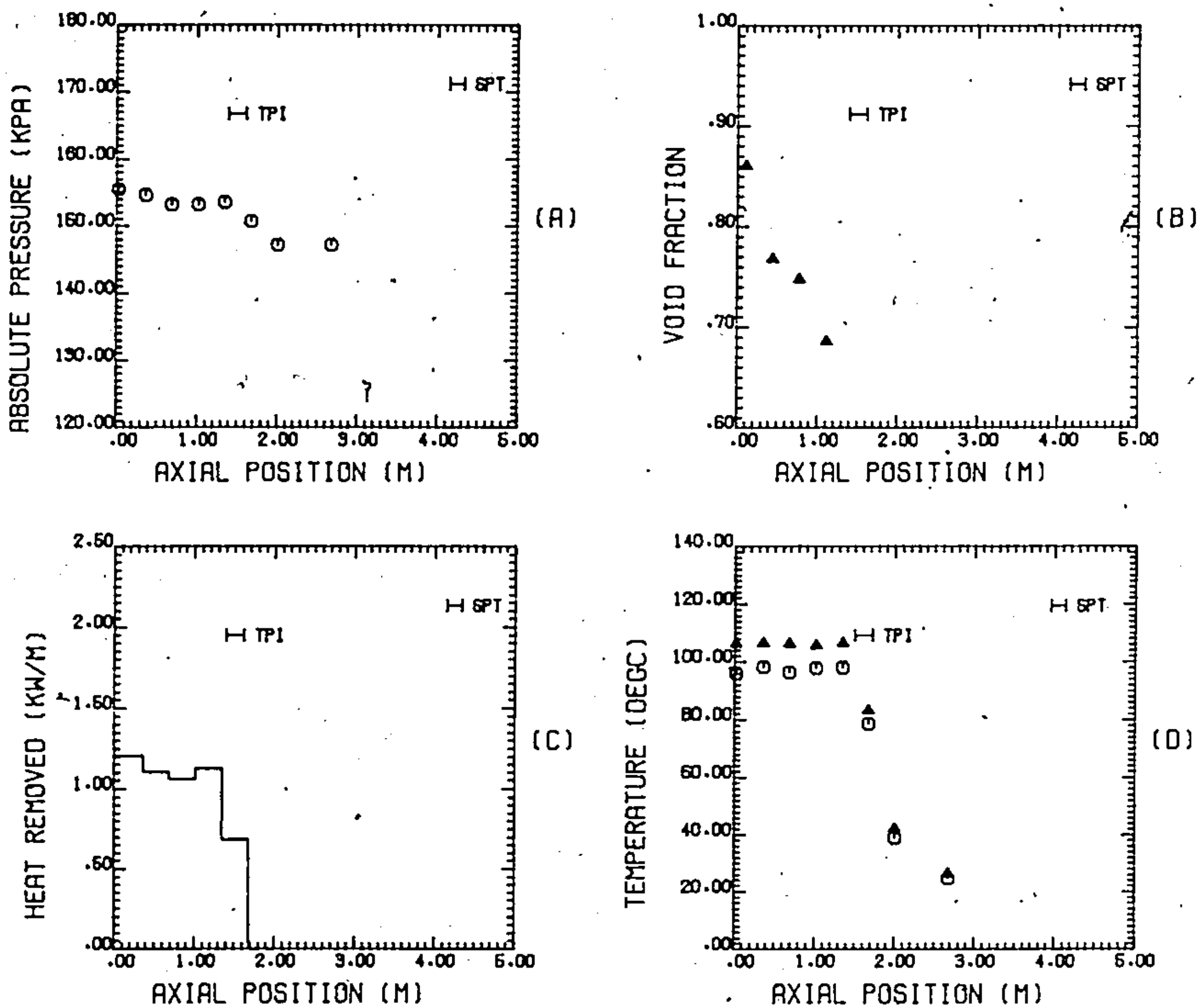

FIGURE G.35
EXPERIMENTAL DATA OF
RUN NO. D10107

TCWI= 45 DEGC
TUBE DIA= 1.91 CM O.D.
PBP= 155.019 KPA
PUP= 125.830 KPA
STMFLW= 67.36 G/MIN
QRMV= 1.6906 KW
SINGLE-PHASE TOP- 3.95/ 4.13 M
(ABBREVIATED AS SPT IN THE PLOTS)

TWO-PHASE INTERFACE- 1.50/ 1.72 M
(ABBREVIATED AS TPI IN THE PLOTS)

LEGEND OF TEMPERATURE PLOT
Θ = NEAR WALL
▲ = CENTER LINE

AVERAGE VOID FRACTIONS

MEASURED = .7663
CALCULATED = .7938

FIGURE G.2.5 : LOCAL MEASUREMENTS IN 1.27 CM O.D. TUBE WITH TCWI = 18°C

FIGURES G.36 TO G.44 : LOCAL MEASUREMENTS IN 1.27 CM O.D. TUBE WITH TCWI = 18°C

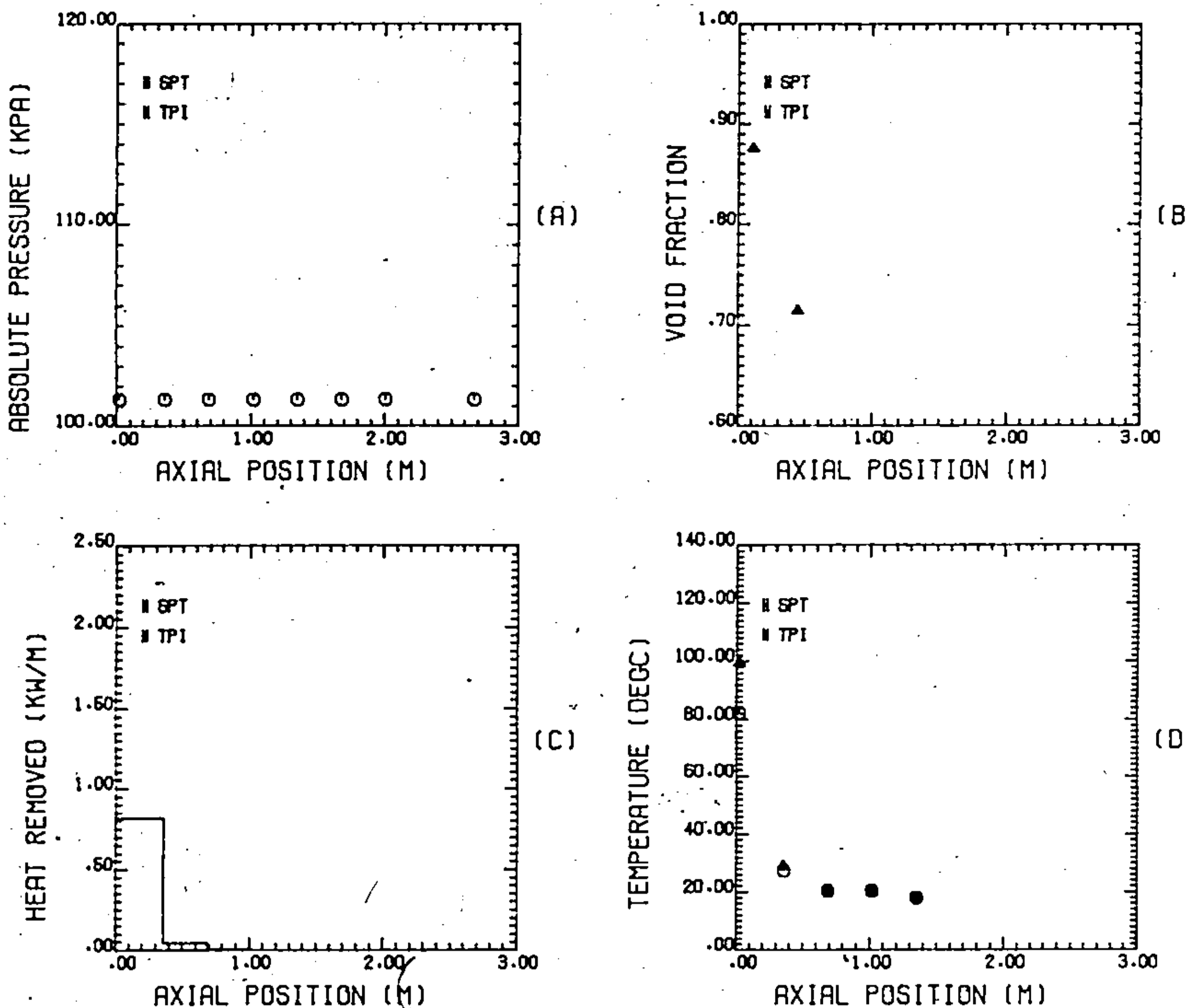

FIGURE G.36
EXPERIMENTAL DATA OF
RUN NO. D23084

TCWI=18 DEGC
TUBE DIA= 1.27 CM O.D.
PBP= 101.325 KPA
PUP= 101.324 KPA
STMFLW= 15.79 G/MIN
QRMV= .2847 KW
SINGLE-PHASE TOP= .20/ .23 M
(ABBREVIATED AS SPT IN THE PLOTS)

TWO-PHASE INTERFACE= .20/ .23 M
(ABBREVIATED AS TPI IN THE PLOTS)

LEGEND OF TEMPERATURE PLOT
⊙ = NEAR WALL
▲ = CENTER LINE

AVERAGE VOID FRACTIONS

MEASURED = .7966
CALCULATED = NOT AVAILABLE

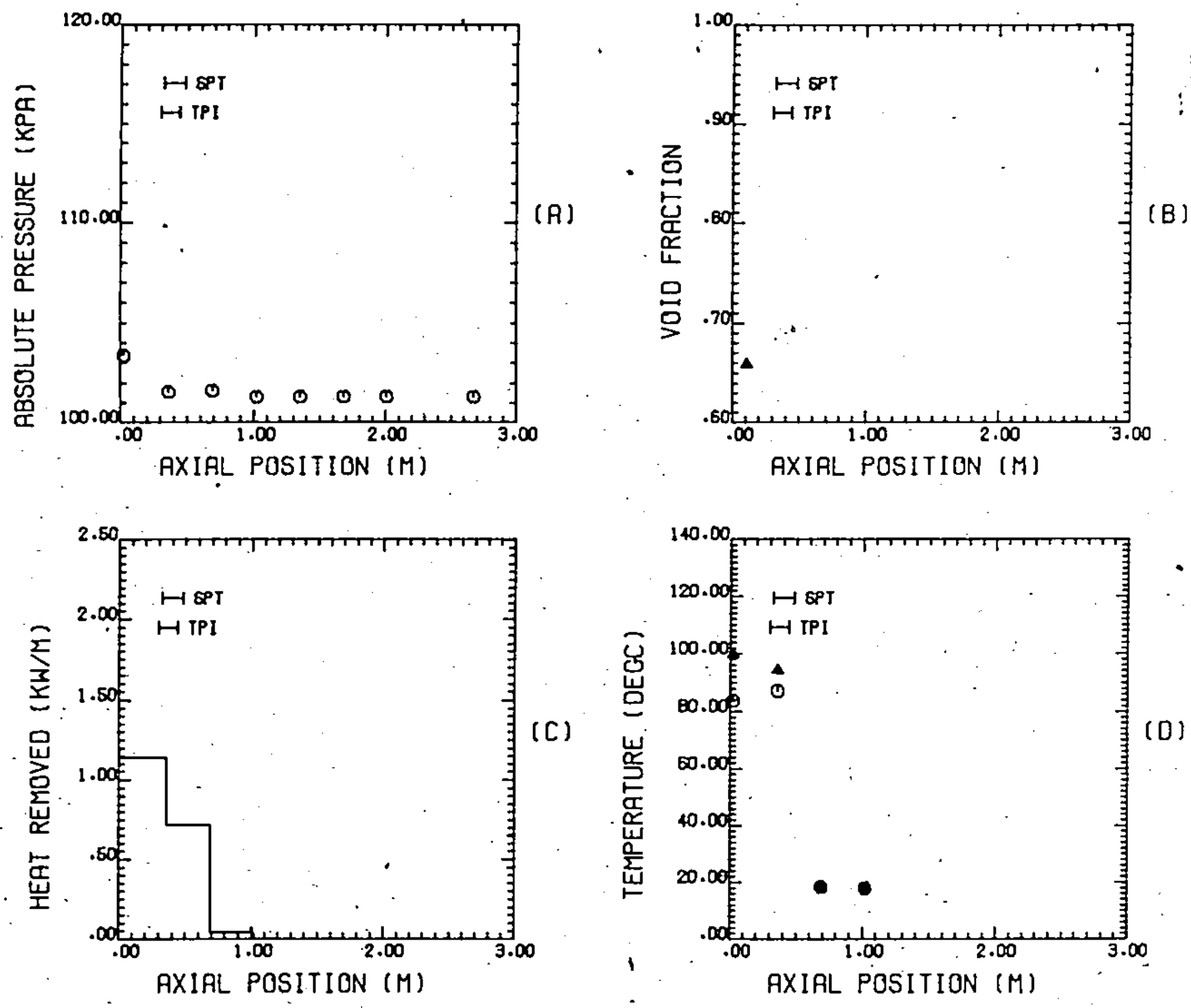

FIGURE G.37
EXPERIMENTAL DATA OF
RUN NO. D03082

TCWI=18 DEGC
TUBE DIA= 1.27 CM O.D.
PBP= 103.356 KPA
PUP= 101.325 KPA
STMFLW= 24.77 G/MIN
QRMV= .6264 KW
SINGLE-PHASE TOP- .32/ .48 M
(ABBREVIATED AS SPT IN THE PLOTS)

TWO-PHASE INTERFACE- .30/ .44 M
(ABBREVIATED AS TPI IN THE PLOTS)

LEGEND OF TEMPERATURE PLOT
⊙ = NEAR WALL
▲ = CENTER LINE

AVERAGE VOID FRACTIONS

MEASURED = .6588
CALCULATED = NOT AVAILABLE

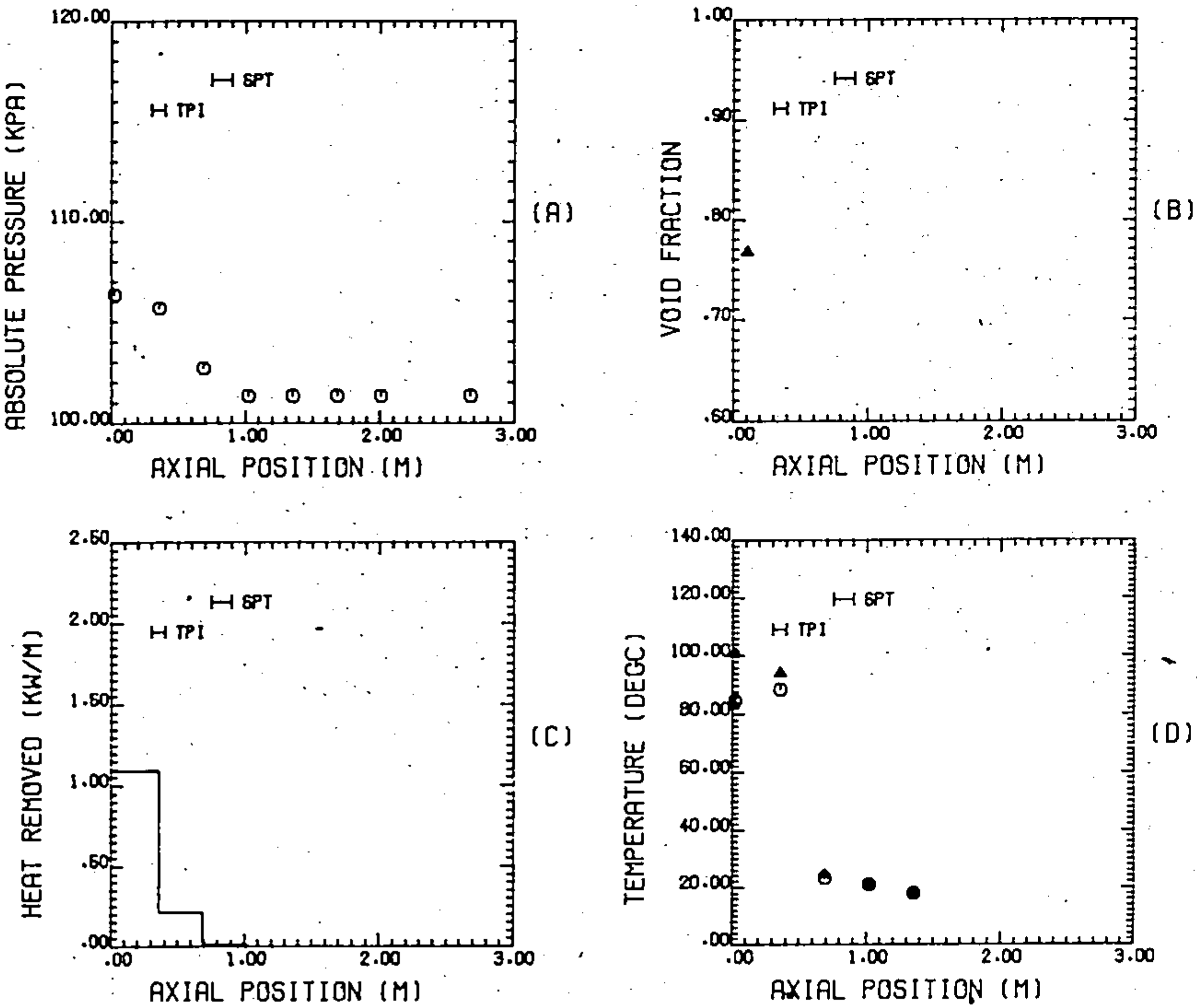

FIGURE G.38
EXPERIMENTAL DATA OF
RUN NO. D21081

TCHI=18 DEGC
TUBE DIA= 1.27 CM O.D.
PBP= 106.358 KPA
PUP= 101.325 KPA
STMFLW= 25.53 G/MIN
QRMV= .4348 KW
SINGLE-PHASE TOP= .75/ .90 M
(ABBREVIATED AS SPT IN THE PLOTS)

TWO-PHASE INTERFACE= .30/ .40 M
(ABBREVIATED AS TPI IN THE PLOTS)

LEGEND OF TEMPERATURE PLOT
Θ = NEAR WALL
▲ = CENTER LINE

AVERAGE VOID FRACTIONS

MEASURED = .7679
CALCULATED = .7945

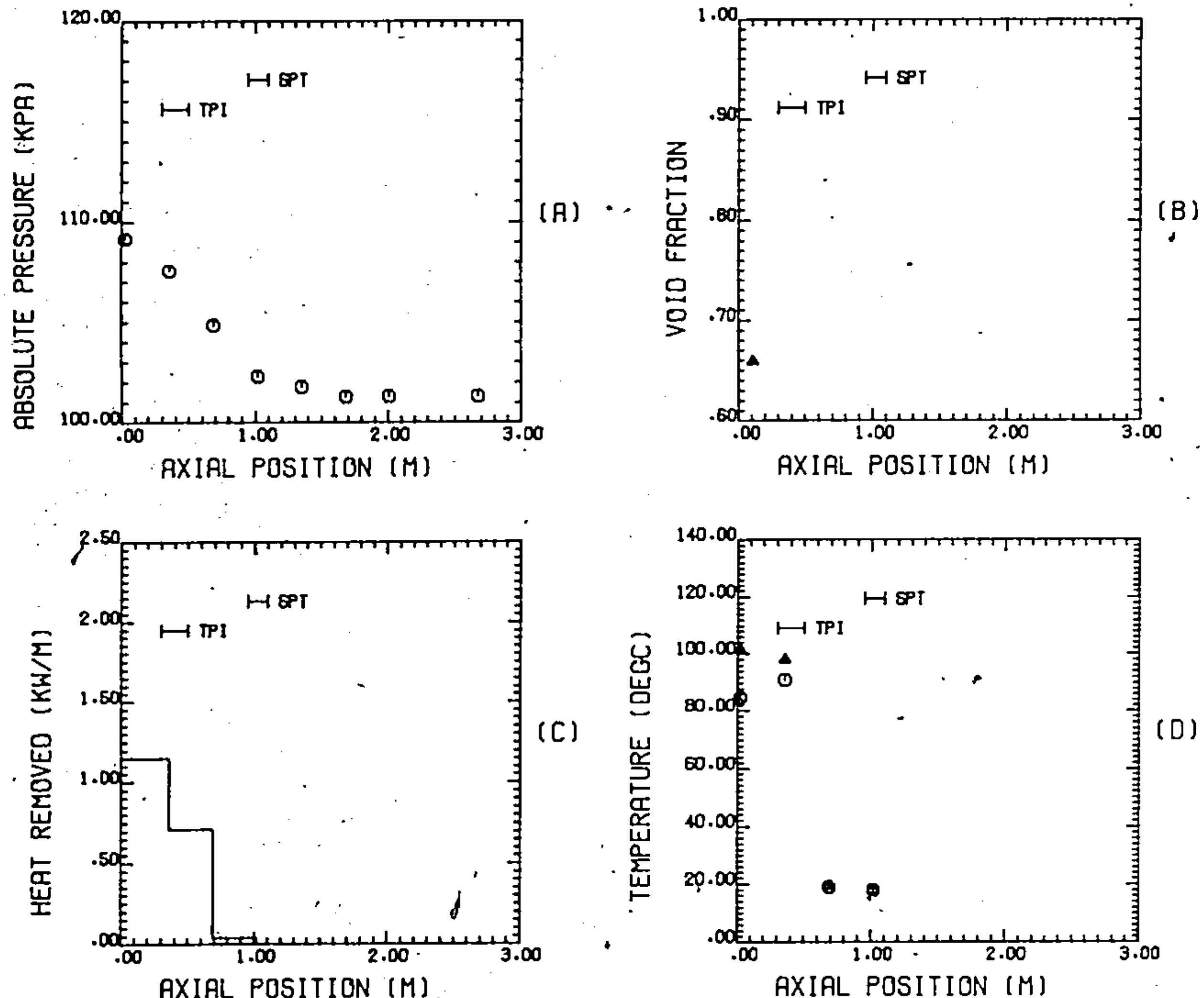

FIGURE G.39
EXPERIMENTAL DATA OF
RUN NO. D03081

TCWI=18 DEGC
TUBE DIA= 1.27 CM O.D.
PBP= 109.167 KPA
PUP= 101.325 KPA
STMFLW= 23.76 G/MIN
QRMV= .6295 KW
SINGLE-PHASE TOP- .95/ 1.10 M
(ABBREVIATED AS SPT IN THE PLOTS)

TWO-PHASE INTERFACE- .30/ .50 M
(ABBREVIATED AS TPI IN THE PLOTS)

LEGEND OF TEMPERATURE PLOT
ʘ = NEAR WALL
▲ = [illegible]TER LINE

AVERAGE VOID FRACTIONS

MEASURED = .6588
CALCULATED = .5723

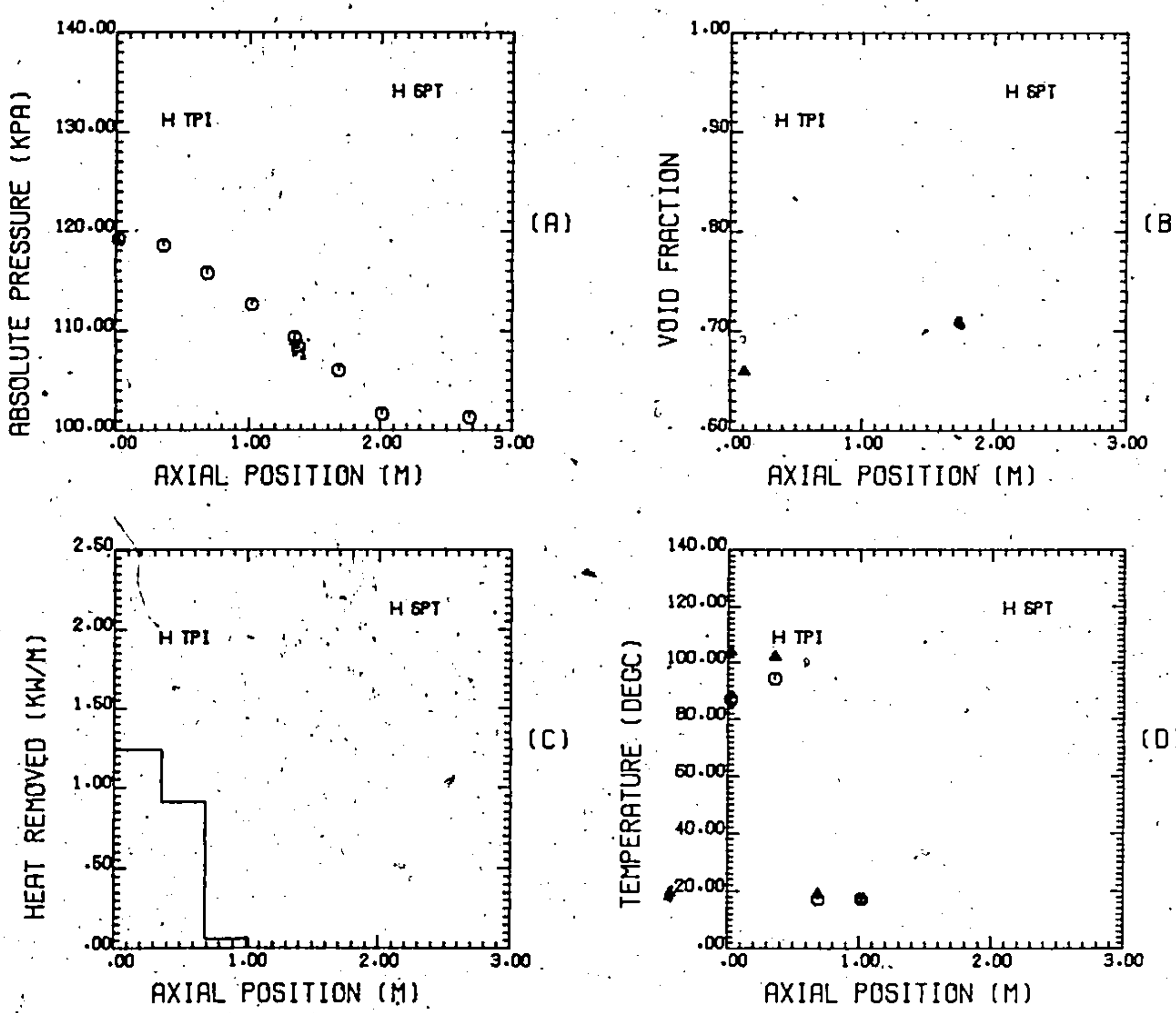

FIGURE G.40
EXPERIMENTAL DATA OF
RUN NO. D21075

TCWI=18 DEGC
TUBE DIA= 1.27 CM O.D.
PBP= 121.769 KPA
PUP= 101.325 KPA
STMFLW= 24.30 G/MIN
QRMV= .7289 KW
SINGLE-PHASE TOP- 2.09/ 2.16 M
(ABBREVIATED AS SPT IN THE PLOTS)

TWO-PHASE INTERFACE- .35/ .42 M
(ABBREVIATED AS TPI IN THE PLOTS)

LEGEND OF TEMPERATURE PLOT
ʘ = NEAR WALL
▲ = CENTER LINE

AVERAGE VOID FRACTIONS

MEASURED = .6588
CALCULATED = .7793

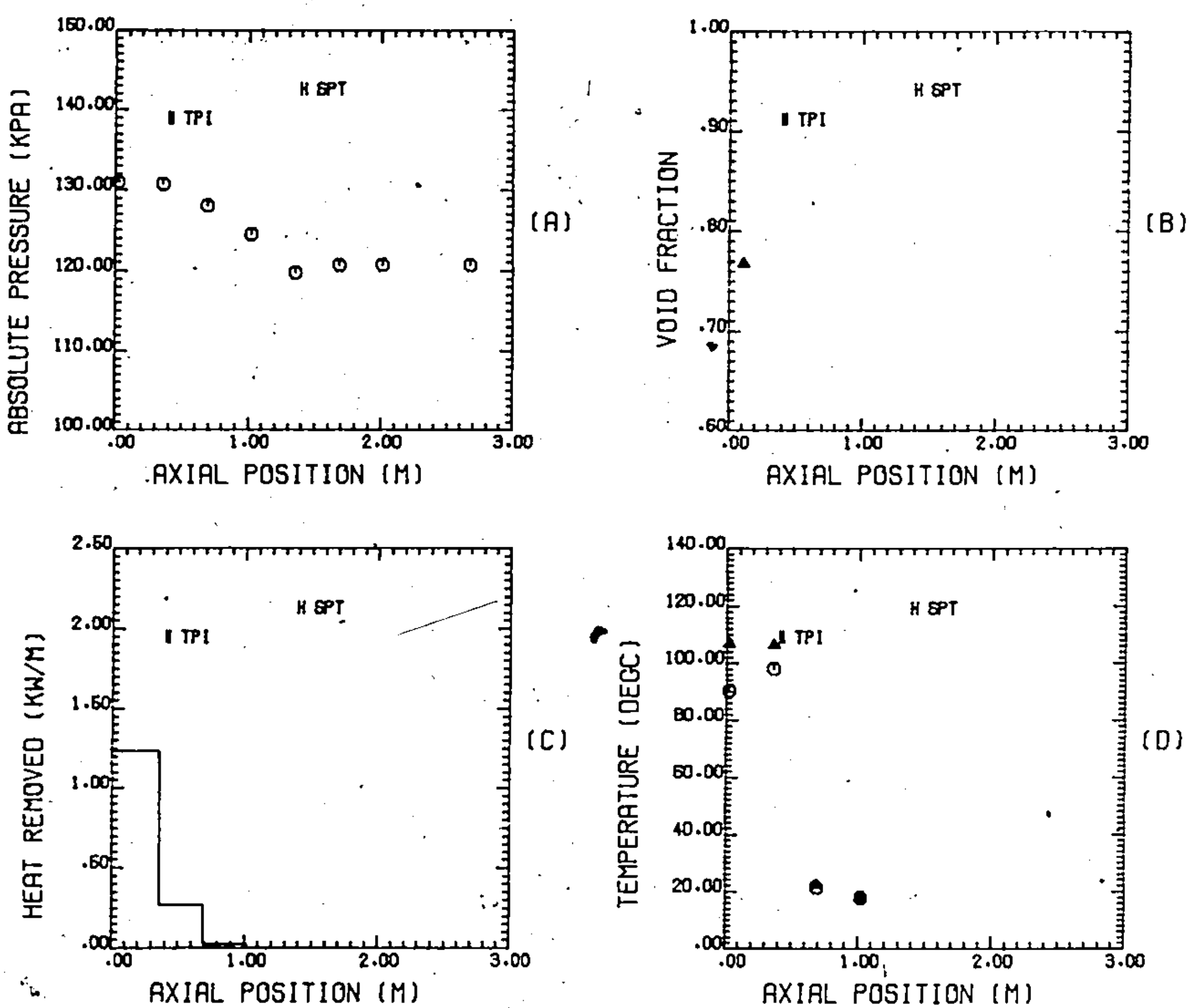

FIGURE G.41
EXPERIMENTAL DATA OF
RUN NO. D14084

TCWI=18 DEGC
TUBE DIA= 1.27 CM O.D.
PBP= 131.048 KPA
PUP= 120.745 KPA
STMFLW= 23.48 G/MIN
QRMV= .5047 KW
SINGLE-PHASE TOP= 1.39/ 1.43 M
(ABBREVIATED AS SPT IN THE PLOTS)

TWO-PHASE INTERFACE= .40/ .43 M
(ABBREVIATED AS TPI IN THE PLOTS)

LEGEND OF TEMPERATURE PLOT
⊖ = NEAR WALL
▲ = CENTER LINE

AVERAGE VOID FRACTIONS

MEASURED = .7679
CALCULATED = .7957

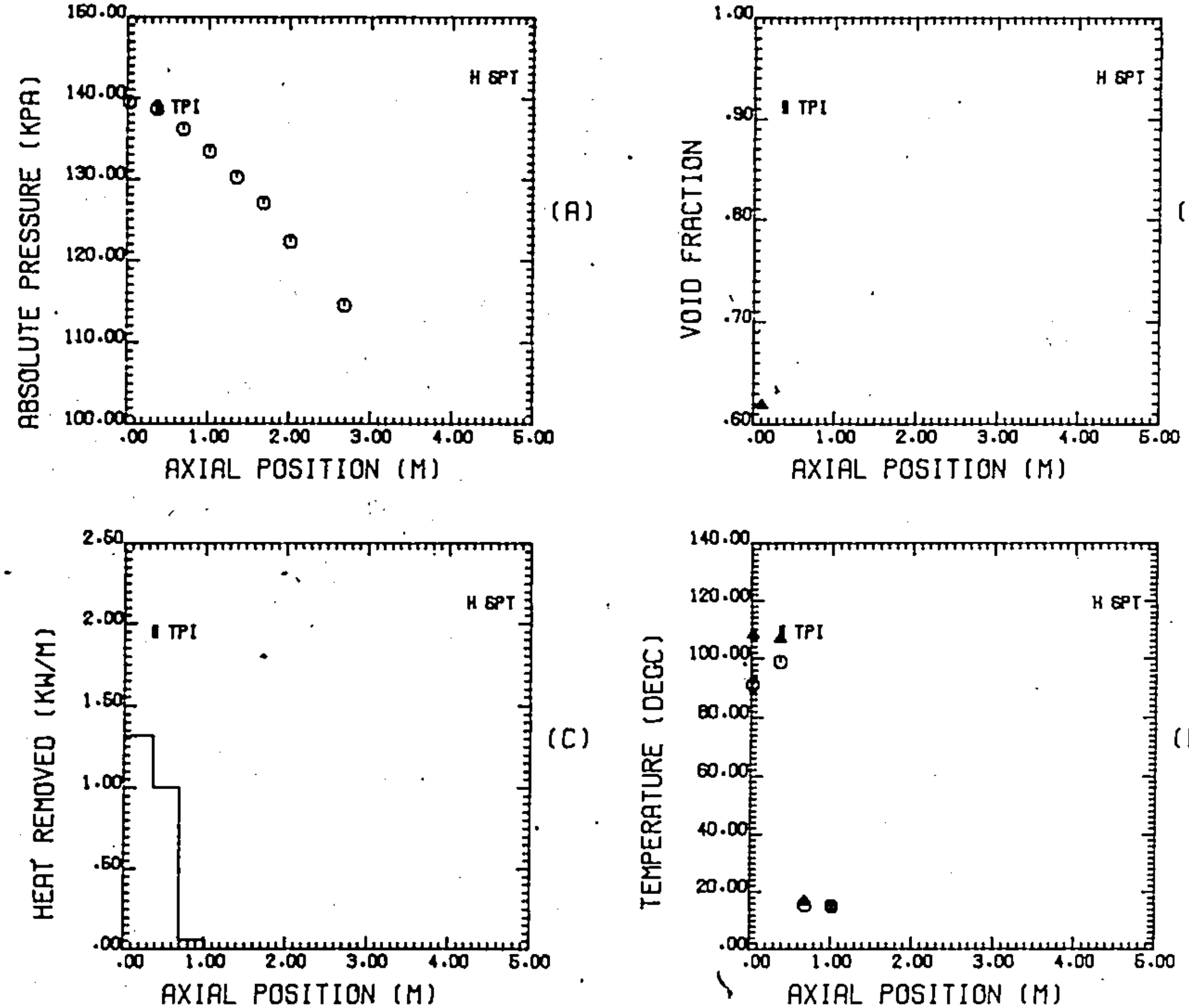

FIGURE G.42
EXPERIMENTAL DATA OF
RUN NO. D21071

TCHI=18 DEGC
TUBE DIA= 1.27 CM O.D.
PBP= 141.676 KPA
PUP= 101.325 KPA
STMFLW= 25.42 G/MIN
QRMV= .7840 KW
SINGLE-PHASE TOP= 4.23/ 4.30 M
(ABBREVIATED AS SPT IN THE PLOTS)

TWO-PHASE INTERFACE= .35/ .40 M
(ABBREVIATED AS TPI IN THE PLOTS)

LEGEND OF TEMPERATURE PLOT
ʘ = NEAR WALL
▲ = CENTER LINE

AVERAGE VOID FRACTIONS

MEASURED = .6191
CALCULATED = .7397

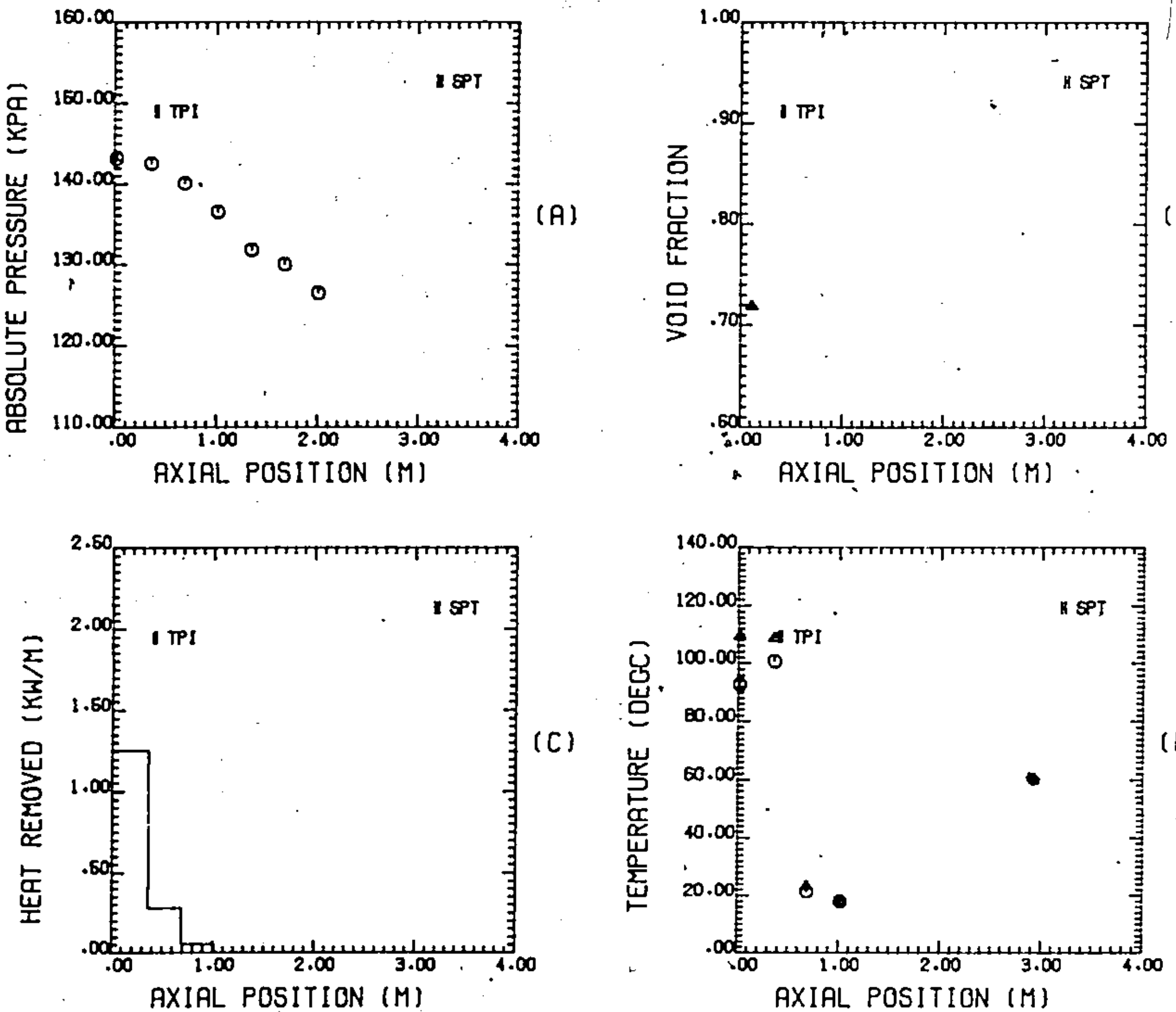

FIGURE G.43
EXPERIMENTAL DATA OF
RUN NO. D14083

TCHI=18 DEGC
TUBE DIA= 1.27 CM O.D.
PBP= 143.126 KPA
PUP= 120.543 KPA
STMFLW= 24.81 G/MIN
QRMV= .5124 KW
SINGLE-PHASE TOP= 3.19/ 3.23 M
(ABBREVIATED AS SPT IN THE PLOTS)

TWO-PHASE INTERFACE= .40/ .43 M
(ABBREVIATED AS TPI IN THE PLOTS)

LEGEND OF TEMPERATURE PLOT
⊙ = NEAR WALL
▲ = CENTER LINE

AVERAGE VOID FRACTIONS

MEASURED = .7188
CALCULATED = .7428

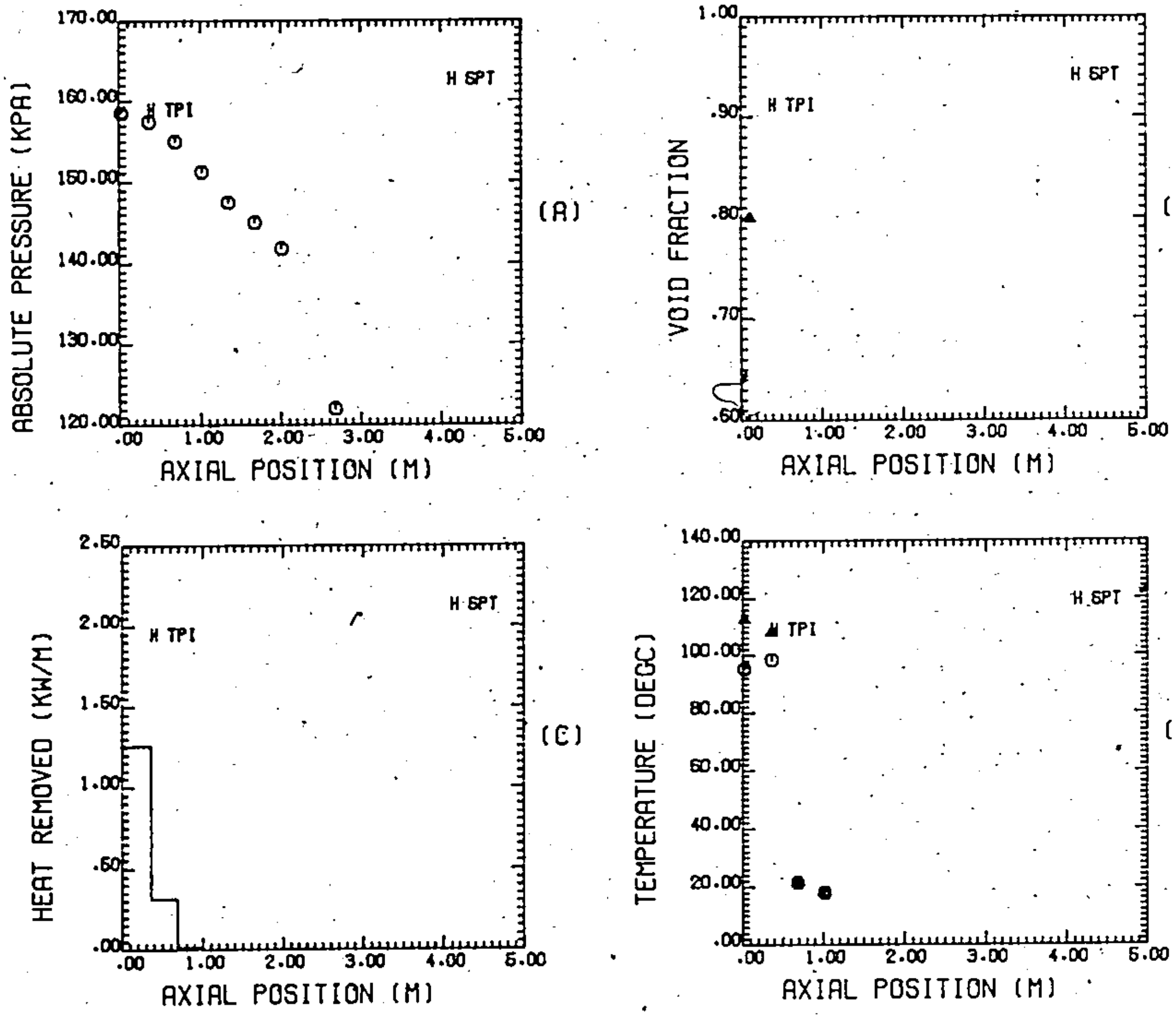

FIGURE G.44
EXPERIMENTAL DATA OF
RUN NO. D14081

TCWI=18 DEGC
TUBE DIA= 1.27 CM O.D.
PBP= 158.512 KPA
PUP= 121.647 KPA
STMFLW= 27.12 G/MIN
QRMV= .5218 KW
SINGLE-PHASE TOP= 4.10/ 4.18 M
(ABBREVIATED AS SPT IN THE PLOTS)

TWO-PHASE INTERFACE= .37/ .43 M
(ABBREVIATED AS TPI IN THE PLOTS)

LEGEND OF TEMPERATURE PLOT
⊙ = NEAR WALL
▲ = CENTER LINE

AVERAGE VOID FRACTIONS

MEASURED = .8000
CALCULATED = .7083

FIGURE G.2.6 : LOCAL MEASUREMENTS IN 1.27 CM
O.D. TUBE WITH TCWI = $45^{o}C$

FIGURES G.45 TO G.50 : LOCAL MEASUREMENTS IN
1.27 CM O.D. TUBE
WITH TCWI = $45^{o}C$

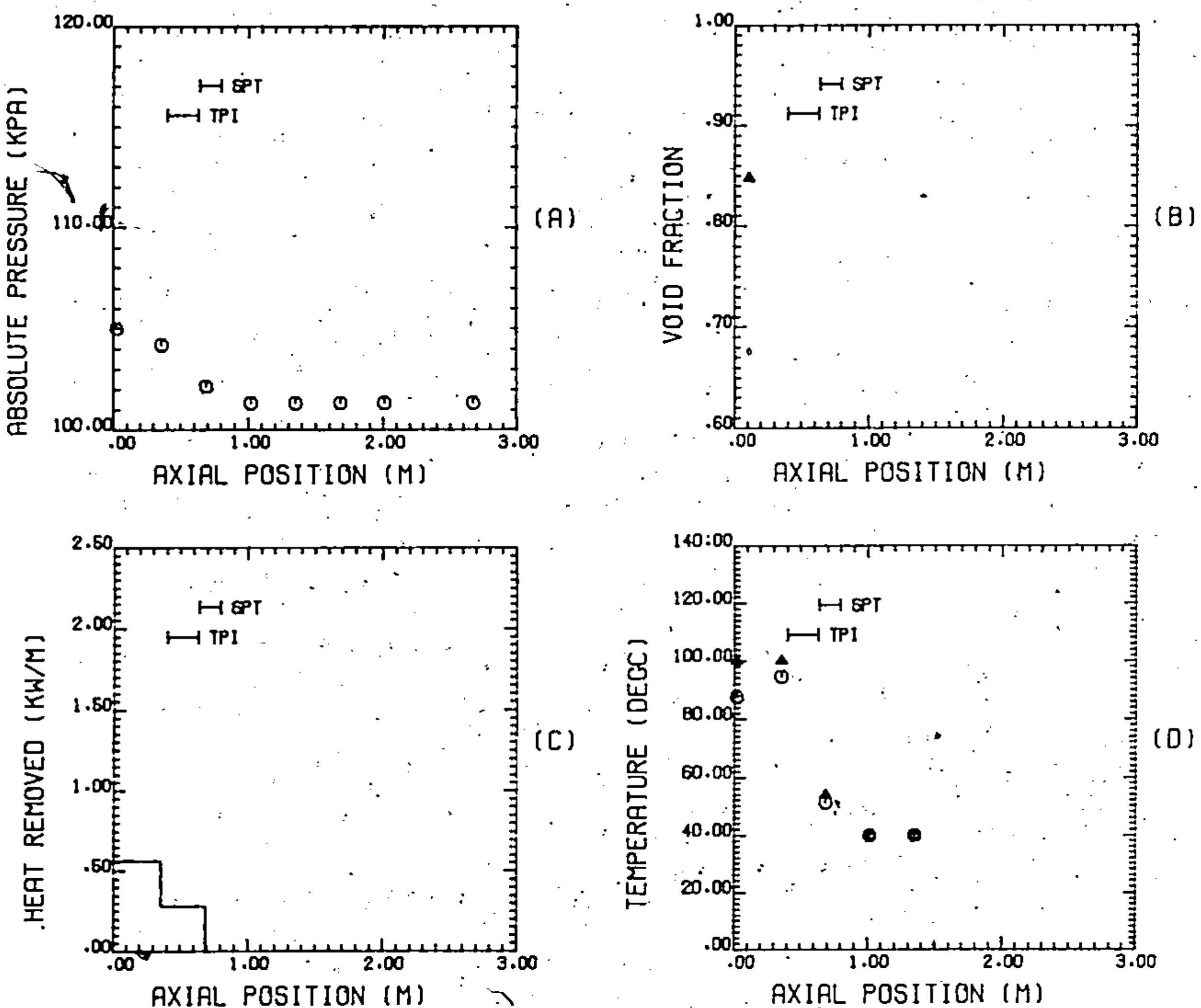

FIGURE G.45
EXPERIMENTAL DATA OF
RUN NO. D11087

TCWI= 45 DEGC
TUBE DIA= 1.27 CM O.D.
PBP= 105.013 KPA
PUP= 101.325 KPA
STMFLW= 21.13 G/MIN
QRMV= .2793 KW
SINGLE-PHASE TOP= .64/ .80 M
(ABBREVIATED AS SPT IN THE PLOTS)

TWO-PHASE INTERFACE= .40/ .63 M
(ABBREVIATED AS TPI IN THE PLOTS)

LEGEND OF TEMPERATURE PLOT
⊙ = NEAR WALL
▲ = CENTER LINE

AVERAGE VOID FRACTIONS

MEASURED = .8474
CALCULATED = .7452

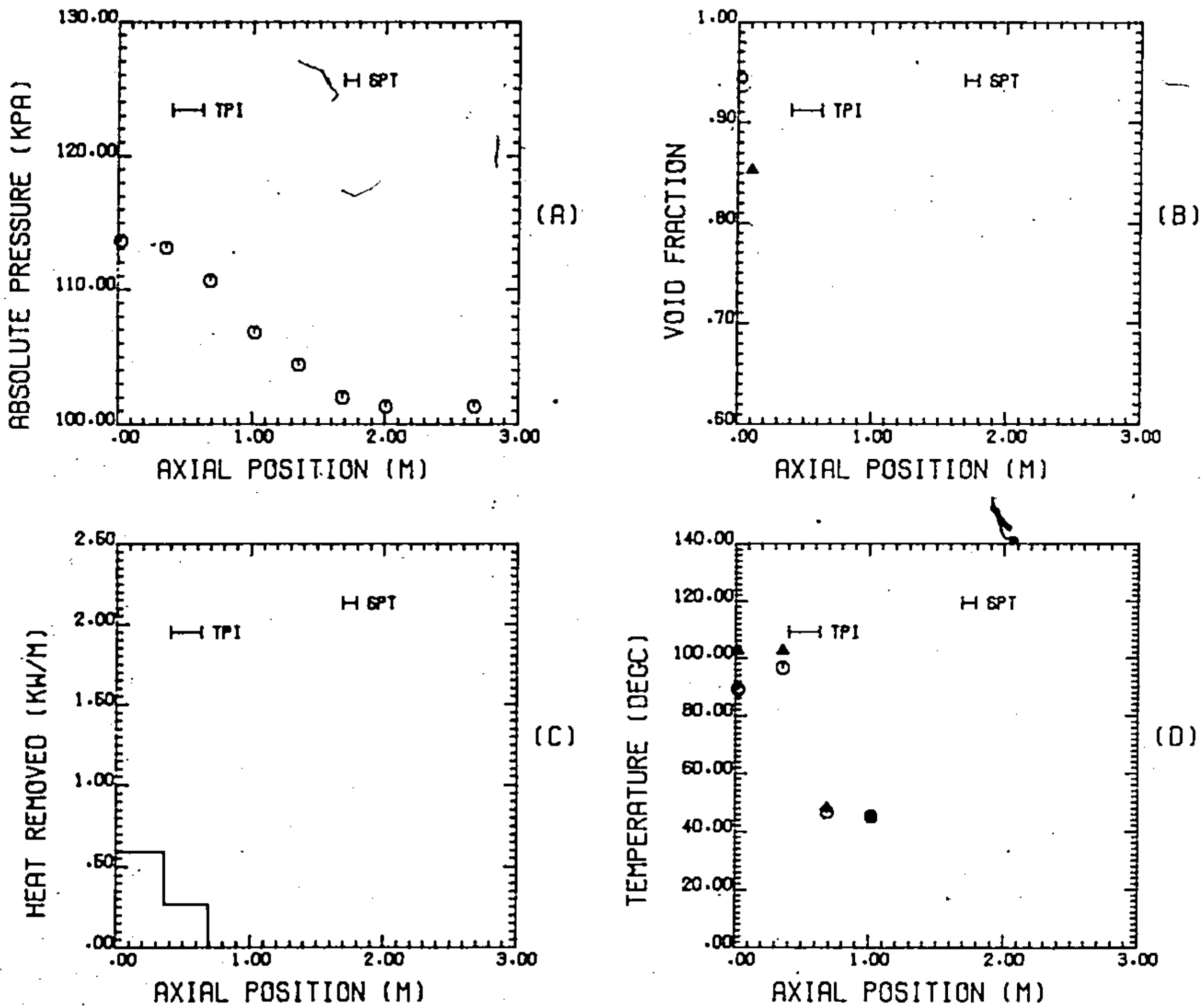

FIGURE G.46
EXPERIMENTAL DATA OF
RUN NO. D11085

TCWI= 45 DEGC
TUBE DIA= 1.27 CM O.D.
PBP= 113.644 KPA
PUP= 101.325 KPA
STMFLW= 21.86 G/MIN
QRMV= .2807 KW
SINGLE-PHASE TOP= 1.69/ 1.79 M
(ABBREVIATED AS SPT IN THE PLOTS)

TWO-PHASE INTERFACE= .40/ .63 M
(ABBREVIATED AS TPI IN THE PLOTS)

LEGEND OF TEMPERATURE PLOT
⊙ = NEAR WALL
▲ = CENTER LINE

AVERAGE VOID FRACTIONS

MEASURED = .8529
CALCULATED = .8199

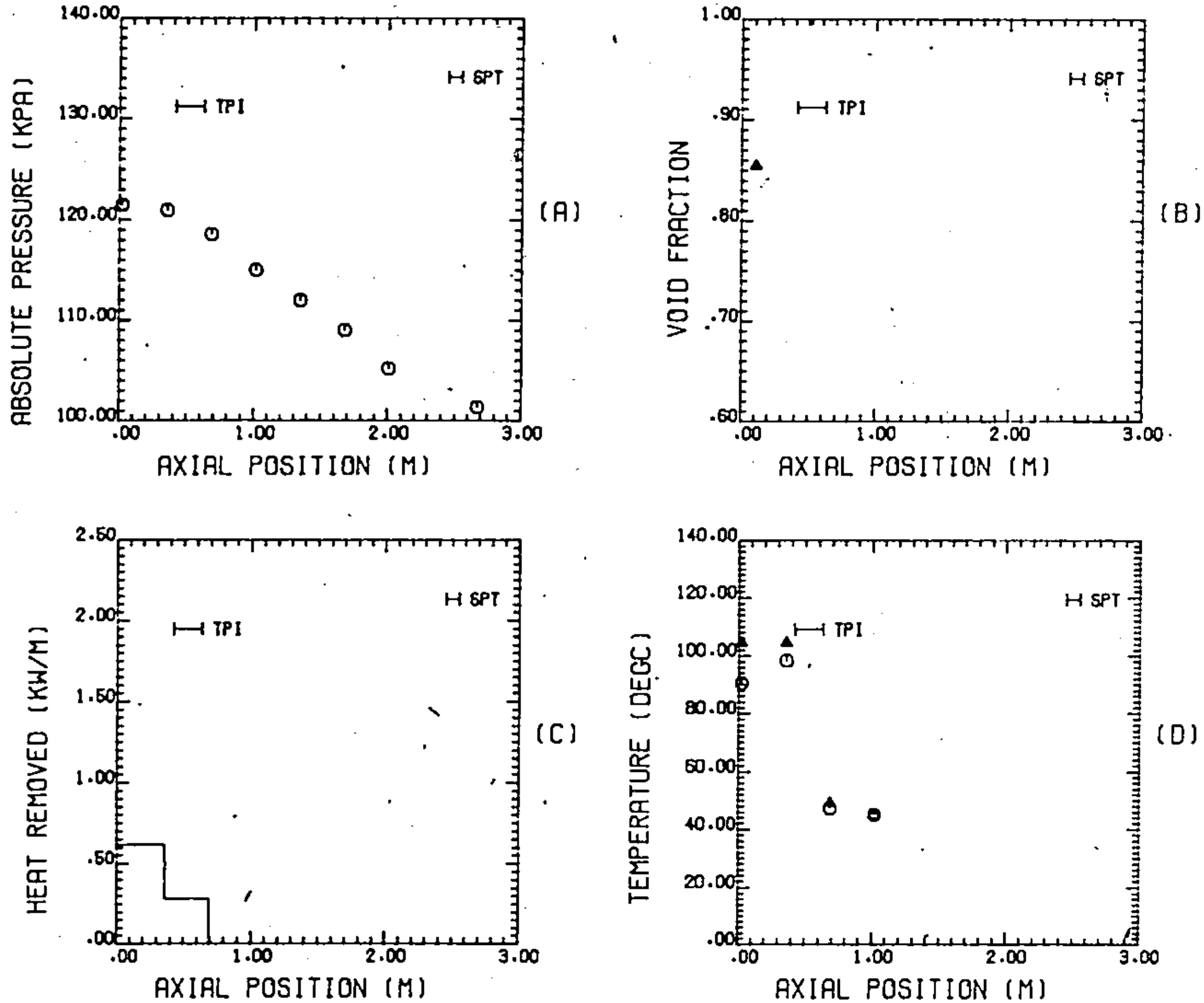

FIGURE G.47
EXPERIMENTAL DATA OF
RUN NO. D11083

TCWI= 45 DEGC
TUBE DIA= 1.27 CM O.D.
PBP= 121.449 KPA
PUP= 101.325 KPA
STMFLW= 22.20 G/MIN
QRMV= .2974 KW
SINGLE-PHASE TOP= 2.45/ 2.55 M
(ABBREVIATED AS SPT IN THE PLOTS)

TWO-PHASE INTERFACE= .42/ .63 M
(ABBREVIATED AS TPI IN THE PLOTS)

LEGEND OF TEMPERATURE PLOT
⊙ = NEAR WALL
▲ = CENTER LINE

AVERAGE VOID FRACTIONS

MEASURED = .8546
CALCULATED = .8462

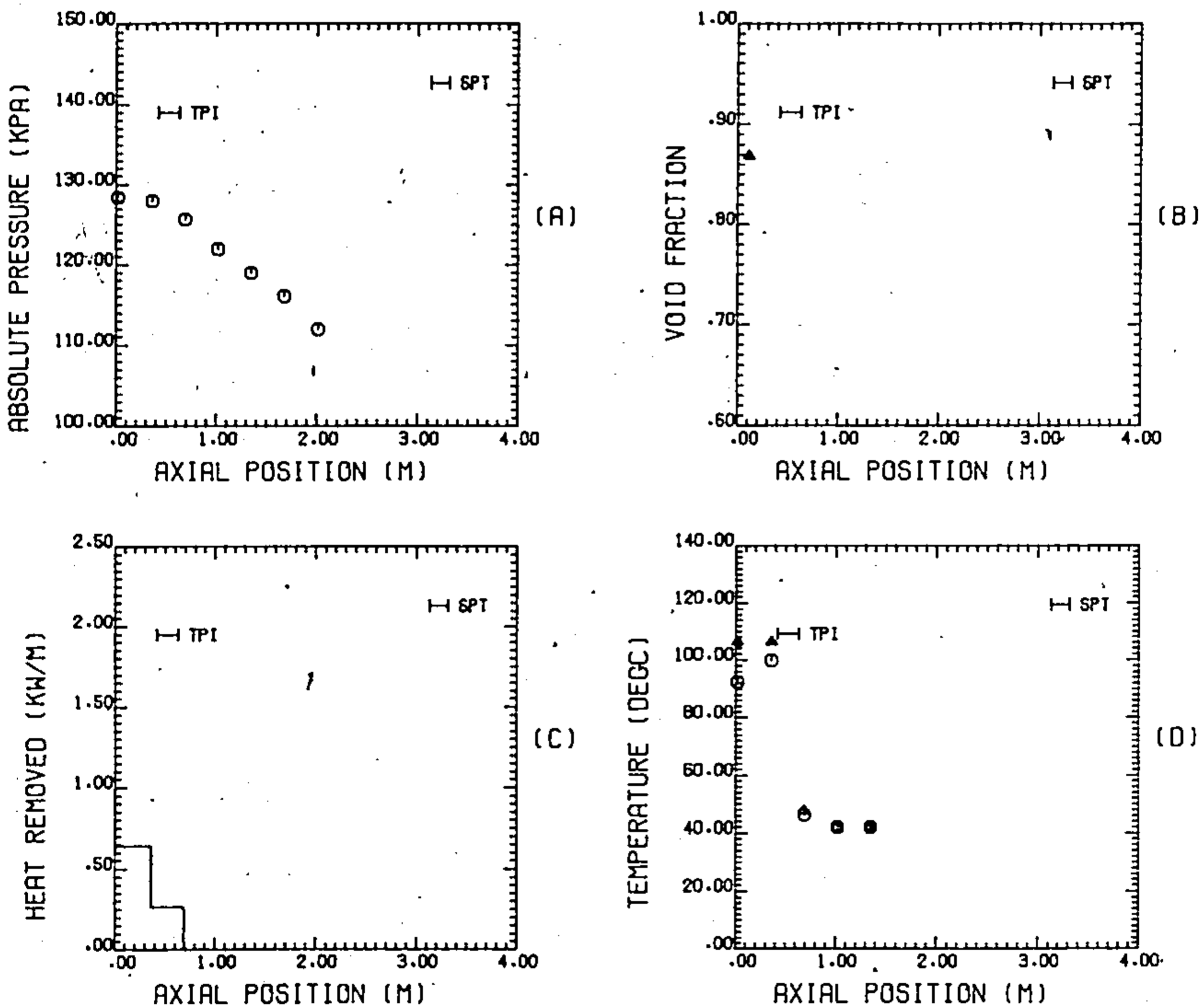

FIGURE G.48
EXPERIMENTAL DATA OF
RUN NO. D11082

TCWI= 45 DEGC
TUBE DIA= 1.27 CM O.D.
PBP= 128.447 KPA
PUP= 101.325 KPA
STMFLW= 23.12 G/MIN
QRMV= .2992 KW

SINGLE-PHASE TOP- 3.13/ 3.31 M
(ABBREVIATED AS SPT IN THE PLOTS)

TWO-PHASE INTERFACE- .42/ .63 M
(ABBREVIATED AS TPI IN THE PLOTS)

*LEGEND OF TEMPERATURE PLOT
⊙ = NEAR WALL
▲ = CENTER LINE

AVERAGE VOID FRACTIONS

MEASURED = .8691
CALCULATED = .8572

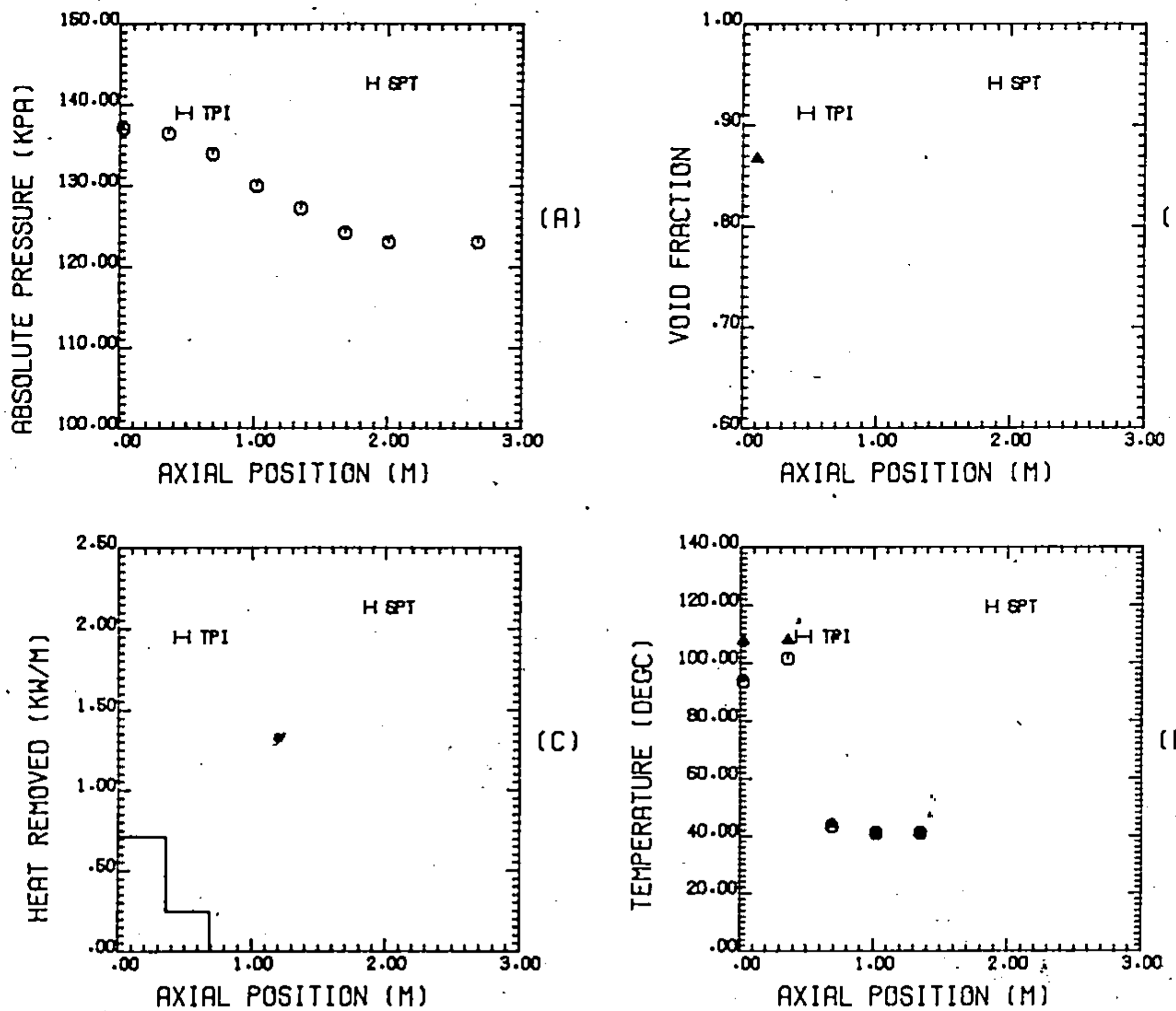

FIGURE G.49
EXPERIMENTAL DATA OF
RUN NO. D110810

TCWI= 45 DEGC
TUBE DIA= 1.27 CM O.D.
PBP= 137.1 KPA
PUP= 123.014 KPA
STMFLW= 23.51 G/MIN
QRMV= .3170 KW
SINGLE-PHASE TOP= 1.84/ 1.92 M
(ABBREVIATED AS SPT IN THE PLOTS)

TWO-PHASE INTERFACE= .42/ .53 M
(ABBREVIATED AS TPI IN THE PLOTS)

LEGEND OF TEMPERATURE PLOT
⊖ = NEAR WALL
▲ = CENTER LINE

AVERAGE VOID FRACTIONS

MEASURED = .8671
CALCULATED = .8055

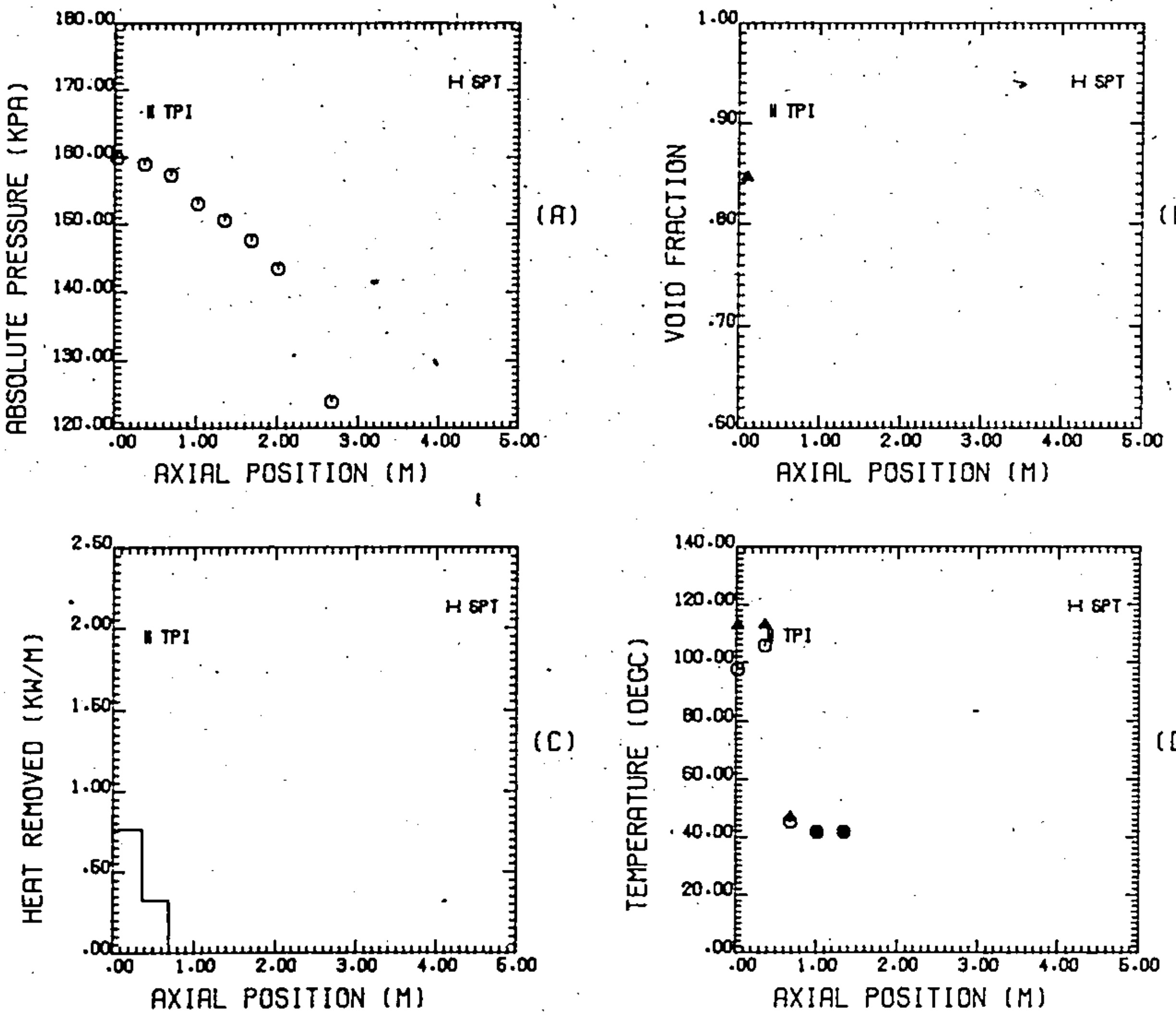

FIGURE G.50
EXPERIMENTAL DATA OF
RUN NO. D11088

TCWI= 45 DEGC
TUBE DIA= 1.27 CM O.D.
PBP= 159.853 KPA.
PUP= 123.869 KPA
STMFLW= 26.70 G/MIN
QRMV= .3603 KW
SINGLE-PHASE TOP= 4.13/ 4.27 M
(ABBREVIATED AS SPT IN THE PLOTS)

TWO-PHASE INTERFACE= .40/ .45 M
(ABBREVIATED AS TPI IN THE PLOTS)

LEGEND OF TEMPERATURE PLOT
⊙ = NEAR WALL
▲ = CENTER LINE

AVERAGE VOID FRACTIONS

MEASURED = .8460
CALCULATED = .7123

REFERENCES

[1] Menely, D.A. and Hancox, W.T., "Prédictions des conséquences d'une perte de caloporteur dans les réacteurs CANDU-PHWR, EACL, Rapport no 7767F, Chalk River, Ontario, septembre 1982.

[2] Feyginberg, Y., Sergejewich, P. and Midvidy, W.I., "A Method for Assessing Reactor Core Cooling without Forced Circulation", The Second International Topical Meeting on Nuclear Reactor Thermal-Hydraulic, Santa Barbara, California, USA, January 11-14, 1983, pp. 808-815.

[3] Deakin, A.W., "Review of Flooding Correlation for Reflux Condensers", AERE-M2923, UKAEA, October 1977.

[4] Mandl, R.M. and Weiss, P.A., "PKL Test On Energy Transfer Mechanisms during Small-Break LOCAs", Nuclear Safety, Vol. 23, No. 2, March-April 1982, pp. 146-154.

[5] Loomis, G.G. and Soda, K., "Results of the Semiscale MOD-2A Natural Circulation Experiments", NUREG/CR-2335, September 1982.

[6] Burchill, W.E., "Physical Phenomena of Small-Break Loss-of-Coolant Accident in a PWR", Nuclear Safety, Vol. 23, No. 5, September-October 1982, pp. 525-536.

[7] Danylo, L., Private communication, Hydro-Québec, Sûreté et analyse centrale nucléaire Gentilly 2, novembre 1983.

[8] Calia, C. and Griffith, P., "Modes of Circulation in an Inverted U-Tube Array with Condensation", HTD-Vol. 15, ASME, New York, 1981.

[9] Nguyen, Q.T. and Banerjee, S., "Flow Regimes and Hea Removal Mechanisms in a Single Inverted U-Tube Steam Condenser", ANS Transactions, Vol. 43, 1982, pp. 788-789.

[10] English, K.G., Jones, W.T., Spiller, R.C., and Orr, V., "Criteria of Flooding and Flooding Correlation Studies with a Vertical Updraft Partial Condenser", Chem.Eng.Prog., Vol. 59, No. 7, 1963.

[11] Diehl, J.E. and Koppany, C.R., "Flooding Velocity Correlations for Gas-Liquid Counterflow in Vertical Tubes", Chem.Eng.Prog.Symp. Series, Vol. 65, No. 92, 1969, pp. 77-88.

[12] Deakin, A.W., Pulling, D.J. and Owen, R.G., "Flooding in Reflux Condensers", Inst. of Chemical Engineering, Birmingham, April 1978.

[13] Wallis, G.B., "One-Dimensional Two-Phase Flow", McGraw-Hill, New York, 1969.

[14] Russell, C.M.B., "Condensation of Steam in a Long Reflux Tube", HTFS 1980, Research Symposium Paper No. HTFS RS 352, July 1980.

[15] Seban, R.A. and Hodgson, J.A., "Laminar Film Condensation in a Tube with Upward Vapor Flow", Int.J. Heat Mass Transfer, Vol. 25, No. 9, 1982, pp. 1291-1300.

[16] Tien, C.L., Fukano, T., Hijikata, K. and Chen, S.J., "Reflux Condensation and Operating Limits of Counter-Current Vapor-Liquid Flows in Closed Tube", EPRI Report No. NP-2648, November 1982.

[17] Sun, B. K-H, Toren, M. and Oh, S. "Reflux Condensation in a Vertical Channel Flow", 2nd Int. Topical Meeting on Nuclear Reactor Thermal-Hydraulics, Santa Barbara, California, January 1983.

[18] . Nusselt, W., Z Ver. Deut. Ing., Vol. 60, 1916, pp. 541-569. (Also in Collier, J.G.,"Convective Boiling and Condensation", McGraw-Hill, 1972, pp. 314-318).

[19] Chung, K.S., "Flooding Phenomena in Counter-Current Two-Phase Flow Systems", Ph.D. Thesis, University of California, Berkeley, 1978.

[20] Tien, C.L., Chung, K.S. and Liu, C.P., "Flooding in Two-Phase Counter-Current Flows-I: Analytical Modeling", Physico-Chemical Hydrodynamics, Vol. 1, 1980, pp. 195-207.

[21] Chung, K.S., Liu, C.P., Tien, C.L., "Flooding in Two-Phase Counter-Current Flows-II: Experimental Investigation", Physico-Chemical Hydrodynamics, Vol. 1, 1980, pp. 209-220.

[22] Kutateladze, S.S., "Elements of Hydrodynamics of Gas-Liquid Systems", Fluid Mechanics-Soviet Research, Vol. 1, 1972, pp. 29-50.

[23] Dukler, A.E. and Smith, L., "Two-Phase Interactions in Counter-Current Flow: Studies of the Flooding Mechanism", NUREG/CR-0617, 1977.

[24] Tien, C.L. and Lice, C.P., "Survey on Vertical Two-Phase Counter-Current Flooding", EPRI Topical Report NP-984, February 1979.

[25] Bankoff, S.G. and Lee, S.C., "A Comparison of Flooding Models for Air-Water and Steam-Water Flow", in Advances in Two-Phase Flow and Heat Transfer, Vol. 1, edited by Kakaç. S. and Ishii, M., Martinus Nyhoof Publis., The Hague, 1983, pp. 745-780.

[26] Suzuki, S. and Ueda, T., "Behaviour of Liquid Films and Flooding in Counter-Current Two-Phase Flow - Part 1: Flow in Circular Tubes", Int.J. Multiphase Flow, Vol. 3, 1977, pp. 517-532.

[27] Hewitt, G.F. and Wallis, G.B., "Flooding and Associated Phenomena in Falling Film Flow in a Vertical Tube", Multi-Phase Flow Symposium, Winter Annual Meering ASME, Philadelphia, 1963, pp. 62-74.

[28] Imura, H., Kusuda, H. and Funatsu, S., "Flooding Velocity in a Counter-Current Annular Two-Phase Flow", Chem.Eng. Science, Vol. 32, 1977, pp. 79-87.

[29] Hawley, D.L. and Wallis, G.B., "Experimental Study of Liquid Film Fraction and Pressure Drop Characteristics in Vertical Counter-Current Annular Flow", EPRI Topical Report No. 2280, February 1982.

[30] Bharathan, D. and Wallis, G.B., "Air-Water Counter-Current Annular Flow", Int.J.Multiphase Flow, Vol. 9, 1983, pp. 349-366.

[31] Clift, R., Prictchard, C.L. and Nedderman, R.M., "The Effect of Viscosity on the Flooding Conditions in Wetted Wall Columns", Chem.Eng.Science, Vol. 21, 1966, pp. 87-95.

[32] Cetinbudaklar, A.G. and Jameson, G.J., "The Mechanism of Flooding in Vertical Counter-Current Two-Phase Flow", Chem.Eng.Science, Vol. 24, 1969, pp. 1669-1680.

[33] Bankoff, S.C. and Lee, S.C., "Stability of Steam-Water Counter-Current Flow in an Inclined Channel Flooding", ASME Journal of Heat Transfer, Vol. 105, November 1983, pp. 713-718.

[34] Shearer, C.J. and Davidson, J.F., "The Investigation of a Standing Wave Due to Gas Blowing Upwards over a Liquid Film; Its Relation to Flooding in Wetted-Wall Columns", J.Fluid Mech., 1965, pp. 321-336.

[35] Wallis, G.B. and Kuo, J.T., "The Behavior of Gas-Liquid Interfaces in Vertical Tubes", Int.J.Multiphase Flow, Vol. 2, 1976, pp. 521-536.

[36] Grolmes, M.A., Lambert, G.A. and Fauske, H.K., "Flooding in Vertical Tubes", AIChE Symposium on Multiphase Flow Systems, Paper 38, 1974.

[37] Richter, H.J., "Flooding in Tubes and Annuli", Int.J.Multiphase Flow, Vol. 7, 1981, pp. 647-658.

[38] Taitel, Y., Barnea, D. and Dukler, A.E., "A Film Model for the Prediction of the Flooding and Flow Reversal for Gas-Liquid Flow in Vertical Tubes", International J. Multiphase Flow, Vol. 8, No. 1, 1982, pp. 1-10.

[39] Lighthill, M.H. and Whitham, G.F., "On Kinematic Waves-I: Flood Movement in Long Rivers:, Proc.Royal Soc. London, Vol. 229-A, 1955, pp. 281-316.

[40] Zvirin, Y., Duffey, R.B., and Sun, B. K-H, "On the Derivation of a Counter-current Flooding Theory", Symp. on Fluid and Heat Transfer Over Rod and Tube Bundles", ASME, New York, 1979, pp. 111-119.

[41] Tien, C.L., "A Simple Analytical Model for Counter-Current Flow Limiting Phenomena with Vapor Condensation", Letters in Heat and Mass Transfer, Vol. 4, 1977, pp. 231-238.

[42] Koh, J.C.Y., "An Integral Treatment of Two-Phase Boundary Layer in Film Condensation", ASME J. of Heat Transfer, August 1961, pp. 359-362.

[43] Chen, M.M., "An Analytical Study of Laminar Film Condensation: Part 1 - Flat Plates", ASME J. of Heat Transfer, February 1961, pp. 48-54.

[44] Unsal, M. and Thomas, W.C., "Linearized Stability Analysis of Film Condensation", ASME J. of Heat Transfer, Vol. 100, November 1978, pp. 629-634.

[45] Schlichting, H., "Boundary Layer Theory", McGraw-Hill, New York, 1968.

[46] Delhaye, J.M., "Thermohydraulics of Two-Phase Systems for Industrial Design and Nuclear Engineering", Hemisphere Publis. Corp., Washington, 1981.

[47] Spindler, B., Solesio, J.N. and Delhaye, J.M., "On the Equation Describing the Instabilities of Liquid Films with Interfacial Phase Change in Two-Phase Momentum Heat and Mass Transfer in Chemical, Process and Energy Engineering Systems", Vol. 1, edited by F. Durst et al., Hemisphere Publis. Corp., Washington, 1979.

[48] Unsal, M., "A Linearized Stability Analysis of Forced Vapor Flow Condensation", in Advances in Two-Phase Flow and Heat Transfer, Vol. I, edited by S. Kakaç and M. Ishii, Martinus Nyhoff Publis., The Hague, 1983, pp. 725-743.

[49] Lamb, H., "<u>Hydrodynamics</u>", Dover Publis., New York, 1945.

[50] Marchal, E. and Lee, C.Y., "Stability Characteristics of Condensate Films", Warme-und Stoffubertragung, Vol. 1, 1973, pp. 32-37.

[51] Hseih, D.Y., "Effects of Heat and Mass Transfer on Rayleigh-Taylor Instability", ASME J. of Basic Eng., March 1972, pp. 156-162.

[52] Spindler, B., "Etude de la stabilité des films liquides avec flux de chaleur à la paroi et changement de phase à l'interface", Rapport CEA-R-5061, Commissariat à l'Energie Atomique, France, 1981.

[53] Brooke-Benjamin, T., "Shearing Flow Over a Wavy Boundary", J. of Fluid Mech., Vol. 6, 1959, pp. 161-205.

[54] Miles, J.W., "On the Generation of Surface Waves by Shear Flows", J. Fluid Mech., Vol. 3, 1957, pp. 185-204.

[55] Ostrack, J. and Koestel, A., "Film Instabilities in Two-Phase Flows", AIChe Journal, Vol. 11, 1966, pp. 294- .

[56] Benedict,. R.P., "Fundamentals of Temperature, Pressure and Flow Measurements", John Wiley, New York,1977.

[57] Hewitt, R.P., "Measurements of Two-Phase Parameters", Academic Press, London, 1978.

[58] Banerjee, S. and Lahey, R.T., Jr., "Advancements in Two-Phase Flow Instrumentation", Adv.Nucl.Sci. &Tech., Vol. 13, 1981, pp. 227-414.

[59] Banerjee. S., Hussein, E. and Menely, D.A., "Simulation of a Neutron Scattering Method for Measuring Void Fraction in Two-Phase Flow", Nuclear Eng. and Design, Vol. 53, 1979, pp. 393-405.

[60] Hussein, E., "Fast Neutron Scattering Method for Local Void Fraction Distribution Measurement in Two-Phase Flow", Ph.D. Thesis, McMaster University, Hamilton, Ontario, 1983.

[61] Hussein, E., "New Trends in Neutron Diagnosis of Multi-Phase Flows", Third Multiphase Flow and Heat Transfer Symposium-Workshop, Miami Beach, Florida, April 18-20, 1983.

[62] Banerjee, S., Chan, A.M.C., Ramanathan, N. and Yuen, P.S.l., "Fast Neutron Scattering and Attenuation Technique for Measurement of Void Fractions and Phase Distribution in Transient Flow Boiling", Proc. of the 6th International Heat Transfer Conference, Toronto, August 1978, p. 351.

[63] Irons, G.A. and Chang, J.S., "Particle Fraction and Velocity Measurement in Gas-Powder Streams by Capacitance Transducers", Int. J. Multiphase Flow, Vol. 9, No. 3, 1983, pp. 289-297.

[64] Ozgu, M.R. and Chen, J.C., "A Capacitance Method for Measurement of Film Thickness in Two Phase Flow", Rev.Sci. Instrument, Vol. 44, No. 12, December 1973, pp. 1714-1716.

[65] Sparrow, E.M., Minkowycz, W.J. and Saddy, M., "Forced Convection Condensation in the Pressure of Non-Condensible and Interfacial Resistance", Int.J.Heat Mass Transfer, Vol. 10, 1967, pp. 1829-1845.

[66] Maitra, D. and Subba Raju, K., "Vapor Void Fraction in Subcooled Flow Boiling", Nuclear Eng. Design, Vol. 32, 1975, pp. 20-28.

[67] Nickerson, J.R., Whelpton, J., Smith, K. and McKenna, J.A., "A Comparison of Radio Frequency Densitometer, Conductance Void Gauge and an Auburn 1080 Monitor in Two-Phase Flows", in Measurement of Polyphase Flows, 1982 AIAA/ASME Joint Fluids, Plasma, Thermophysics and Heat Transfer Conference, St.Louis, Missouri, June 7-11, 1982.

[68] Orear, J. "Least Squares When Both Variables Have Uncertainties", Am.J.Physics, Vol. 50, October 1982, pp. 912-916.

[69] Bevington, P.R., "<u>Data Reduction and Error Analysis for the Physical Sciences</u>", McGraw-Hill, 1969.

[70] Wallis, G.B., deSieyes, D.C., Rosselli, R.J. and Lacombe, J., "Countercurrent Annular Flow Regimes for Steam and Subcooled Water in a Vertical Tube", EPRI Report NP-1336, 1980.

[71] UPDATE, Version 1, Reference Manual, Document No. 60449900, Control Data Corporation, Sunnyvale, California, 1982.

[72] Girard, R., "Listings of the Data Acquisition and Processing Software", Report to the Dept. of Eng. Physics, McMaster University, 1985.

[73] Banerjee, S. et al., "Ontario Hydro Contract on Transient Two-Phase Flow", Dept. of Eng. Physics, McMaster University, 1980.

[74] Chang, J.S. et al., "Ontario Hydro Contract on Transient Two-Phase Flow", Dept. of Eng. Physics, McMaster University, 1982.

[75] Marxman, G.A. and Burlage, H., "Expansion Coefficients for Orifice Meters in Pipes Less Than One Inch in Diameter", ASME Journal of Basic Engineering, June 1961, pp. 289-298.

[76] Reed. S.B. and Sprange, M.D., "Flowmeter Calibrated for Any Gas in the Range of 1 to 500 Liters per Hour", I&EC Fundamentals, Vol. 7, No. 4, November 1968, pp. 651-655.

[77] Grace, H.P. and Lapple, C.E., "Discharge Coefficients for Small-Diameter Orifices and Flow Nozzles", Trans. of ASME, pp. 639-647, July 1951.

[78] Filbran, T.J. and Griffin, W.A., "Small-Diameter-Orifice Metering", ASME Journal of Basic Engineering, September 1960, pp. 735-740.

[79] "Fluid Meters, Their Theory and Application", 5th ed., ASME, New York, 1959.

[80] Holman, J.P., "Experimental Methods for Engineers", 3rd edition, McGraw-Hill, New York, 1978, pp. 216-220.

[81] Masek, J.A., "Orifice Flange Assemblies in Steam Piping", Heating, Piping & Air Conditioning, October 1967, pp. 133-136.

[82] 1967 ASME Steam Tables - Thermodynamics and Transport Properties of Steam", ASME, New York, December 1967.

[83] Miesse. C.C. and Curth, O.E., "How to Select a Flowmeter", Prod.Eng., May 8, 1961, p. 35.

[84] Vivier, P., Personal Communication, Groupe d'analyse nucléaire, June 1984.

[85] Collier, J.G., "Convective Boiling and Condensation", McGraw-Hill, London, 1972.

[86] Banerjee, S., Chang, J.-S., Girard, R., and Krishman, V.S., "Reflux Condensation and Transition to Natural Circulation in a Vertical U-Tube", ASME Journal of Heat Transfer, Vol. 103, pp. 719-727, 1983.

[87] Nguyen, A. and Banerjee, S., "Criteria for Flow Regime Transition in a Vertical Inverted U-Tube Condenser", 22nd Heat Transfer Conference, Niagara Falls, New York, August 5-8, 1984.

[88] Chang, J.S., Girard, R., Revankar, S., Wan, P.T., Midvidy, W.I., Pauls, R.E., and Sergejewick, P., "Heat Removal Capability of Steam Generators under Reflux Cooling Modes in a CANDU-PHT System", 4th Annual Canadian Nuclear Society Conference, 1983.

[89] Chang, J.S., Girard, R., Raman, R., and Tran, F.B.P., "Measurement of Void Fraction in Vertical Gas-Liquid Two-Phase Flow by Ring Type Capacitance Transducers", Winter Annual Meeting of ASME, New Orleans, Louisiana, December 9-14, FED - Vol. 17, 1984, pp. 93-99.

[90] Bird, R.B., Stewart, W.E., and Lightfoot, E.N., "Transport Phenomena", 7th printing, John Wiley, New York, 1960.

[91] Burmeister, L.C., "Convective Heat Transfer", John Wiley and Son, New York, 1983.

[92] Jacobs, H.R., "An Integral Treatment of Combined Body Force and Forced Convection in Laminar Film Condensation", Int.J.Heat Mass Transfer, Vol. 9, 1966, pp. 637-648.

[93] Schmidt, E., "Properties of Water and Steam in SI-Units", Springer-Verlag, New York, 1982.

[94] Fujii, T., Uehare, H., and Oda, K., "Film-Wise Condensation on a Surface with Uniform Heat Flux and Body Force Convection", Heat Transfer Res. Japan, Vol. 1, 1972, pp. 76-83.

[95] Hewitt, G.F. and Hall-Taylor, N.S., "Annular Two-Phase Flow", Pergamon Press, Oxford, 1970.

[96] Liu, C.P., Tien, C.L., McCarthy, G.E., "Flooding in Vertical Gas-Liquid Counter-Current Flow Through Parallel Paths", EPRI Report NP-2262, 1982.

[97] Spindler, B., "Equations gouvernant l'écoulement plan d'un film liquide avec flux de chaleur de la paroi et changement de phase à l'interface", Rapport CEA-R-5061, Commissariat à l'Energie Atomique, France, 1981.

[98] Popov, N.K. and Rohatgi, V.S., "Effect of Interfacial Shear and Entrainement Models on Flooding Predictions", AIChe Symposium Series, Heat Transfer - Seattle 1983, Vol. 79, No. 225, pp. 190-199.

[99] Craik, A.D.D., "Wind-Generated Waves in Thin Liquid Films", Journal of Fluid Mechanics, Vol. 26, Part 2, 1966, pp. 369-392.

[100] Kays, W.M. and Crawford, M.E., "Convective Heat and Mass Transfer", McGraw-Hill, New York, 1980.

[101] Anshus, B.E. and Goren, S.L., "A Method of Getting Approximate Solutions to the Orr-Sommerfeld Equation for Flow on a Vertical Wall", AIChE Journal, Vol. 12, No. 5, September 1966, pp. 1004-1008.

[102] Solésio, J.N., "La méthode de quadrature par différentiation appliquée à l'hydrodynamique des films liquides", Rapport CEA-R-4888, Commissariat à l'Energie Atomique, France, 1977.

[103] Powell, M.J.D., "A FORTRAN Subroutine for Solving Systems of Non-Linear Algebraic Equations", AERE-R-5847, 1968.

[104] Taitel, Y. and Barnea, D., "A Film Model for the Prediction of Flooding and Flow Reversal for Gas-Liquid Flow in Vertical Tubes", Int.J.Multiphase Flow, Vol. 8, No. 1, 1982, pp. 1-10.

[105] Maron, D.M., and Dukler, A.E., "Flooding and Upward Film Flow in Vertical Tubes - II: Speculations on Film Flow Mechanisms, Int.J.Multiphase Flow, Vol. 10, 1984, pp. 599-621.

[106] Wan, P.T., Girard, R., and Chang, J.S., "The Role of Flooding Phenomena in Reflux Condensation in a Vertical Inverted U-Tube", in Multi-Phase Flow and Heat Transfer III. Part B: Applications edited --- Vezirogly, I.N. and Bergles, A.E., Elsevier Science Publishers B.V., Amsterdam, 1984.

[107] Na, T.Y., and Chiou, J.P., "Turbulent Natural Convection Over a Slender Circular Cylinder", Warme-und Stoffubertragung, Vol. 14, 1980, pp. 157-164.

[108] Chang, J.S., and Girard, R., "Reflux Condensation Phenomena in a Vertical Tube Side Condenser" in Advancement in Heat Exchanger, G.F. Hewitt ed., Hemisphere Publisher, Washington, 1980.

[109] Rayleigh, L.,"Theory of Sound - Vol. II", Dover, New York, 1945.

[110] Bhatt, B.L., and Wedekind, C.L., A Self-Sustained Oscillatory Flow Phenomena in Two-Phase Condensing Flow Systems", ASME Journal of Heat Transfer, Vol. 102, November 1980, pp. 694-700.

[111] Friedly, J.C., "Dynamic Behavior of Processes", Prentice-Hall, Englewood Cliffs, New Jersey, 1972.

[112] Hirschburg, R.I., and Florshuetz, L.W., "Laminar Wavy-Film Flow: Part I - Hydrodynamic Analysis, Part II - Condensation and Evaporation", J. Heat Transfer, Vol. 104, pp. 452-464, 1982.

[113] Sofrata, H., "Theoretical Study of Film-Wise Condensation Considering Wave Initiation", Warme-und Stoffubertragung, Vol. 14, pp. 201-210, 1980.